APPLIED COMPUTATIONAL ELECTROMAGNETICS SOCIETY JOURNAL

December 2025
Vol. 40 No. 12
ISSN 1054-4887

The ACES Journal is abstracted in INSPEC, in Engineering Index, DTIC, Science Citation Index Expanded, the Research Alert, and to Current Contents/Engineering, Computing & Technology.

The illustrations on the front cover have been obtained from the ARC research group at the Department of Electrical Engineering, Colorado School of Mines

Published, sold and distributed by: River Publishers, Alsbjergvej 10, 9260 Gistrup, Denmark

THE APPLIED COMPUTATIONAL ELECTROMAGNETICS SOCIETY
http://aces-society.org

EDITORS-IN-CHIEF

Atef Elsherbeni
Colorado School of Mines, EE Dept.
Golden, CO 80401, USA

Sami Barmada
University of Pisa, ESE Dept.
56122 Pisa, Italy

ASSOCIATE EDITORS

Mauro Parise
University Campus Bio-Medico of Rome
00128 Rome, Italy

Yingsong Li
Harbin Engineering University
Harbin 150001, China

Riyadh Mansoor
Al-Muthanna University
Samawa, Al-Muthanna, Iraq

Giulio Antonini
University of L Aquila
67040 L Aquila, Italy

Antonio Musolino
University of Pisa
56126 Pisa, Italy

Abdul A. Arkadan
Colorado School of Mines, EE Dept.
Golden, CO 80401, USA

Mona El Helbawy
University of Colorado
Boulder, CO 80302, USA

Sounik Kiran Kumar Dash
SRM Institute of Science and Technology
Chennai, India

Vinh Dang
Sandia National Labortories
Albuquerque, NM 87109, USA

Ibrahim Mahariq
Gulf University for Science and Technology
Kuwait

Wenxing Li
Harbin Engineering University
Harbin 150001, China

Sihua Shao
EE, Colorado School of Mines
USA

Wei-Chung Weng
National Chi Nan University, EE Dept.
Puli, Nantou 54561, Taiwan

Alessandro Formisano
Seconda Universita di Napoli
81031 CE, Italy

Piotr Gas
AGH University of Science and Technology
30-059 Krakow, Poland

Long Li
Xidian University
Shaanxa, 710071, China

Steve J. Weiss
US Army Research Laboratoy
Adelphi Laboratory Center (RDRL-SER-M)
Adelphi, MD 20783, USA

Jiming Song
Iowa State University, ECE Dept.
Ames, IA 50011, USA

Santanu Kumar Behera
National Institute of Technology
Rourkela-769008, India

Daniele Romano
University of L Aquila
67100 L Aquila, Italy

Alireza Baghai-Wadji
University of Cape Town
Cape Town, 7701, South Africa

Kaikai Xu
University of Electronic Science
and Technology of China
China

Maria Evelina Mognaschi
University of Pavia
Italy

Rui Chen
Nanjing University of Science and Technology
China

Luca Di Rienzo
Politecnico di Milano
20133 Milano, Italy

Lei Zhao
Jiangsu Normal University
Jiangsu 221116, China

Sima Noghanian
Commscope
Sunnyvale, CA 94089, USA

Nunzia Fontana
University of Pisa
56122 Pisa, Italy

Stefano Selleri
DINFO - University of Florence
50139 Florence, Italy

Fatih Kaburcuk
Sivas Cumhuriyet University
Sivas 58140, Turkey

Huseyin Savci
Istanbul Medipol University
34810 Beykoz, Istanbul

Zhixiang Huang
Anhui University
China

Marco Arjona López
La Laguna Institute of Technology
Torreon, Coahuila 27266, Mexico

Sheng Sun
University of Electronic Science and
Tech. of China
Sichuan 611731, China

Qiuhua Huang
Colorado School of Mines
USA

Francesca Venneri
DIMES, Università della Calabria
Italy

EDITORIAL ASSISTANTS

Matthew J. Inman
University of Mississippi, EE Dept.
University, MS 38677, USA

Shanell Lopez
Colorado School of Mines, EE Dept.
Golden, CO 80401, USA

EMERITUS EDITORS-IN-CHIEF

Duncan C. Baker
EE Dept. U. of Pretoria
0002 Pretoria, South Africa

Allen Glisson
University of Mississippi, EE Dept.
University, MS 38677, USA

Ahmed Kishk
Concordia University, ECS Dept.
Montreal, QC H3G 1M8, Canada

Robert M. Bevensee
Box 812
Alamo, CA 94507-0516

Ozlem Kilic
Catholic University of America
Washington, DC 20064, USA

David E. Stein
USAF Scientific Advisory Board
Washington, DC 20330, USA

EMERITUS ASSOCIATE EDITORS

Yasushi Kanai
Niigata Inst. of Technology
Kashiwazaki, Japan

Mohamed Abouzahra
MIT Lincoln Laboratory
Lexington, MA, USA

Alexander Yakovlev
University of Mississippi, EE Dept.
University, MS 38677, USA

Levent Gurel
Bilkent University
Ankara, Turkey

Sami Barmada
University of Pisa, ESE Dept.
56122 Pisa, Italy

Ozlem Kilic
Catholic University of America
Washington, DC 20064, USA

Erdem Topsakal
Mississippi State University, EE Dept.
Mississippi State, MS 39762, USA

Alistair Duffy
De Montfort University
Leicester, UK

Fan Yang
Tsinghua University, EE Dept.
Beijing 100084, China

Rocco Rizzo
University of Pisa
56123 Pisa, Italy

Atif Shamim
King Abdullah University of Science and Technology (KAUST)
Thuwal 23955, Saudi Arabia

William O'Keefe Coburn
US Army Research Laboratory
Adelphi, MD 20783, USA

Mohammed Hadi
Kuwait University, EE Dept.
Safat, Kuwait

Amedeo Capozzoli
Univerita di Naoli Federico II, DIETI
I-80125 Napoli, Italy

Maokun Li
Tsinghua University
Beijing 100084, China

Lijun Jiang
University of Hong Kong, EEE Dept.
Hong, Kong

Shinishiro Ohnuki
Nihon University
Tokyo, Japan

Kubilay Sertel
The Ohio State University
Columbus, OH 43210, USA

Salvatore Campione
Sandia National Laboratories
Albuquerque, NM 87185, USA

Toni Bjorninen
Tampere University
Tampere, 33100, Finland

Paolo Mezzanotte
University of Perugia
I-06125 Perugia, Italy

Yu Mao Wu
Fudan University
Shanghai 200433, China

Amin Kargar Behbahani
Florida International University
Miami, FL 33174, USA

Laila Marzall
University of Colorado, Boulder
Boulder, CO 80309, USA

Qiang Ren
Beihang University
Beijing 100191, China

EMERITUS EDITORIAL ASSISTANTS

Khaleb ElMaghoub
Trimble Navigation/MIT
Boston, MA 02125, USA

Kyle Patel
Colorado School of Mines, EE Dept.
Golden, CO 80401, USA

Christina Bonnington
University of Mississippi, EE Dept.
University, MS 38677, USA

Anne Graham
University of Mississippi, EE Dept.
University, MS 38677, USA

Madison Lee
Colorado School of Mines, EE Dept.
Golen, CO 80401, USA

Allison Tanner
Colorado School of Mines, EE Dept.
Golden, CO 80401, USA

Mohamed Al Sharkawy
Arab Academby for Science and Technology, ECE Dept.
Alexandria, Egypt

DECEMBER 2025 REVIEWERS

Hristos T. Anastassiu
Giulio Antonini
Dinesh Kumar Reddy Basani
Andrea Gaetano Chiariello
Goga Cvetkovski
Arkaprovo Das
Alessandro Formisano
Yassen Gorbounov
Lu Guo
Nada Habeeb
Bernhard J. Hoenders
Shian Hwu
Taha Imeci
Lihua Li
Maria Evelina Mognaschi
Mahdi Oliaei
Andrew Peterson
Giuseppe Pettanice
S. M. Rao
Alain Reineix
Manthan Shah
Jingjing Song
Zhonggen Wang
Julia Wolff

THE APPLIED COMPUTATIONAL ELECTROMAGNETICS SOCIETY JOURNAL

Vol. 40 No. 12 December 2025

TABLE OF CONTENTS

Space and Frequency Extrapolation for Deep Learning Design of Coupling Matrix for Microwave Filters

Tarek Sallam and Qun Wang

School of Computer Science and Technology
Shandong Xiehe University, Jinan 250109, Shandong, China
tarek.sallam@feng.bu.edu.eg

***Abstract* –** In this paper, we propose a deep-learning-based neural network namely, a convolutional neural network (CNN) for predicting frequency response of a microwave filter as a function of its extrapolated coupling parameters. Thus, in this paper, coupling properties of a microwave filter comprise its design space. This space characterizes the filter's frequency response in complex domain. Moreover, we propose a CNN-based method to extrapolate the response in frequency. Thereby, excessive simulations and long computational time can be avoided as opposed to electromagnetic (EM) solvers. The training of the proposed CNN is based on a circuit model. In order to exhibit the robustness of the new technique, it is applied on 5- and 8-pole filters and compared with a shallow neural network namely, radial basis function neural network (RBFNN). The results reveal that the CNN can achieve extrapolation in both design space and frequency for microwave filters with high accuracy and speed. For a 5-pole filter, the percentage root mean square error (RMSE) between ideal and predicted response of CNN is found to be 0.28% and 0.09% for design space exploration (DSE) and frequency extrapolation (FE), respectively. For an 8-pole filter, the percentage RMSE of CNN is found to be 0.38% and 0.11% for DSE and FE, respectively.

***Index Terms* –** Convolutional neural network (CNN), coupling matrix, deep learning, microwave filters, radial basis function neural network (RBFNN).

I. INTRODUCTION

Microwave filters are widely used in all types of electronic systems [1, 2]. Tuning of microwave filters is an inevitable process in the design procedure of microwave filters. For the case of coupled resonator filters, either computing *S*-parameters for a given coupling matrix or extracting the coupling matrix from the required *S*-parameters is a crucial problem. Solving either problem becomes extremely difficult since it is a highly nonlinear problem [3, 4]. Classical methods dealt with problem need to be repeated for many iterations in different conditions [5, 6]. Consequently, the process of filter design suffers from the time-consuming and complicated parameters extraction.

Some conventional (shallow or non-deep) Neural network (NN) techniques were developed for microwave filter modeling [7–12]. However, these techniques are not suitable for high-dimensional problems because data generation and model training become too complicated. Deep learning (DL)-based methods were also proposed for microwave filter design and modeling [13, 14]. However, in these methods, the training data is generated using full-wave electromagnetic (EM) model through simulation or measurement which becomes impractical when large training data is needed. Therefore, collection of training data using EM-based models to cover input/output parameter range over the interested frequency band can be an overwhelmingly time-consuming task. Different from EM models, circuit models can be used to introduce fast accurate models for different electronic designs. They are usually straightforward to build, and fast to evaluate. In [15], a convolutional neural network (CNN) [16, 17], a variant of deep network framework, is used to extract the coupling matrix of ideal (target) *S*-parameters based on a circuit model. The CNN first extracts the features of *S*-parameters by using convolution layers and pooling layers, which are then mapped to the coupling matrix by full connection and output layers.

Microwave filters can be designed by using EM solvers to obtain their frequency responses. While a full-wave EM simulation is accurate, it solves complex equations iteratively to compute the frequency response of the structure. This makes the simulation utilize a high amount of computational resource and time because of the high dimensionality of input space. Given a frequency response of the filter for a certain input design, it is often necessary to have information about out-of-bound design space response. In a traditional way, it

Submitted On: January 22, 2025
Accepted On: January 25, 2026

https://doi.org/10.13052/2025.ACES.J.401201

may be required to perform EM simulations again. This makes design space exploration (DSE) of microwave filters indispensable.

Initial DSE techniques involved statistically derived design-of-experiment (DoE) analysis [18, 19]. However, these methods do not cope well with the increasing dimensionality and nonlinearity of design spaces [20, 21]. To address these limitations, evolutionary algorithms for DSE were developed [22, 23]. The advantage with evolutionary techniques is that they made no assumptions about the nature of the design space. However, they often require a large number of function evaluations and convergence rates are problem-dependent leading to long computation times [24, 25]. In [26], the authors provide a machine learning (ML)-based architecture that accomplishes DSE with high accuracy for microwave and RF components. However, this architecture requires long training and execution times compared to DL-based techniques.

In most scenarios, only band-limited data is available because broadband data might be computationally expensive to be simulated or measured. Therefore, extrapolation along the frequency axis or frequency extrapolation (FE) becomes a compelling concept because it enables us to estimate the frequency response over a larger range without performing extra measurements or simulations. Although FE has been discussed in the past [27–36], these approaches only deal with responses with few resonant frequencies and fail to deal with responses having multiple resonant peaks and dips. Knowledge-based NNs are used in [37] to provide extrapolated results for the design space parameters for microwave modeling and design. While this approach works for DSE, it may not be applicable to FE. In [38], a Hilbert-based long short-term memory recurrent neural networks (HilbertNet) architecture is proposed to extrapolate the frequency response of EM structures. The problem with HilbertNet is that it consumes a long training time, besides it becomes less confident with less training data and in predictions where the frequency points are far off from the cutoff frequency.

DL-based approaches [39] overcome several of the aforementioned challenges: they can be applied to predict complex responses covering much larger design spaces, and it can predict output response in far less computational time, in either training or execution, than traditional methods. In this paper, the DL-based approach used in [15], namely CNN, is extended to accomplish extrapolation in both DSE and FE for microwave filters. To validate the effectiveness of the proposed CNN, it is applied on 5- and 8-pole microwave filters. The proposed CNN model is able to predict the frequency response in either DSE or FE with high accuracy and speed (in both training and execution) compared with a radial basis function neural network (RBFNN) [40–43] which is a shallow (non-deep) NN.

II. CNN FOR CIRCUIT MODEL-BASED DSE AND FE

The circuit model-based equation that relate the coupling matrix M and filter S-parameters is given by [44]:

$$S_{11} = 1 + 2jR_1[\gamma\mathbf{I} - j\mathbf{R} + \mathbf{M}]^{-1}_{11}$$

$$S_{21} = -2j\sqrt{R_1R_2}[\gamma\mathbf{I} - j\mathbf{R} + \mathbf{M}]^{-1}_{N1}, \qquad (1)$$

where $\gamma = (f_0/BW)((f/f_0) - (f_0/f))$, f, f_0, and BW are the frequency, filter center frequency, and filter bandwidth, respectively, N is the filter order, $\mathbf{I}$ is $N \times N$ identity matrix, $\mathbf{M}$ is the $N \times N$ symmetric coupling matrix, $\mathbf{R}$ is a $N \times N$ matrix with all entries are zero except $[\mathbf{R}]_{11} = R_1$ and $[\mathbf{R}]_{NN} = R_2$, and R_1 and R_2 are the filter's input and output coupling parameters, respectively, as shown in Fig. 1 [44].

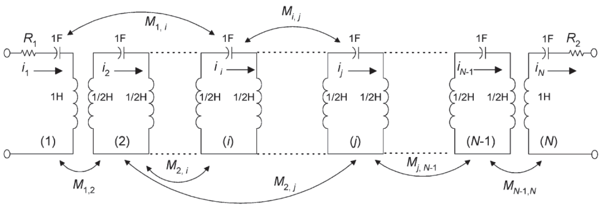

Fig. 1. Equivalent circuit of an N-coupled resonator filter.

A. Design space exploration

The CNN model for DSE, shown in Fig. 2 (a), uses forward mapping. The input of the CNN is the vector of nonzero coupling parameters $\boldsymbol{M}_{nz}$. The output of the CNN is the required vectors $|\boldsymbol{S}_{11}|$ and $|\boldsymbol{S}_{21}|$, representing the scalar magnitudes of the two S-parameters at $\mathcal{R}_{DSE}$ frequency points in the full frequency range of interest. Therefore, the total number of outputs is $2\mathcal{R}_{DSE}$. In the case of DSE, the number of the frequency points $\mathcal{R}_{DSE} = 2001$.

In order to generate the training and validation data of CNN, we assume a training space for every ideal nonzero coupling parameter. Here, the assumed training space is composed of two ranges: $[\boldsymbol{M}^{ideal}_{nz} - \mathbf{1.5}, \boldsymbol{M}^{ideal}_{nz} - \mathbf{0.5}]$ and $[\boldsymbol{M}^{ideal}_{nz} + \mathbf{0.5}, \boldsymbol{M}^{ideal}_{nz} + \mathbf{1.5}]$, where $\boldsymbol{M}^{ideal}_{nz}$ is the vector of ideal nonzero coupling parameters. $\mathbf{1.5}$ and $\mathbf{0.5}$ are two vectors of the same length as $\boldsymbol{M}^{ideal}_{nz}$ and whose all elements are 1.5 and 0.5, respectively. We then use 12500 (10000 for training and 2500 for validation) uniformly distributed random samples in this space for coupling parameters. For each sample of coupling parameters, (1) is used to obtain the corresponding

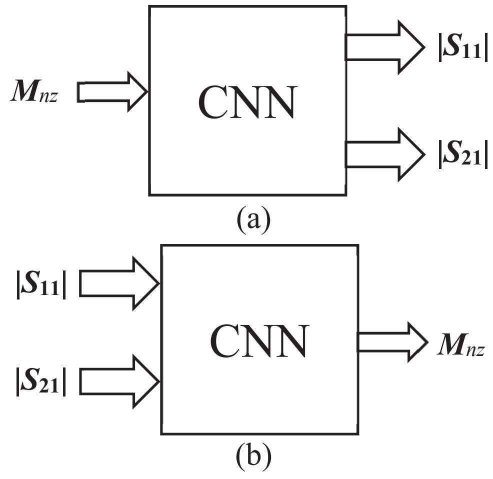

Fig. 2. Circuit model-based CNN for coupling matrix extraction: (a) design space exploration (DSE) and (b) frequency extrapolation (FE).

S-parameters. In this way, we can get the training and validation data for the DSE model. Once trained, the frequency response of an input coupling tuple is predicted, which is beyond the bounds of the training space, namely, the extrapolation coupling tuple. In this case, the extrapolation coupling tuple is the vector of ideal nonzero coupling parameters $\boldsymbol{M}_{nz}^{ideal}$. Then, the predicted frequency response is compared to the ideal one. The accuracy of the predicted frequency response for the extrapolated coupling tuple is a measure of the generalization capability of the network.

B. Frequency extrapolation

Extrapolating the frequency response is important since designers need to determine if there are any resonances in proximity to the simulated (or measured) data which are bandlimited. The CNN model for FE, shown in Fig. 2 (b), uses what so called inverse mapping. In contrast with DSE model, the input of the FE model is the vectors $|\boldsymbol{S}_{11}|$ and $|\boldsymbol{S}_{21}|$ at $\mathcal{R}_{FE}$ frequency points along only a half of the frequency range of interest. The model is trained along the first half of the frequency range while extrapolated (tested) along the second half. In either case, $\mathcal{R}_{FE}$ is 1001 frequency points, thus the total input is $2\mathcal{R}_{FE} = 2002$. The output of the CNN is the vector of *nonzero* coupling parameters $\boldsymbol{M}_{nz}$.

In order to generate the training and validation data of CNN, we assume a tolerance of ±0.5 for every ideal nonzero coupling parameter. We then use 12500 (10000 for training and 2500 for validation) uniformly distributed random samples in this range for coupling parameters. For each sample of coupling parameters, (1) is used to obtain the corresponding *S*-parameters along the training frequency range. By swapping the data of coupling parameters and *S*-parameters, we can get the training and validation data for the FE model. The trained CNN is tested by the ideal set of *S*-parameters (corresponding to the ideal $\boldsymbol{M}_{nz}$) along the extrapolated frequency range. Then, the extrapolated (predicted) frequency response is compared to the ideal one. It should be noted that the layouts for DSE and FE, shown in Figs. 2 (a) and (b), have proved their efficacy [26]. This also will be seen throughout the results in the paper.

III. PROPOSED STRUCTURES

A. RBFNN model

RBFNN is a special three-layer feedforward network, which consists of an input layer, an output layer, and a single hidden layer as shown in Fig. 3. In the hidden layer, the nonlinear functions are usually considered to be Gaussian functions of appropriately chosen means and variance. The weights from the hidden to the output layer are determined by considering a supervised learning procedure. Assume that the input, hidden, and the output layers have *J*, *K*, *P* nodes, respectively. The network output vector is given by

$$w_p = \sum_{k=1}^{K} \omega_{p,k} e^{-\frac{\|\mathbf{z}-\mathbf{c}_k\|^2}{\sigma_k^2}} \qquad (p = 1,\ldots,P), \tag{2}$$

where $\mathbf{z} = [z_1 \; z_2 \; \ldots \; z_J]$ is the input vector, $\mathbf{c}_k$ and σ_k are the center vector and the standard deviation (spread parameter) of the k^{th} Gaussian function, respectively, and $\{\omega_{p,k}; p = 1,\ldots,P; k = 1,\ldots,K\}$ is the weight from the k^{th} hidden node to p^{th} output node.

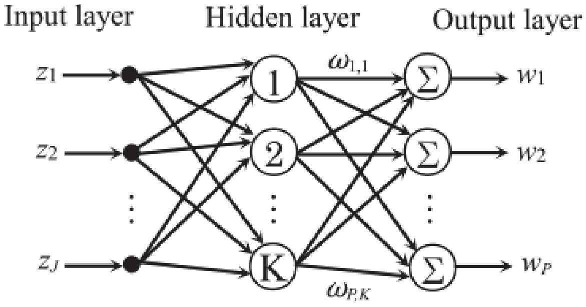

Fig. 3. Architecture of the RBFNN.

B. CNN model

CNNs have one or more convolutional and pooling layers to learn the discriminative features from the input data. After all the convolutional and pooling layers, these learned features are then aggregated to the vectors by the fully connected layers for the regression task [45]. After many simulation trials, it is found that the CNN structures for DSE and FE which provide the best accuracy

Table 1: Proposed CNN structures for DSE and FE

Layer	**Size**		**Nodes**		**Stride**		**Padding**		**Activation**	
	FE	**DSE**	**FE**	**DSE**	**FE**	**DSE**	**FE**	**DSE**	**FE**	**DSE**
Input (Image)	–		$1 \times 2 \times 1001 = 2002$	$1 \times 1 \times Length\{\boldsymbol{M}_{nz}\} = Length\{\boldsymbol{M}_{nz}\}$	–		–		–	
Conv1	2×2	3×3	8	64	1		same		ReLU	
MaxPool1		2×2	–		2				–	
Conv2		3×3	16	128	1				ReLU	
MaxPool2		2×2	–		2				–	
Conv3		3×3	32	256	1				ReLU	
MaxPool3		2×2	–		2				–	
50% Dropout										
FC	–		50	500	–		–		ELU	
Output	–		$Length\{\boldsymbol{M}_{nz}\}$	4002	–		–		Linear	

and ensure optimal network performance are detailed in Table 1. There are three convolutional (Conv) layers and three maximum pooling (MaxPool) layers. The number of feature maps at each convolutional layer is as twice as the previous layer. Each convolutional layer is followed by a pooling layer to reduce the dimension of network parameters. All convolutional layers have a stride of 1 and 'same' padding. All pooling layers have a size of 2×2, stride 2, and 'same' padding. After the sequence of convolutional and pooling layers, there is a single fully connected (FC) layer followed by the output layer. In order to avoid overfitting during training, a dropout operation with a rate of 50% is used at the end of the convolutional and pooling layers. The activation functions used in the convolutional layers and the fully connected layer are rectified linear unit (ReLU) and exponential linear unit (ELU), respectively. Since this is a regression problem instead of a classification problem, no activation is used at the output layer (linear activation).

For DSE structure, the input vector is first reshaped into a $1 \times 1 \times Length\{\boldsymbol{M}_{nz}\}$ input image. The first convolutional layer comprises of 64 feature maps. There are 128 and 256 feature maps in the second and third layers, respectively. The size of the feature map in each convolutional layer is fixed at 3×3. The FC layer has 500 nodes. The output layer has $2\mathcal{R}_{DSE} = 4002$ nodes.

The FE model is used to predict the frequency response over only half of the frequency range of interest. Its structure is simpler than that of the DSE, as shown in Table 1. First, its total 2002 inputs are reshaped into a $1 \times 2 \times 1001$ input image. The three convolutional layers have 8, 16, and 32 feature maps, respectively. The size of the feature map in any convolutional layer is fixed at 2×2. The FC layer has 50 nodes. The output layer has a number of nodes equals the number of nonzero coupling parameters. It should be noted that RBFNN has the same number of inputs and output as the CNN except it cannot accept an image or 2D input. Therefore, the input vector in this case is 1D.

IV. EXAMPLES

To verify the performance of the CNN-based DSE and FE models, they are applied on 5- and 8-pole microwave filters. The Adam (adaptive momentum) optimization algorithm [46] is used to update the network weights and the loss function used for this network is the mean squared error. The initial value of the learning rate is 0.001. During the training, the learning rate is decreased by a rate of 0.1 each 40% of number of epochs. The batch size is 40 and number of epochs is 10. To further verify the performance of the CNN, it is compared to that of the RBFNN. In all examples, the filter's input and output coupling parameters are assumed to be equal, i.e., $R_1 = R_2$. The CNN is implemented (trained, validated, tested) using MATLAB R2024a using Deep Learning Toolbox. The RBFNN is trained using the training function "newrb" in the same toolbox, in which a hidden node is added each epoch (iteration) until a target mean square error (MSE) is reached.

A. 5-pole filter

In this example, we use the proposed CNN to develop DSE and FE models for a 5-pole dielectric resonator filter with a 3.4 GHz center frequency and a 54 MHz bandwidth [44]. The nonzero coupling parameters are $\boldsymbol{M}_{nz} = [R_1 \; M_{12} \; M_{14} \; M_{23} \; M_{34} \; M_{45}]^T$ with their ideal values $\boldsymbol{M}_{nz}^{ideal} = [1.1330, 0.8660, -0.2520, 0.7920, 0.5950, 0.9010]^T$.

Figure 4 shows the DSE predicted frequency responses of CNN and RBFNN compared to the ideal one. As can be seen, there is a perfect agreement between the ideal and CNN responses compared with the RBFNN response, that is, owing to the capability of CNN to extract the hidden features in the input data, automatically. On the other hand, because the RBFNN is shallow, it cannot strengthen the network training process by reconstructing the input coupling parameters. The used shallow RBFNN, has only one hidden layer with 200 neurons, cannot represent this

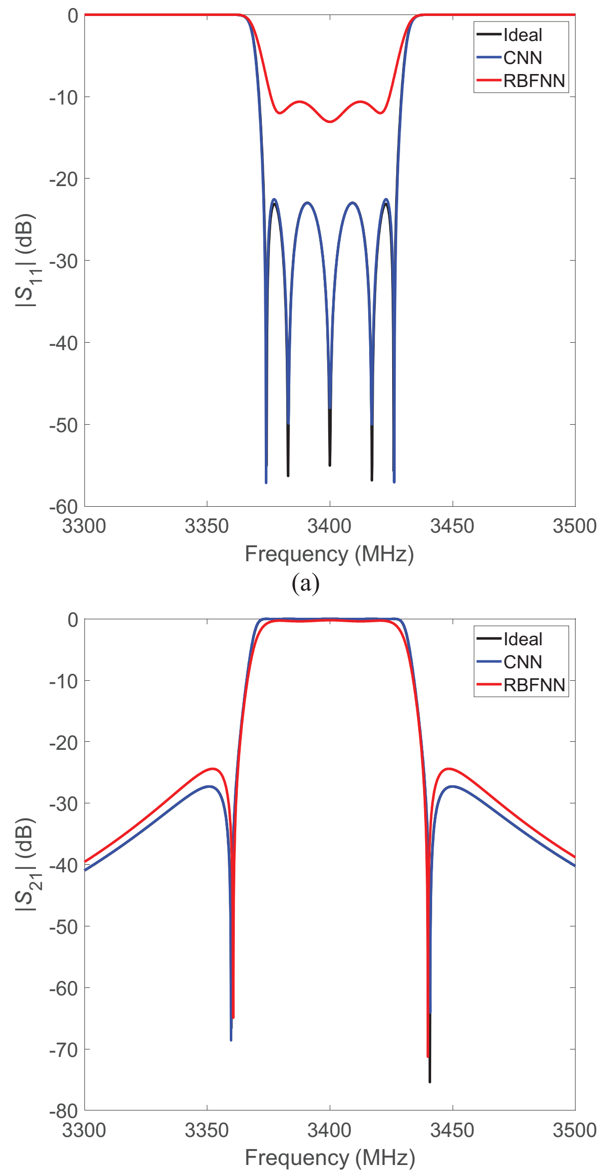

(a)

(b)

Fig. 4. DSE responses of a 5-pole filter: (a) return loss and (b) insertion loss.

high-dimensional input-output relationship effectively. Our proposed CNN modeling technique is suitable for this high-dimensional modeling problem. The training and validation losses of CNN for DSE are found to be 0.0358 and 0.0319, respectively.

Figure 5 shows the corresponding FE responses. As shown, the CNN and RBFNN are trained only on the first half of the response to extrapolate the second half. As can be seen, the extrapolated CNN response exactly follows the ideal one compared to RBFNN which is away from accuracy. In general, conventional shallow NNs cannot extrapolate. This is because they are meant to create a mapping from the input function space to output function space. Given an input testing point way beyond the training range, the network is highly prone to errors depending on whether it is overfitting or underfitting the data. The training and validation losses of CNN for FE are found to be 0.3030 and 0.2914, respectively.

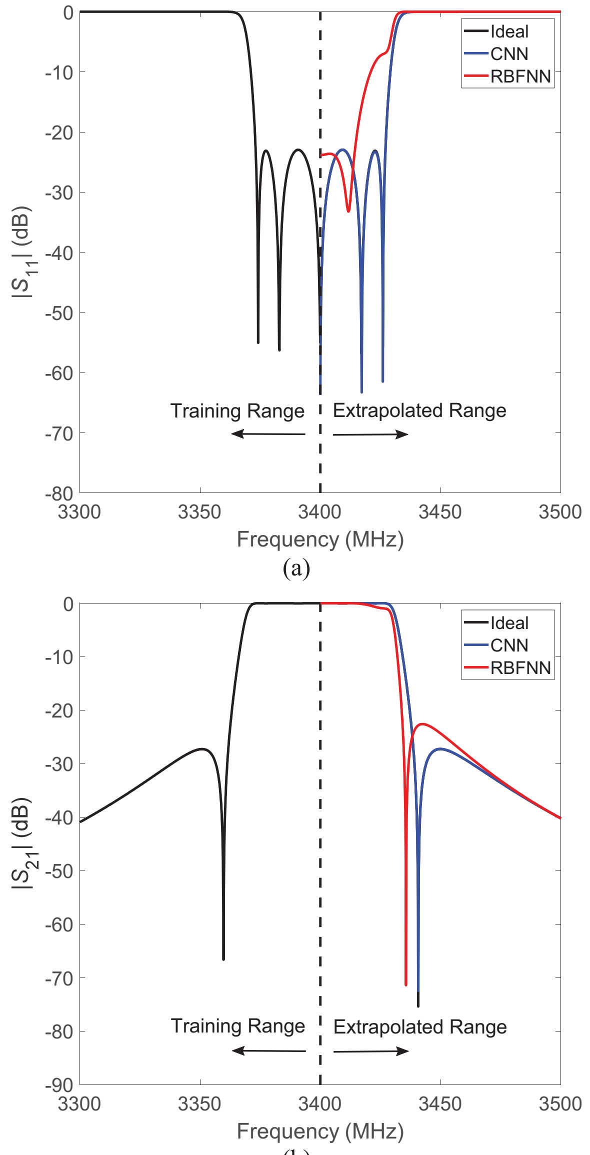

(a)

(b)

Fig. 5. FE responses of a 5-pole filter: (a) return loss and (b) insertion loss.

B. 8-pole filter

The second example involves the DSE and FE of an 8-pole elliptic-function filter with 30 MHz bandwidth centered at 3 GHz [47]. The nonzero couplings are R_1, M_{12}, M_{23}, M_{27}, M_{34}, M_{36}, M_{45}, M_{56}, M_{67}, M_{78}. However, the coupling matrix of this filter is dual-symmetrical

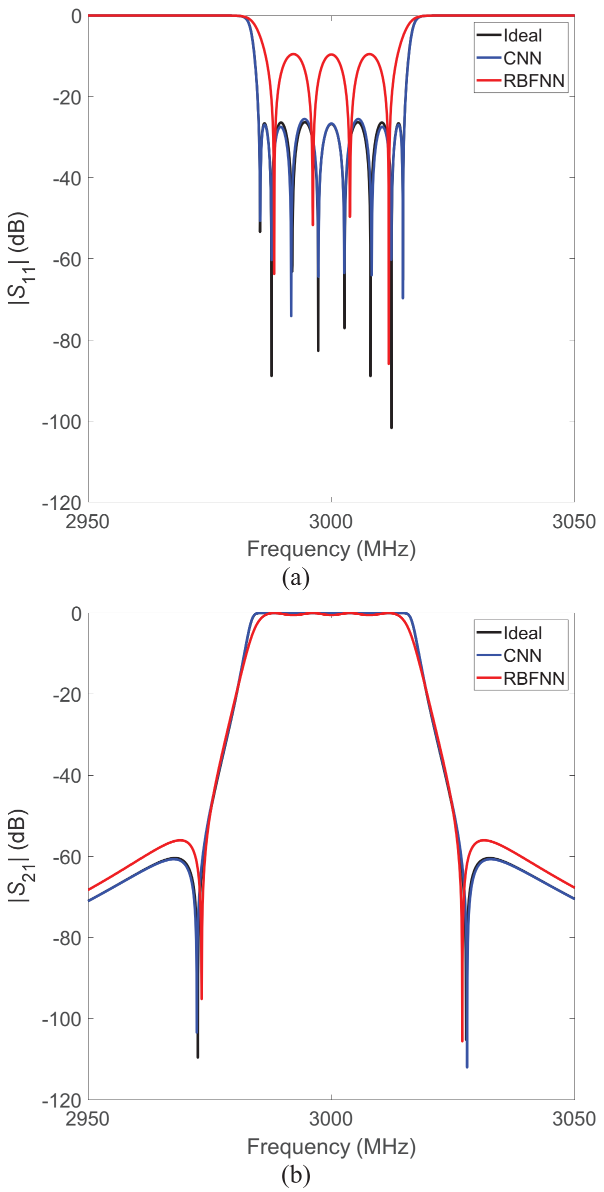

Fig. 6. DSE responses of an 8-pole filter: (a) return loss and (b) insertion loss.

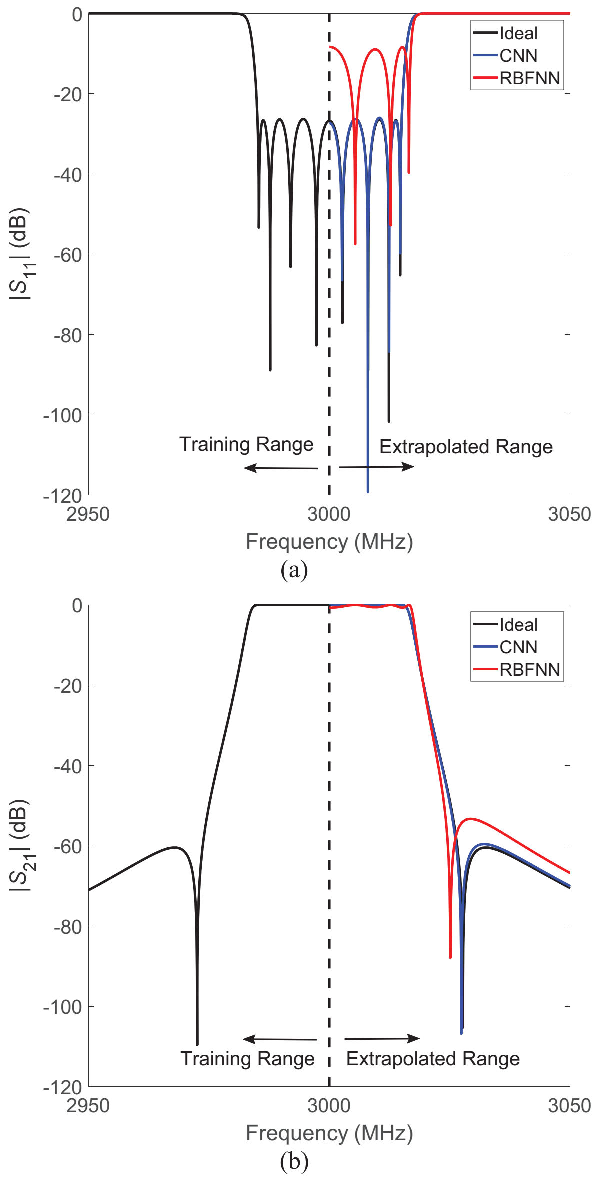

Fig. 7. FE responses of an 8-pole filter: (a) return loss and (b) insertion loss.

meaning that it is symmetrical with respect to its anti-diagonal as well as its diagonal [48]. Therefore, $M_{12} = M_{78}$, $M_{23} = M_{67}$, and $M_{34} = M_{56}$. Consequently, the output of NNs is $\boldsymbol{M}_{nz} = [R_1\ M_{12}\ M_{23}\ M_{27}\ M_{34}\ M_{36}\ M_{45}]^T$. The ideal values are

$$\boldsymbol{M}_{nz}^{ideal} = \begin{bmatrix} 1.2420,\ 0.9380,\ 0.6310,\ -0.0180, \\ 0.5760,\ 0.0660,\ 0.5190 \end{bmatrix}^T$$

The predicted DSE and FE S-parameters by both NNs along with the ideal ones are shown in Figs. 6 and 7, respectively. As shown in Figs. 6 (a) and 7 (a), the CNN captures all the resonant peaks and dips along passband with very high accuracy in contrast with RBFNN. In general, there is excellent correlation between the ideal and CNN responses, compared to RBFNN. The RBFNN architecture fails to learn the frequency response because of a lack of learning data dependencies. This shows that CNN architecture allows for parameter sharing and exploitation of spatial dependencies in data to learn a complex frequency response. We conclude that the CNN is much more accurate than the RBFNN for DSE and FE of microwave filters. The CNN training and validation losses for DSE are found to be 0.0227 and 0.0169, while they are 0.2843 and 0.2913 for FE, respectively.

Table 2: Percentage RMSE, training, and execution times of CNN and RBFNN for DSE and FE for 5- and 8-pole filters

NN	**5-Pole Filter**			**8-Pole Filter**		
	Training Time	Execution Time	RMSE (%)	Training Time	Execution Time	RMSE (%)
			DSE			
CNN	6.2 min	0.05 s	0.28	6.35 min	0.06 s	0.38
RBFNN	2.9 h (200 hidden neurons)	1.4 s	14.72	7.1 h (400 hidden neurons)	1.7 s	16.85
			FE			
CNN	34 s	0.04 s	0.09	35 s	0.05 s	0.11
RBFNN	1.8 h (150 hidden neurons)	0.14 s	13.8	3.2 h (350 hidden neurons)	0.19 s	15.81

Table 2 shows the training and execution times as well as the percentage root mean square error (RMSE) between ideal and predicted responses by NNs for DSE and FE for 5- and 8-pole filters. Table 2 also shows the number of hidden neurons in the hidden layer of RBFNN for each response. It can be seen that the CNN modeling for either DSE or FE is with much higher accuracy and much shorter training and execution times than the RBFNN modeling. As mentioned earlier, the RBFNN is a shallow type NN (only has one hidden layer whatever the number of hidden neurons used). That is why it takes much longer training time when dealing with high-dimensional problems (like the present one). On the other hand, the DL-based CNN can retrieve features from data with high dimensions with much shorter training and execution times due to its sparse connectivity and shared weights enabling CNNs to have small numbers of parameters.

Since FE structure, in general, is simpler than the DSE structure, it has less error and shorter training and execution times than those of DSE. Also, compared to a 5-pole filter, the 8-pole filter has higher error and higher training and execution times whether for DSE or FE, because it has a more complex frequency response than that of a 5-pole filter.

For CNN, the training data generation times of a 5-pole filter for DSE and FE are 2.4 min and 1.6 min, respectively. For an 8-pole filter, they are 2.7 min and 2.1 min, respectively. This indicates that the full time required to achieve a result from a trained CNN network for either filter (including the dataset generation) is still very small compared with the time required to achieve the same result in a classical way using direct models. Moreover, our proposed circuit model-based CNN can provide extrapolation results instantly (its execution time is a fraction of a second as shown in Table 2), while the classical full-wave EM model-based methods can take hours to do that by repetitively simulating/measuring the filter during optimization iterations. Although a large training dataset may be required for network training, it can be implemented offline. After training, it can be used online (in the execution phase) for DSE and FE of microwave filters. In other words, the network training (including the dataset generation) is done only once after that the network can be used as a real-time design space and frequency extrapolator for microwave filters.

V. CONCLUSION

A circuit model-based CNN is proposed for design space and frequency extrapolation of microwave filters. In this paper, the coupling parameters of microwave filter constitute its design space. The CNN-based approach is used to predict the frequency response as a function of the coupling properties. The results show that the proposed CNN method can be used reliably to perform the DSE and FE for microwave filters. Compared to the shallow neural network, the deep-learning-based CNN is much more accurate and faster whether in training or execution. Unlike the full-wave EM model-based methods, our proposed CNN model does not need to simulate and/or measure the filter iteratively, therefore saving much computational time and resources. For a 5-pole filter, the training time of CNN is found to be 6.2 min and 34 s for DSE and FE, respectively. For an 8-pole filter, the training time of CNN is found to be 6.35 min and 35 s for DSE and FE, respectively. In general, the execution time of CNN is a fraction of second. The CNN training and validation losses are found to be comparable indicating that CNN is not overtrained. Once the CNN model is developed (trained and validated), it can be utilized as an instant design space and frequency extrapolator for microwave filters for similar tasks, i.e., it can be used for design space and frequency extrapolation for any N-pole filter.

REFERENCES

[1] R. J. Cameron, C. M. Kudsia, and R. T. Mansour, *Microwave Filters for Systems: Fundamentals, Design and Applications*. Hoboken, NJ: Wiley, 2018.

[2] S. Saleh, W. Ismail, I. S. Z. Abidin, and M. H. Jamaluddin, “Compact 5G hairpin bandpass filter using non-uniform transmission lines theory,” *Applied Computational Electromagnetics Society (ACES) Journal*, vol. 36, no. 2, pp. 126–131, Feb. 2021.

[3] L. Accatino, “Computer-aided tuning of microwave filters,” in *IEEE MTT-S Int. Microw. Symp. Dig.*, pp. 249–252, June 1986.

[4] M. Yu and W. C. Tang, “A fully automated filter tuning robots for wireless base station diplexers,” in *Proc. Workshop, Comput. Aided Filter Tuning, IEEE Int. Microw. Symp.*, Philadelphia, PA, pp. 8–13, June 2003.

[5] G. Macchiarella and D. Traina, “A formulation of the Cauchy method suitable for the synthesis of lossless circuit models of microwave filters from Lossy measurements,” *IEEE Microw. Wireless Compon. Lett.*, vol. 16, no. 5, pp. 243–245, May 2006.

[6] C.-K. Liao, C.-Y. Chang, and J. Lin, “A vector-fitting formulation for parameter extraction of lossy microwave filters,” *IEEE Microw. Wireless Compon. Lett.*, vol. 17, no. 4, pp. 277–279, Apr. 2007.

[7] H. Kabir, Y. Wang, M. Yu, and Q. J. Zhang, “High dimensional neural network techniques and applications to microwave filter modeling,” *IEEE Trans. Microwave Theory Tech.*, vol. 58, no. 1, pp. 145–156, Jan. 2010.

[8] C. Zhang, J. Jin, W. Na, Q.-J. Zhang, and M. Yu, “Multivalued neural network inverse modeling and applications to microwave filters,” *IEEE Trans. Microwave Theory Tech.*, vol. 66, no. 8, pp. 3781–3797, Aug. 2018.

[9] J.-J. Sun, X. Yu, and S. Sun, “Coupling matrix extraction for microwave filter design using neural networks,” in *2018 IEEE International Conference on Computational Electromagnetics (ICCEM)*, pp. 1–2, 2018.

[10] J. Jin, F. Feng, W. Zhang, J. Zhang, Z. Zhao, and Q.-J. Zhang, “Recent advances in deep neural network technique for high-dimensional microwave modeling,” in *2020 IEEE MTT-S International Conference on Numerical Electromagnetic and Multiphysics Modeling and Optimization (NEMO)*, pp. 1–3, 2020.

[11] Z. S. Tabatabaeian and M. H. Neshati, “Design investigation of an X-band SIW H-plane band pass filter with improved stop band using neural network optimization,” *Applied Computational Electromagnetics Society (ACES) Journal*, vol. 30, no. 10, pp. 1083–1088, Aug. 2021.

[12] Z. S. Tabatabaeian and M. H. Neshati, “Development of a low profile and wideband backward-wave directional coupler using neural network,” *Applied Computational Electromagnetics Society (ACES) Journal*, vol. 31, no. 12, pp. 1404–1409, Aug. 2021.

[13] J. J. Sun, S. Sun, X. Yu, Y. P. Chen, and J. Hu, “A deep neural network based tuning technique of lossy microwave coupled resonator filters,” *Microw. Opt. Technol. Lett.*, vol. 61, no. 9, pp. 2169–2173, 2019.

[14] Y. Zhang, Y. Wang, Y. Yi, J. Wang, J. Liu, and Z. Chen, “Coupling matrix extraction of microwave filters by using one-dimensional convolutional autoencoders,” *Front. Phys.*, vol. 9, Nov. 2021.

[15] T. Sallam and A. Attiya, “Convolutional neural network for coupling matrix extraction of microwave filters,” *Applied Computational Electromagnetics Society (ACES) Journal*, vol. 37, no. 7, pp. 805–810, July 2022.

[16] Y. Wang, Z. Zhang, Y. Yi, and Y. Zhang, “Accurate microwave filter design based on particle swarm optimization and one-dimensional convolution autoencoders,” *Int. J. RF Microw. Comput. Aided Eng.*, vol. 32, no. 4, 2022.

[17] H. Arab, I. Ghaffari, L. Chioukh, S. O. Tatu, and S. Dufour, “A convolutional neural network for human motion recognition and classification using a millimeter-wave doppler radar,” *IEEE Sensors Journal*, vol. 22, no. 5, pp. 4494–4502, Mar. 2022.

[18] D. C. Montgomery, *Design and Analysis of Experiments*, 5th ed. New York: Wiley-Interscience, 2000.

[19] A. Norman, D. Shykind, M. Falconer, and K. Ruffer, “Application of Design of Experiments (DOE) methods to high-speed interconnect validation,” in *Proc. Electrical Performance Electrical Packaging*, Princeton, NJ, pp. 15–18, 2003.

[20] V. Sathanur, V. Jandhyala, and H. Braunisch, “A hierarchical simulation flow for return-loss optimization of microprocessor package vertical interconnects,” *IEEE Trans. Adv. Packag.*, vol. 33, no. 4, pp. 1021–1033, Nov. 2010.

[21] E. Matoglu, N. Pham, D. N. de Araujo, M. Cases, and M. Swaminathan, “Statistical signal integrity analysis and diagnosis methodology for high-speed systems,” *IEEE Trans. Adv. Packag.*, vol. 27, no. 4, pp. 611–629, Nov. 2004.

[22] N. Singh, B. Mutnury, C. Wesley, N. Pham, E. Matoglu, M. Cases, and D. N. de Araujo, “Swarm intelligence for electrical design space exploration,” in *Proc. 2007 IEEE Electrical Performance Electronic Packaging*, Atlanta, pp. 21–24, 2007.

[23] C. Wesley, B. Mutnury, N. Pham, E. Matoglu, and M. Cases, “Electrical design space exploration for high-speed servers,” in *Proc. 2007 57th Electron. Compon. Technol. Conf.*, Reno, NV, pp. 1748–1753, 2007.

[24] J. Panerati, D. Sciuto, and G. Beltrame, “Optimization strategies in design space exploration,” in *Handbook of Hardware/Software Codesign*, S. Ha and J. Teich, Eds. Dordrecht: Springer-Verlag, pp. 192–194, 2017.

[25] M. Senthil Arumugam, M. V. C. Rao, and A. W. C. Tan, “A novel and effective particle swarm optimization like algorithm with extrapolation technique,” *Appl. Soft Comput.*, vol. 9, no. 1, pp. 308–320, 2009.

[26] O. W. Bhatti, N. Ambasana, and M. Swaminathan, “Design space and frequency extrapolation: Using neural networks,” *IEEE Microwave Magazine*, vol. 22, no. 10, pp. 22–36, Oct. 2021.

[27] R. S. Adve, T. K. Sarkar, S. M. Rao, E. K. Miller, and D. R. Pflug, “Application of the Cauchy method for extrapolating/interpolating narrowband system responses,” *IEEE Trans. Microw. Theory Techn.*, vol. 45, no. 5, pp. 837–845, May 1997.

[28] S. M. Narayana, G. Rao, R. Adve, T. K. Sarkar, V. C. Vannicola, M. C. Wicks, and S. A. Scott, “Interpolation/extrapolation of frequency domain responses using the Hilbert transform,” *IEEE Trans. Microw. Theory Techn.*, vol. 44, no. 10, pp. 1621–1627, Oct. 1996.

[29] J. M. Frye and A. Q. Martin, “Extrapolation of time and frequency responses of resonant antennas using damped sinusoids and orthogonal polynomials,” *IEEE Trans. Antennas Propag.*, vol. 56, no. 4, pp. 933–943, Apr. 2008.

[30] J. Cho, J. Ahn, J. Kim, J. Park, Y. Shin, K. Kim, J. Choi, and S. Ahn, “Low- and high-frequency extrapolation of band-limited frequency responses to extract delay causal time responses,” *IEEE Trans. Electromagn. Compat.*, vol. 63, no. 3, pp. 888–901, June 2021.

[31] L. L. Barannyk, H. H. Tran, A. Elshabini, and F. D. Barlow, “Time delay extraction from frequency domain data using causal Fourier continuations for high-speed interconnects,” *Electronics*, vol. 4, pp. 799–826, 2015.

[32] J. Becerra, F. Vega, and F. Rachidi, “Extrapolation of a truncated spectrum with Hilbert transform for obtaining causal impulse responses,” *IEEE Trans. Electromagn. Compat.*, vol. 59, no. 2, pp. 454–460, Apr. 2017.

[33] M. Yuan, P. M. van den Berg, and T. K. Sarkar, “Direct extrapolation of a causal signal using low-frequency and early-time data based on integral equations,” in *Proc. IEEE Antennas Propag. Soc. Int. Symp.*, pp. 688–691, 2005.

[34] M. Yuan, P. M. van den Berg, and T. K. Sarkar, “Direct extrapolation of a causal signal using low-frequency and early-time data based on matrix equations,” in *Proc. IEEE Antennas Propag. Soc. Int. Symp.*, pp. 615–618, 2005.

[35] J. Cho, K. Hwang, S. Jeung, and S. Ahn, “An efficient extrapolation method of band-limited *S*-parameters for extracting causal impulse responses,” *IEEE Trans. Comput.-Aided Design Integrated Circuits Syst.*, vol. 38, no. 11, pp. 2086–2098, Nov. 2019.

[36] S. L. Ho and M. Xie, “The use of ARIMA models for reliability forecasting and analysis,” *Comput. Ind. Eng.*, vol. 35, no. 1/2, pp. 213–216, 1998.

[37] W. Na, W. Liu, L. Zhu, F. Feng, J. Ma, and Q. Zhang, “Advanced extrapolation technique for neural-based microwave modeling and design,” *IEEE Tran. Microw. Theory Techn.*, vol. 66, no. 10, pp. 4397–4418, Oct. 2018.

[38] O. W. Bhatti, H. M. Torun, and M. Swaminathan, “HilbertNet: A probabilistic machine learning framework for frequency response extrapolation of electromagnetic structures,” *IEEE Transactions on Electromagnetic Compatibility*, vol. 64, no. 2, pp. 405–417, Apr. 2022.

[39] Y. Zhang, “Deep learning method for predicting electromagnetic emission spectrum of aerospace equipment,” *IET Science, Measurement & Technology*, vol. 18, no. 4, pp. 193–201, 2024.

[40] T. Sallam, A. B. Abdel-Rahman, M. Alghoniemy, Z. Kawasaki, and T. Ushio, “A neural-network-based beamformer for phased array weather radar,” *IEEE Transactions on Geoscience and Remote Sensing*, vol. 54, no. 9, pp. 5095–5104, Sep. 2016.

[41] T. Sallam, A. B. Abdel-Rahman, M. Alghoniemy, and Z. Kawasaki, “A novel approach to the recovery of aperture distribution of phased arrays with single RF channel using neural networks,” in *2014 Asia-Pacific Microwave Conference*, Sendai, Japan, pp. 879–881, 2014.

[42] S. Haykin, *Neural Network: A Comprehensive Foundation*. Upper Saddle River, NJ: Prentice-Hall, 1999.

[43] X. Jia, Q. Ouyang, T. Zhang, and X. Zhang, “A novel adaptive tracking algorithm for the resonant frequency of EMATs in high temperature,” *Applied Computational Electromagnetics Society (ACES) Journal*, vol. 33, no. 11, pp. 1243–1249, July 2021.

[44] M. A. Ismail, D. Smith, A. Panariello, Y. Wang, and M. Yu, “EM-based design of large-scale dielectric-resonator filters and multiplexers by space mapping,” *IEEE Trans. Microw. Theory Tech.*, vol. 52, no. 1, pp. 386–392, Jan. 2004.

[45] T. Sallam and A. M. Attiya, “Convolutional neural network for 2D adaptive beamforming of phased array antennas with robustness to array imperfections,” *International Journal of Microwave and Wireless Technologies*, vol. 13, no. 10, pp. 1096–1102, Dec. 2021.

[46] D. P. Kingma and J. Ba, “Adam: A method for stochastic optimization,” in *Proc. of the 3rd Int. Conf. on Learning Representations (ICLR)*, San Diego, CA, 2015.

[47] H.-T. Hsu, Z. Zhang, K. A. Zaki, and A. E. Ati, “Parameter extraction for symmetric

coupled-resonator filters," *IEEE Trans. Microw. Theory Techn.*, vol. 50, no. 12, pp. 2971–2978, Dec. 2002.

[48] J. W. Bandler, S. H. Chen, and S. Daijavad, "Exact sensitivity analysis for the optimization of coupled cavity filters," *J. Circuit Theory Applicat.*, vol. 31, pp. 63–77, 1986.

Tarek Sallam was born in Cairo, Egypt, in 1982. He received the B.S. degree in electronics and telecommunications engineering, the M.S. degree in engineering mathematics from Benha University, Cairo, Egypt, in 2004 and 2011, respectively, and the Ph.D. degree in electronics and communications engineering from Egypt-Japan University of Science and Technology, Alexandria, in 2015. In 2006, he joined the Faculty of Engineering at Shoubra, Benha University. In 2019, he joined Huaiyin Institute of Technology, Huai'an, China. In 2022, he joined Qujing Normal University, Qujing. In 2024, he joined the School of Computer Science and Technology, Shandong Xiehe University, Jinan, where he is currently an Associate Professor. He was a Visiting Researcher with the Electromagnetic Compatibility Laboratory, Osaka University, Osaka, Japan. His research interests include evolutionary optimization, neural networks and deep learning, phased array antennas with array signal processing and adaptive beamforming.

Qun Wang was born in Jinan, China, in 1986. She holds a master's degree in Engineering Management from Ocean University of China. She served as a director of Shandong Computer Society, a director of Shandong Software Industry-Education Alliance, and a member of Jinan Vocational Education Society. In 2008, she joined Shandong Shichuang Software Training Institute of Ambow Education Group and served as director of the Training Center. In 2022, she joined the School of Computer Science and Technology, Shandong Xiehe University, Jinan, where she currently holds the position of Deputy Dean of Research. Her research interests include machine vision, neural networks, and deep learning.

Parallel Structured Mesh Generation for FDTD Simulations by MPI Implementation

Jiale Guo and Juan Chen

Department of Information and Communication Engineering
Xi’an Jiaotong University, Xi’an, Shaanxi, China
gjl_0610@163.com, chen.juan.0201@mail.xjtu.edu.cn

***Abstract* –** A parallel structured mesh generation method is proposed for FDTD (Finite Difference Time Domain) simulation in this paper by MPI (Message Passing Interface) implementation. This parallel method is based on serial projection and ray tracing. It completely implements the process from surface triangles recorded in a STL (STereoLithography) file to solid hexahedral grids. Furthermore, the parallel method realizes the balanced task allocation for processes which provides almost linear parallelism. Experimental results show that the running time of the MPI program increases in a nearly linear way. As the number of processes increases, the efficiency of the parallel program consistently remains above 80%.

***Index Terms* –** FDTD, MPI, parallel projection, ray tracing, STL file, structured mesh generation.

I. INTRODUCTION

The finite difference time domain (FDTD) method is one of the most common methods in the field of computational electromagnetics since Yee proposed it [1]. It solves Maxwell equations by space and time discretization. The computation space needs to be divided into hexahedral units which are called Yee cells. The Yee cell size determines the accuracy and efficiency of FDTD. Therefore, mesh generation is essential for FDTD simulation.

Since the Yee cell concept was first proposed for FDTD simulation in 1966, numerous FDTD mesh generation methods have been proposed, such as projection [2], volume rendering [5], ray tracing [9], and tetrahedral conversion [16]. These methods realize accurate identification of Yee cells for all kinds of models. However, when the target model is complex or large-scale, the computation time rises. A parallel method is needed to shorten computation time.

To fully improve efficiency of mesh generation in such cases, this paper proposes a parallel structured mesh generation method by MPI (Message Passing Interface) technique for FDTD simulation. The parallel method is based on serial projection-ray tracing. For models which are complex or large, different parallel schemes are designed. The parallel projection method realizes the best allocation for all primitives. The parallel ray tracing method realizes the most average allocation for all grids. Furthermore, parallel IO technology is used to realize data transmission among different modules. To verify the efficiency of the parallel method, a large-scale submarine is simulated with billion-scale grids. According to the simulation result, the parallelism of our method maintains at over 80% which can significantly shorten runtime.

II. PARALLEL METHOD

Before FDTD simulation, spatial discretization is needed. To realize the mapping from surface triangles recorded in the STL (STereoLithography) file to hexahedral Yee cells, we propose the serial projection-ray tracing method from our previous work [20, 21]. As shown in Fig. 1, the serial method requires three steps: generate adaptive mesh lines, identify the surface Yee cells (surface fitting), then fill in the internal Yee cells (internal filling). After finishing the three steps, the surface triangles of the object are converted to structured grids for FDTD simulation.

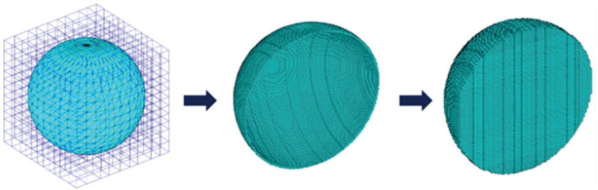
(a) (b) (c)

Fig. 1. Process from surface triangles to hexahedral Yee cells: (a) generate adaptive mesh lines, (b) surface fitting, (c) internal filling.

Though the projection-ray tracing method proposed realizes fast grid generation for FDTD method, it still consumes much time when it comes to complex models with enormous primitive elements and the billions of

Submitted On: March 11, 2024
Accepted On: October 25, 2025

https://doi.org/10.13052/2025.ACES.J.401202

Yee cells required by large-scale models. A parallel method is needed to accelerate the algorithm for such cases. In terms of the serial method, the adaptive mesh line generation is difficult to parallelize for its frequent global operations while the remainder of the method is parallelizable. Thus, the parallel method includes the paralleled projection method and the paralleled ray-tracing method mainly. The paralleled projection method aims at allocating primitive elements evenly to different processes. The paralleled ray-tracing method aims at allocating Yee cells evenly to different processes. Parallel IO (input and output) is used for data transmission among processors. The specific parallel method follows.

A. Parallel projection method

In the proposed projection method, we convert the triangle elements to the corresponding surface structured grids. The mapping between the two is nonlinear which is hard to parallelize directly. This paper proposes a parallel projection method which can achieve linear parallelism nearly based on the projected area. According to the proposed projection method, the actual computational load is relevant to the number of grids in the projection area. Our parallel strategy is to allocate triangles to processors so that they have similar grid amounts. As shown in Fig. 2, the triangle (assume its number is i) is projected onto three coordinate planes, forming the projected area S_1, S_2, S_3. Assume the grid number of the projected area is $x_{\min} \sim x_{\max}$ in the X-direction, $y_{\min} \sim y_{\max}$ in the Y-direction, $z_{\min} \sim z_{\max}$ in the Z-direction, the corresponding grid areas S_1, S_2, S_3 are Q_{s_1}, Q_{s_2}, Q_{s_3}. Then, for triangle i, the total grid Q_i is calculated as:

$$Q_i = Q_{S_1} + Q_{S_2} + Q_{S_3}, \tag{1}$$

where Q_{s_1}, Q_{s_2}, Q_{s_3} are:

$$\begin{aligned} Q_{S_1} &= (x_{\max} - x_{\min} + 1) \times (z_{\max} - z_{\min} + 1) \\ Q_{S_2} &= (x_{\max} - x_{\min} + 1) \times (y_{\max} - y_{\min} + 1) \\ Q_{S_3} &= (y_{\max} - y_{\min} + 1) \times (z_{\max} - z_{\min} + 1). \end{aligned} \tag{2}$$

The total number of grids of all triangles Q_{total} is:

$$Q_{total} = \sum_{i=0} Q_i. \tag{3}$$

Assuming there are N processes for accelerating totally, to obtain linear parallelism, the ideal grids amount allocated to each process $\overline{Q}$ is:

$$\overline{Q} = Q_{total}/P. \tag{4}$$

However, the actual grids amount Q_p of each process cannot be completely equal to $\overline{Q}$ under the condition that one triangle cannot be split by different processes but can only be allocated to a single process. Thus, the ideal allocation for the triangles is to make σ^2 minimum. The calculation method of σ^2 is:

$$\sigma^2 = \sum_{p=0}^{p=P-1} (Q_p - \overline{Q})^2. \tag{5}$$

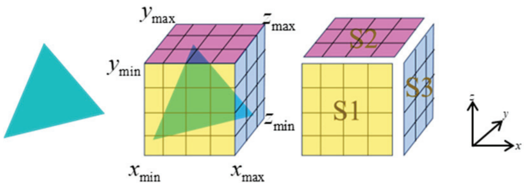

Fig. 2. Parallel projection method based on projected area.

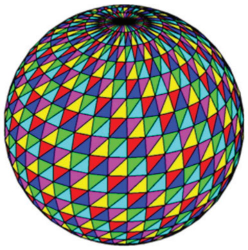

Fig. 3. Balanced allocation for triangles on the sphere.

By optimized resource scheduling according to equation (6), the distribution of Q_p is close to $\overline{Q}$. As shown in Fig. 3, the triangles are allocated to different processes (each color represents a process). Each process has similar computation under the most balanced allocation based on (6). In this way, the acceleration ratio achieves almost linear growth.

B. Parallel ray tracing method

The ray tracing method is completely parallelizable for the independence of paralleled rays. According to the algorithm, the whole area can be divided to subareas along the direction of the rays. The subareas are also completely independent which doesn't require process communication. As shown in Fig. 4, assume the ray is along the Z-direction, the whole area is divided to four subareas which are split evenly in the X-direction and the Y-direction according to the amount of processes. Each process executes the ray tracing method independently for its corresponding subarea and the ultimate results can be gathered by all processes. Because those subareas cover similar numbers of grids, the parallelism of the ray tracing method is perfectly linear.

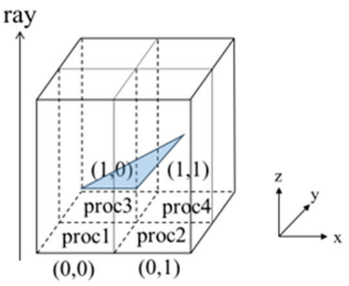

Fig. 4. Parallel ray tracing method.

C. Parallel IO

Because the projection method and ray tracing method take a different parallel strategy, the global data needs be transmitted among different processes. The ultimate result needs to be gathered and output as Yee cells' data for electromagnetic calculation. As shown in Fig. 5, parallel IO is used to realize data transmission through a common file interface, which also supports nearly linear parallelism when there aren't too many processes. On the stage of surface fitting, processes are allocated with different triangles. As soon as all processes finish surface fitting, the local data of each process is written parallelly to the common file. Then all processes read the whole common file to get global data. Following that, global data are reallocated to different processes according to the regional location to carry out internal filling. Finally, complete data are output parallelly to a result file.

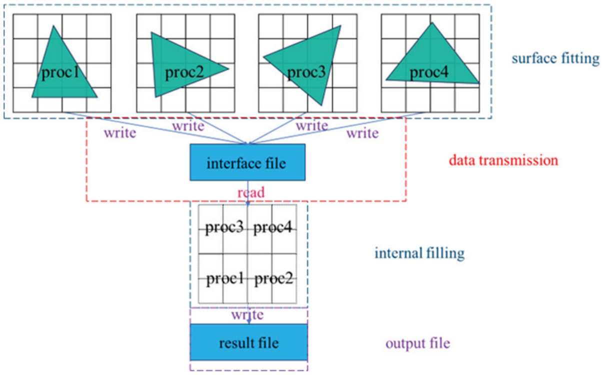

Fig. 5. Parallel projection-ray tracing method scheme.

Based on the parallel method projection module, the ray tracing module and the IO module are completely linearly parallel except for the adaptive mesh line generation module. However, the computation time of the module is relatively small. Therefore, the whole process achieves nearly linear parallelism ignoring the computation time of adaptive mesh line generation.

III. SIMULATION RESULTS

To demonstrate the parallelism of the proposed parallel projection-ray tracing method, a large-scale model (submarine) is considered which has more geometric primitives and generates more Yee cells.

The submarine model and material mapping result are shown in Fig. 6. The length of the submarine is 62 m. The width is 11 m and the height is 20 m. It includes 10695 triangle elements. The simulation time of the sequential program reaches hundreds of seconds which greatly speeds up using the parallel method.

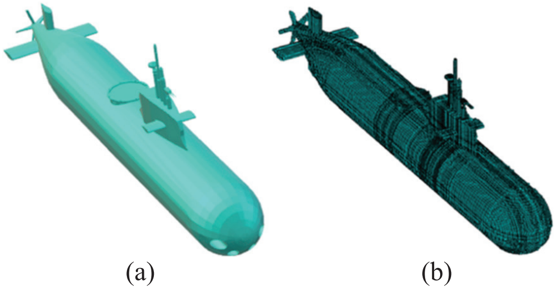
(a) (b)

Fig. 6. Simulation of submarine: (a) original model and (b) structured mesh generated.

We choose 200, 400, and 1700 million grids for multi-point parallelism testing. The time of three modules, total time, acceleration ratio, and efficiency are shown in Tables 1–3. The three modules include the mesh line generation module, the surface fitting module, the internal filling module, and the parallel IO module. Total time is slightly more than the sum of the four main modules, allowing extra time for MPI function expenses and synchronous operations. Speedup and Efficiency are calculated as follows.

Assume there are N processes for accelerating, T_N represents total time of N processes, S_N represents speedup of N processes, E_N represents efficiency of N processes, T_1 represents total time of one process, which is equal to sequential time. Then, S_N and E_N are calculated as:

$$S_N = \frac{T_1}{T_N}, \tag{6}$$

$$E_N = \frac{T_1}{T_N \times N}. \tag{7}$$

According to the simulation time results shown in Tables 1–3, the time of the Mesh Line Generation module is a tiny number which barely influences the total time of the program, the rest of the modules (Surface Fitting, Internal Filling, Parallel IO) consume half of the time with the number of processes growing exponentially. The Efficiency of the parallel program maintains at over 80% for 1–8 processes and the Speedup rises

Table 1: Simulation time comparison on 200 million grids of 1, 2, 4, 8, 16 processes for submarine

Process Amount	**Mesh Line Generation**	**Surface Fitting**	**Internal Filling**	**Parallel IO**	**Total Time**	**Total Speedup**	**Total Efficiency**
1	0.43 s	38.03 s	23.22 s	36.87 s	99.93 s	–	–
2	0.43 s	21.75 s	11.44 s	18.26 s	52.13 s	1.91	0.96
4	0.43 s	11.86 s	5.69 s	9.47 s	27.85 s	3.59	0.90
8	0.44 s	7.37 s	2.78 s	4.86 s	15.91 s	6.29	0.80
16	0.44 s	4.86 s	1.41 s	2.73 s	9.77 s	10.23	0.64

Table 2: Simulation time comparison on 400 million grids of 1, 2, 4, 8, 16 processes for submarine

Process Amount	**Mesh Line Generation**	**Surface Fitting**	**Internal Filling**	**Parallel IO**	**Total Time**	**Total Speedup**	**Total Efficiency**
1	0.48 s	59.93 s	49.62 s	84.82 s	197.27 s	–	–
2	0.48 s	35.01 s	24.54 s	42.89 s	107.03 s	1.84	0.92
4	0.48 s	19.19 s	8.49 s	21.53 s	53.83 s	3.66	0.92
8	0.50 s	11.97 s	5.83 s	10.96 s	31.37 s	6.29	0.80
16	0.51 s	6.95 s	3.05 s	6.32 s	17.14 s	11.51	0.72

Table 3: Simulation time comparison on 1700 million grids of 1, 2, 4, 8, 16 processes for submarine

Process Amount	**Mesh Line Generation**	**Surface Fitting**	**Internal Filling**	**Parallel IO**	**Total Time**	**Total Speedup**	**Total Efficiency**
1	0.61 s	151.65 s	186.56 s	320.01 s	674.22 s	–	–
2	0.61 s	80.07 s	89.47 s	155.37 s	331.67 s	2.00	1.00
4	0.61 s	42.56 s	43.67 s	80.27 s	173.50 s	3.89	0.97
8	0.62 s	28.60 s	21.46 s	40.68 s	93.39 s	7.22	0.90
16	0.62 s	16.20 s	10.76 s	23.72 s	53.03 s	12.71	0.80

nearly linearly. With the number of processes increasing, MPI function expenses and synchronous operations between processes cause the decline of Speedup and Efficiency. Except for the Mesh Line Generation module, the rest of the modules show good linear parallelism. This method has better speedup and efficiency when the amount of grids increase. In general, the program shows a nearly linear parallelism, neglecting delay effects.

IV. CONCLUSION

This paper presents a parallel structured mesh generation method for FDTD simulation. The method takes the STL file as input file, uses the projection method for surface fitting, and the ray tracing method for internal filling. As the result, the surface triangle elements recorded in the STL file are converted to Yee cells for electromagnetic calculation using the FDTD method. To reduce excessive computation time caused by enormous geometric primitives and billion-scale grids, the parallel projection method and parallel ray tracing method are proposed. To verify the parallelism of the method, a submarine is simulated with 200, 400, and 1700 million grids. The simulated result shows that the method has nearly linear parallelism for both simulations. It shows the proposed parallel method is helpful to deal with large-scale problems for the FDTD method.

ACKNOWLEDGMENT

This work was supported in part by the Key Research and Development Program of China (No. 2020YFA0709800), in part by the National Natural Science Foundation of China (62122061), and in part by the Shaanxi Natural Science Basic Research Project of Shaanxi Science and Technology Office (No. 2023-JC-QN-0673).

REFERENCES

[1] K. Yee, “Numerical solution of initial boundary value problems involving Maxwell’s equations in isotropic media,” *IEEE Trans. Antennas Propagat.*, vol. AP-14, no. 3, pp. 302–307, May 1966.

[2] W. Sun, C. A. Balanis, M. P. Purchine, and G. Barber, “Three-dimensional automatic FDTD mesh generation on a PC,” in *Proc. IEEE Int. Symp. Antennas and Propagation*, Ann Arbor, MI, USA, pp. 30–33, 1993.

[3] C. Mou and J. Chen, “Adaptive FDTD mesh generation technique based on cuboid ray column intersection method,” in *2021 International Applied*

Computational Electromagnetics Society (*ACES-China*) *Symposium*, Chengdu, China, pp. 1–2, 2021.

[4] G. Junkin and J. Parron, “A robust 3D mesh generator for the Dey-Mittra conformal FDTD algorithm,” in *Proc. EuCAP*, Edinburgh, pp. 1–6, 2007.

[5] X. Mao, L. Hong, and A. Kaufman, “Splatting of curvilinear volumes,” in *Proceedings Visualization ’95*, Atlanta, GA, USA, pp. 61–68, 1995.

[6] A. Van Gelder and J. Wilhelms, “Rapid exploration of curvilinear grids using direct volume rendering,” in *Proceedings Visualization ’93*, San Jose, CA, USA, pp. 70–77, 1993.

[7] N. Max, P. Hanrahan, and R. Crawfis, “Area and volume coherence for efficient visualization of 3D scalar functions,” *Computer Graphics*, vol. 24, no. 2, pp. 27–33, 1990.

[8] F. M. Miranda and W. Celes, “Accurate volume rendering of unstructured hexahedral meshes,” in *2011 24th SIBGRAPI Conference on Graphics, Patterns and Images*, Alagoas, Brazil, pp. 93–100, 2011.

[9] Y. Srisukh, J. Nehrbass, F. L. Teixeira, J.-F. Lee, and R. Lee, “An approach for automatic grid generation in three-dimensional FDTD simulations of complex geometries,” *IEEE Antennas and Propagation Magazine*, vol. 44, no. 4, pp. 75–80, Aug. 2002.

[10] M. K. Berens, I. D. Flintoft, and J. F. Dawson, “Structured mesh generation: Open-source automatic nonuniform mesh generation for FDTD simulation,” *IEEE Antennas and Propagation Magazine*, vol. 58, no. 3, pp. 45–55, June 2016.

[11] M. Garrity, “Raytracing irregular volume,” *Computer Graphics*, vol. 24, no. 2, pp. 35–40, 1990.

[12] L. Hong and A. E. Kaufman, “Fast projection-based ray-casting algorithm for rendering curvilinear volumes,” *IEEE Transactions on Visualization and Computer Graphics*, vol. 5, no. 4, pp. 322–332, Oct.–Dec. 1999.

[13] J. Hill, “Efficient implementation of mesh generation and FDTD simulation of electromagnetic fields,” M.S. thesis, Dept. Electrical and Computer Engineering, Worcester Polytechnic Inst., MA, 1996.

[14] X. C. Bo, J. F. Zhang, and T. J. Cui, “Investigation of corner singularity in conformal FDTD structured mesh generation based on ray tracing,” in *Proc. 4th IEEE Int. Conf. Comput. Electromagn.*, Chengdu, China, pp. 1–3, 2018.

[15] X. C. Bo, X. Jin, J. F. Zhang, and C. T. Jun, “Study of corner singularity in conformal structured mesh generation for the finite-difference time-domain method based on ray tracing,” *IEEE Transactions on Microwave Theory and Techniques*, vol. 67, no. 1, pp. 57–69, Jan. 2019.

[16] D. J. Riley and C. D. Turner, “Interfacing unstructured tetrahedron grids to structured-grid FDTD,” *IEEE Microwave and Guided Wave Letters*, vol. 5, no. 9, pp. 284–286, Sep. 1995.

[17] T. Rylander, “Finite element methods with stable hybrid explicit-implicit time-integration schemes,” in *2007 International Conference on Electromagnetics in Advanced Applications*, Turin, Italy, pp. 383–386, 2007.

[18] Z. Xiao, B. Wei, and D. Ge, “A hybrid mesh DGTD algorithm based on virtual element for tetrahedron and hexahedron,” *IEEE Transactions on Antennas and Propagation*, vol. 69, no. 4, pp. 2242–2248, Apr. 2021.

[19] P. Moran and D. Ellsworth, “Visualization of AMR data with multi-level dual-mesh interpolation,” *IEEE Transactions on Visualization and Computer Graphics*, vol. 17, no. 12, pp. 1862–1871, Dec. 2011.

[20] J. Chen, J. Guo, C. Mou, Z. Xu, and J. Wang, “A structured mesh generation based on improved ray-tracing method for finite difference time domain simulation,” *Electronics*, vol. 13, no. 7, p. 1189, Mar. 2024.

[21] C. Wang, J. Chen, C. Mou, and J. Guo, “A high-precision structured mesh generation method for FDTD algorithm,” in *2024 International Applied Computational Electromagnetics Society Symposium* (*ACES-China*), Xi’an, China, pp. 1–3, 2024.

Jiale Guo was born in Shanxi, China. He received the D.E. in information engineering from Xi’an Jiaotong University, Xi’an, in 2021. He is currently pursuing a master’s degree in electromagnetic field and microwave technology at Xi’an Jiaotong University, Xi’an. His research interests include the computational electromagnetics with focus on mesh generation.

Juan Chen was born in Chongqing, China. She received the Ph.D. degree from Xi’an Jiaotong University, Xi’an, in 2008, in electromagnetic field and microwave technology. She is currently working at Xi’an Jiaotong University, Xi’an, as a professor. Her research interests include the computational electromagnetics and microwave device design.

An Enhanced Bayesian Compressive Sensing Method of Moments for Monostatic Scattering Problems

Longhui Sun[1], Zhonggen Wang[1], and Chenlu Li[2]

[1]School of Electrical and Information Engineering
Anhui University of Science and Technology, Huainan 232001, China
15556361695@163.com, zgwang@ahu.edu.cn

[2]School Electrical and Information Engineering
Hefei Normal University, Hefei 230061, China
chenluli@hfnu.edu.cn

Abstract – In this paper, an Enhanced Bayesian Compressive Sensing method based on the Method of Moments (EBCS-MoM) is proposed to accelerate the solution of three-dimensional electromagnetic scattering problems. Unlike conventional Bayesian Compressive Sensing method based on the Method of Moments (BCS-MoM) approaches, EBCS-MoM employs a Gaussian Scale Mixture prior to model parameters and introduces Laplace or Student's T hyperpriors to induce sparsity. To reduce the high computational cost of matrix inversion in traditional BCS-MoM, EBCS-MoM uses a surrogate function to approximate the Gaussian likelihood, allowing for an analytical posterior form. The algorithm then maximizes the marginal likelihood to construct a joint optimization problem, which is efficiently solved under the Majorization–Minimization framework using a Block Coordinate Descent method. This reduces the per-iteration complexity to $o(n^2)$. Numerical results demonstrate that the proposed method significantly accelerates computation while maintaining accuracy.

Index Terms – Bayesian compressive sensing, method of moments, monostatic scattering problems.

I. INTRODUCTION

In the context of electromagnetic scattering problems, the Method of Moments (MoM) [1] is a high-precision approach that transforms integral equations into matrix equations. However, during the computational process of the MoM, the complexities in terms of memory and time are $o(N^2)$ and $o(N^3)$, respectively, which significantly restricts its practical application. To address this limitation, various fast algorithms have been proposed, including the Fast Multipole Method (FMM) [2], the Multilevel Fast Multipole Algorithm (MLFMA) [3], and the Adaptive Integral Method (AIM) [4]. Despite their advancements, these algorithms still exhibit constraints in terms of computational complexity and processing time. Consequently, more efficient algorithms have emerged, such as the Adaptive Cross Approximation (ACA) algorithm [5], the Characteristic Basis Function Method (CBFM) [6], the Hierarchically Off-Diagonal Low-Rank (HODLR) method [7], and the Compressive Sensing-based Method of Moments (CS-MoM) [8, 9]. These innovative methods demonstrate remarkable efficiency in handling electromagnetic scattering problems.

Sparse Bayesian Learning (SBL) [10, 11] is a widely popular machine learning algorithm. In [11], SBL was introduced into the framework of Compressive Sensing (CS), leading to the development of Bayesian Compressive Sensing (BCS), which has been extensively employed for sparse signal recovery. In the realm of electromagnetic scattering problems, Bayesian compressive sensing is primarily applied in two aspects. The first pertains to bistatic electromagnetic scattering models, where, in [12], BCS techniques were utilized to accelerate the solution of bistatic electromagnetic scattering problems. The second involves monostatic electromagnetic scattering models, with [13] introducing BCS into monostatic electromagnetic scattering computations. Compared to the traditional CS-MoM [9], BCS can adaptively determine the number of measurements. However, BCS based on relevance vector machines necessitates matrix inversion at each iteration, severely limiting its application to large-scale data. In recent years, several fast SBL algorithms have been proposed [14–16]. Among them, [14] introduced a greedy approach that starts from an empty model and iteratively adds and removes basis functions to reduce computational time. Leveraging this strategy, a fast Bayesian algorithm based on a Laplace prior model was developed [15] for reconstructing sparse signals and images. Subsequently, by analyzing the stable points

Submitted On: August 19, 2025
Accepted On: November 20, 2025

https://doi.org/10.13052/2025.ACES.J.401203

of variational update expressions, a fast SBL algorithm based on Variational Bayesian Inference (VBI) was proposed [16]. Nevertheless, these approaches have not fundamentally resolved the computational bottleneck when handling large-scale data. Recently, the Generalized Approximate Message Passing (GAMP) [17] framework has been adopted to approximate the posterior distribution, thereby avoiding matrix inversion. However, this algorithm introduces an iterative method to replace the E-step of Expectation-Maximization (EM)-based SBL, which still fails to alleviate the computational burden associated with large-scale data. In [18], an Efficient Sparse Bayesian Learning (ESBL) Algorithm Based on Gaussian-Scale Mixtures was proposed. This algorithm exhibits a computational complexity of merely $o(n^2)$ per iteration, significantly mitigating the matrix inversion challenge encountered in the solution process of traditional SBL methods. It has been widely applied in sparse signal recovery and image reconstruction.

In this paper, we have innovatively integrated the ESBL algorithm into the CS-MoM, thereby proposing the Enhanced Bayesian Compressive Sensing method based on the Method of Moments (EBCS-MoM). The EBCS-MoM method achieves sparse modeling of parameters by incorporating a Gaussian Scale Mixture (GSM) prior within a Bayesian framework. To tackle the high computational complexity arising from the need for matrix inversion at each iteration in traditional BCS, EBCS-MoM constructs a tight lower bound for the likelihood function and introduces a surrogate function to approximate the posterior distribution, thereby transforming the joint optimization problem into a decomposable non-convex problem. Subsequently, the Block Coordinate Descent (BCD) algorithm [19] is employed within the Majorization-Minimization (MM) [20] framework to alternately optimize model parameters and hyperparameters. At each step, analytical formulas involving only vector and diagonal matrix operations are utilized, reducing the overall computational complexity to $o(n^2)$. Numerical simulation results demonstrate that, compared to the conventional Bayesian Compressive Sensing-based Method of Moments (BCS-MoM) [13], the proposed EBCS-MoM method offers faster computational efficiency while maintaining comparable accuracy.

II. THEORY

A. Combination of BCS and MoM

According to the MoM, the integral equation for the monostatic electric field can be transformed into the following matrix equation:

$$\begin{aligned}&\mathbf{Z}_{N\times N}[\mathbf{I}(\theta_1),\mathbf{I}(\theta_2),\ldots,\mathbf{I}(\theta_n)]_{N\times n}\\&\quad=[\mathbf{V}(\theta_1),\mathbf{V}(\theta_2),\ldots,\mathbf{V}(\theta_n)]_{N\times n},\end{aligned}\quad(1)$$

where $\mathbf{Z}$ represents the impedance matrix with dimensions of $N\times N$, $\theta_1,\theta_2\ldots\theta_n$ denote the incident angles, $\mathbf{I}(\theta_i)$ corresponds to the induced current for the given incident angle, and $\mathbf{V}(\theta_i)$ is the excitation vector associated with that incident angle. Solving equation (1) using the MoM for each incident angle involves a tremendous computational burden. In [13], the BCS-MoM was introduced to address this challenge.

Each row in matrix $[\mathbf{I}(\theta_1),\mathbf{I}(\theta_2)\ldots\mathbf{I}(\theta_n)]_{N\times n}$ represents a one-dimensional complex signal of length n. Sparse projection of these N signals yields the following expression:

$$\begin{aligned}[\mathbf{I}(\theta_1),\mathbf{I}(\theta_2),\ldots,\mathbf{I}(\theta_n)]^T&=\psi_{n\times n}\begin{bmatrix}y(\theta_1)^T\\y(\theta_2)^T\\\vdots\\y(\theta_n)^T\end{bmatrix}\\&=\psi_{n\times n}\omega_{n\times N},\end{aligned}\quad(2)$$

where $\psi_{n\times n}$ is a sparse matrix and $\omega_{n\times N}$ is a sparse coefficient matrix. For the convenience of description, let $[y(\theta_1),y(\theta_2),\ldots,y(\theta_n)]^T=\omega_{n\times N}$.

According to the BCS theory, we construct an independently and identically distributed Gaussian measurement matrix $\phi_{mn}=[C_{ij}|i=1,2\ldots m;j=1,2\ldots n],m\ll n$. By transposing both sides of equation (1) and multiplying them simultaneously by ϕ_{mn}, the following expression can be obtained:

$$\begin{aligned}&\begin{bmatrix}C_{11}&C_{12}&\cdots&C_{1n}\\C_{21}&C_{22}&\cdots&C_{2n}\\\vdots&\vdots&\ddots&\vdots\\C_{m1}&C_{m2}&\cdots&C_{mn}\end{bmatrix}\begin{bmatrix}\mathbf{I}(\theta_1)^T\\\mathbf{I}(\theta_2)^T\\\vdots\\\mathbf{I}(\theta_n)^T\end{bmatrix}\mathbf{Z}^T\\&=\begin{bmatrix}C_{11}&C_{12}&\cdots&C_{1n}\\C_{21}&C_{22}&\cdots&C_{2n}\\\vdots&\vdots&\ddots&\vdots\\C_{m1}&C_{m2}&\cdots&C_{mn}\end{bmatrix}\begin{bmatrix}\mathbf{V}(\theta_1)^T\\\mathbf{V}(\theta_2)^T\\\vdots\\\mathbf{V}(\theta_n)^T\end{bmatrix},\end{aligned}\quad(3)$$

which can be rewritten as:

$$\phi_{mn}\begin{bmatrix}\mathbf{I}(\theta_1)^T\\\mathbf{I}(\theta_2)^T\\\vdots\\\mathbf{I}(\theta_n)^T\end{bmatrix}\mathbf{Z}^T=\phi_{mn}\begin{bmatrix}\mathbf{V}(\theta_1)^T\\\mathbf{V}(\theta_2)^T\\\vdots\\\mathbf{V}(\theta_n)^T\end{bmatrix}.\quad(4)$$

Substituting equation (2) into equation (4) yields:

$$\phi_{mn}\psi_{n\times n}\begin{bmatrix}y(\theta_1)^T\\y(\theta_2)^T\\\vdots\\y(\theta_n)^T\end{bmatrix}\mathbf{Z}^T=\phi_{mn}\begin{bmatrix}\mathbf{V}(\theta_1)^T\\\mathbf{V}(\theta_2)^T\\\vdots\\\mathbf{V}(\theta_n)^T\end{bmatrix}.\quad(5)$$

Let $\phi_{mn}[\mathbf{V}(\theta_1),\mathbf{V}(\theta_2),\ldots,\mathbf{V}(\theta_n)]^T$ be set as $[\mathbf{V}^{BCS}_{N\times m}]^T$, where each row represents a new excitation, and there are a total of m new excitations. Similarly, let $\phi_{mn}\psi_{n\times n}[y(\theta_1),y(\theta_2),\ldots,y(\theta_n)]^T$ be set as $[\mathbf{I}_{N\times m}^{BCS}]^T$, which represents the induced current under the new excitations. Therefore, equation (5) can be rewritten as:

$$\mathbf{Z}\mathbf{I}_{N\times m}^{BCS}=\mathbf{V}_{N\times m}^{BCS}. \tag{6}$$

$\mathbf{I}_{N\times m}^{BCS}$ can be computed using the MoM. Consequently, the following equation can be derived:

$$\mathbf{I}_{m\times N}^{BCS}=\phi_{m\times n}\psi_{n\times n}\boldsymbol{\omega}_{n\times N}, \tag{7}$$

where $\mathbf{I}_{m\times N}^{BCS}$ is the observation matrix, which is the transpose of $\mathbf{I}_{N\times m}^{BCS}$. By extracting the first-column data from matrices $\mathbf{I}_{m\times N}^{BCS}$ and $\boldsymbol{\omega}_{n\times N}$, then adding noise vectors ξ to both sides of the equation, we derive the following Bayesian model-compliant formulation:

$$\mathbf{I}_1^{BCS}=\phi_{m\times n}\psi_{n\times n}\boldsymbol{\omega}_1+\boldsymbol{\xi}=\boldsymbol{\Phi}\boldsymbol{\omega}_1+\boldsymbol{\xi}, \tag{8}$$

where Φ serves as the sensing matrix. Within the Bayesian framework, in order to conduct inference, we need to make prior assumptions about model (8). Typically, it is assumed that $\boldsymbol{\omega}_1$ and $\boldsymbol{\xi}$ follow the following Gaussian prior models:

$$p(\boldsymbol{\omega}_1|\boldsymbol{\alpha})=\prod_{i=1}^{n}\mathrm{N}(\omega_1^i|0,\alpha_i^{-1}),\quad i=1,2\ldots n, \tag{9}$$

$$p(\boldsymbol{\xi}|\lambda)=\prod_{m=1}^{m}\mathrm{N}(\xi_i|0,\lambda),\quad i=1,2\ldots n, \tag{10}$$

where $\boldsymbol{\alpha}$ and λ are hyperparameters of the model. Each element of $\boldsymbol{\alpha}=[\alpha_1,\alpha_2\ldots\alpha_n]^T$ is independent of one another, and the same holds true for each element of $\lambda=[\lambda_1,\lambda_2\ldots\lambda_n]^T$. Furthermore, we assume that λ_i follows Gamma distributions: $p(\lambda_i)\sim Gamma(a_0,b_0)$, where a_0 and b_0 are given parameters.

Based on the aforementioned assumptions, a multivariate Gaussian likelihood model for $\mathbf{I}_1^{BCS}$ can be derived:

$$p(\mathbf{I}_1^{BCS}|\boldsymbol{\omega}_1,\lambda)=(2\pi\lambda)^{\frac{-m}{2}}\exp\left(-\frac{\|\mathbf{I}_1^{BCS}-\boldsymbol{\Phi}\boldsymbol{\omega}_1\|^2}{2\lambda}\right). \tag{11}$$

From equations (9) and (11), the marginal distribution of $\mathbf{I}_1^{BCS}$ can be derived:

$$\begin{aligned}&p(\mathbf{I}_1^{BCS}|\boldsymbol{\alpha},\lambda)\\&\quad=(2\pi)^{\frac{-m}{2}}|D|^{\frac{-1}{2}}\exp\left(-\frac{1}{2}(\mathbf{I}_1^{BCS})^{\mathrm{T}}\mathbf{D}^{-1}\mathbf{I}_1^{BCS}\right),\end{aligned} \tag{12}$$

where $\mathbf{D}=\lambda\mathbf{E}+\boldsymbol{\Phi}\mathbf{A}^{-1}\Phi^{\mathrm{T}}$ and $\mathbf{A}=diag(\alpha_1,\alpha_2\ldots\alpha_N)$. According to the Bayesian formula, the sparse posterior distribution of $\boldsymbol{\omega}_1$ is given by:

$$\begin{aligned}&p(\boldsymbol{\omega}_1|\mathbf{I}_1^{BCS},\boldsymbol{\alpha},\lambda)\\&\quad=\frac{p(\mathbf{I}_1^{BCS}|\boldsymbol{\omega}_1,\lambda)p(\boldsymbol{\omega}_1|\boldsymbol{\alpha})}{p(\mathbf{I}_1^{BCS}|\boldsymbol{\alpha},\lambda)}\\&\quad=(2\pi)^{\frac{-m}{2}}\left|\sum\right|^{\frac{-1}{2}}\\&\qquad\times\exp\left(\frac{1}{2}(\boldsymbol{\omega}_1-u)^{\mathrm{T}}\sum\nolimits^{-1}(\boldsymbol{\omega}_1-u)\right),\end{aligned} \tag{13}$$

where $\boldsymbol{\omega}_1$ mean and covariance are:

$$u=\lambda\sum\boldsymbol{\Phi}^{\mathrm{T}}\mathbf{I}_1^{BCS}, \tag{14}$$

$$\sum=(\mathbf{A}+\lambda\boldsymbol{\Phi}^{\mathrm{T}}\boldsymbol{\Phi})^{-1}. \tag{15}$$

The update of hyperparameters can be regarded as a learning problem in the context of relevant vector bases. According to equation (12), the Type-II maximum likelihood estimates of the hyperparameters can be obtained:

$$\alpha_i^{new}=\frac{\gamma_i}{u_i^2}, \tag{16}$$

$$\gamma_i=1-\alpha_i\sum\nolimits_{ii}, \tag{17}$$

$$(\lambda)^{new}=\frac{\|\mathbf{I}_1^{BCS}-\boldsymbol{\Phi}u\|^2}{n-\sum_i\gamma_i}, \tag{18}$$

where u_i is the ith posterior mean weight from (14) and $\sum_{ii}$ is the ith diagonal element of the covariance in (15).

In order to compute the sparse vector ω_1, this algorithm performs an iterative update process by continuously applying (16) and (18) while updating the posterior statistics of (14) and (15) until the convergence condition is satisfied. Finally, the sparse coefficient vector $\boldsymbol{\omega}_1$ is approximately equal to u. Similarly, performing BCS-MoM restoration on each column of matrix $\boldsymbol{\omega}$ in equation (7) allows reconstruction of the sparse coefficient matrix $\boldsymbol{\omega}$. By substituting $\boldsymbol{\omega}$ into equation (2), $[\mathbf{I}(\theta_1),\mathbf{I}(\theta_2),\ldots,\mathbf{I}(\theta_n)]^T$ can be obtained. Figure 1 illustrates the algorithm flowchart of the BCS-MoM.

B. Proposed method

To address the high computational complexity issue arising when the traditional BCS-MoM solves equation (15), this paper proposes the EBCS-MoM algorithm. By introducing a GSM prior, this algorithm constructs a lower bound function for the likelihood and employs the BCD method to optimize each parameter step by step, thereby reducing the computational load per iteration. For the detailed implementation process of EBCS, refer to [18].

Algorithm 1: BCS-MoM Algorithm

```
Date: sensing matrix $\mathbf{\Phi}$, observation matrix $\mathbf{I}_1^{BCS}$,
sparse coefficient vector $\boldsymbol{\omega}_1$, noise vector $\xi$;
Result: estimated value $\boldsymbol{\omega}_1^{new}$;
Initialize: maximum iteration count $K$,
    convergence threshold $T$, current iteration count
    $k$, hyperparameters $\boldsymbol{\alpha}$ and $\lambda$;
While true do
    Calculated from (14) $u$;
    Calculated from (15) $\Sigma$;
    Calculated from (16) $\alpha_i^{new}$;
    Calculated from (18) $(\lambda)^{new}$;
    Update the value of $\boldsymbol{\omega}_1^{new}$ to $u$;
    if $\| \boldsymbol{\omega}_1^{new} - \boldsymbol{\omega}_1^{old} \|_2 \le T \vee k = K$
        break;
    else
        Update the value of $\boldsymbol{\omega}_1^{old}$ to $\boldsymbol{\omega}_1^{new}$;
        Update $\mathbf{A}$ to $diag(\alpha_1, \alpha_2 ... \alpha_N)$.
    end
end
```

Fig. 1. Flowchart of BCS-MoM algorithm.

In EBCS-MoM, each element of $\boldsymbol{\omega}_1$ is assumed to follow a GSM prior:

$$p(\omega_1^i) = \int p(\omega_1^i|\gamma_i)p(\gamma_i)d\gamma_i,\ i = 1,2...n, \tag{19}$$

$$p(\omega_1^i|\gamma_i) = (2\pi\gamma_i)^{-\frac{1}{2}} \exp\left(-\frac{(\omega_1^i)^2}{2\gamma_i}\right) \sim N(\theta_i|0,\gamma_i), i = 1,2...n, \tag{20}$$

where γ_i is a hyperparameter that controls the sparsity of each parameter. Typically, γ_i can be chosen from different distributions, such as the exponential distribution and the Gamma distribution. In this paper, we assume that γ_i follows independent and identically distributed Gamma distributions: $p(\gamma_i) \sim Gamma(c_0, d_0)$, where c_0 and d_0 are given parameters.

To avoid computing equation (11) at each iteration, EBCS introduces a lower bound of the likelihood function. By introducing auxiliary variables β to replace the true parameter model $\boldsymbol{\omega}_1$, and letting $f(\boldsymbol{\omega}_1) = \|\mathbf{I}_1^{BCS} - \mathbf{\Phi}\boldsymbol{\omega}_1\|^2$, an upper-bound function $R(\boldsymbol{\omega}_1,\beta)$ is constructed as follows:

$$f(\boldsymbol{\omega}_1) \le R(\boldsymbol{\omega}_1,\beta) = \|\mathbf{I}_1^{BCS} - \mathbf{\Phi}\beta\|^2 + 2(\boldsymbol{\omega}_1 - \beta)^T\mathbf{\Phi}^T(\mathbf{\Phi}\beta - \mathbf{I}_1^{BCS}) + s_0\|\boldsymbol{\omega}_1 - \beta\|^2, \tag{21}$$

where $s_0 = eig(\mathbf{\Phi}^T\mathbf{\Phi}) + \tau$ and τ is a constant. This function is equal to $f(\boldsymbol{\omega}_1)$ at the point where $\boldsymbol{\omega}_1 = \beta$.

Based on the aforementioned approximation, a surrogate likelihood function $\tilde{p}(\mathbf{I}_1^{BCS}|\boldsymbol{\omega}_1,\lambda,\beta)$ can be constructed:

$$\tilde{p}(\mathbf{I}_1^{BCS}|\boldsymbol{\omega}_1,\lambda,\beta) = (2\pi\lambda)^{\frac{-m}{2}} \exp\left(-\frac{\lambda R(\boldsymbol{\omega}_1,\beta)}{2}\right). \tag{22}$$

Thus, the following equation is established:

$$p(\mathbf{I}_1^{BCS}|\boldsymbol{\omega}_1,\lambda) = \max_{\beta} \tilde{p}(\mathbf{I}_1^{BCS}|\boldsymbol{\omega}_1,\lambda,\beta). \tag{23}$$

By replacing $p(\mathbf{I}_1^{BCS}|\boldsymbol{\omega}_1,\lambda)$ with its lower bound $\tilde{p}(\mathbf{I}_1^{BCS}|\boldsymbol{\omega}_1,\lambda,\beta)$, an approximate posterior density of $\boldsymbol{\omega}_1$ can be obtained, where $\hat{\beta}$ is fixed. According to Bayesian principles, the following approximation can be derived:

$$p(\boldsymbol{\omega}_1|\mathbf{I}_1^{BCS},\lambda,\gamma) \approx \frac{\tilde{p}(\mathbf{I}_1^{BCS}|\boldsymbol{\omega}_1,\lambda,\hat{\beta})p(\boldsymbol{\omega}_1|\gamma)}{\int \tilde{p}(\mathbf{I}_1^{BCS}|\boldsymbol{\omega}_1,\lambda,\hat{\beta})p(\boldsymbol{\omega}_1|\gamma)d\boldsymbol{\omega}_1} \sim N\left(u_{\boldsymbol{\omega}_1}, \sum\nolimits_{\boldsymbol{\omega}_1}\right), \tag{24}$$

with:

$$\sum\nolimits_{\boldsymbol{\omega}_1} = (\Gamma^{-1} + s_0\lambda\mathbf{E})^{-1},\ \Gamma = diag(\gamma), \tag{25}$$

$$u_{\boldsymbol{\omega}_1} = \lambda \sum\nolimits_{\boldsymbol{\omega}_1}(s_0\hat{\beta} - \mathbf{\Phi}^T\mathbf{\Phi}\hat{\beta} + \mathbf{\Phi}^T\mathbf{I}_1^{BCS}). \tag{26}$$

Therefore, the point estimate of $\boldsymbol{\omega}_1$ is given by:

$$\hat{\boldsymbol{\omega}}_1 = (\Gamma_{MP}^{-1} + s_0\lambda_{MP}\mathbf{E})^{-1}\lambda_{MP}(s_0\hat{\beta} - \mathbf{\Phi}^T\mathbf{\Phi}\hat{\beta} + \mathbf{\Phi}^T\mathbf{I}_1^{BCS}), \tag{27}$$

where λ_{MP} and Γ_{MP} are hyperparameters to be estimated.

The subsequent critical step involves optimizing parameters λ, γ, and β. During the Type-II Maximum Likelihood Estimation process, hyperparameters can be estimated by maximizing the joint probability density function. Consequently, λ, γ, and β are obtained through the following optimization problem:

$$(\lambda,\gamma,\beta) = \arg\max_{\lambda,\gamma,\beta} \times \int \tilde{p}(\mathbf{I}_1^{BCS}|\boldsymbol{\omega}_1,\lambda,\beta)p(\boldsymbol{\omega}_1|\gamma)p(\lambda)p(\gamma)d\boldsymbol{\omega}_1, \tag{28}$$

and, subsequently, the cost function L in the joint space of model parameters and hyperparameters can be obtained:

$$L(\boldsymbol{\omega}_1,\beta,\sigma^2,\gamma) = \sum_{i=1}^{n}\left(\ln(\sigma^2+s_0\gamma_i)+c_1\ln\gamma_i+\frac{2d_0+(\omega_1^i)^2}{\gamma_i}\right) - n_1\ln\sigma^2+\frac{R(\boldsymbol{\omega}_1,\beta)+2b_0}{\sigma^2}, \tag{29}$$

where $n_1 = n+2-m-2a_0$, $c_1 = 2c_0-2$, $\sigma^2=\lambda^{-1}$ and $R(\boldsymbol{\omega}_1,\beta)$ is provided in (21).

EBCS decomposes the cost function into convex and concave parts, leverages the MM framework for optimization, and progressively optimizes each parameter using the BCD method. Ultimately, the update formulas for all parameters can be obtained:

$$\sum\nolimits_{\boldsymbol{\omega}_1}^{(k)} = \left(\Gamma^{(k)^{-1}}+\frac{s_0}{(\sigma^2)^k}\mathbf{E}\right)^{-1}, \tag{30}$$

$$\boldsymbol{\omega}_1^{(k+1)} = \frac{1}{(\sigma^2)^{(k)}}\sum\nolimits_{\boldsymbol{\omega}_1}^{(k)}(s_0\beta^{(k)}-\boldsymbol{\Phi}^T\boldsymbol{\Phi}\beta^{(k)}+\boldsymbol{\Phi}^T\mathbf{I}_1^{BCS}), \tag{31}$$

$$\beta^{(k+1)} = \boldsymbol{\omega}_1{}^{(k+1)}, \tag{32}$$

$$\rho^{(k+1)} = \sum_{i=1}^{n}\frac{1}{(\sigma^2)^{(k)}+s_0\gamma_i^{(k)}}, \tag{33}$$

$$(\sigma^2)^{(k+1)} = \frac{n_1+\sqrt{n_1^2+4\rho^{(k+1)}(\|\mathbf{I}_1^{BCS}-\boldsymbol{\Phi}\beta\|^2+2b_0)}}{2\rho^{(k+1)}}, \tag{34}$$

$$\gamma_i^{(k+1)} = \sqrt{\frac{\gamma_i^{(k)}((\sigma^2)^{(k)}+s_0\gamma_i^{(k)})(2d_0+(\omega_1^i)^{(k+1)2})}{(c_1+1)s_0\gamma_i^{(k)}+c_1(\sigma^2)^{(k)}}}, \quad i=1,2\ldots n. \tag{35}$$

The iteration stop threshold for EBCS is defined as:

$$\frac{\|\boldsymbol{\omega}_1{}^{(k+1)}-\boldsymbol{\omega}_1{}^{(k)}\|}{\|\boldsymbol{\omega}_1{}^{(k+1)}\|}\leq\delta, \tag{36}$$

where δ is defined as the threshold. The EBCS-MoM method iteratively optimizes the parameters until equation (36) is satisfied, thereby obtaining the sparse coefficient vector $\boldsymbol{\omega}_1$. Similarly, performing EBCS-MoM restoration on each column of matrix $\boldsymbol{\omega}$ in equation (7) allows reconstruction of the sparse coefficient matrix $\boldsymbol{\omega}$. The obtained $\boldsymbol{\omega}$ is then substituted into equation (2) to derive the original current $[\mathbf{I}(\theta_1),\mathbf{I}(\theta_2),\ldots,\mathbf{I}(\theta_n)]^T$. Figure 2 illustrates the algorithm flowchart of the EBCS-MoM.

Algorithm 2: EBCS-MoM Algorithm

```
Date: sensing matrix $\boldsymbol{\Phi}$ , observation matrix $\mathbf{I}_1^{BCS}$ ,
sparse coefficient vector $\boldsymbol{\omega}_1$ , noise vector $\xi$ ;
Result: estimated value $\boldsymbol{\omega}_1$ ;
Initialize: maximum iteration count $K$ , current
  iteration count k, convergence threshold $\delta$ ,
  hyperparameters $(\sigma^2)^{(0)}$ and $(\gamma)^{(0)}, (\beta)^{(0)}$ ;
While true do
    Calculated from (30) $\sum_{\boldsymbol{\omega}_1}^{(k)}$ ;
    Calculated from (31) $\boldsymbol{\omega}_1^{(k+1)}$ ;
    Calculated from (33) $\beta^{(k+1)}$ ;
    Calculated from (33) $\rho^{(k+1)}$ ;
    Calculated from (34) $(\sigma^2)^{(k+1)}$ ;
    Calculated from (35) $\gamma_i^{(k+1)}$ ;
    if $\frac{\|\boldsymbol{\omega}_1{}^{(k+1)}-\boldsymbol{\omega}_1{}^{(k)}\|}{\|\boldsymbol{\omega}_1{}^{(k+1)}\|}\leq\delta\vee k=K$ break;
end
$\boldsymbol{\omega}_1=\boldsymbol{\omega}_1{}^{(k+1)}$
```

Fig. 2. Flowchart of EBCS-MoM algorithm.

C. Computational complexity analysis

The computational complexity for impedance matrix filling and $\mathbf{I}_{N\times m}^{BCS}$ is the same in both BCS-MoM and EBCS-MoM methods. Therefore, here we only compare the computational complexity of the two methods in solving equation (8).

1. BCS-MoM

   The computational cost per iteration primarily centers on the inversion of the covariance matrix and the calculation of the posterior mean. The computational complexities for solving equations (14) and (15) are $o(n^2)$ and $o(n^3)$, respectively.

2. EBCS-MoM

   The computational cost per iteration primarily focuses on matrix multiplication. When solving equation (30), it mainly involves the inversion of a diagonal matrix, with a computational complexity of $o(n)$. When solving equations (31), (34), and (35), the computation involves calculating $\boldsymbol{\Phi}^T\boldsymbol{\Phi}$, with a computational complexity of $o(n^2)$.

Therefore, the proposed method substantially decreases the computational complexity per iteration.

III. NUMERICAL RESULTS

To demonstrate the validity of the EBCS-MoM, numerical simulations of different three-dimensional conductor models are performed. Furthermore, the BCS-MoM and the GGAMP-SBL approach [17] based on the Method of Moments (GGAMP-SBL-MoM) were selected as benchmark methods for experimental comparison. To enable quantitative assessment of computational accuracy, the root-mean-square error (RMSE) metric for the monostatic radar cross section (RCS) is defined as:

$$RMSE = \sqrt{\frac{1}{N_a}\sum_{i=1}^{N_a} |\mathrm{RCS}_{\mathrm{cal},i} - \mathrm{RCS}_{\mathrm{ref},i}|^2}, \tag{37}$$

where $\mathrm{RCS}_{\mathrm{cal},i}$ is the calculation result obtained through methods EBCS-MoM, GGAMP-SBL-MoM and BCS-MoM, $\mathrm{RCS}_{\mathrm{ref},i}$ is the calculation result using MoM, and N_a is the number of sampling points.

First, the monostatic scattering problem of a missile is analyzed at the angle of incidence from $\theta = 0^\circ$ to $\theta = 180^\circ$ and $\varphi = 0^\circ$, which has an incident frequency of 1.4 GHz. The target is discretized into 9178 triangles, causing 13676 unknowns.

In (2), sparse transformation is applied to $[\mathbf{I}(\theta_1), \mathbf{I}(\theta_2), \ldots, \mathbf{I}(\theta_n)]^T$. To determine an appropriate sparse basis, Fig. 3 illustrates the errors corresponding to two commonly used sparse bases under different numbers of measurements. It can be observed that as the number of measurements increases, the errors associated with both methods decrease. Moreover, when the same number of measurements is employed, the Hermite sparse basis yields better performance compared to the Discrete Cosine Transform sparse basis (DCT). Therefore, in this paper, the Hermite sparse basis is selected.

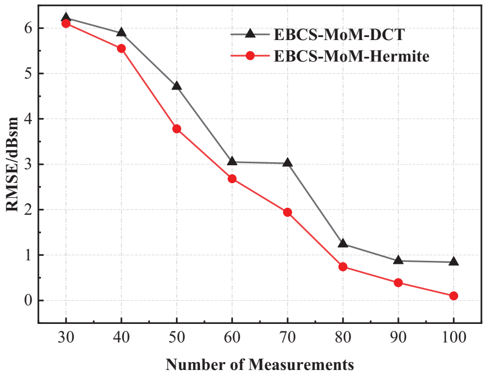

Fig. 3. RMSE of BCS-MoM-DCT and EBCS-MoM-Hermite with different number of measurements.

To analyze the impact of varying iteration counts on the computational time and accuracy of two methods, Fig. 4 presents the time and accuracy results for both methods across different iteration counts. As observed from Fig. 4, the accuracy of both methods consistently improves as the number of iterations increases. Notably, when the iteration count exceeds 90, EBCS-MoM achieves higher accuracy. Furthermore, due to its lower computational complexity per iteration, EBCS-MoM requires significantly less computational time.

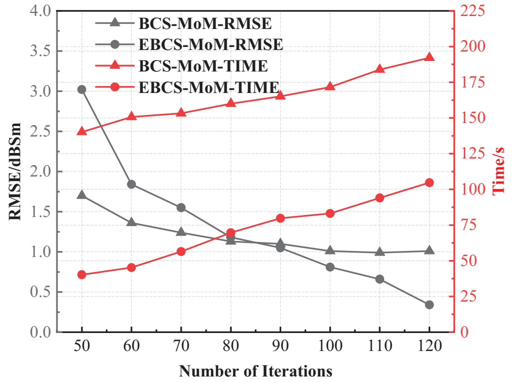

Fig. 4. RMSE and solution time of BCS-MoM and EBCS-MoM with different number of iterations.

To demonstrate the advantages of the proposed method, Fig. 5 presents the computational time and error corresponding to the two methods under different numbers of measurements. As seen in Fig. 5, under varying numbers of measurements, EBCS-MoM exhibits faster computational time compared to BCS-MoM. Additionally, in comparison with the BCS-MoM method, EBCS-MoM also demonstrates certain accuracy advantages.

To demonstrate the accuracy of the proposed method, Fig. 6 presents the average current values obtained MoM and the EBCS-MoM under different incident angles, while Fig. 7 displays the RCS calculation results from three methods. As evident from Fig. 6, the current distributions computed by EBCS-MoM exhibit excellent agreement with those obtained by the MoM. From Fig. 7, it is evident that the RCS results of three methods align well with those obtained by the MoM. Moreover, EBCS-MoM exhibits superior accuracy.

Second, the scattering problem of an array target consisting of 16 PEC objects with two different shapes is analyzed. The frequency of the incident wave is set to 1.3 GHz, and the incident excitations are a set of H-polarized plane waves from $\theta = 0^\circ$ to $\theta = 180^\circ$ and $\varphi = 0^\circ$. The target is discretized into 27216 triangles, causing 40824 unknowns.

Figure 8 illustrates the average current values obtained by the MoM and EBCS-MoM under different incident angles, demonstrating excellent agreement between the current distributions computed by EBCS-MoM and those derived from the MoM. Finally, the monostatic RCS of the array target calculated by three methods are displayed in Fig. 9. Apparently, the RCS

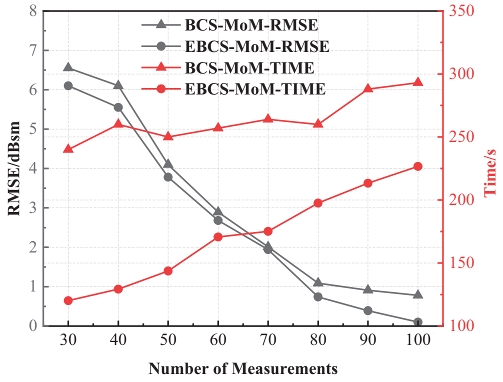

Fig. 5. RMSE and solution time of BCS-MoM and EBCS-MoM with different number of measurements.

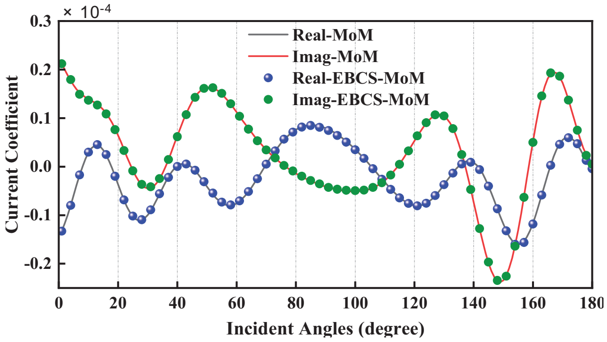

Fig. 6. The average value of induced current under different incident angles.

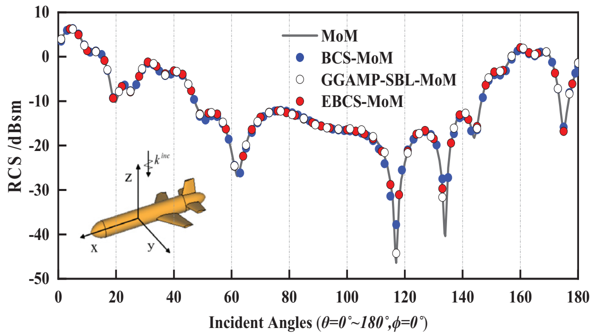

Fig. 7. Monostatic RCS of missile in horizontal polarization.

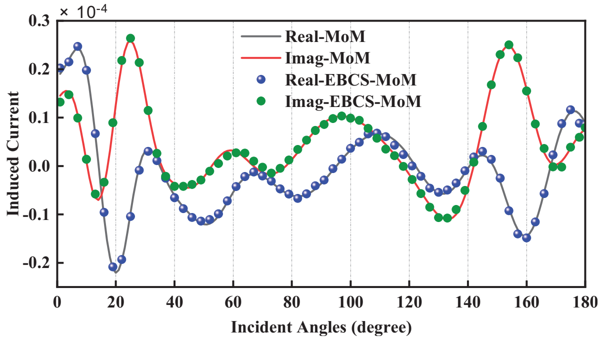

Fig. 8. The average value of induced current under different incident angles.

results obtained from the three methods, namely BCS-MoM, GGAMP-SBL-MoM, and EBCS-MoM, show good agreement with those calculated by the MoM.

The comparison of computation time, memory usage, and RMSE using different methods for the two models is shown in Table 1. Here, the observation current is $\mathbf{I}_{m\times N}^{BCS}$. Given that the primary memory consumption stems from the storage of the impedance matrix, excitation sources, and currents, there is little difference in the memory requirements among these methods. As can be seen from Table 1, when comparing with the BCS-MoM method, the EBCS-MoM reduces the computational times 30.91% and 26.56%. Similarly, when compared with the GGAMP-SBL-MoM method, it reduces the computational times 12.94% and 13.34%. It significantly accelerates the computation while maintaining accuracy.

Table 1: Comparison of computation time, memory usage and RMSE

Model	**Method**	**Unknown**	**Calculating Observation Current Time (s)**	**Recovery Induced Current Time (s)**	**Total Time (s)**	**RMSE (dBsm)**	**Memory (GB)**
Missile	MoM	13676	–	259.98	259.98	–	2.86
	BCS-MoM		114.12	171.63	285.75	1.09	2.87
	GGAMP-SBL-MoM		114.12	112.63	226.75	0.75	2.87
	EBCS-MoM		114.12	83.28	197.40	0.61	2.87
Array Target	MoM	40824	–	2164.54	2164.54	–	25.05
	BCS-MoM		1083.25	795.30	1878.55	0.75	25.06
	GGAMP-SBL-MoM		1083.25	508.72	1591.97	0.64	25.06
	EBCS-MoM		1083.25	296.27	1379.52	0.68	25.06

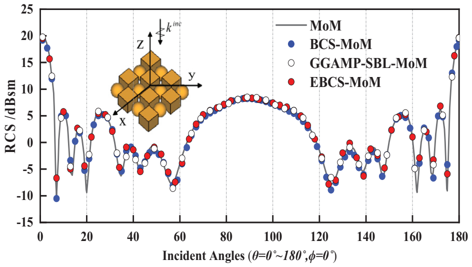

Fig. 9. Monostatic RCS of the array target in horizontal polarization.

IV. CONCLUSION

In this paper, an enhanced electromagnetic scattering algorithm is presented. The EBCS-MoM method constructs a sparse model by incorporating a GSM prior and utilizes a surrogate function to approximate the Gaussian likelihood, thereby circumventing matrix inversion. By integrating the approach of maximizing marginal likelihood, a joint optimization problem is formulated. This problem is then efficiently solved using the BCD method within the MM framework, achieving a rapid computational complexity of only $o(n^2)$ per iteration. Finally, numerical results validate the superiority of the proposed method.

ACKNOWLEDGMENT

This work was supported by the Fund of Anhui Mining Machinery and Electrical Equipment Coordination Innovation Center (Anhui University of Science and Technology) under grant No. KSJD202406.

REFERENCES

[1] R. F. Harrington, *Field Computation by Moment Method*. New York, NY: Macmillan, 1968.

[2] J. Dugan, T. J. Smy, and S. Gupta, "Accelerated IE-GSTC solver for large-scale metasurface field scattering problems using fast multipole method (FMM)," *IEEE Trans. Antennas Propag.*, vol. 70, no. 10, pp. 9524–9533, Oct. 2022.

[3] H. L. Zhang, Y. X. Sha, X. Y. Guo, M. Y. Xia, and C. H. Chan, "Efficient analysis of scattering by multiple moving objects using a tailored MLFMA," *IEEE Trans. Antennas Propag.*, vol. 67, no. 3, pp. 2023–2027, Mar. 2019.

[4] E. Bleszynski, M. Bleszynski, and T. Jaroszewicz, "AIM: Adaptive integral method for solving large-scale electromagnetic scattering and radiation problems," *Radio Sci.*, vol. 31, no. 5, pp. 1225–1251, Sep. 1996.

[5] K. Zhao, M. N. Vouvakis, and J.-F. Lee, "The adaptive cross approximation algorithm for accelerated Method of Moments computations of EMC problems," *IEEE Trans. Electromagn. Compat.*, vol. 47, no. 4, pp. 763–773, Nov. 2005.

[6] V. V. S. Prakash and R. Mittra, "Characteristic basis function method: A new technique for efficient solution of Method of Moments matrix equations," *Microw. Opt. Technol. Lett.*, vol. 36, no. 2, pp. 95–100, Jan. 2003.

[7] N. Zhang, Y. Chen, Y. Ren, and J. Hu, "A modified HODLR solver based on higher order basis functions for solving electromagnetic scattering problems," *IEEE Antennas Wireless Propag. Lett.*, vol. 21, no. 12, pp. 2452–2456, Dec. 2022.

[8] Z. Wang, D. Dong, F. Guo, Y. Sun, W. Nie, and P. Wang, "Fast construction of measurement matrix and sensing matrix with dual adaptive cross approximation," *IEEE Antennas Wireless Propag. Lett.*, vol. 24, no. 1, pp. 13–17, Jan. 2025.

[9] S.-R. Chai and L.-X. Guo, "Compressive sensing for monostatic scattering from 3-D NURBS geometries," *IEEE Trans. Antennas Propag.*, vol. 64, no. 8, pp. 3545–3553, Aug. 2016.

[10] M. E. Tipping, "Sparse Bayesian learning and the relevance vector machine," *J. Mach. Learn. Res.*, vol. 1, pp. 211–244, Sep. 2001.

[11] S. Ji, Y. Xue, and L. Carin, "Bayesian compressive sensing," *IEEE Transactions on Signal Processing*, vol. 56, no. 6, pp. 2346–2356, June 2008.

[12] Z. Wang, L. Sun, W. Nie, Y. Sun, D. Dong, and Y. Liu, "Rapid calculation of bistatic scattering problems based on Bayesian compressive sensing," *Electromagnetics*, vol. 45, no. 4, pp. 320–333, May 2025.

[13] H.-H. Zhang, X.-W. Zhao, Z.-C. Lin, and W. E. I. Sha, "Fast monostatic scattering analysis based on Bayesian compressive sensing," *Applied Computational Electromagnetics Society (ACES) Journal*, vol. 31, no. 11, pp. 1279–1285, Nov. 2016.

[14] M. E. Tipping and A. C. Faul, "Fast marginal likelihood maximization for sparse Bayesian models," in *Proc. 9th Int. Workshop Artif. Intell. Statist.*, pp. 1–13, 2003.

[15] S. D. Babacan, R. Molina, and A. K. Katsaggelos, "Bayesian compressive sensing using Laplace priors," *IEEE Trans. Image Process.*, vol. 19, no. 1, pp. 53–63, Jan. 2010.

[16] D. Shutin, T. Buchgraber, S. R. Kulkarni, and H. V. Poor, "Fast variational sparse Bayesian learning with automatic relevance determination for superimposed signals," *IEEE Trans. Signal Process.*, vol. 59, no. 12, pp. 6257–6261, Dec. 2011.

[17] M. Al-Shoukairi, P. Schniter, and B. D. Rao, "A GAMP-based low complexity sparse Bayesian learning algorithm," *IEEE Trans. Signal Process*, vol. 66, no. 2, pp. 294–308, Jan. 2018.

[18] W. Zhou, H.-T. Zhang, and J. Wang, "An efficient sparse Bayesian learning algorithm based on Gaussian-scale mixtures," *IEEE Transactions on Neural Networks and Learning Systems*, vol. 33, no. 7, pp. 3065–3078, July 2022.

[19] D. Bertsekas, *Nonlinear Programming*. Belmont, MA: Athena Scientific, 1999.

[20] D. R. Hunter and K. Lange, “A tutorial on MM algorithms,” *Amer. Statistician*, vol. 58, no. 1, pp. 30–37, Feb. 2004.

Longhui Sun received the B.E. degree from Fuyang Normal University, China, in 2022. He is currently pursuing the M.S degree at Anhui University of Science and Technology. His current research interest lies in the application of Bayesian compressive sensing in electromagnetic scattering.

Zhonggen Wang received the Ph.D. degree in electromagnetic field and microwave technique from the Anhui University of China (AHU), Hefei, P. R. China, in 2014. Since 2014, he has been with the School of Electrical and Information Engineering, Anhui University of Science and Technology. His research interests include computational electromagnetics, array antennas, and reflect arrays.

Chenlu Li received the Ph.D. degree from Anhui University, China, in 2017. She is currently working at Hefei Normal University. Her research interests electromagnetic scattering analysis of targets and filtering antenna design.

Design of Ultra-Wideband Antenna Based on Gaussian Process Regression and Genetic Algorithms

Da Li Mi[1], Xi Wang Dai[1,2], Jun Shi Zhao[1], Ze Li[1], Gang Li[3], and Hui Hong[1]

[1]Shaoxing Integrated Circuit Institute & School of Electronics and Information
Hangzhou Dianzi University, Hangzhou, Zhejiang 310018, China
mi_dali@qq.com, xwdai@hdu.edu.cn, 1258042732@qq.com, 1223406727@qq.com, hongh@hdu.edu.cn

[2]State Key Laboratory of Millimeter Waves
Southeast University, Nanjing 210096, China

[3]Hubei Key Laboratory of Low Dimensional Optoelectronic Materials and Devices
Hubei University of Arts and Science, Xiangyang 441053, China
ligang_hbuas@vip.163.com

Abstract – Gaussian Process Regression (GPR) algorithm and Genetic Algorithms (GA) are used to design a scheme suitable for antenna optimization in this paper. GPR algorithms are used to build so-called surrogate models, or machine learning models, to replace full-wave simulation calculations to save time. GA is used to find the optimal solution that satisfies the optimization objective. The optimal solution obtained by GA is re-calculated with full-wave electromagnetic simulation. The surrogate model can be updated with new data when the full-wave simulation results don't meet the target. An ultra-wideband (UWB) antenna is designed by using this optimization scheme. Six structural parameters of the UWB antenna are used to optimize the design, and a total of 10 groups are used to train the surrogate model. Finally, the optimization is completed through 7 iterations. Finally, the UWB antenna is analyzed, fabricated and tested, which shows an operating frequency band of 2.95–11.43 GHz, and a physical size of $30\times27\times1.6$ mm^3.

Index Terms – Gaussian Process Regression (GPR), Genetic Algorithms (GA), ultra-wideband (UWB) antenna.

I. INTRODUCTION

Ultra-wideband (UWB) technology is a practical and effective wireless communication technology, widely used in local area network, intelligent transportation, radio frequency identification and other fields, and has strong anti-interference performance, low transmission power spectrum density, high positioning accuracy and many other advantages. As a device for transmitting and receiving wireless signals, antennas have different types according to different application scenarios. The antenna coving 3.1–10.6 GHz can be suitable for UWB application according to the regulations of the United States Federal Communications Commission (FCC).

The common methods to realize UWB antenna include loading parasitic patch, impedance loading technology and slot technology. Among them, the parasitic patch and slot technology are used to form multiple resonant frequencies, and make the resonant frequencies close together, to achieve the purpose of broadening the bandwidth. However, there is no theoretical formula to describe the relationship between the size of the parasitic patch and the operating bandwidth of antennas. Designers usually calculate its performance parameters, such as the scattering parameters, through electromagnetic simulation software. Machine learning (ML) algorithms [1–4] can make up for this shortcoming and build a so-called surrogate model between the two to describe this nonlinear relationship. This surrogate model of the antenna is known as the ML model. At present, ML algorithms used for antenna optimization include support vector machine (SVM) [5–7], deep neural network (DNN) [8, 9] and K-nearest neighbor (KNN) [10]. The Gaussian process is a new supervised learning algorithm that learns the input-output relationship of functions based on empirical data. In the 1990s, Poggio and Girosi first combined Gaussian processes with neural networks for research. The Gaussian Process Regression (GPR) algorithm is also widely used in antenna design [11–13]. Furthermore, these methods can obtain scattering parameters from specific physical models. However, physical dimensions cannot be obtained from the scattering parameters. First proposed by Professor J. Holland in 1975, Genetic Algorithm (GA) is a randomized search method that draws on the evolutionary laws of the

Submitted On: July 07, 2024
Accepted On: December 01, 2025

1054-4887 © ACES

https://doi.org/10.13052/2025.ACES.J.401204

biological world. The GA can quickly obtain the optimal solution of an equation or system of equations. In the antenna design, GA can obtain a specific antenna model that meets certain conditions [14–17]. UWB and dual-band antennas are designed with GPR and GA in [18]. However, the surrogate model cannot be updated with new data, and the size of antenna is relatively large. With the concept of performance-driven modelling, the technologies of Kriging, radial basis functions, or polynomial chaos expansion are also recently proposed and developed for antenna design [19–22].

In this paper, an optimization scheme is designed based on GPR and GA, and a UWB antenna is designed based on this optimization scheme. There is also a dual-band antenna as an additional example. Although the antenna optimization design can be completed by full-wave electromagnetic software such as HFSS and CST, the optimization efficiency is relatively low. Full-wave calculations are invoked when using GA for optimization in simulation software, which is the most time-consuming step. For the UWB structure proposed in this paper, a full-wave simulation takes 31.4 seconds at a time, while the surrogate model trained with GPR takes only 118 milliseconds. When iterations are ongoing, the time savings are considerable. Another advantage of using algorithms to complete optimization algorithms is that there is no need for the designer to think about the relationship between physical size parameters and antenna performance parameters. The GPR can establish a nonlinear relationship. The designed UWB antenna is obtained by 7 iterations. Its operating frequency band is 2.95–11.43 GHz and its physical size is $30\times27\times1.6\ \mathrm{mm}^3$.

II. ANTENNA STRUCTURE AND OPTIMIZATION SCHEME

The circuits of the designed UWB antenna are printed on the FR4 substrate with a dielectric constant of 4.4 and a loss tangent of 0.02, as shown in Fig. 1. The front patch (in red) is an irregular polygon. The back patch (in blue) is a polygon of a large rectangle dug out of a small rectangle. The aim of the algorithm proposed is to design an UWB antenna within a specified size range. The objective of the design is measured by the $|S_{11}|$ value less than -10 dB in the 3.1–10.6 GHz band range.

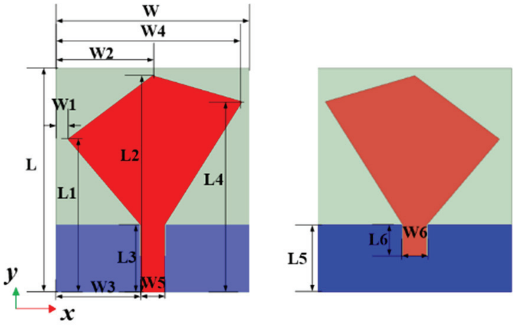

(a) (b)

Fig. 1. Geometry of proposed UWB antenna: (a) top view and (b) bottom view.

Table 1: Parameters of antenna (units: mm)

Parameter	**L_1**	**W_1**	**L_2**	**W_2**	**L_3**
Value	20.49	1.62	29	13.5	9
Parameter	**W_3**	**L_4**	**W_4**	**L_5**	**W_5**
Value	11.4	25.51	25.01	9	3.2
Parameter	**L_6**	**W_6**	**L**	**W**	**/**
Value	4.18	3.5	30	27	/

Figure 1 shows the structure after optimization. The specific size parameters are shown in Table 1. Since there is no theoretical formula to guide the optimal design for the physical size of the front and back patches and the scattering parameters of this antenna, the GPR algorithm is used to establish the surrogate model to describe this nonlinear relationship between the two. This surrogate model is also the GPR model. Further, the GA is used to find the physical size values that satisfy the optimization conditions. The overall flow chart of the designed optimization scheme is shown in Fig. 2, which can be divided into five steps.

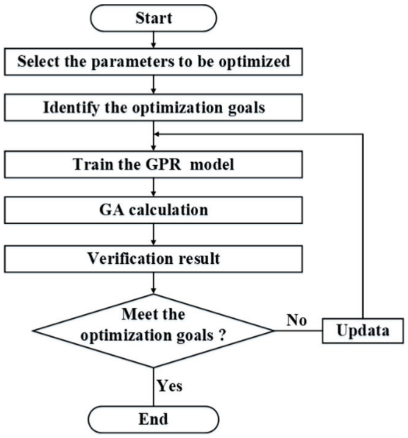

Fig. 2. Flowchart of the optimization scheme.

Step 1: Analyze the characteristics of the antenna model and set the performance index. Through full-wave electromagnetic simulation software (such as HFSS and CST) scanning analysis of parameters, the physical size of the UWB antenna parameters L_1, W_1, L_4, W_4, L_6, W_6 and frequency to a total of seven parameters as the input variables of the surrogate model, $|S_{11}|$ as the performance index (that is, the output variables of the surrogate model). The optimal solution obtained by the

GA is the six structural parameters of this antenna. The reason for choosing these six parameters is that they have the greatest effect on the S-parameter of this antenna. As the target of the design is the UWB antenna, the $|S_{11}|$ value is required to be less than -10 dB in the frequency range of 3.1–10.6 GHz. Thus, that's the optimization condition that needs to be met.

Step 2: Collect the initial dataset (sample set). First, the variable range of the input variable is determined. L_1: 20–26 mm, W_1: 0.5–3.5 mm, L_4: 20–26 mm, W_4: 23.5–26.5 mm, L_6: 2–6 mm, W_6: 3–6 mm. In the frequency range (2–12 GHz), 101 frequencies are selected at equal intervals (equidistant sampling), that is, the step value of frequency is 0.1 GHz. The initial dataset is the $|S_{11}|$ values of 10 groups of UWB antennas in this frequency range. Each set of data (101 frequencies) requires an HFSS simulation to collect. There are a total of 1010 data here. One HFSS simulation took 31.4 seconds, for a total of 314 seconds. The physical dimension parameter is evaluated by the Latin Hypercube Sampling (LHS), which is required to sample 10 times. The LHS is divided into three steps: stratification, sampling and out-of-order. The samples extracted by LHS are relatively uniform, which can avoid the phenomenon of data aggregation to some extent.

Step 3: Parameter selection of the GPR model (surrogate model). This step trains the GPR model in the dataset collected in the previous step. This model uses the coefficient of determination (R^2) as the evaluation index. When its value is greater than 0.9, the GPR model can be used; otherwise, it needs to be retrained. The GPR model is also the surrogate model of the UWB antenna. The calculation formula of R^2 is:

$$R^2 = 1 - \frac{\sum_{i=1}^{n}(y_i - \hat{y})^2}{\sum_{i=1}^{n}(y_i - \bar{y})^2}, \tag{1}$$

where y_i is the real observed values, $\bar{y}$ is the average value of real observed values, and $\hat{y}$ is the predicted value [23]. The larger R^2, the more accurate the GPR model. The value of R^2 is between 0 and 1.

Step 4: Objective function setting and parameter selection of the GA. In this step, according to the design rules of the objective function of GA, the optimization objective of the antenna needs to be abstracted into the maximum or minimum value of a function (the so-called objective function). This optimization can be considered successful when the values of $f \in [3.1, 10.6]$ and $|S_{11}|$ is less than -10 dB. Let the objective function $U(L_1, W_1, L_4, W_4, L_6, W_6)$ be the number of frequencies when $|S_{11}|$ is greater than -10 dB. When the minimum value of U is 0, the optimization is successful. It can be expressed by the formula:

$$Min\{U(L_1, W_1, L_4, W_4, L_6, W_6)\} = 0. \tag{2}$$

There are three important operations in GA, namely selection, crossover and mutation. The GA used in this paper is the differential evolution template. The coding method is real integer (RI) mixed coding, the population size is 50, the maximum number of generations is 50, and the crossover probability is 0.7.

Step 5: Validation and iterative optimization. After setting GA in the previous step, the iterative calculation can be carried out, and the obtained result is the physical size value of the UWB antenna (the optimal solution of the objective function).

It is worth mentioning that GA calculates the $|S_{11}|$ value through the GPR model trained in the third step instead of the full-wave electromagnetic calculation. This step not only obtains the optimal solution but also saves a lot of time. A surrogate model trained with GPR algorithm takes only 118 milliseconds. The optimal solution obtained by GA is re-calculated with full-wave electromagnetic simulation for verification. If the simulation value still completes the target, it indicates that the optimization is completed. If the simulation value does not reach the target, it needs to be re-optimized, that is, enter the iteration. Each iteration will add a new value to the initial dataset. This is the update to the dataset. Each iteration includes GPR model training, GA calculation and full-wave simulation verification. The time for one iteration is 41 seconds.

III. TEST RESULTS AND ANALYSIS

After only 7 iterations, the UWB antenna is obtained as shown in Fig. 1. The time for iterations is 287 seconds, which does not include the initial data sampling time. This is the optimized structure. The reference structure before optimization is shown in Fig. 4. The result after the completion of the first iteration is shown in Fig. 3. After the completion of each iteration, there are similar results and tips. Each iteration for proposed algorithm includes steps of GA calculation and electromagnetic (EM) simulation verification, shown in Fig. 2. EM simulation verification alone takes approximately 31.4 s. GA is a stochastic optimization algorithm. When the optimal solution of the objective function is obtained, the simulation speed of GA will be accelerated.

Line 1 represents the initial dataset structure, with 1010 samples. There are 10 full-wave simulation results. Each simulated result is sampled 101 data from 2 GHz to 12 GHz with a step of 0.1 GHz.

Line 2 indicates that the R^2 of the trained GPR model is 0.9863, indicating that the accuracy meets the requirements.

Line 3 shows the results given by the GA.

Line 4 indicates that when the GPR model is used for calculation, the value of the objective function is 0,

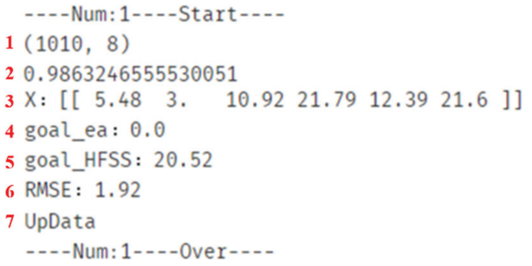

```
  ----Num:1----Start----
1 (1010, 8)
2 0.9863246555530051
3 X: [[ 5.48  3.    10.92 21.79 12.39 21.6 ]]
4 goal_ea: 0.0
5 goal_HFSS: 20.52
6 RMSE: 1.92
7 UpData
  ----Num:1----Over----
```

Fig. 3. Result of the first iteration.

which indicates that the GA has calculated the optimal solution.

Line 5 indicates that the objective function value obtained by the full-wave simulation software (HFSS) is 20, which does not meet the requirements. The number 20 indicates that 20 frequencies do not meet the requirement. The optimal solution is obtained by iterative calculation.

Line 6 indicates that the root-mean-square error (RMSE) between the full-wave simulation value and the GPR model calculation value is 1.92 under the dimension parameter value in Line 3.

Update in Line 7 indicates that the initial dataset has been updated. When the value of *goal_HFSS* in Line 5 is 0, it indicates that the optimization goal is completed and the iteration can be quit. If there is a second iteration, the sample number is updated to 1111.

The optimized antenna dimensions are $L_1 = 20.49$ mm, $W_1 = 1.62$ mm, $L_4 = 25.51$ mm, $W_4 = 25.01$ mm, $L_6 = 4.18$ mm, $W_6 = 3.50$ mm. This is also the optimal solution obtained by the GA. The patch structure of the original antenna is a parallelogram, that is, $L_1 = L_4 = 19$ mm, $W_1 = 3.5$ mm, $W_4 = 23.5$ mm, as shown in Fig. 4. Of course, as the optimization goal changes, the number of iterations and the optimal solution will also change. The final optimization results show that the optimization method using the algorithm can break through the traditional regular polygon structure.

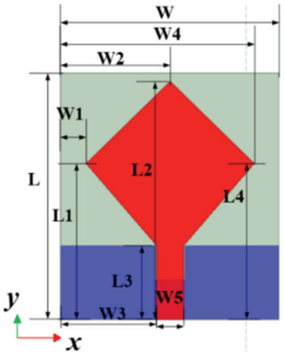

Fig. 4. Geometry of the reference antenna.

Take this antenna as the reference and compare it with the optimized antenna's $|S_{11}|$ curve, as shown in Fig. 5. It can be seen that the optimized scheme has achieved good results. Within the frequency band 3.1–10 GHz, the optimized $|S_{11}|$ values are less than -10 dB. For the reference antenna, only part of the frequency band meets the requirements.

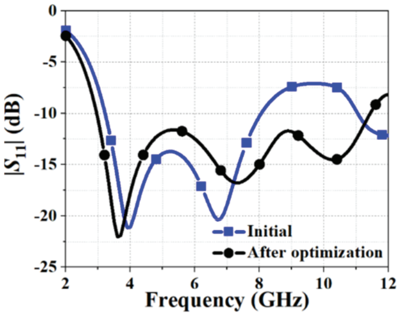

Fig. 5. $|S_{11}|$ curve before and after optimization.

The optimized structural parameters of UWB antenna are shown in Table 1. The overall geometry is fabricated with Printed Circuit Board (PCB) technology, and is shown in Fig. 6.

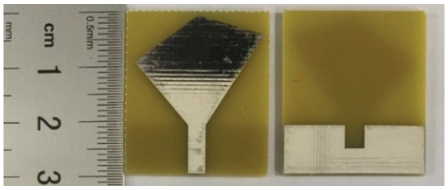

(a) (b)

Fig. 6. Photograph of the fabricated antenna: (a) top view and (b) bottom view.

The scattering parameters of the antenna were measured using a vector network analyzer. Figure 7 compares the simulated and measured $|S_{11}|$ results. Overall, the measured data show good agreement with the simulations, and the operating frequency bands are consistent. Slight discrepancies are observed at 6 GHz and 8 GHz, which can be attributed to differences between the actual and modeled substrate properties, such as the relative dielectric constant and loss tangent of FR4, as well as the effect of the longer coaxial feeding cable used during measurements. These factors do not affect the overall validation of the antenna performance.

The radiation pattern and gain curve of the UWB antenna are tested in a microwave anechoic chamber. When this antenna works in the frequency range of 3 to 10 GHz, the gain curve obtained from the test is shown in Fig. 8, and the test value is roughly consistent with the simulation value. There are some fluctuations for the

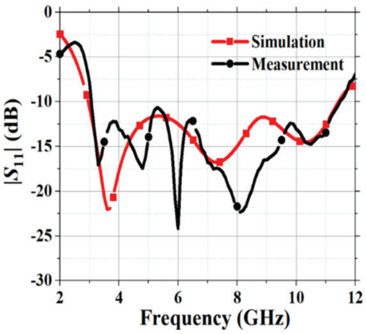

Fig. 7. $|S_{11}|$ curve of the UWB antenna.

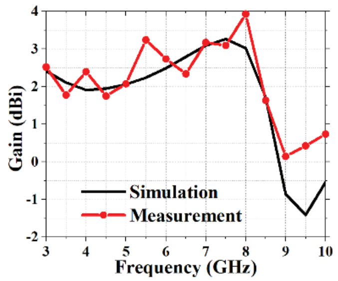

Fig. 8. Gain curves of the UWB antenna.

measured gain. We measured the gain of each frequency separately with the standard horn antenna and the far-field test system. A gain error of ±0.5 dB for test system and testing environment, these will have an impact on the measured gain results. At 5.0 GHz, the normalized XOZ- and YOZ-plane radiation directions of the UWB antenna are shown in Figs. 9 (a) and 9 (b). Similarly, the normalized XOZ- and YOZ-plane radiation directions of the UWB antenna at 7 GHz are shown in Figs. 9 (c) and 9 (d), respectively. There are some differences between simulation and measurement, especially in the XOZ plane. This is mainly caused by the addition of SMA connectors at the antenna feed and the test cable being located on the back of the antenna during testing. In general, the test results and simulation results maintain similar radiation patterns and have the same cross polarization level values. The measured results are in good agreement with the simulation results. Since the focus of this paper is to optimize the S-parameters of the antenna, only the radiation pattern of one frequency is given here.

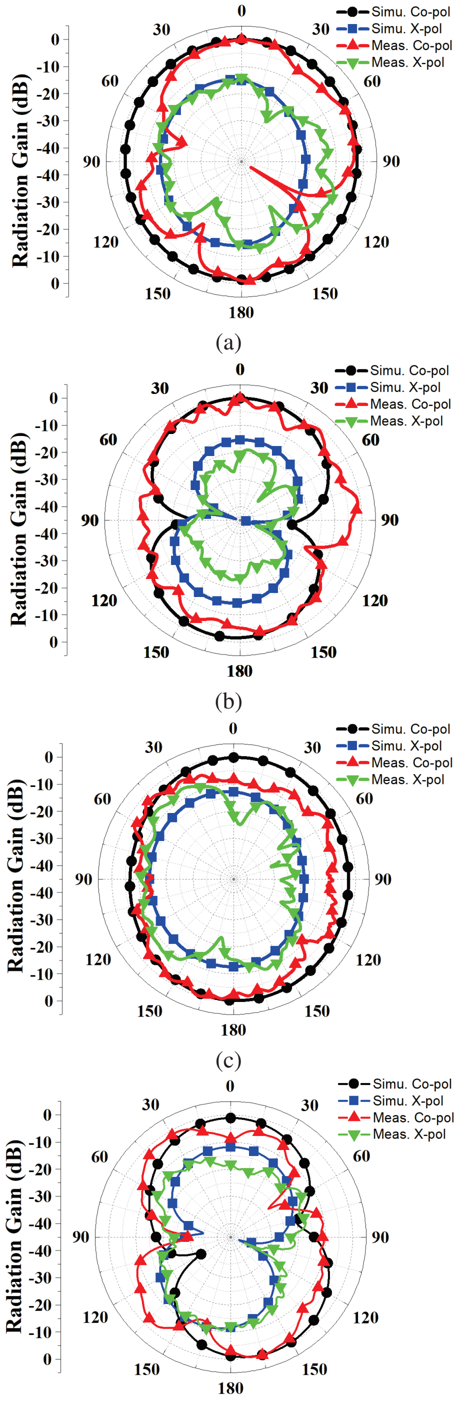

(a)

(b)

(c)

(d)

Fig. 9. 2D radiation patterns of the fabricated antenna: (a) XOZ-plane @5 GHz, (b) YOZ-plane @ 5 GHz, (c) XOZ-plane @ 7 GHz, (d) YOZ-plane @ 7 GHz.

In conclusion, compared with the different UWB antennas that have been publicly reported, this design has significant advantages, such as small size and wide bandwidth, simplified design without complex feed network, and low manufacturing cost, which are shown in Table 2. Compared with the UWB antenna [24, 26], the proposed design has a broader working frequency band. Although the slot type antennas [25, 27] can have some advantages in operation frequency band, their large size brings many limitations to practical. The peak gain of proposed design is moderate, mainly due to the reduction in equivalent radiation area brought about by its miniaturized structure. In addition, the structure

Table 2: Comparison of the performance of UWB antennas (f_0 is the center frequency)

Ref.	**Operation Frequency Band (GHz)**	**Type**	**f_0 (GHz) Size (λ_0)**	**Peak Gain (dBi)**
[24]	3.4–9	Monopole	6.2 $0.83\times0.83\times0.03$	/
[25]	1.55–17.6	Slot	9.575 $6.38\times6.38\times0.03$	10.2
[26]	2.95–10.8	MIMO	6.875 $1\times1\times0.04$	4.0
[27]	2.1–11.5	Slot	6.8 $1.15\times1.15\times0.03$	5.8
This Work	2.95–11.43	Monopole	7.19 $0.72\times0.65\times0.04$	4.0

in this paper is simpler, the cost is easy to control, and there is no need for a feed network. This work can be a potential candidate for applications in UWB communication, positioning, and IoT systems.

IV. ANOTHER EXAMPLE

To verify the effectiveness of the algorithm, a dual-band antenna is selected as the optimization objective. This antenna is of the same type as the UWB antenna mentioned earlier and both belong to patch antennas. Patch antennas [28, 29] have a wide range of applications and a relatively simple manufacturing process. It is meaningful to extend the optimization method combining GPR and GA to patch antennas.

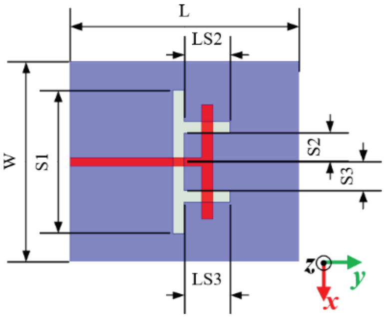

Fig. 10. Geometry of the dual-band antenna.

The geometry of dual-band antenna is given in Fig. 10. The front of the antenna is a T-shaped patch, and the back is etched with Π Type gap. The substrate is FR4 with a relative dielectric constant of 4.4 and a loss tangent of 0.02. The antenna has an overall size of $80\times70\times1.6$ mm^3. The optimization goal is to design the antenna as a dual band antenna, with two resonance frequencies of $f_1 = 2.44$ GHz and $f_2 = 3.62$ GHz, respectively. The proposed algorithm in above section is used to construct surrogate model and searching target, while the parameters of LS_2, LS_3, S_2, and S_3 are used as the optimization variables. The initial values are: $LS_2 = LS_3 = 20$ mm, $S_2 = S_3 = 10$ mm. Obviously, the optimization goal can be other antenna performance. Similarly, 10 full-wave simulation data is collected as the initial dataset. The simulation frequency band is 2–4 GHz, step by 0.01 GHz, and each simulation has a total of 201 frequency points. A total of 10 simulations are 2010 data points. The comparison diagram of S_{11} curves before and after final optimization is shown in Fig. 11. The optimized dual band antenna operates in the frequency bands of 2.44–2.46 GHz and 3.50–3.74 GHz and can be applied to WiFi and 5G. The corresponding parameters are $LS_2 = 11$ mm, $LS_3 = 19$ mm, $S_2 = 8$ mm, $S_3 = 9$ mm. The normalized radiation patterns at 2.45 GHz and 3.6 GHz are also given in the Fig. 12. The cross-polarization curves are also added for evaluating the performance in Figs. 12 (a) and 12 (b), which shows cross polarization levels of more than 10 dB at two different frequencies. The proposed dual-band antenna exhibits stable broadside radiation, and two radiation nulls at YOZ plane. The algorithm is repeated 5 times on the same initial dataset, and the average optimization time is 277.47 seconds. This indicates that the optimization scheme combining GA and GPR can facilitate and quickly design antenna structures.

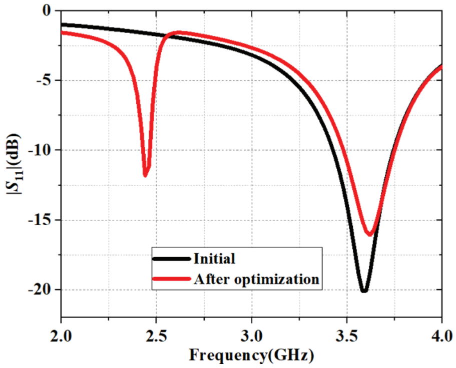

Fig. 11. Performance of the dual-band antenna (S parameters).

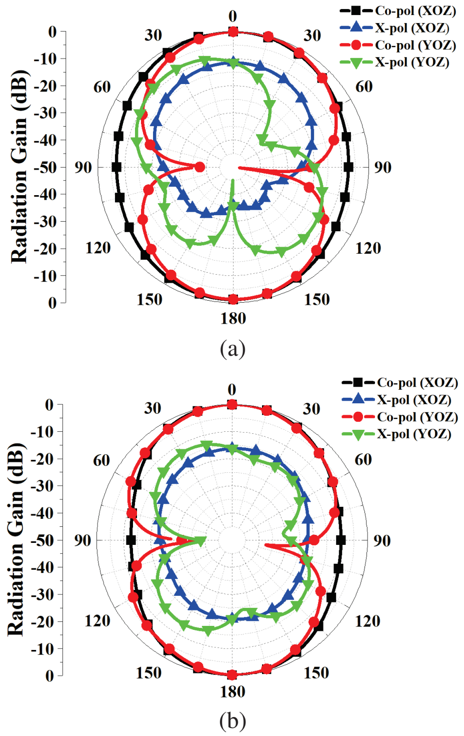

Fig. 12. 2D radiation patterns of the simulated antenna: (a) 2.45 GHz and (b) 3.6 GHz.

V. CONCLUSION

In this paper, a complete optimization scheme is designed by using the GPR and GA. After only 7 iterations, the optimization design of a UWB antenna with irregular patches is completed. In this optimization design, the average time to complete one iteration is 41 seconds. The optimization took a total of 601 seconds, including the time of initial 10 full-wave electromagnetic simulations (314 seconds) to collect the initial sample set and the time of 7 iterations. Then the optimization algorithm is carried, and the design target can be achieved with 7 iterations. Among each iteration, the time of full-wave electromagnetic simulation is 31.4 seconds, the time of the training GPR model is118 milliseconds, the trained GPR model has 6 input variables, and each generation of GA with a population size of 50 needs about 185 milliseconds.

The optimized UWB antenna has an operating band of 2.95–11.43 GHz, a relative bandwidth of 117.94%, and a physical size of only 30×27×1.6 mm^3 (length × width × height). The patch of the antenna exhibits an irregular polygonal structure, highlighting how algorithm optimization not only enhances design efficiency but also facilitates the creation of innovative structures. Finally, the designed antenna is fabricated and tested. The measured frequency band and radiation direction are in good agreement with the simulated values. The effectiveness of the ML algorithm in UWB antenna design is proved.

ACKNOWLEDGMENT

This work is supported partly by “Pioneer” and “Leading Goose” R&D program of Zhejiang under contract of 2022C01119, partly by the National Natural Science Foundation of China under Contract of 62171169, partly by Project of State Key Laboratory of Millimeter Waves under contract of K202414.

REFERENCES

[1] J. Y. Park and J. Choo, “Zigzag antenna design based on machine learning,” *Applied Computational Electromagnetics Society (ACES) Journal*, vol. 40, no. 01, pp. 20–25, Jan. 2025.

[2] J. Dou, “Convolutional neural networks aided reinforcement learning for accelerated optimization of antenna topology,” *Applied Computational Electromagnetics Society (ACES) Journal*, vol. 40, no. 01, pp. 35–41, Jan. 2025.

[3] Y. Chen, V. Demir, S. Bhupatiraju, A. Z. Elsherbeni, J. Gavilan, and K. Stoynov, “Prediction of antenna performance based on scalable data-informed machine learning methods,” *Applied Computational Electromagnetics Society (ACES) Journal*, vol. 39, no. 04, pp. 275–290, Apr. 2024.

[4] E. Demircioglu, M. H. Sazlı, S. Taha İmeci, and O. Sengul, “Soft computing techniques on multi-resonant antenna synthesis and analysis,” *Microwave and Optical Technology Letters*, vol. 55, no. 11 pp. 2643–2648, Nov. 2013.

[5] L. W. Mou, Y. J. Cheng, Y. F. Wu, M. H. Zhao, and H. N. Yang, “Design for array-fed beam-scanning reflector antennas with maximum radiated power efficiency based on near-field pattern synthesis by support vector machine,” *IEEE Transactions on Antennas and Propagation*, vol. 70, no. 7, pp. 5035–5043, July 2022.

[6] D. R. Prado, P. Naseri, J. A. López-Fernández, S. V. Hum, and M. Arrebola, “Support vector regression-enabled optimization strategy of dual circularly-polarized shaped-beam reflectarray with improved cross- polarization performance,” *IEEE Transactions on Antennas and Propagation*, vol. 71, no. 1, pp. 497–507, Jan. 2023.

[7] X. W. Dai, D. L. Mi, H. T. Wu, and Y. H. Zhang, “Design of compact patch antenna based on support vector regression,” *Radioengineering*, vol. 31, no. 3, pp. 339–345, Sep. 2022.

[8] S. Koziel, N. Çalık, P. Mahouti, and M. A. Belen, “Accurate modeling of antenna structures by means of domain confinement and pyramidal deep neural networks,” *IEEE Transactions on Antennas and Propagation*, vol. 70, no. 3, pp. 2174–2188, Mar. 2022.

[9] A. M. Montaser and K. R. Mahmoud, "Deep learning-based antenna design and beam-steering capabilities for millimeter-wave applications," *IEEE Access*, vol. 9, pp. 145583–145591, 2021.

[10] L. Cui, Y. Zhang, R. Zhang, and Q. H. Liu, "A modified efficient KNN method for antenna optimization and design," *IEEE Transactions on Antennas and Propagation*, vol. 68, no. 10, pp. 6858–6866, Oct. 2020.

[11] J. Jacobs and J. de Villiers, "Modeling of planar dual-band microstrip patch antenna using Gaussian process regression," in *The 3rd European Wireless Technology Conference*, Paris, France, pp. 253–256, 2010.

[12] J. P. Jacobs, "Efficient resonant frequency modeling for dual-band microstrip antennas by Gaussian process regression," *IEEE Antennas and Wireless Propagation Letters*, vol. 14, pp. 337–341, 2015.

[13] B. Woosley, J. Twigg, J. G. Rogers, and F. Dagefu, "Learning antenna radiation patterns through Gaussian process regression," in *2022 IEEE International Symposium on Antennas and Propagation and USNC-URSI Radio Science Meeting* (*AP-S/URSI*), Denver, CO, USA, pp. 637–638, 2022.

[14] H. Ibili, A. C. Gungor, M. Maciejewski, J. Smajic, and J. Leuthold, "Genetic algorithm-based geometry optimization of terahertz plasmonic modulator antennas," in *2022 23rd International Conference on the Computation of Electromagnetic Fields* (*COMPUMAG*), Cancun, Mexico, pp. 1–4, 2022.

[15] K. Choi, D.-H. Jang, S.-I. Kang, J.-H. Lee, T.-K. Chung, and H.-S. Kim, "Hybrid algorithm combing genetic algorithm with evolution strategy for antenna design," in *IEEE Transactions on Magnetics*, vol. 52, no. 3, pp. 1–4, Mar. 2016.

[16] A. J. Kerkhoff and H. Ling, "Design of a band-notched planar monopole antenna using genetic algorithm optimization," *IEEE Transactions on Antennas and Propagation*, vol. 55, no. 3, pp. 604–610, Mar. 2007.

[17] X.W. Dai, W. H. Hu, Y. H. Fu, J. Liu, and Z. X. Chen, "Automatic design of microwave filters by using relational induction neural networks," *Int. J. Numer. Model*, vol. 36, no. 6, e3102, 2023.

[18] J. P. Jacobs and J. P. de Villiers, "Gaussian-process-regression-based design of ultrawide-band and dual-band CPW-FED slot antennas," *Journal of Electromagnetic Waves and Applications*, vol. 24, no. 13, pp. 1763–1772, 2012.

[19] A. Pietrenko-Dabrowska, S. Koziel, and M. Al-Hasan, "Cost-efficient bi-layer modeling of antenna input characteristics using gradient Kriging surrogates," *IEEE Access*, vol. 8, pp. 140831–140839, 2020.

[20] A. Pietrenko-Dabrowska and S. Koziel, "Simulation-driven antenna modeling by means of response features and confined domains of reduced dimensionality," *IEEE Access*, vol. 8, pp. 228942–228954, 2020.

[21] S. Koziel and A. Pietrenko-Dabrowska, "Reliable data-driven modeling of high-frequency structures by means of nested Kriging with enhanced design of experiments," *Engineering Computations*, vol. 36, no. 7, pp. 2293–2308, 2019.

[22] A. Pietrenko-Dabrowska and S. Koziel, "Reliable surrogate modeling of antenna input characteristics by means of domain confinement and principal components," *Electronics*, vol. 9, no. 5, p. 877, 2020.

[23] T. O. Kvålseth, "Cautionary note about R^2," *The American Statistician*, vol. 39, no. 4, pp. 279–285, 1985.

[24] M. N. Hasan and M. Seo, "A planar 3.4–9 GHz UWB monopole antenna," in *2018 International Symposium on Antennas and Propagation* (*ISAP*), Busan, Korea (South), pp. 1–2, 2018.

[25] Y. Wang and W. Dou, "A low profile UWB antenna on a large flat conductor," in *2021 International Symposium on Antennas and Propagation* (*ISAP*), Taipei, Taiwan, pp. 1–2, 2021.

[26] Y.-Y. Liu and Z.-H. Tu, "Compact differential band-notched stepped-slot UWB-MIMO antenna with common-mode suppression," *IEEE Antennas and Wireless Propagation Letters*, vol. 16, pp. 593–596, 2017.

[27] P. M. Paul, K. Kandasamy, M. S. Sharawi, and B. Majumder, "Dispersion-engineered transmission line loaded slot antenna for UWB applications," *IEEE Antennas and Wireless Propagation Letters*, vol. 18, no. 2, pp. 323–327, Feb. 2019.

[28] B. Tutuncu, H. Torpi, and S. Taha Imeci, "Directivity improvement of microstrip antenna by inverse refraction metamaterial," *Journal of Engineering Research*, vol. 7, no. 4, pp. 151–164, Dec. 2019.

[29] S. Salihovic and S. Taha Imeci, "A stub microstrip patch antenna for sub 6 GHz – 5G applications," *Heritage and Sustainable Development Original Research*, vol. 5, no. 1, pp. 99–106, June 2023.

Da Li Mi was born in Haining, Zhejiang, China. He received his master's degree in electronic information from Hangzhou Dianzi University, Hangzhou, Zhejiang, in 2023. His current interests include artificial intelligence, antennas, and electromagnetic compatibility.

Xi Wang Dai was born in Caoxian, Shandong, China. He received the B.S. and M.S. degrees in Electronic Engineering from Xidian University, Xi'an, Shanxi, in 2005 and 2008, and he received the Ph.D. degree in Electromagnetic Fields and Microwave Technology from Xidian University in 2014. From March 2008 to August 2011, he worked at Guangdong Huisu Corporation as a manager of the antenna department. He currently works at Hangzhou Dianzi University, Hangzhou. His current research interests involve metamaterials, AI-assisted design antenna, MIMO antenna and low-profile antenna.

Jun Shi Zhao was born in Zhoukou, Henan, China. He received the B.S. degree in Electronic Information Engineering from Xi'an Shiyou University, Xi'an, Shanxi, in 2023. He is currently pursuing the master's degree with Hangzhou Dianzi University, Hangzhou, Zhejiang. His current research interests include broadband antenna and microstrip antenna.

Ze Li was born in Wenzhou, Zhejiang, China, in 2001. He received the B.S. degree in electronic information engineering from Hangzhou Dianzi University Information Engineering College, Hangzhou, in 2023. He is currently pursuing the M.S. degree in the Hangzhou Dianzi University, Hangzhou. His current research interests include orbital angular momentum and metasurface antenna.

Gang Li was born in Suizhou, Hubei, China. He received the B.S. degrees in electronic engineering from Xidian University, Xi'an, Shaanxi, in 2005, and the Ph.D. degree in electromagnetic fields and microwave technology at Xidian University in 2009. From May 2010 to August 2012, he worked at Huawei Technologies Co. Ltd. as an EMC Engineer. He currently works at Hubei University of Arts and Science, Xiangyang. His current research interests involve broadband antenna, RCS and metasurface.

Hui Hong received the Ph.D. degree in electronic science and technology from the College of Information Science & Electronic Engineering, Zhejiang University, Hangzhou, China, in 2007. Currently, he is a Full Professor with the School of Electronics and Information Engineering, Hangzhou Dianzi University, Hangzhou. His research interests include brain–computer interface, microsystem integration, and biological signal processing.

Use of Plasma in Developing Stealth Technology

Surendra Singh

Department of Electrical & Computer Engineering
The University of Tulsa, Tulsa, OK 74104, USA
surendra-singh@utulsa.edu

Abstract – The objective of this work is to study the scattering characteristics of multiple coatings of plasma coated cylinders and spheres. Both dielectric and conducting cases are considered. The dielectric constant or the refractive index of plasma has a significant impact on the radar cross-section (RCS) of the geometries under study. Using experimentally reported plasma dielectric constants obtained from collision frequency and plasma frequency, we observed that in some cases, depending on the choice of parameters, we see reduction of RCS whereas in others the RCS is enhanced. As a result, designers need to apply plasma with care when it is used as an absorber for RCS reduction. The results of this work are expected to be applicable to the development of plasma stealth technology, which has gained a lot of interest lately.

Index Terms – Plasma, radar cross-section, scattering, stealth technology.

I. INTRODUCTION

During the past few years, the use of plasma to reduce the radar cross-section (RCS) of airborne platforms has received considerable attention. The concept of using plasma as an absorber of electromagnetic energy was noted in a report by Musal [1] who observed a drastic reduction of RCS of a body when it is surrounded by a plasma sheath having specific spatial and electromagnetic properties. A similar observation is noted by a number of researchers who have reported communication "blackout" when a spacecraft re-enters the earth's atmosphere [2]. It is noted that, during the space vehicle's re-entry, it is enveloped in a "plasma sheath" or "plasma plume" that blocks RF communication. Depending on the frequency of the signal, the plasma sheath either reflects or severely attenuates the reception or transmission of signals that results in communication blackout. This led to the observation that plasma is able to cause disruption in communication as well as make the airborne platform invisible to radar due to reduced RCS. It is well known that the RCS is dependent upon the shape as well as the material constituents of a structure. Traditionally, radar absorbing materials (RAM) have been used to absorb incoming radar energy but this concept works only for certain frequencies and angles of incidence. The maintenance of RAM coated structures is also very expensive due to the nature of coatings. For this reason, it appears that a plasma stealth may be a technology that can provide considerable advantages over RAM coatings in reducing RCS.

Collisional and unmagnetized plasma has a complex dielectric constant. As a result, it can be used as a good absorber of EM waves over a wide range of frequencies. Vidmar [3] noted that plasma generated in air or helium at atmospheric pressure acts as a broadband absorber from VHF to X-band. Chaudhury and Chaturvedi [4, 5] reported on the RCS of a flat plate covered with cold collisional plasma using the finite difference time domain (FDTD) method. Yuan and coworkers [6] reported that a multilayered radar-absorbing structure coated with plasma/RAM reduced the power of the incident wave over a wide frequency band. FDTD in conjunction with Z-transform was utilized to study the RCS of a perfectly conducting (PEC) cylinder covered with unmagnetized plasma [7]. Several researchers have considered scattering of a plane wave by an anisotropic plasma coated conducting sphere [8–11]. However, none of the works consider multiple layers of plasma, which is the primary focus of this work.

The formulation of the scattering mechanism is already known and available in the literature. The main contribution of this paper is to use plasma coating and show that in some instances the plasma coating can enhance scattering whereas in others it can reduce scattering. This results in an impact on RCS, which is the primary focus of study in this work. Moreover, the dielectric constant of plasma is taken from experimentally observed values, which has not been done in previous publications. Hence, the results and the observations presented in this work are significant.

This paper is organized as follows. Plasma parameters are defined in section II. In section III, the basic formulations to compute scattering width (SW) or RCS are provided for simple geometries that include

Submitted On: February 14, 2025
Accepted On: December 28, 2025

https://doi.org/10.13052/2025.ACES.J.401205

a conducting or dielectric cylinder covered with multilayered plasma and a conducting or dielectric sphere covered with multilayered plasma. The numerical results obtained from the formulations are provided in section IV. In section V, the main conclusions of the work are reported.

II. PLASMA PARAMETERS

Plasma is a collection of free electrically charged particles including negatively charged electrons and positively charged ions resulting in a net neutral charge. Plasma exists at a variety of temperatures, densities and frequencies, and may be derived from a host of gas mixtures. In the following analysis we assume that the electron-neutral collision frequency in the plasma is such that the mean free path between the collisions is much smaller than the Debye length. The dielectric constant, ε_r, for collisional and unmagnetized plasma may be written as:

$$\varepsilon_r(\omega_0) = 1 + \frac{\omega_p^2}{\omega_0(j\omega_c - \omega_0)} = \left(1 - \frac{\omega_p^2}{\omega_0^2 + \omega_c^2}\right) - j\left(\frac{\omega_p^2 \omega_c}{\omega_0(\omega_0^2 + \omega_c^2)}\right), \quad (1)$$

$$\omega_p = 2\pi f_p = \sqrt{\frac{e^2 N_e}{m_e \varepsilon_0}}. \quad (2)$$

f_p is the plasma frequency (hertz), $\omega_c = 2\pi f_c$, f_c is the plasma collision frequency (hertz), N_e is the electron density (m^{-3}), e is the electron charge (coulomb), m_e is the electron mass (kg), ε_0 is permittivity of free space, $\omega_0 = 2\pi f_0$, and f_0 is the frequency (hertz) of the incident electromagnetic wave.

III. SCATTERING WIDTH RCS OF MULTILAYERED GEOMETRIES

A. Scattering from a conducting (PEC) infinite cylinder covered with a cylindrical dielectric layer (TM_z)

Consider an infinite (in z-direction) conducting cylinder of radius, a, covered with a cylindrical dielectric layer (plasma) of radius, b, with permeability and permittivity of the dielectric cylinder (μ_b, ε_b), as shown in Fig. 1.

The incident electric field (TM_z), E_z^i, and the scattered electric field, E_z^s, in air, for $\rho \geq b$, can be expressed as:

$$E_z^i = E_0 e^{-jk_0 x} = E_0 \sum_{n=-\infty}^{\infty} j^{-n} J_n(k_0\rho) e^{jn\phi}, \quad 0 \leq \phi \leq 2\pi. \quad (3)$$

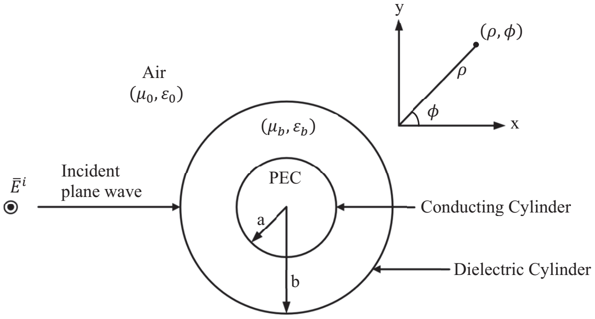

Fig. 1. Conducting (PEC) cylinder covered with a plasma layer (TM_z).

$$E_z^s = E_0 \sum_{n=-\infty}^{\infty} j^{-n} a_n H_n^{(2)}(k_0\rho) e^{jn\phi}, \quad 0 \leq \phi \leq 2\pi. \quad (4)$$

The electric field in the dielectric (plasma) region, for $a \leq \rho \leq b$ and $0 \leq \phi \leq 2\pi$, is given by

$$E_z^b = E_0 \sum_{n=-\infty}^{\infty} j^{-n} [b_n J_n(k_b\rho) + c_n H_n^{(2)}(k_b\rho)] e^{jn\phi}, \quad (5)$$

where b_n and c_n are unknown expansion coefficients, $k_0 = \omega\sqrt{\mu_0\varepsilon_0}$ is the wave number in free space, and $k_b = \omega\sqrt{\mu_b\varepsilon_b}$ is the wave number in the dielectric region with $\mu_b = \mu_{r_b}\mu_0$ and $\varepsilon_b = \varepsilon_{r_b}\varepsilon_0$, μ_0 is permeability of free space, and ε_0 is permittivity of free space. With the computation of the scattering coefficient, SW can then be computed as [12]:

$$SW_{2-D} = \lim_{\rho\to\infty}\left[2\pi\rho \frac{|E_z^s|^2}{|E_z^i|^2}\right] = \frac{2\lambda}{\pi}\left|\sum_{n=0}^{\infty} K_n a_n \cos(n\phi)\right|^2, \quad K_n = \begin{cases} 1, & n = 0 \\ 2, & n \neq 0 \end{cases}. \quad (6)$$

The above formalism can be extended to any number of layers by defining the fields in each layer and applying the continuity of the tangential electric and magnetic fields at each boundary layer. In this work, we extended the formulation to 5 layers. The TE_z case can be handled similarly by defining the z-component of incident magnetic field and applying the appropriate boundary conditions.

Next, consider a dielectric cylinder covered with a cylindrical dielectric layer as shown in Fig. 2.

Note that the electric field inside the dielectric cylinder for TM_z case can be defined as

$$E_z^a = E_0 \sum_{n=-\infty}^{\infty} j^{-n} d_n J_n(k_a\rho) e^{jn\phi}, \quad 0 \leq \phi \leq 2\pi, \quad \rho \leq a, \quad (7)$$

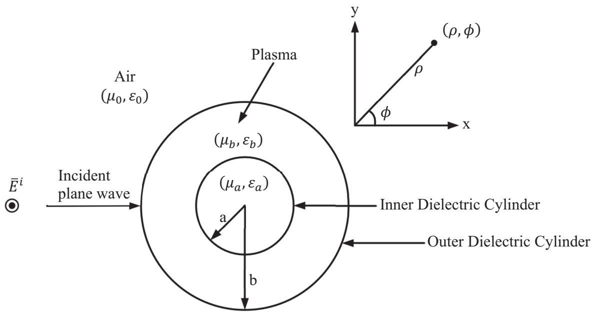

Fig. 2. Dielectric cylinder covered with a cylindrical dielectric (plasma) layer (TM_z).

where d_n is the unknown expansion coefficient, $k_a = \omega\sqrt{\mu_a\varepsilon_a}$ is the wave number of the dielectric material inside the cylinder. RCS can be computed easily using (6) once the scattering coefficient is determined by applying appropriate boundary conditions at each dielectric layer. The TE_z case for the layered dielectric cylinder is trivial as it can be obtained by application of duality.

B. Scattering from a Conducting (PEC) Sphere

Consider a conducting (PEC) sphere of radius, a, illuminated by the electric field of a plane wave polarized in the x-direction and propagating along the z-axis as shown in Fig. 3.

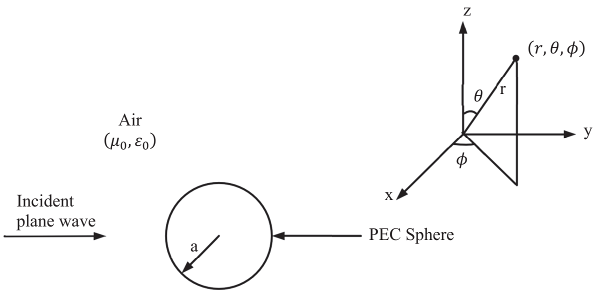

Fig. 3. Conducting (PEC) sphere illuminated by a plane wave.

The incident electric field, $E_x^i = E_0 e^{-jk_0 z} = E_0 e^{-jk_0 r cos\theta}$. Following the development in [12], the incident and scattered fields by the sphere can be expressed as superposition of TE^r and TM^r fields. The TM^r fields are constructed by having $\bar{A} = \hat{r}A_r(r,\theta,\phi)$ and $\bar{F} = \bar{0}$, where $\bar{A}$ is the magnetic vector potential and $\bar{F}$ is the electric vector potential. Similarly, the TE^r fields are constructed by having $\bar{F} = \hat{r}F_r(r,\theta,\phi)$ and $\bar{A} = \bar{0}$.

The scattered electric field, E_θ^s and E_ϕ^s can be computed by using the scattered magnetic vector potential, A_r^s, and the electric vector potential, F_r^s. The far field approximations are then made for the scattered fields to arrive at the bistatic RCS of the conducting sphere [12]:

$$RCS(Bistatic) = \lim_{r\to\infty}\left[4\pi r^2 \frac{|\overline{E}^s|^2}{|\overline{E}^i|^2}\right]$$

$$= \frac{\lambda^2}{\pi}[cos^2\phi|A_\theta|^2 + sin^2\phi|A_\phi|^2], \quad (8)$$

where

$$|A_\theta|^2 = \left|\sum_{n=1}^{\infty} j^n \left[b_n sin\theta P_n^{1'}(cos\theta) - c_n \frac{P_n^1(cos\theta)}{sin\theta}\right]\right|^2. \quad (9)$$

$$|A_\phi|^2 = \left|\sum_{n=1}^{\infty} j^n \left[b_n \frac{P_n^1(cos\theta)}{sin\theta} - c_n sin\theta P_n^{1'}(cos\theta)\right]\right|^2. \quad (10)$$

C. Scattering from a conducting (PEC) sphere covered with a spherical dielectric layer

Next, consider the conducting sphere of Fig. 3 covered with a dielectric sphere of radius, b, as shown in Fig. 4.

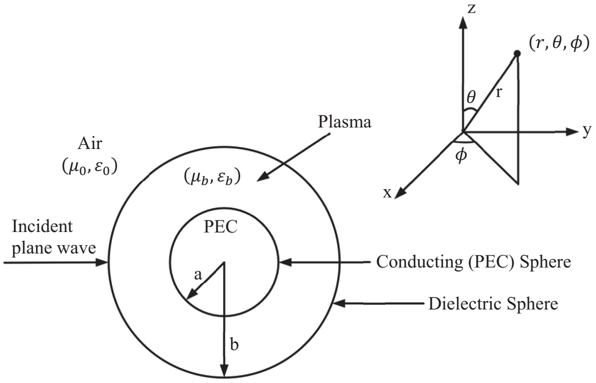

Fig. 4. Conducting (PEC) sphere covered with a spherical dielectric layer.

The electric and magnetic fields in the dielectric sphere ($a \le r \le b$) can be obtained by defining the vector potentials:

$$A_r^b = E_0 \frac{cos\phi}{\omega} \sum_{n=1}^{\infty} [\hat{J}_n(k_b r)d_n + e_n \hat{H}_n^{(2)}(k_b r)] P_n^1(cos\theta),$$

$$a \le r \le b. \quad (11)$$

$$F_r^b = E_0 \frac{sin\phi}{\omega\eta_b} \sum_{n=1}^{\infty} [f_n \hat{J}_n(k_b r) + g_n \hat{H}_n^{(2)}(k_b r)] P_n^1(cos\theta),$$

$$a \le r \le b. \quad (12)$$

In (12), η_b is the intrinsic impedance of dielectric medium, $\eta_b = \sqrt{\frac{\mu_b}{\varepsilon_b}}$. Application of the boundary conditions provides the framework needed to solve for the scattering coefficients, b_n, c_n, d_n, e_n, f_n, and g_n. This formalism can be extended to any number of layers by defining the fields in each spherical layer and applying the continuity of the tangential electric and magnetic fields at each boundary layer. In this work, we extended the formulation to 5 layers. The case of the dielectric sphere covered with a plasma layer, shown in Fig. 5, differs from the stated approach in the boundary condition on the dielectric sphere. That is, we require the continuity of the tangential electric and magnetic fields on the surface of the dielectric sphere at $r = a$ as well. The fields inside the dielectric sphere, $r \leq a$, can be determined by defining the potential functions, A_r^a and F_r^a:

$$A_r^a = E_0 \frac{cos\phi}{\omega} \sum_{n=1}^{\infty} h_n \hat{J}_n(k_a r) P_n^1(cos\theta), \quad r \leq a. \tag{13}$$

$$F_r^a = E_0 \frac{sin\phi}{\omega\eta_a} \sum_{n=1}^{\infty} k_n \hat{J}_n(k_a r) P_n^1(cos\theta), \quad r \leq a. \tag{14}$$

In (14), η_a is the intrinsic impedance of dielectric medium, $\eta_a = \sqrt{\frac{\mu_a}{\varepsilon_a}}$.

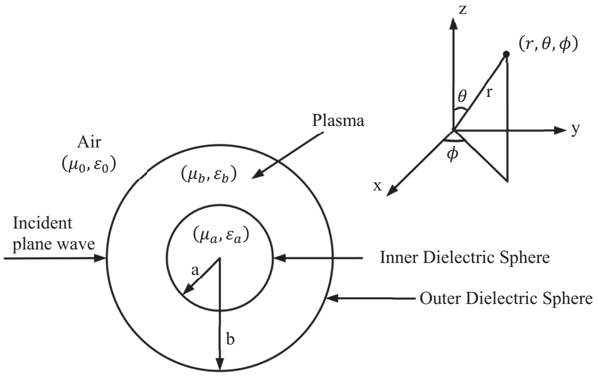

Fig. 5. Dielectric sphere covered with a spherical dielectric (plasma) layer.

IV. RESULTS AND DISCUSSION

The formulation for calculating the SW of the cylindrical geometries and the RCS of the spherical geometries were coded in MATLAB. The number of modes in computing the SW in (6) and RCS in (9) and (10), is taken to be 50. This number of modes is arrived after numerical experimentation to find the convergence of the series. In this section, the numerical results are presented. First, the codes were tested to compare results with numerical data available in the literature to validate the analytical work presented in section III as well as to validate the MATLAB codes. The multilayered (1 to 5 layers) cylinder and sphere codes were first tested for self-consistency. This meant that we set the material properties of the added layers (1 to 5) to that of free space and found the result to match with that of a cylinder or sphere with no layers. In the results to follow, we provide comparison with results that were available in the literature. In each case, we also tested the multilayered formulation in which the extra layers were set to free space. Note that the increasing values of radii of cylinders or spheres (beyond the ones shown in section III) are denoted by letters c, d, e, and f. The bistatic SW of a conducting cylinder coated with a double negative (DNG) coating for TM_z and TE_z cases for $a = 0.05$ m, $b = 0.10$ m, $f_0 = 1$ GHz, $\mu_b = -\mu_0$, $\varepsilon_b = -9.8\varepsilon_0$, $\phi = 180°$, shown in Figs. 6 and 7, respectively, are in good agreement with Zainud-Deen's result [13]. The bistatic RCS of a PEC sphere covered with 2 spherical dielectric layers for E-plane scan is shown in Fig. 8 for $f_0 = 1$ GHz. This result is in good agreement with Sheng et al. [14] and it is obtained with the code for a PEC sphere covered with 5 dielectric layers. The PEC sphere radius $a = 0.75\lambda_0$. The dielectric sphere radii: $b = 0.8\lambda_0$, $c = 0.85\lambda_0$, $[d = 0.9\lambda_0$, $e = 0.95\lambda_0$, $f = 1.2\lambda_0]$, $\mu_{r_b} = 2 - j$, $\varepsilon_{r_b} = 3 - j2$, $\mu_{r_c} = 3 - j2$, $\varepsilon_{r_c} = 2 - j$, $[\mu_{r_i} = 1$ and $\varepsilon_{r_i} = 1$ for $i = d, e, f]$. The quantities in the square parenthesis indicate that these are needed to run the 5-layer case since we only have 2 dielectric layers. For this reason, the relative permeability and relative permittivity of these 3 additional layers are set to free space. The same is true in the next two results where we show the bistatic RCS of a PEC sphere covered with 3 dielectric spherical layers. These results, shown in Fig. 9 for E-plane scan ($\phi^i = 0°$) and in Fig. 10 for H-plane scan ($\phi^i = 90°$), are in good agreement with Lei [15]. In these two cases, the incident EM wave frequency, $f_0 = 1$ GHz and the PEC sphere radius, $a = 0.5\lambda_0$. Dielectric sphere radii:

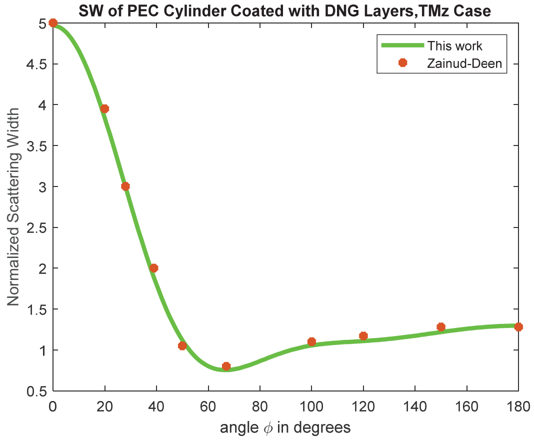

Fig. 6. Scattering width of conducting cylinder covered with DNG layer TM_z.

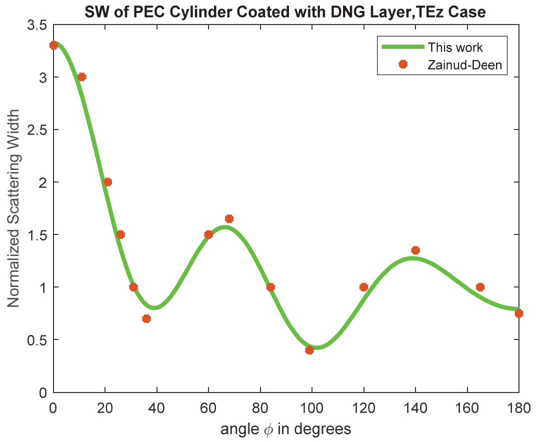

Fig. 7. Scattering width of conducting cylinder covered with DNG layer TE_z.

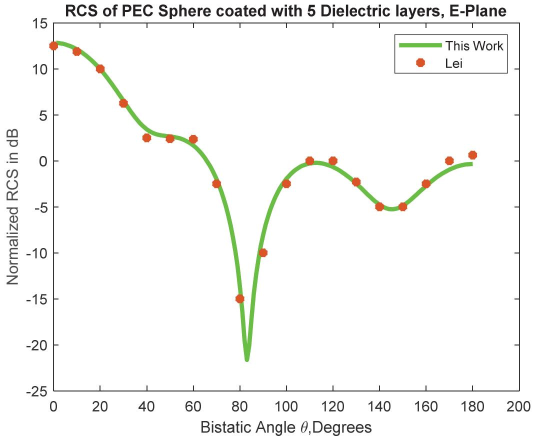

Fig. 9. RCS of a PEC sphere covered with 3 dielectric layers E-plane scan.

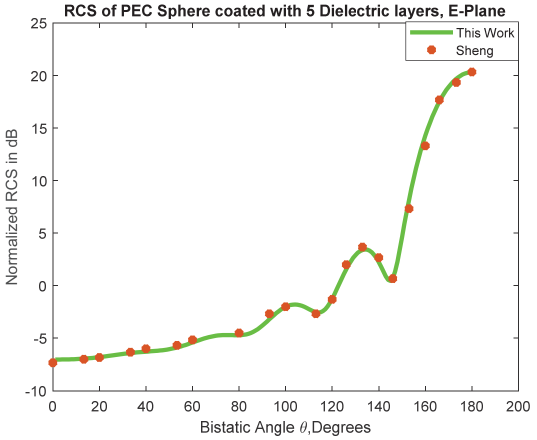

Fig. 8. RCS of a PEC sphere covered with 2 dielectric layers E-plane scan.

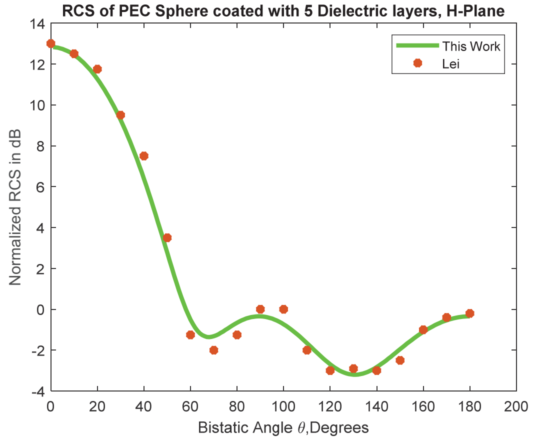

Fig. 10. RCS of a PEC sphere covered with 3 dielectric layers H-plane scan.

$b = 0.51\lambda_0$, $c = 0.52\lambda_0$, $d = 0.53\lambda_0$, [$e = 0.54\lambda_0$, $f = 0.55\lambda_0$], $\mu_{r_b} = 1$, $\varepsilon_{r_b} = 2$, $\mu_{r_c} = 2 - j2$, $\varepsilon_{r_c} = 2 - j2$, $\mu_{r_d} = 2$, $\varepsilon_{r_d} = 2$ [$\mu_{r_i} = 1$ and $\varepsilon_{r_i} = 1$ for $i = e, f$]. Note that the two outermost layers are free space or air.

Next, we look at the impact of the collision frequency on the plasma dielectric constant. The set of results presented in Figs. 11–14 are for frequency of incident EM wave, $f_0 = 1$ GHz, $a = 1.2\lambda_0$, $b = 1.25\lambda_0$, $c = 1.3\lambda_0$, $d = 1.35\lambda_0$, $e = 1.4\lambda_0$, $f = 1.5\lambda_0$. In (1), if we take the electron density, $n_e = 10^{17} m^{-3}$, and electron collision frequency, $f_c = 10$ GHz, we obtain the resulting plasma dielectric constant, $\varepsilon_r = 0.9202 - j0.7984$, and the plasma frequency, $f_p = 2.8397$ GHz. All of the 5 plasma layers are set to have the same dielectric constant, that is, $\varepsilon_{r_i} = 0.9202 - j0.7984$ for $i = b, c, d, e, f$. In Fig. 11, we show the SW of a dielectric cylinder, TE_z case, with and without plasma layers. For this case, the dielectric constant and relative permeability of the dielectric cylinder are given by $\varepsilon_{r_a} = 4$ and $\mu_{r_a} = 1$, respectively. The SW of a PEC cylinder for the TM_z cases with and without plasma layers is shown in Fig. 12. In Fig. 13, we show the bistatic RCS of a dielectric sphere for the E-plane scan ($\phi^i = 0°$) with and without plasma layers. For this case, the dielectric constant and relative permittivity of the dielectric sphere are given by $\varepsilon_{r_a} = 4$ and $\mu_{r_a} = 1$, respectively. We show the bistatic RCS of a PEC sphere for the H-plane scan with and without plasma layers in Fig. 14. In Figs. 11–14, we observe that when the plasma collision frequency f_c (10 GHz) is higher than the frequency of the incident wave f_0 (1 GHz), the scattering is significantly reduced, thereby, making the plasma a lossy material or a good absorber of electromagnetic energy.

In the next set of results, we look at the impact of reducing the collision frequency below the operating frequency. The results presented in Figs. 15–18 are for

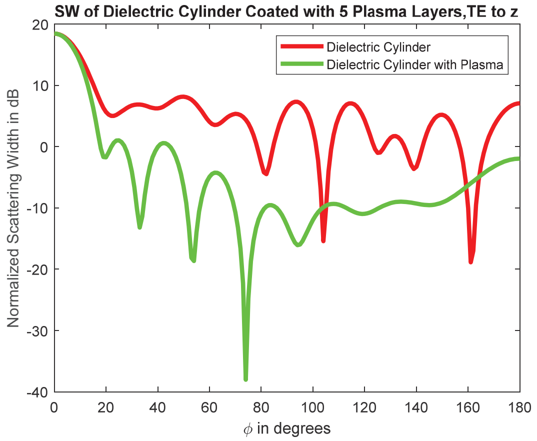

Fig. 11. Scattering width of a dielectric cylinder covered with 5 plasma layers TE_z.

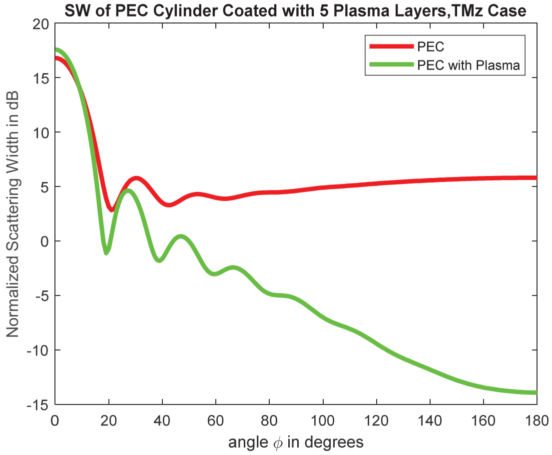

Fig. 12. Scattering width of a PEC cylinder covered with 5 plasma layers TM_z.

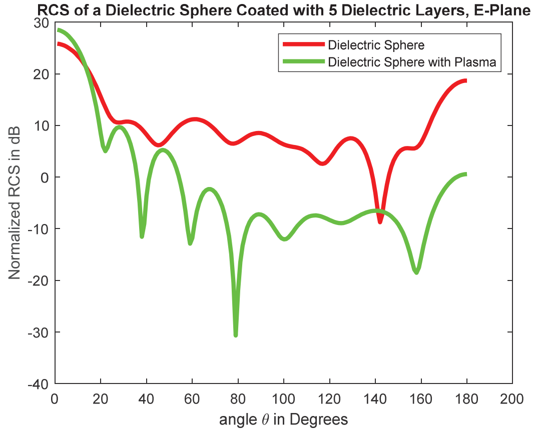

Fig. 13. RCS of a dielectric sphere covered with 5 plasma layers E-plane scan.

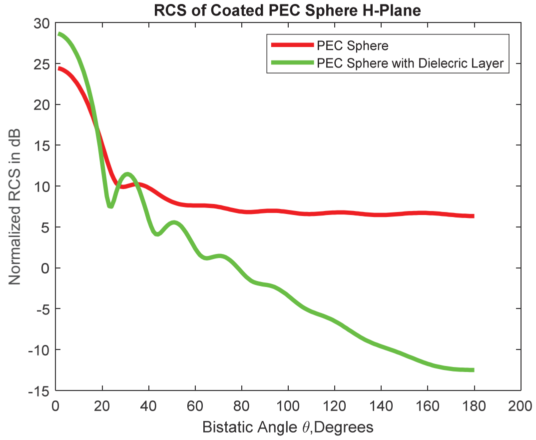

Fig. 14. RCS of a PEC sphere covered with 5 plasma layers H-plane scan.

frequency of incident EM wave, $f_0 = 1$ GHz, $a = 1.2\lambda_0$, $b = 1.25\lambda_0$, $c = 1.3\lambda_0$, $d = 1.35\lambda_0$, $e = 1.4\lambda_0$, $f = 1.5\lambda_0$. Using (1), if we take the electron density, $n_e = 10^{17} m^{-3}$, and electron collision frequency, $f_c = 0.01$ GHz, we obtain the resulting plasma dielectric constant, $\varepsilon_r = -7.0629 - j0.0806$, and the plasma frequency, $f_p = 2.8397$ GHz. All of the 5 plasma layers are set to have the same dielectric constant, that is, $\varepsilon_{r_i} = -7.0629 - j0.0806$ for $i = b,c,d,e,f$. In Fig. 15, we show the SW of a dielectric cylinder, TM_z case, with and without plasma layers. For this case, the dielectric constant and relative permeability of the dielectric cylinder are given by $\varepsilon_{r_a} = 4$ and $\mu_{r_a} = 1$, respectively. We show the SW of a PEC cylinder for the TE_z case in Fig. 16 with and without plasma layers. In Fig. 17, we show the bistatic RCS of a dielectric sphere for the E-plane scan ($\phi^i = 0°$) with and without plasma layers. For this case, the dielectric constant and relative permittivity of the dielectric sphere are given by $\varepsilon_{r_a} = 4$ and $\mu_{r_a} = 1$, respectively. We show the bistatic RCS of a PEC sphere for the H-plane scan in Fig. 18 with and without plasma layers.

From the results in Figs. 15–18, we make an important observation that when the collision frequency of plasma f_c (0.01 GHz) is much lower than the frequency of the incident wave f_0 (1 GHz), the scattering is significantly enhanced to the point where the plasma starts acting as a reflector or partially conducting media.

Even though the plasma layers were all taken to have the same electrical properties, the multi-layered formulation is expected to help in modeling inhomogeneous plasma where each layer may have different electrical characteristics. This is certainly an important and interesting case, the results of which will be reported in the near future.

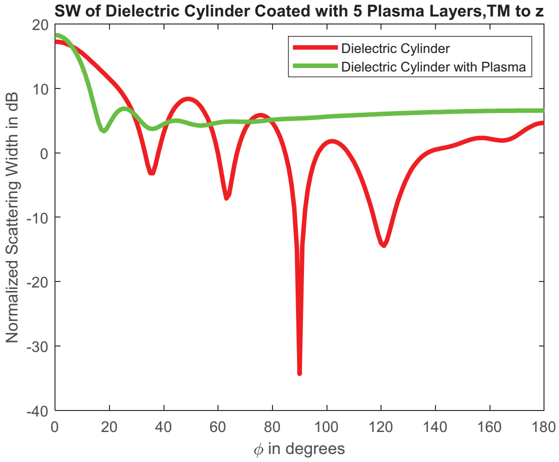

Fig. 15. Scattering width of a dielectric cylinder covered with 5 plasma layers TM_z.

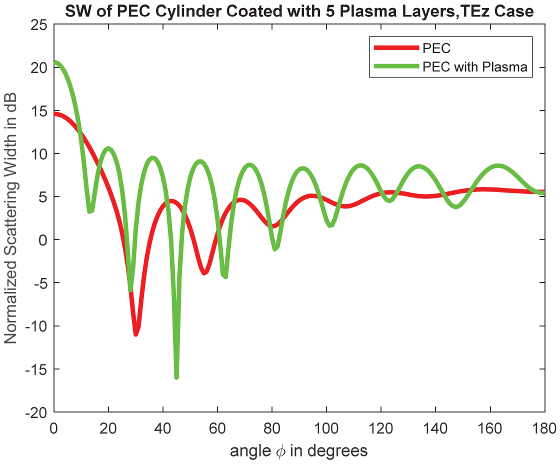

Fig. 16. Scattering width of a PEC cylinder covered with 5 plasma layers TE_z.

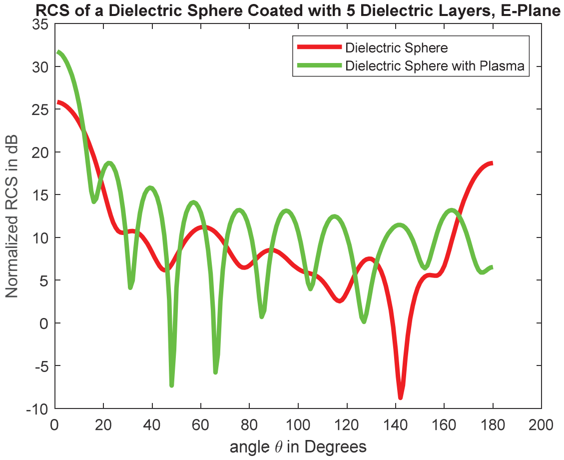

Fig. 17. RCS of a dielectric sphere covered with 5 plasma layers E-plane scan.

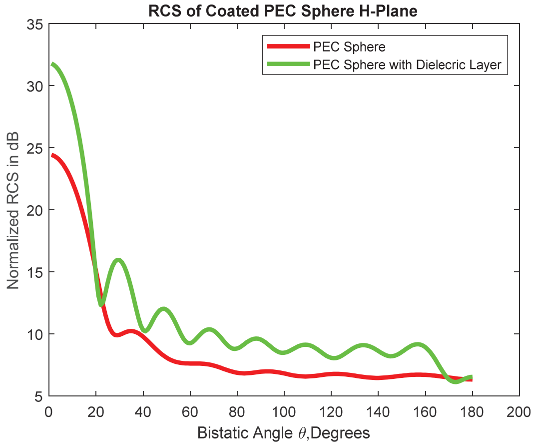

Fig. 18. RCS of a PEC sphere covered with 5 plasma layers H-plane scan.

V. CONCLUSION

In this paper, a comprehensive analysis of scattering from conducting and dielectric cylinders coated with multiple layers (up to 5) of plasma and conducting and dielectric spheres coated with multiple layers (up to 5) of plasma is provided. The variation of the SW for the cylindrical case and RCS for the spherical case is provided as a function of angle. It is shown that plasma can act as a reflector or absorber of incoming electromagnetic energy depending on the frequency of the incoming wave and refractive index of the plasma layers. It is noted that electron collision frequency has a significant impact on the dielectric constant of the plasma and consequently on enhancing or reducing the scattering. We make an important observation that when the plasma collision frequency f_c (10 GHz) is higher than the frequency of the incident wave f_0 (1 GHz), the scattering is significantly reduced, thereby, making the plasma a lossy material or a good absorber of electromagnetic energy. Moreover, when the collision frequency of plasma f_c (0.01 GHz) is much lower than the frequency of the incident wave f_0 (1 GHz), the scattering is significantly enhanced to the point where the plasma starts acting as a reflector or partially conducting media. The results presented here are expected to aid in the study of plasma coatings as a function of the plasma collision frequency in development of stealth technology.

REFERENCES

[1] H. M. Musal, "On the theory of the radar-plasma absorption effect," GM defense Research Laboratories, Contract NO. DA-04-495-ORD-3567(Z), July 1963.

[2] L. Zheng, Q. Zhao, and X. J. Xing, "Effect of plasma on electromagnetic wave propagation and

THz communications for reentry flight," *Applied Computational Electromagnetics Society (ACES) Journal,* vol. 30, pp. 1241–1245, Nov. 2015.

[3] R. J. Vidmar, "On the use of atmospheric pressure plasmas as electromagnetic reflectors and absorbers," *IEEE Trans. Plasma Sci.*, vol. 18, no. 4, pp. 733–741, 1990.

[4] B. Chaudhury and S. Chaturvedi, "Study and optimization of plasma-based radar cross-section reduction using three-dimensional computations," *IEEE Trans. Plasma Sci.*, vol. 37, no. 11, pp. 2116–2127, 2009.

[5] B. Chaudhury and S. Chaturvedi, "Three-dimensional computation of reduction in radar cross-section using plasma shielding," *IEEE Trans. Plasma Sci.*, vol. 33, no. 6, pp. 2027–2034, 2005.

[6] C. Yuan, Z. Zhou, J. W. Zhang, X. Xiang, Y. Feng, and H. Sun, "Properties of propagation of electromagnetic wave in multilayer radar- absorbing structure with plasma- and radar-absorbing material," *IEEE Trans. Plasma Sci.*, vol. 39, no. 9, pp. 1768–1775, 2011.

[7] M. Yan, K. R. Shao, X. W. Hu, Y. Guo, J. Zhu, and J. D. Lavers, "Z-transform based FDTD analysis of perfectly conducting cylinder covered with unmagnetized plasma," *IEEE Trans. Magnetics*, vol. 43, no. 6, pp. 2968–2970, June 2007.

[8] Y. Geng, "Scattering of a plane wave by an anisotropic plasma-coated conducting sphere," *Int. J. Antennas and Propagation*, vol. 2011.

[9] A. Ghaffar, M. Z. Yaqoob, M. A. S. Alkanhal, M. Sharif, and Q. A. Naqvi, "Electromagnetic scattering from anisotropic plasma-coated perfect electromagnetic conductor cylinders," *Int. J. Electronics and communication (AEU)*, vol. 68, no. 8, pp. 767–772, 2014.

[10] Z. Rao, G. Zhu, S. He, C. Li, Z. K. Yang, and J. Liu, "Simulation and analysis of electromagnetic scattering from anisotropic plasma-coated electrically large and complex targets," *Remote Sensing*, vol. 14, p. 764, 2022.

[11] Y. Geng, "Analysis of electromagnetic scattering by a plasma anisotropic sphere," *Radio Science*, vol. 38, no. 6, 2003.

[12] C. A. Balanis, *Advanced Engineering Electromagnetics*, 2nd ed. Hoboken, NJ: John Wiley & Sons, pp. 610, 655–661, 2012.

[13] S. H. Zainud-Deen, A. Z. Botros, and M.S. Ibrahim, "Scattering from bodies coated with metamaterial using FDTD method," *Prog. Electromagn. Res.*, vol. 2, pp. 279–290, 2008.

[14] X. Q. Sheng, J. M. Jin, J. Song, C. C. Lu, and W. C. Chew, "On the formulation of hybrid finite element and boundary-integral methods for 3-D scattering," *IEEE Trans. Antennas Propagat.*, vol. 46, no. 3, pp. 303–311, 1998.

[15] L. Lei, J. Hu, and H.-Q. Hu, "Solving scattering from conducting body coated by thin-layer material by hybrid shell vector element with boundary integral method," *Int. J. Antennas and Propagation*, vol. 2012, 2012.

Surendra Singh is a professor of electrical and computer engineering at The University of Tulsa, USA. He obtained his B.S. degree in electronics and communication engineering from Kurukshetra University, M.Tech. degree in electrical engineering from Indian Institute of Technology, Kanpur, India, and Ph.D. degree in electrical engineering from University of Mississippi, Oxford, MS. He joined the University of Tulsa in 1985 where he teaches electrical engineering and is engaged in computational electromagnetics research. He has participated in over 60 panels at NSF in reviewing for SBIR Phase I and Phase II funding. He actively participates in the Air Force Summer Faculty Fellowship Program.

Effect of the Inner Shape on the Scattering Cross-Section of an Aperture on an Electrically Large High-*Q* Cavity

Feng Tian[1], Feng Fang[1], Bo Peng[2], Yongjiu Zhao[1], and Qian Xu[1,*]

[1]College of Electronic and Information Engineering
Nanjing University of Aeronautics and Astronautics, Nanjing 211106, China
Tianfeng1010@126.com, fangfeng@nuaa.edu.cn, yjzhao@nuaa.edu.cn, emxu@foxmail.com
*Corresponding Author

[2]Beijing Institute of Radio Metrology and Measurement
Beijing 100854, China
amazingpbcjf@126.com

Abstract – This paper presents the effect of the inner shape on the statistical properties of the scattering cross-section of an aperture on a high-*Q* cavity. By combining the full-wave method and Monte Carlo simulations, the mean scattered far-field pattern of the aperture on a high-*Q* cavity can be obtained accurately. We show that the cosine roll-off distribution for the scattered far-field pattern is only an approximation for ideal cases, while the thickness and the inner shape of the aperture can affect the scattered far-field pattern significantly. Different models are used to demonstrate this phenomenon and the results are compared against the ideal cosine roll-off.

Index Terms – Cavity scattering, Monte Carlo simulation, scattering cross-section.

I. INTRODUCTION

Efficient simulation of electromagnetic scattering from an aperture on a high-*Q* cavity is always a challenging problem, as it involves the full-wave (FW) simulation of the electromagnetic field integral [1–3]. The existing computer electromagnetic (CEM) methods for calculating the scattering cross-section have developed for many years, including the finite-difference time-domain (FDTD) method [4–6], method of moments (MoMs) [7–10], multi-level fast multipole method (MLFMM) [11], shooting and bouncing rays (SBR) [12], and physical optics (PO) [13, 14]. The algorithms are applied choicely according to the target size of wavelength, simulation accuracy and time.

Early research on aperture scattering can be traced back to Bethe's small-hole theory [15], in which a subwavelength hole in a perfectly conducting (PEC) plane is represented by equivalent electric and magnetic dipoles, providing quantitative relationships for the transmitted fields and powers in terms of aperture size and wavelength. Based on this foundation, Butler et al. [16] systematized the general integral-differential equations and numerical solution techniques for electromagnetic penetration (EMP) through apertures in PEC surfaces, providing numerical results for electrically small apertures of practical EMP engineering.

Harrington and Mautz [17] subsequently introduced a generalized network formulation in which the two regions separated by an aperture can be modeled via independent aperture admittance matrices. Within the same framework, Harrington [18] later analyzed the resonant behavior of electrically small apertures backed by conducting bodies, demonstrating that appropriate loading can drive "aperture–conductor resonance" and increase the transmission cross-section up to $3\lambda^2/4$ in the lossless limit.

In complex engineering environments, such as inlet ducts, open waveguides, and partially open cavities, aperture scattering is coupled with multimode cavity resonances and high-frequency effects. Anastassiu et al. [19] provided a comprehensive survey of the aperture scattering calculation methods for these structures, covering PO, modal expansions, and FW hybrid algorithms, highlighting their respective advantages, limitations, and computational trade-offs. From studies above, an evolution of the aperture-scattering research from simple small aperture models toward integrated modeling of aperture–cavity systems can be observed. However, most existing works address apertures on electrically small cavities. For apertures on electrically large high-*Q* cavities, the statistical scattering characteristics have not been systematically analyzed and concluded.

In an electrically large high-*Q* cavity, the EM wave propagation is described by the Hill's equation [21], which is related to the *Q*-factor and volume of the cavity. Therefore, in the previous work of [22], by combining

Submitted On: October 09, 2025
Accepted On: December 22, 2025

https://doi.org/10.13052/2025.ACES.J.401206

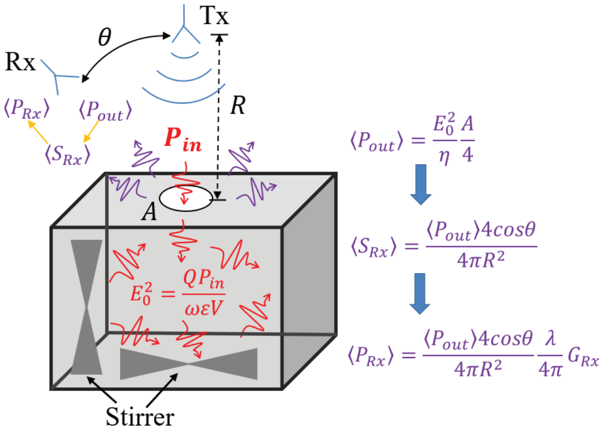

Fig. 1. Schematic of the incident and scattered waves of an aperture on a high-Q cavity.

Hill's equation with the Friis equation of free space, both the theoretical deviation and numerical verification for the scattering cross-section of an ideal aperture on a high-Q cavity were carried out. It was concluded that the average scattering cross-section of the ideal aperture with surface area A (projected in normal direction) on a high-Q cavity can be approximated by

$$\langle \sigma_A \rangle \approx 4A\cos\gamma\cos\theta, \tag{1}$$

where γ and θ are the incident and observation angles of the transmitting (Tx) and receiving (Rx) ports outside the cavity, respectively.

However, when the aperture has depth with a certain thickness, the results will deviate from the ideal case. Besides, practical apertures have some inner shapes, such as the air intakes of aircrafts and vents for large ships. The inner shapes of the apertures are significant factors in determining the scattered far field, as they constrain the plane wave spectrum into a limited region.

To further investigate the aperture scattering on an electrically large high-Q cavity, this paper estimates the scattered far-field pattern of apertures with different inner shapes. Because of the chaotic properties of high-Q cavities [20], the field results exhibit strongly statistical behaviors. The fields inside a high-Q cavity are reflected many times, thus the fields can be modeled as the superposition of random plane waves. When the Q-factor is low, the number of incident waves decreases, and the random plane wave model is no longer valid. Similar modeling approaches have been adopted for reverberation chambers (RC) in [21]. Since the analysis in this paper relies on the random plane wave model, the results are applicable only to high-Q cavities.

Considering that conventional FW simulations for electrically large cavities are time-consuming, this paper proposes an efficient approach that combines the FW simulations with Monte Carlo methods [23–27] to accurately obtain the statistical properties of the scattered far-field pattern, greatly accelerating the computational process. Based on the full-wave Monte Carlo (FWMC) method, the effect of the inner shape on the scattered far field is evaluated. This nonideal effect could be interesting and we examine this in detail in the following sections. An actual RC is also modeled and simulated for comparison with the FWMC method-based results.

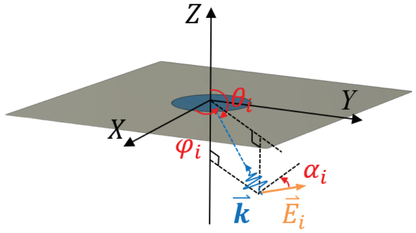

Fig. 2. Schematic of a plane wave inside the cavity incident on an ideal aperture (zero thickness).

The theoretical derivation is detailed in section II and the numerical validations are given in section III. Conclusions are summarized in section IV.

II. THEORY

A schematic plot is illustrated in Fig. 1, an electrically large aperture with surface area A (projected in normal direction) is on an electrically large high-Q cavity. Stirrers inside the cavity are used to redistribute the EM field. We evaluate the scattering cross-section of the aperture in the far-field region under illumination by an EM wave propagating into the cavity along the z-axis. The radiated power of the Rx antenna is P_{Rx}, the gain of the Rx antenna is G_{Rx}. Assuming the high-Q cavity is well stirred, the E-field is statistically uniform and isotropic. For the incident power P_{in}, the mean E-field [21] is

$$E_0^2 = \frac{QP_{in}}{\omega\varepsilon V}, \tag{2}$$

where $E_0^2/3 = \langle |E_x|^2 \rangle = \langle |E_y|^2 \rangle = \langle |E_z|^2 \rangle$ represents the average value of E-field over all polarizations in the high-Q cavity, $\langle\cdot\rangle$ denotes the mean value of the ensemble E-fields, Q is the Q-factor of the cavity, $\omega = 2\pi f$ is the angular frequency, ε is the permittivity of the dielectric in the cavity, and V is the volume of the cavity.

It can be seen that the E_0 becomes the radiated source for the scattered far field of the aperture in Fig. 1. However, FW simulations of the E_0 within the electrically large high-Q cavity costs much time and occupies large computing resources. To efficiently obtain the scattered far field, multiple random plane waves are used to simulate the random scattering environment for the aperture of the high-Q cavity. Each plane wave is

$$\vec{\boldsymbol{E}}_{\boldsymbol{i}} = \vec{\boldsymbol{A}}_{\boldsymbol{i}} \exp(-j\vec{\boldsymbol{k}}_{\boldsymbol{i}}\cdot\vec{\boldsymbol{r}}_{\boldsymbol{i}}), \tag{3}$$

where i denotes the index of the plane wave, $\vec{\boldsymbol{A}}_{\boldsymbol{i}}$ is a complex vector whose initial amplitude and phase have Rayleigh and uniform distribution respectively, $\vec{\boldsymbol{k}}_{\boldsymbol{i}} = k\vec{\boldsymbol{u}}_{\boldsymbol{i}}$ is the wave vector of the plane wave (k is the wave number and $\vec{\boldsymbol{u}}_{\boldsymbol{i}}$ denotes the unit direction vector of the plane wave), and $\vec{\boldsymbol{r}}_{\boldsymbol{i}} = (x_i, y_i, z_i)^T$ represents the position vector pointing from the origin (or the source reference point) to the observation point in space. For N plane waves, we have

$$\vec{\boldsymbol{E}}_{\boldsymbol{inc}} = \sum_{i=1}^{N} \vec{\boldsymbol{E}}_{\boldsymbol{i}} = \sum_{i=1}^{N} \vec{\boldsymbol{A}}_{\boldsymbol{i}} \exp(-j\vec{\boldsymbol{k}}_{\boldsymbol{i}}\cdot\vec{\boldsymbol{r}}_{\boldsymbol{i}}). \tag{4}$$

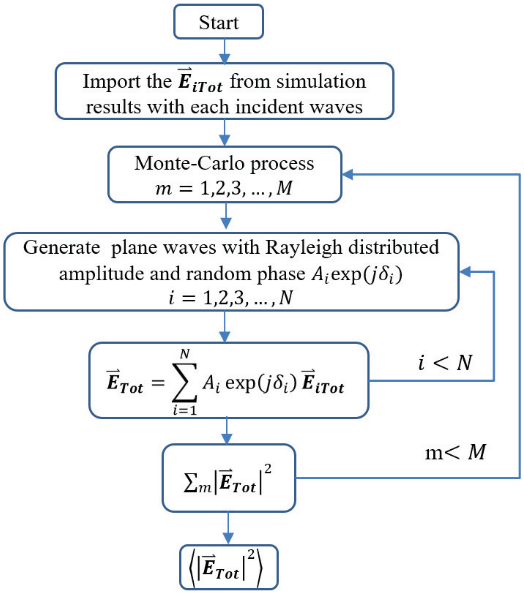

Fig. 3. Workflow of the Monte Carlo simulation.

For each plane wave, according to the angular definitions in Fig. 2, the EM wave propagation direction can be expressed as

$$u_{xi} = -\sin\theta_i \cos\varphi_i, \tag{5}$$

$$u_{yi} = -\sin\theta_i \sin\varphi_i, \tag{6}$$

$$u_{zi} = -\cos\theta_i, \tag{7}$$

and the unit direction vector $\vec{e}_i$ of E-field can be expressed as

$$e_{xi} = \cos\alpha_i \cos\theta_i \cos\varphi_i - \sin\alpha_i \sin\varphi_i, \tag{8}$$

$$e_{yi} = \cos\alpha_i \cos\theta_i \sin\varphi_i + \sin\alpha_i \cos\varphi_i, \tag{9}$$

$$e_{zi} = -\cos\alpha_i \sin\theta_i, \tag{10}$$

where θ_i is the polar angle, φ_i is the azimuth angle, α_i is the polarization angle of E-field, and $\alpha_i = 0°$ and $\alpha_i = 90°$ represents the TE and TM waves, respectively. Based on the descriptions above, the mean E-field E_0 in (2) can also be written as $E_0^2 = \langle|A_i \vec{e}_i|^2\rangle$.

When each plane wave E_i is incident on the aperture, the total field $\vec{E}_{iTot}$ for the aperture of the high-Q cavity, including the scattered field and incident field, can be simulated using the FDTD method in CST (normalized to 1 V/m incident wave). When multiple plane waves are incident on the aperture simultaneously, the total E-field in the scattered far-field region for the aperture can be calculated by [19]

$$\vec{\boldsymbol{E}}_{\boldsymbol{Tot}} = \sum_{i=1}^{N} A_i \exp(j\delta_i)\, \vec{\boldsymbol{E}}_{\boldsymbol{iTot}}, \tag{11}$$

where A_i is Rayleigh distributed amplitude, δ_i is uniform distributed phase, and N is the number of the plane waves.

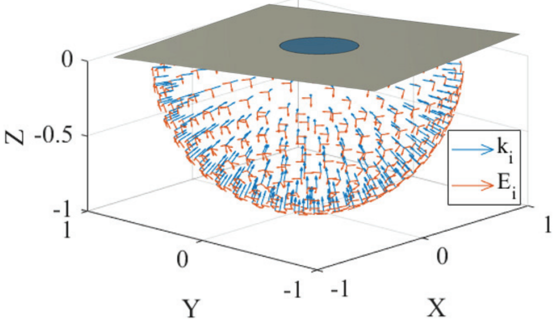

Fig. 4. Schematic of the plane wave sources in an ideal aperture.

After finishing the FW simulation for each incident wave, the total field data in the scattered far-field region are saved in the memory. To estimate the scattered far field of the aperture on the high-Q cavity accurately and quickly, the simulated results are imported into Monte Carlo simulations. The Monte Carlo simulation is performed to simulate a well-stirred high-Q cavity, as illustrated in Fig. 3. The number of Monte Carlo iterations is denoted as M, which corresponds to the number of independent stirrer positions. According to the statistical field distributions described in [21], the magnitude of any E-field component inside a well-stirred cavity, such as $|E_x|$, follows a Rayleigh distribution and its squared magnitude $|E_x|^2$ follows a Gamma distribution. To reproduce the EM environment inside a well-stirred cavity, the amplitudes of the random incident plane waves in the Monte Carlo process are generated using a Rayleigh distribution. In the next section, the scattered far-field patterns of the different apertures are shown and compared with the theoretical values.

III. SIMULATION RESULTS AND COMPARISONS

In FWMC simulations, 610 plane wave sources, shown in Fig. 4, are used to generate plane waves over $\theta = 90 \sim 180^\circ$ and $\varphi = 0 \sim 360^\circ$. Each plane wave contains two polarizations with $\alpha = 0^\circ$ and $\alpha = 90^\circ$. Therefore, a total of $N = 1220$ plane waves are simulated to obtain scattered near field $\vec{E}_{NiTot}$ and far field $\vec{E}_{FiTot}$ (the magnitude of the plane waves is normalized to 1 V/m). In this paper, only a single frequency point at 1 GHz is considered, which corresponds to a wavelength λ of 300 mm. The simulation frequency ranges from 0.7 GHz to 1.3 GHz so that the frequency of interest lies at the center of simulated frequency band.

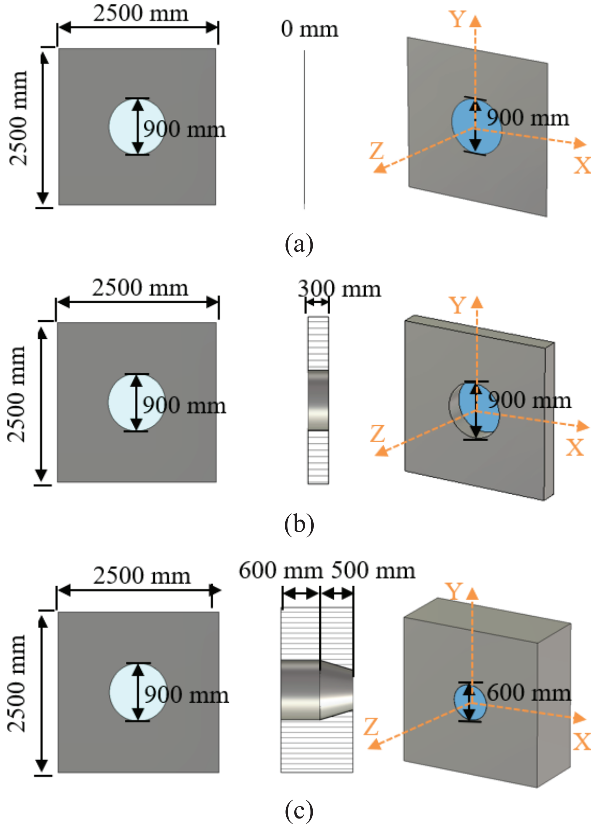

(a)

(b)

(c)

Fig. 5. (a) Ideal aperture, (b) aperture with tubular inner shape, (c) aperture with conical inner shape.

After FW simulations, a Monte Carlo simulation is performed with $M = 10000$ to emulate a well-stirred cavity, as illustrated in Fig. 3. In each iteration, a new sequence of A_i and δ_i is generated. To obtain the scattered results based on the normalized squared magnitude, we set $2\sigma_{RC}^2$ to 3, yielding $\sigma_{RC} = \sqrt{3/2}$. Considering the superposition of the power density for N plane waves, the amplitude A_i in (11) is randomly generated by [22]

$$p_A(x) = \frac{x}{\sigma_{RC}^2} e^{-\frac{x^2}{2\sigma_{RC}^2}}, \quad x = A_i, \tag{12}$$

where $\sigma_{RC} = \sqrt{3/2}/\sqrt{N}$. The δ_i are uniform distributed over $[0, 2\pi)$. Upon completing the Monte Carlo simulations, the mean scattered near field and scattered far field of the aperture on an electrically large high-Q cavity can be obtained.

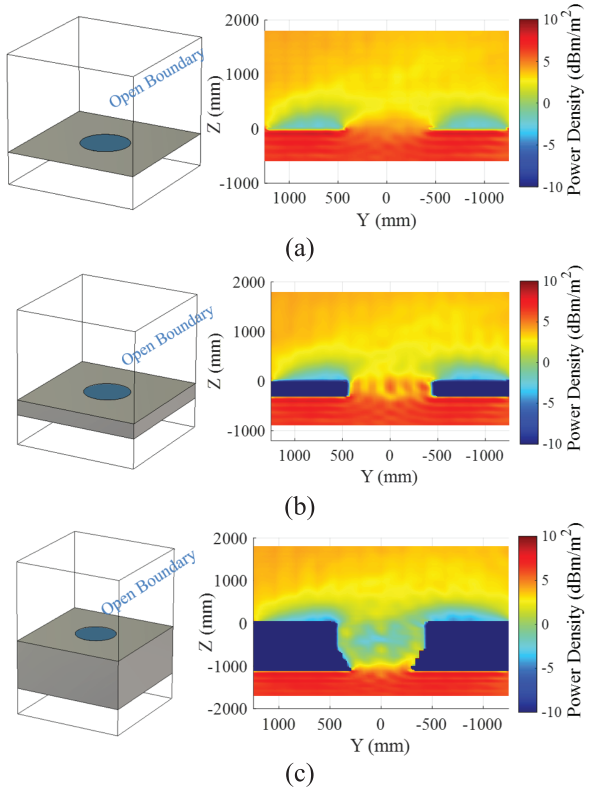

(a)

(b)

(c)

Fig. 6. Simulated setting and average power density of the scattered near field at 1 GHz on the yoz plane for the aperture with (a) ideal, (b) tubular and (c) conical inner shape.

A. Simulated results

Considering the inner shape of the aperture on the high-Q cavity, the three models shown in Fig. 5 are simulated to obtain the scattered far field, which includes an ideal aperture, an aperture with tubular inner shape and an aperture with conical inner shape, respectively. The dimension of the aperture metal ground is 2500 mm × 2500 mm. As shown in Fig. 6, open boundaries (perfectly matched layers) are attached to the edge of the planar model. Thus, the simulation boundaries can be approximated as an infinite plane, which reduces the influence of reflected waves on the scattered field. The simulated region is limited to 2500 mm × 2500 mm. The diameter of the ideal aperture is 900 mm, which is 3λ. For the aperture with tubular inner shape, the depth of the tubular inner shape is 300 mm. The other aperture has a conical inner shape, whose depth is 500 mm and bottom diameter is 600 mm (2λ).

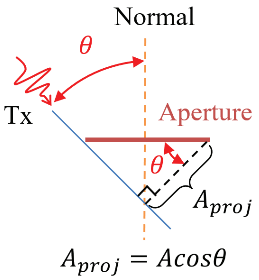

Fig. 7. Schematic of the aperture's projected area.

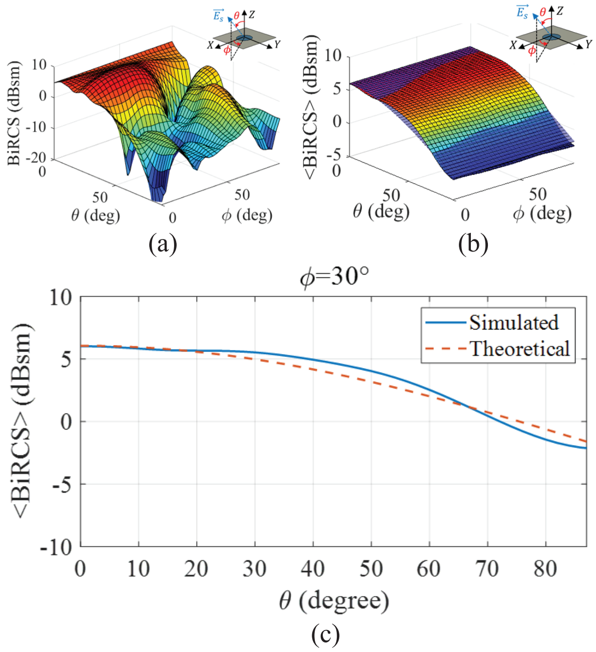

Fig. 8. (a) Typical 3D pattern of the scattered far field at one stirrer position, (b) 3D pattern of the mean scattered far field, (c) simulated and theoretical $\langle \text{BiRCS} \rangle$ over $\theta = 0^\circ - 90^\circ, \phi = 30^\circ$ at 1 GHz from the ideal aperture.

To estimate the effect of the apertures' inner shape on the incident wave, the scattered near fields at 1 GHz on the *yoz* plane of the different apertures are simulated under all incident plane waves. Figures 6 (a)–(c) show the average power density of the scattered near field calculated using the FWMC method. It can be seen that the scattered near field within the working volume of the RC is uniform. Although the apertures are geometrically symmetrical, the scattered near fields shown in Fig. 6 are not fully symmetrical because of the numerical discretization in simulation.

The average power density distributions surrounding the ideal apertures differ significantly from those for apertures with various inner geometries. In the case of an aperture with a tubular inner shape, the propagation of EM waves through the aperture is marginally affected. In contrast, the aperture with a conical inner shape significantly impacts EM wave propagation. The average power density in the central region of the aperture decreases from 6.62 dBm/m^2 with a tubular inner shape to 1.46 dBm/m^2 with a conical inner shape. Furthermore, the conical geometry causes the electric field to concentrate near the metal boundary, thereby limiting the propagation of electromagnetic waves toward the edge of the aperture.

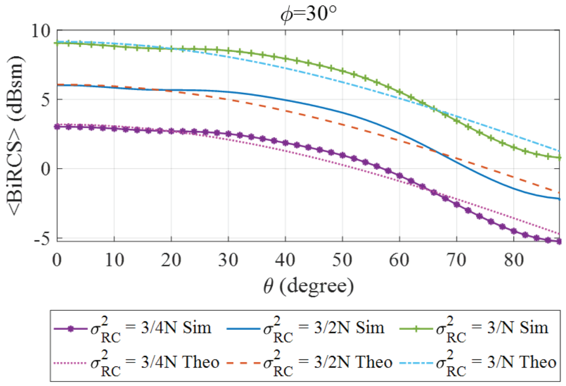

Fig. 9. $\langle \text{BiRCS} \rangle$ of the ideal aperture for different σ_{RC} over $\theta = 0^\circ - 90^\circ, \phi = 30^\circ$.

In the far-field region, when the aperture is observed from different directions, its projected area varies with the observation angle θ of Rx port, as can be seen in Fig. 7. Because the projected area of the aperture varies according to a cosine function, the energy radiates or scatters in different directions also following this cosine pattern. As a result, the scattered far field over the hemispherical surface exhibits a cosine distribution. As mentioned in section II, the incident wave from Tx port propagates into the cavity along the z-axis, thus $\gamma = 0^\circ$ and (1) can be simplified as

$$\langle \sigma_A \rangle \approx 4Acos\theta, \tag{13}$$

where θ is the observation angle for the Rx antenna.

Figure 8 (a) illustrates the 3D pattern of the scattered far field at a single stirrer position from the ideal aperture. The 3D pattern of the mean scattered far field is shown in Fig. 8 (b). It can be observed that the patterns at a single rotation position exhibit variations with respect to the angle θ. Moreover, these variations are more pronounced than those of the mean pattern. The average bistatic RCS ⟨BiRCS⟩ at $\phi = 30°$ is compared with the theoretical prediction, as depicted in Fig. 8 (c). It can be seen that the simulated ⟨BiRCS⟩ closely approximates the theoretical prediction ($4Acos\theta$) over $\theta = 0°$ to $30°$. As for θ ranging from 30° to 90°, the estimated value exhibits minor fluctuations around the theoretical value.

Because the scattered far-field pattern of an aperture illuminated by light is sensitive to the statistical field, the sensitivity of the average scattered far field for an aperture on a high-Q cavity is also evaluated. Figure 9 compares simulated and theoretical ⟨BiRCS⟩ of the ideal aperture for three different values of $\sigma_{RC} = \sqrt{3/4N}$, $\sqrt{3/2N}$ and $\sqrt{3/N}$. As expected, the value of ⟨BiRCS⟩ increases with larger σ_{RC}, since the magnitude of E-field inside the cavity depends on σ_{RC}. Meanwhile, the overall distribution shape remains unchanged for different values of σ_{RC}^2, which can be attributed to the uniformity of the field inside the high-Q cavity.

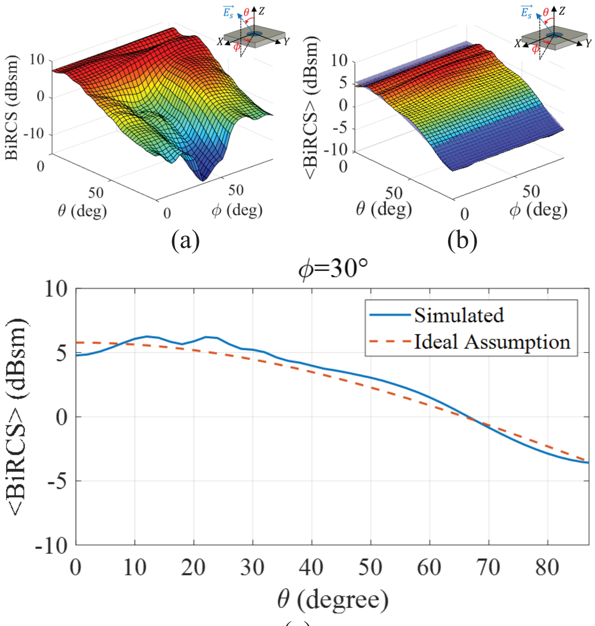

(a) (b)

(c)

Fig. 10. (a) Typical 3D pattern of the scattered far field at one stirrer position, (b) 3D pattern of the mean scattered far field, (c) simulated and ideal assumption ⟨BiRCS⟩ over $\theta = 0° - 90°, \phi = 30°$ at 1 GHz from the aperture with a tubular inner shape.

Figure 10 (a) presents the 3D pattern of the scattered far field from an aperture with a tubular inner shape at a single stirrer position. The 3D pattern of the mean scattered far field is shown in Fig. 10 (b). It can be observed that the tubular structure leads to a high ⟨BiRCS⟩ in the center region of the aperture, indicating a concentration of mean scattered far-field energy in this area. As illustrated in Fig. 10 (c), ⟨BiRCS⟩ exceeds the ideal assumption ($4Acos\theta$) within the range $\theta = 10°$ to 65°, while it falls below the ideal assumption over $\theta = 65°$ to 85°.

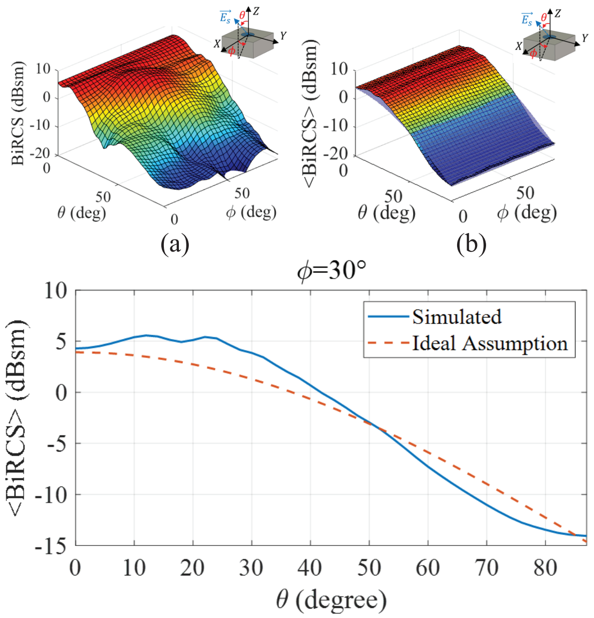

(a) (b)

(c)

Fig. 11. (a) Typical 3D pattern of the scattered far field at one stirrer position, (b) 3D pattern of the mean scattered far field, (c) simulated and ideal assumption ⟨BiRCS⟩ over $\theta = 0° - 90°, \phi = 30°$ at 1 GHz from the aperture with a conical inner shape.

For the aperture with a conical inner shape, the 3D patterns of the scattered far field at a single stirrer position and mean scattered far field are shown in Figs. 11 (a) and 11 (b). It can be found that the overall ⟨BiRCS⟩ are less than those of other apertures, especially for the values over $\theta = 50°$ to 85°. This phenomenon indicates that the reduction of the inner cross-section diameter from 900 mm to 600 mm has resulted in a decrease of the mean scattered far field. Additionally, this finding also corroborates the simulated scattered near field results presented in Fig. 6 (c). Figure 11 (c) shows a comparison between the simulated values and ideal assumption at $\phi = 30°$. It can be seen that the mean scattered far field in the edge region of the aperture (approximately $\theta = 60° - 90°$) with a conical inner shape is lower than the ideal assumption. For θ ranging from 0° to 50°, the simulated value is higher than ideal assumption, while for θ from 50° to 85°, it is lower than the ideal assumption.

From the results, the underlying physical mechanisms can be explained from several perspectives. First, for the ideal aperture, the energy distributed over the hemispherical surface follows a cosine pattern because the effective projected area of the aperture varies with the outside incident angle, as discussed previously. Second, for the tubular aperture, the finite thickness behaves like a short waveguide section. This waveguide-like structure alters the cosine-shaped projection effect and forces the EM wave inside the cavity to propagate through the tube, resulting in a scattered far field that is concentrated on the center region of the aperture. Third, for the conical aperture, the reduced inner diameter further concentrates the scattered far field towards the aperture center. In addition, the free space originally located at the aperture peripheral region is replaced by the metallic wall, which enhances shielding effects and suppresses radiation from the edge of the aperture. As a result, the scattered far-field pattern amplitude decreases significantly in the range of approximately 50° to 85°.

B. Comparisons

An RC with different apertures is simulated to verify the calculated results using the proposed method. The RC model with dimensions 4.68 m × 3.9 m × 3 m is shown in Fig. 12 (a). Two stirrers are applied to redistribute the E-field inside the RC; the frequency of interest is set at 1 GHz. An aperture of 900 mm in diameter is hollowed on the metal wall. The schematic of the incident and scattered waves is illustrated in Fig. 12 (b).

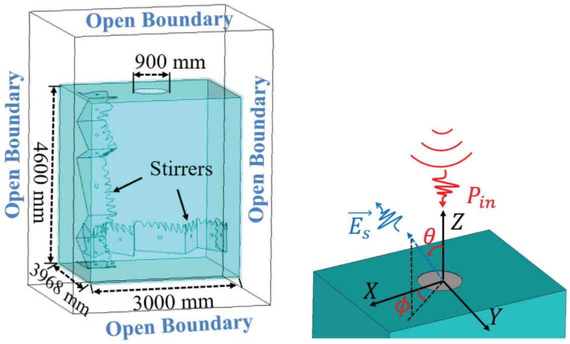

(a) (b)

Fig. 12. (a) Simulated setup of the RC model with an ideal aperture, (b) Schematic of the incident and scattered waves for RC with an ideal aperture.

In this paper, the scattered far field is considered to originate from the leakage E-field of an electrically large cavity. Therefore, the proposed method is applied to a metallic cavity with internally stored energy, under the assumption that no surface currents exist outside the cavity. Figure 12 (b) shows the schematic of the incident and scattered waves for the RC with an ideal aperture. It can be observed that incident plane waves propagate along the z-axis to excite resonant electric fields inside the cavity. To eliminate the influence of reflective waves on the scattered far field, radio absorbing materials (RAM) are coated on the top metal surface of the RC.

Table 1: Comparison of simulated requirements between FW simulations and FWMC method

Method	**Scenarios**	**Total Time**	**Peak Memory**
FW	RC with apertures	63 hours	29.8 GB
FW+MC	Apertures	23.9+1.5 hours	0.6 GB

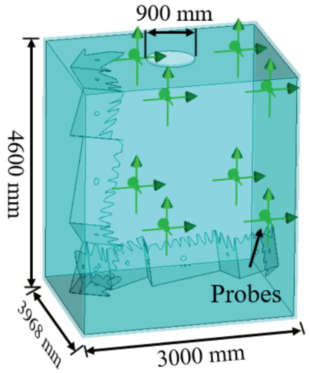

Fig. 13. FU simulated setup of the RC with an ideal aperture.

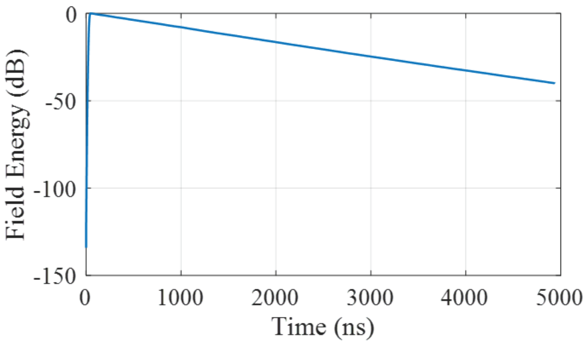

Fig. 14. Simulated field energy in the RC at 1 GHz.

The MLFMM in CST is applied to simulate the scattered near field and far field. Twelve stirrer positions with a step of 30° are used to generate a uniform field distribution. FW simulation with MLFMM is repeated for each stirrer position. The iterative stopping criterion of the simulation is set as −40 dB, meaning the simulation terminates only when the residual error converges below this threshold. The lower bound of the cell number per wavelength is higher than 10 and the edges have been refined. The number of total cells is 554,771. Since the simulation results have been verified for the ideal cases, when the same settings are applied to similar scenarios, the results should also be reliable. The boundaries are set to open boundary, as shown in Fig. 12 (a). The simulations for the RC with different apertures are accelerated using an NVIDIA GPU 4060Ti (8 GB). The computer is equipped with an Intel Core (TM) i5-13600KF CPU and 32 GB of running memory.

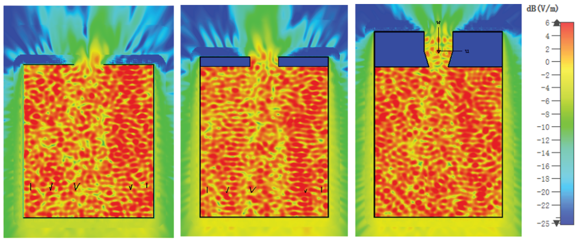

(a) (b) (c)

Fig. 15. Simulated scattered near field of the RC with (a) ideal, (b) tubular and (c) conical aperture at a typical stirring position.

Based on the identical simulation conditions described above, Table 1 summarizes the total processing time (including both FW simulation and Monte Carlo post-processing) and the peak memory requirements for the three apertures using conventional FW simulation and the proposed FWMC method. It can be observed that the FWMC method accelerates overall simulation process and significantly reduces the required peak memory. Moreover, as the number of stirring position increases, the computational burden of the FW simulations grows rapidly. Consequently, the proposed FWMC approach provides an efficiency and accurate alternative for estimating the scattered far field of apertures on electrically large cavities.

To validate the FU (field uniformity) of the RC, the simulation setup is configured according to IEC 61000-4-21 [28], as shown in Fig. 13. Eight E-field probes are placed on the perimeter of the working volume to measure the E_x, E_y and E_z components. The working volume is defined as the region located at least $\lambda/4$ away from the stirrers and chamber walls. The FU can be calculated by

$$\sigma_{FU}=\sqrt{\frac{\sum_{m=1}^{8}\sum_{n=1}^{3}\left(\vec{E}_{mn}-\langle\vec{E}\rangle_{24}\right)^{2}}{24-1}},\tag{14}$$

$$FU=20\log_{10}\left(\frac{\sigma_{FU}+\langle\vec{E}\rangle_{24}}{\langle\vec{E}\rangle_{24}}\right),\tag{15}$$

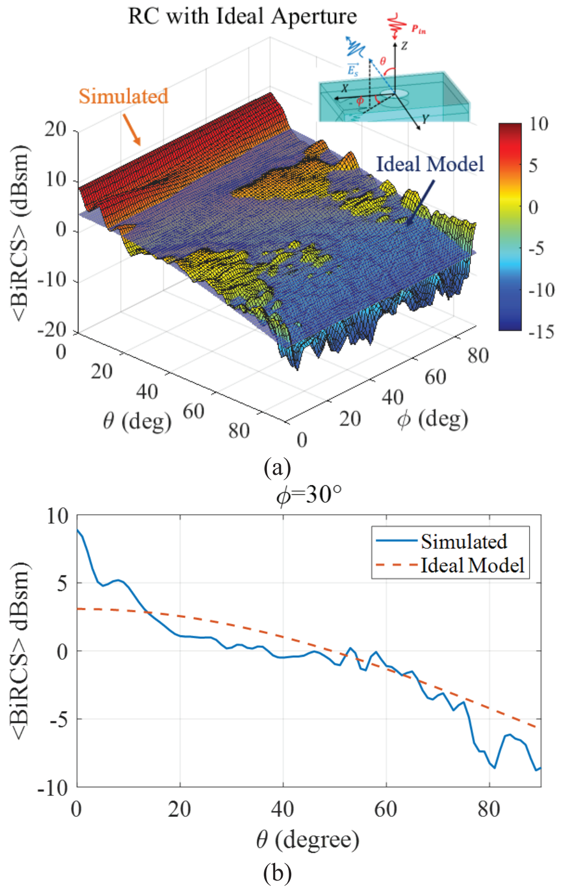

(a)

(b)

Fig. 16. (a) 3D patterns of simulated ⟨BiRCS⟩ and ideal model over the $\theta=0^\circ-90^\circ,\phi=30^\circ$; (b) simulated ⟨BiRCS⟩ and ideal model over $\theta=0^\circ-90^\circ,\phi=30^\circ$ at 1 GHz from RC with an ideal aperture.

where $\vec{E}_{mn}$ is the simulated E-field at probe location m (ranging from 1 to 8) along isotropic axis n (ranging from 1 to 3, corresponding to the x, y, and z directions, respectively). $\langle\vec{E}\rangle_{24}$ is the arithmetic mean of the maximum E-field (in V/m) across all probe axes and stirrer positions. Using the simulated E-field data from 12 stirrer positions and applying (14)–(15), the FU of the RC with an ideal aperture at 1 GHz is calculated to be 1.588 dB, which satisfies the FU limit of 3 dB at 1 GHz as required by IEC-61000-4-21. Besides FU, the field energy in the RC at 1 GHz is simulated and shown in Fig. 14. According to [29], the Q-factor and time constant of the RC can be calculated from the field energy

$$\tau_{RC}=-\frac{10}{k_s\ln(10)},\tag{16}$$

$$Q=\omega\tau_{RC}=2\pi f\tau_{RC},\tag{17}$$

where k_s is the slope of the field energy decay. Based on the simulated results in Fig. 13, $\tau_{RC}=1671.9$ ns and $Q=10505.1$ at 1 GHz.

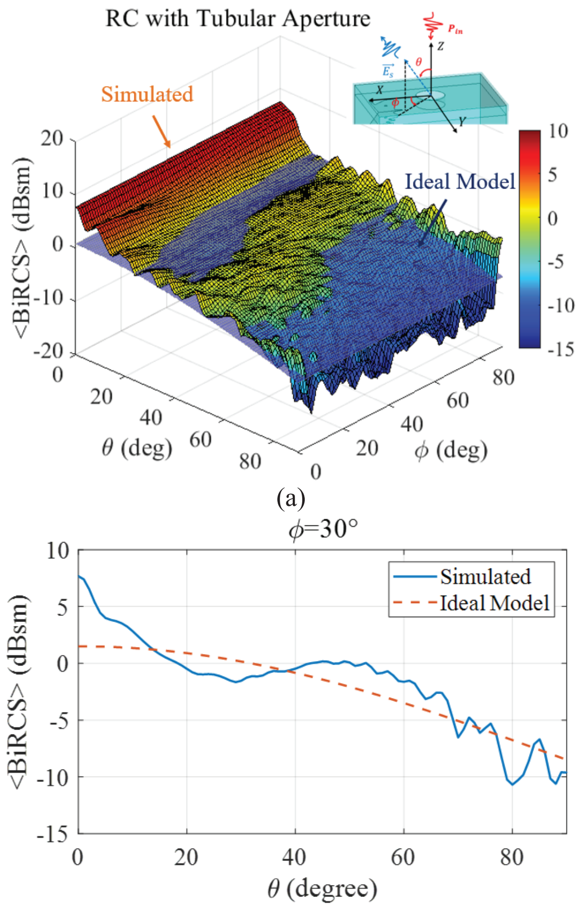

(a)

(b)

Fig. 17. (a) 3D patterns of simulated ⟨BiRCS⟩ and ideal model over the $\theta = 0° - 90°, \phi = 30°$; (b) simulated ⟨BiRCS⟩ and ideal model over $\theta = 0° - 90°, \phi = 30°$ at 1 GHz from the RC with a tubular aperture.

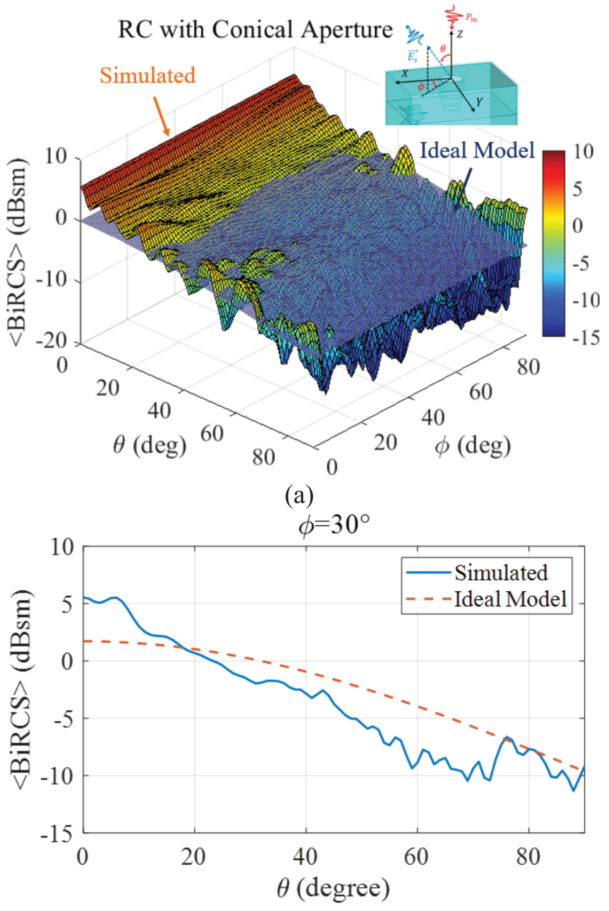

(a)

(b)

Fig. 18. (a) 3D patterns of simulated ⟨BiRCS⟩ and ideal model over the $\theta = 0° - 90°, \phi = 30°$; (b) simulated ⟨BiRCS⟩ and ideal model over $\theta = 0° - 90°, \phi = 30°$ at 1 GHz from the RC with a conical aperture.

The scattered near fields at a typical stirring position of the RC with three inner shapes are shown in Fig. 15. It can be observed that the inner shape has a significant effect on the EM waves propagation through the aperture. ⟨BiRCS⟩ from 12 stirrer positions for different apertures are illustrated in Figs. 16–18. Although the outer surface of the RC is coated with RAM, reflections from bottom metal surface of the RC cannot be completely eliminated. These reflections enhance the scattered far field over $\theta = 0° - 20°$. For $\theta = 70° - 90°$, the RAM effectively reduces the scattered near field strength, as shown in Fig. 15, resulting in a scattered far field lower than the ideal model ($4Acos\theta$) in section A. With the increase of the aperture's depth, it can be found that ⟨BiRCS⟩ exhibits scattered far-field concentrations compared with the ideal model. Meanwhile, the overall scattered level of ⟨BiRCS⟩ decreases due to the reduction in the aperture's inner cross-section diameter. These variations are consistent with the results presented in section A, verifying the feasibility of the proposed method. Furthermore, compared with the conventional RC model method, the proposed method significantly reduces the simulation time, which improves the efficiency for evaluating the scattering cross-section of different apertures in actual applications.

IV. CONCLUSIONS

Based on the statistical properties of the high-Q cavity and the full-wave simulation results, we have obtained the mean scattered far-field pattern of apertures with different inner shapes on a high-Q cavity by using the FWMC method. The mean scattered far-field pattern of the ideal aperture of the high-Q cavity agrees with the theoretical values well.

However, for general cases, the apertures of the cavity have different inner shapes, which will limit the incident wave directions (plane-wave spectrum) from the cavity and will affect propagation of the EM waves. Therefore, we estimated the scattered far field of the different apertures as shown in Fig. 5. From the analysis, it can be concluded that the cosine roll-off is only an approximation for ideal cases. For apertures with specific shapes, the scattered far fields exhibit distribution characteristics distinct from the cosine roll-off, such as energy concentration at the center and attenuation at the edges of the aperture. As for the different apertures, the general FWMC simulation can give a numerical description of the distribution of the scattered far field. A comparison of simulation time between the proposed method and conventional RC model method verifies the efficiency of the proposed method.

ACKNOWLEDGMENT

This work was supported in part by the Foundation of National Key Laboratory of Science and Technology on Space Microwave under Grant 2018SSFNKLSMT-09 and in part by the Beijing Institute of Radio Metrology and Measurement under Grant JLKG2024001A002.

REFERENCES

[1] X. Mei, Y. Zhang, and H. Lin, "A new efficient hybrid SBR/MoM technique for scattering analysis of complex large structures," in *IEEE International Conference on Computational Electromagnetics*, Hong Kong, China, pp. 306–308, 2015.

[2] E. F. Knott, *Radar Cross-Section Measurements*. Berlin: Springer Science & Business Media, 2012.

[3] M. H. Ahmad and D. P. Kasilingam, "Spectral domain fast multipole method for solving integral equations of electromagnetic wave scattering," *Progress in Electromagnetics Research*, pp. 121–131, 2019.

[4] N. Oswald and D. R. Monismith, "Radar cross-sections of objects with simulated defects using the parallel FDTD method," in *IEEE Symposium on Electromagnetic Compatibility, Signal Integrity and Power Integrity (EMC, SI & PI)*, Long Beach, CA, USA, pp. 12–17, 2018.

[5] S. Stewart, S. Moslemi-Tabrizi, T. J. Smy, and S. Gupta, "Modified explicit finite-difference time-domain method for nonparaxial wave scattering from electromagnetic metasurfaces," *IEEE Antennas and Wireless Propagation Letters*, vol. 18, no. 6, pp. 1238–1242, 2019.

[6] Y. Wu, Z. Chen, W. Fan, J. Wang, and J. Li, "A wave-equation-based spatial finite-difference method for electromagnetic time-domain modeling," *IEEE Antennas and Wireless Propagation Letters*, vol. 17, no. 5, pp. 794–798, 2018.

[7] H. Zhao and Z. Shen, "Fast wideband analysis of reverberation chambers using hybrid discrete singular convolution-method of moments and adaptive frequency sampling," *IEEE Transactions on Magnetics*, vol. 51, no. 3, pp. 1–4, 2015.

[8] D. Dault and B. Shanker, "An interior penalty method for the generalized method of moments," *IEEE Transactions on Antennas and Propagation*, vol. 63, no. 8, pp. 3561–3568, 2015.

[9] X. Cao, M. Chen, X. Wu, M. Kong, J. Hu, and Y. Zhu, "Dual compressed sensing method for solving electromagnetic scattering problems by method of moments," *IEEE Antennas and Wireless Propagation Letters*, vol. 17, no. 2, pp. 267–270, 2018.

[10] S. M. Rao, "A true domain decomposition procedure based on method of moments to handle electrically large bodies," *IEEE Transactions on Antennas and Propagation*, vol. 60, no. 9, pp. 4233–4238, 2012.

[11] T. F. Eibert and T. B. Hansen, "Propagating plane-wave fast multipole translation operators revisited – standard, windowed, gaussian beam," *IEEE Transactions on Antennas and Propagation*, vol. 69, no. 9, pp. 5851–5860, 2021.

[12] H. Ling, R. C. Chou, and S. W. Lee, "Shooting and bouncing rays: Calculating the RCS of an arbitrarily shaped cavity," *IEEE Transactions on Antennas and Propagation*, vol. 37, no. 2, pp. 194–205, 1989.

[13] J. Li, Y. Pan, L. Guo, Z. Ren, and K. Li, "A bi-iterative model electromagnetic scattering from a ship floating on sea surface," in *International Symposium on Antennas, Propagation and EM Theory (ISAPE)*, Hangzhou, China, pp. 1–4, 2018.

[14] H. Zhou, X. H. Wang, L. Xiao, and B. Z. Wang, "Efficient EDM-PO method for the scattering from electrically large objects with the high-order impedance boundary condition," *IEEE Transactions on Antennas and Propagation*, vol. 70, no. 9, pp. 8242–8249, 2022.

[15] H. A. Bethe, "Theory of diffraction by small holes," *Physic Review*, vol. 66, no. 7, pp. 163–182, 1944.

[16] C. Butler, Y. Rahmat-Samii, and R. Mittra, "Electromagnetic penetration through apertures in conducting surfaces," *IEEE Transactions on Antennas and Propagation*, vol. AP-26, no. 1, pp. 82–93, 1978.

[17] R. F. Harrington and J. R. Mautz, "A generalized network formulation for aperture problems," *IEEE Transactions on Antennas and Propagation*, vol. AP-24, no. 6, pp. 870–873, 1976.

[18] R. F. Harrington, "Resonant behavior of a small aperture backed by a conducting body," *IEEE Transactions on Antennas and Propagation*, vol. AP-30, no. 2, pp. 205–212, 1982.

[19] H. T. Anastassiu, "A review of electromagnetic scattering analysis for inlets, cavities and open ducts," *IEEE Antennas and Propagation Magazine*, vol. 45, no. 6, pp. 27–40, 2003.

[20] K. Selemani, J. B. Gros, E. Richalot, O. Legrand, O. Picon, and F. Mortessagne, "Comparison

of reverberation chamber shapes inspired from chaotic cavities," *IEEE Transactions on Electromagnetic Compatibility*, vol. 57, no. 1, pp. 3–11, 2015.

[21] D. A. Hill, *Electromagnetic Fields in Cavities: Deterministic and Statistical Theories*. Hoboken, NJ: Wiley-IEEE Press, 2009.

[22] Q. Xu, F. Tian, X. Chen, L. Xing, Y. Zhao, and Y. Huang, "Estimating the scattering cross-section of an electrically large aperture on a high-Q cavity," *IEEE Antennas and Wireless Propagation Letters*, vol. 22, no. 12, pp. 2960–2964, 2023.

[23] Q. Xu, K. Chen, X. Shen, and Y. Huang, "Simulating boundary fields of arbitrary-shaped objects in a reverberation chamber," *Applied Computational Electromagnetics Society (ACES) Journal*, vol. 36, pp. 1132–1138, 2021.

[24] J. M. Ladbury, "Monte Carlo simulation of reverberation chambers," in *Gateway to the New Millennium. 18th Digital Avionics Systems Conference. Proceedings*, pp. 10.C.1–10.C.1, 1999.

[25] B. Plaum, "Estimation of the effects of spurious modes in linear microwave systems using a Monte Carlo algorithm," *IEEE Journal of Microwaves*, vol. 3, no. 3, pp. 1061–1067, 2023.

[26] P. Wijesinghe, U. Gunawardana, and R. Liyanapathirana, "Combined flat histogram Monte Carlo method for efficient simulation of communication systems," *IEEE Communications Letters*, vol. 16, no. 1, pp. 80–82, 2012.

[27] R. Yuan, J. Ma, P. Su, Y. Dong, and J. Cheng, "Monte Carlo integration models for multiple scattering based optical wireless communication," *IEEE Transactions on Communications*, vol. 68, no. 1, pp. 334–348, 2020.

[28] *IEC 61000-4-21, Electromagnetic compatibility (EMC) – Part 4-21: Testing and measurement techniques – Reverberation chamber test methods*, IEC Standard, Ed 2.0, 2011-01.

[29] Q. Xu and Y. Huang, *Anechoic and Reverberation Chambers: Theory, Design, and Measurements*. Hoboken, NJ: Wiley-IEEE Press, 2018.

Feng Tian received the B.Eng. degree from University of Electronic Science and Technology of China, Chengdu, China, in 2008, and received M.Eng. degree from CETC 14th Institute, Nanjing, in 2011. He is currently a Ph.D. student at the College of Electronic and Information Engineering, Nanjing University of Aeronautics and Astronautics, China. His research interests include power amplifier, EMC, and antennas.

Feng Fang received the B.Eng. and M.Eng. degrees in microwave technology from the Nanjing University of Aeronautics and Astronautics, Nanjing, China, in 2020 and 2023, respectively. He is currently working toward the Ph.D. degree in electromagnetic field and microwave technology from Nanjing University of Aeronautics and Astronautics. His main research interests include patch antenna, antenna array, reverberation chamber, computational electromagnetics and statistical electromagnetics, Over-the-Air (OTA) testing and electromagnetic compatibility (EMC).

Bo Peng received the master's degree in physical electronics from the Institute of Electrics, Chinese Academy of Sciences, Beijing, China, in 2012. He is currently with the Beijing Institute of Radio Metrology and Measurement, Beijing. His research interests mainly include electromagnetic field and microwave technology.

Yongjiu Zhao received the M.Eng. and Ph.D. degrees in electronic engineering from Xidian University, Xi'an, China, in 1990 and 1998, respectively. Since March 1990, he has been with the Department of Mechano-Electronic Engineering, Xidian University, where he was a professor in 2004. From December 1999 to August 2000, he was a Research Associate with the Department of Electronic Engineering, The Chinese University of Hong Kong. His research interests include antenna design, microwave filter design, and electromagnetic theory.

Qian Xu received the B.Eng. and M.Eng. degrees in electrical engineering and electronics from the Department of Electronics and Information, Northwestern Polytechnical University, Xi'an, China, in 2007 and 2010, and the Ph.D. degree in electrical engineering from the University of Liverpool, UK, in 2016. He was as an RF engineer in Nanjing, in 2011, an Application Engineer with CST Company, Shanghai, in 2012. He is currently an Associate Professor with the College of Electronic and Information Engineering, Nanjing University of Aeronautics and Astronautics, Nanjing. His work at University of Liverpool was sponsored by Rainford EMC Systems Ltd (now part of Microwave Vision Group) and Centre for Global Eco-Innovation. He has designed many chambers for the industry and has authored the book *Anechoic and Reverberation Chambers: Theory, Design, and Measurements* (Wiley-IEEE, 2019). His research interests include statistical electromagnetics, reverberation chamber, EMC, and over-the-air testing.

Design and Experimental Validation of a Compact 10 dB Microstrip Directional Coupler for 2.4 GHz Applications

Mehmet O. Kok[1], Fatih Kaburcuk[2], and Atef Z. Elsherbeni[3]

[1]Department of Electrical and Electronics Engineering
Nevsehir Haci Bektas Veli University, Nevsehir 50300, Turkey
onurkok@nevsehir.edu.tr

[2]Department of Electrical and Electronic Engineering
Sivas University of Science and Technology, Sivas 58000, Turkey
fkaburcuk@sivas.edu.tr

[3]Department of Electrical Engineering
Colorado School of Mines, Golden 80401, USA
aelsherb@mines.edu

Abstract – This paper presents the design, simulation, fabrication, and measurement of a compact 10 dB microstrip directional coupler operating at 2.4 GHz and fabricated on a cost-effective FR-4 substrate. The design process integrates analytical even-odd mode impedance synthesis, circuit-level simulation using ADS LineCalc, and full-wave electromagnetic (EM) optimization to control coupling, isolation, and insertion loss with high fidelity. The measured coupling factor was -10.3 dB at 2.4 GHz, with isolation exceeding 18 dB and insertion loss below -0.65 dB. The simulation-to-measurement deviation was only 0.4 dB, indicating strong design-to-fabrication correlation. A reflection coefficient less than -20 dB confirms excellent impedance matching, while the single-layer, compact layout enables easy integration into wireless front ends, antenna feeding networks, and RF measurement systems. Compared with similar FR-4 based couplers in the literature, this proposed design achieves competitive electrical performance and demonstrates better simulation–measurement deviation, without requiring premium substrates, multilayer fabrication, or lumped-element compensation.

Index Terms – Coupling factor, directional coupler, wireless communications.

I. INTRODUCTION

Directional couplers are essential passive components in radio-frequency (RF) and microwave engineering, extensively used for monitoring signal power, sampling, and power distribution in wireless communication systems, radar front ends, and measurement instrumentation [1–3]. These devices enable signal tapping without significant disturbance to the main transmission path, supporting critical functionalities such as antenna feeding, signal routing, and power measurement. Among the numerous directional coupler implementations, microstrip-based designs have gathered significant attention due to their inherently low fabrication cost, planar geometry, and compatibility with standard printed circuit board (PCB) manufacturing processes. This planar form factor also facilitates straightforward integration with other RF front-end components, making microstrip couplers particularly attractive for compact and mass-producible systems. Despite these advantages, microstrip directional couplers inherently face several design challenges that impact their performance metrics such as coupling accuracy, isolation, bandwidth, and reflection coefficient. A fundamental issue lies in the phase velocity mismatch between the even and odd propagation modes of the coupled microstrip lines, which degrades the directivity and isolation of the device [4]. This mode imbalance limits the operational bandwidth and reduces the overall signal fidelity. Additional design complexities arise from the sensitivity of microstrip lines to fabrication tolerances and variations in substrate properties. These factors lead to performance discrepancies between simulated models and fabricated devices, particularly when low-cost substrates such as FR-4 are used.

FR-4 substrates, while widely used due to their affordability and ease of processing, present unique challenges for microwave applications. Their relatively high dielectric loss tangent introduces insertion losses that can compromise signal integrity, and the frequency-dependent dielectric constant introduces dispersion effects that affect phase velocity and impedance

Submitted On: October 22, 2025
Accepted On: January 05, 2026

https://doi.org/10.13052/2025.ACES.J.401207

matching. Additionally, batch-to-batch variations in FR-4 material properties and inconsistent manufacturing processes further exacerbate performance variability, making accurate prediction and repeatability of directional coupler behavior difficult [5, 6].

Over the past two decades, significant research efforts have pursued to overcome these limitations through innovative design methodologies and novel structural configurations. Phase velocity equalization techniques such as the incorporation of epsilon-negative (ENG) transmission lines [7], fragment-type compensation to balance even/odd modes and raise directivity [8], compact, broadband layouts aimed at high-power handling [9], small-footprint couplers that preserve high directivity [10], application-driven prototypes validated for satellite links [11], and shunt-inductor loading that equalizes phase velocities for systematic directivity enhancement [12]. Other approaches include lumped-element backward couplers [13], tight-coupling fragment-type variants [14], and capacitive compensation using matching networks for wider-bandwidth control [15]. Broader contexts span on-chip lumped couplers [16], asymmetric 2.4 GHz electrical-balance designs [17], and stripline implementations optimized for integration [18]. Additional innovations include calibration techniques enabling accurate incident-power readout in instrumentation [19] and impedance-transforming, high-directivity microstrip couplers [20]. Foundational perspectives derived from composite right/left-handed (CRLH) coupled lines [21] and overlay full-wave analyses [22], together with recent compact broadband branch-line and ultra-compact microstrip realizations [23, 24], define the trade space among bandwidth, directivity, size, and fabrication complexity.

This paper addresses these challenges by presenting a compact, fabrication-tolerant 10 dB microstrip directional coupler operating at 2.4 GHz, implemented entirely on a cost-effective FR-4 substrate. The design methodology integrates a structured computational workflow that combines analytical even–odd mode impedance synthesis, physical dimension extraction via Keysight ADS LineCalc, circuit-level schematic optimization, and full-wave electromagnetic (EM) simulation incorporating realistic fabrication constraints such as conductor thickness, substrate losses, and bending discontinuities. The coupler prototype was fabricated using an LPKF PCB milling machine, with SubMiniature version A (SMA) connectors soldered for measurement purposes. To ensure measurement reliability, all scattering parameter (S-parameter) measurements were performed on a calibrated vector network analyzer using a full two-port SOLT (short–open–load–thru) calibration at the end of the coaxial cables. The measurement uncertainty was estimated to be within ± 0.05 dB for magnitude and $\pm 0.5^\circ$ for phase, based on repeat measurements of the same device under identical test conditions. The measured device exhibits a coupling factor of -10.3 dB and high isolation, closely matching simulation results with a deviation below 0.4 dB, confirming the robustness of the design approach. The compact footprint and low-cost implementation make this design highly suitable for integration in wireless communication front ends, antenna feeding networks, and RF measurement instrumentation.

The proposed 10 dB microstrip directional coupler achieves a simulation–measurement coupling deviation of only 0.4 dB at 2.4 GHz, which is among the lowest reported for FR-4-based designs in the 2–3 GHz range. To substantiate this claim, a systematic literature survey was conducted covering publications from 2010 to 2024 and including only designs fabricated on FR-4 substrates that reported measured S-parameters and a clearly defined operating bandwidth. Designs using alternative substrates, lacking measurement data, or omitting bandwidth specifications were excluded to ensure comparability. Table 1 presents the published results, listing coupling deviation, isolation, reflection coefficient, and bandwidth for each comparable design. While directivity was not directly measured in this work, the measured isolation of 18 dB at the center frequency serves as the primary high-port-separation metric, with further justification provided in section IV. This expanded comparison demonstrates that the proposed coupler combines excellent coupling accuracy with acceptable isolation for WLAN and ISM-band applications, while maintaining a cost-effective single-layer FR-4 implementation that makes it practical for integration into low-cost RF front-end and measurement systems.

II. DESIGN METHODOLOGY

The multi-step design approach combines analytical calculations, circuit simulation, and full-wave EM modeling. This process provides a robust framework for realizing microstrip directional couplers with high fidelity between simulation and practical measurement. The resulting device dimensions are optimized for manufacturability and performance on cost-effective substrates.

A. Coupled-line theory and even-odd mode analysis

The directional coupler design is based on coupled microstrip line theory, where two parallel microstrip transmission lines exhibit EM coupling that excites two distinct propagation modes: even and odd. These modes are characterized by different characteristic impedances, denoted as the even-mode impedance (Z_{0e}) and odd-mode impedance (Z_{0o}). The coupling coefficient (C), expressed in decibels (dB), is defined as:

$$\boldsymbol{C_{\{dB\}} = 20\, log_{\{10\}} k}, \tag{1}$$

where k is the voltage coupling coefficient. For a symmetric directional coupler referenced to $Z_0 = 50\ \Omega$, the even- and odd-mode impedances satisfy the standard relations in (2) and (3). These relations are derived from quasi-static coupled-line analysis and are well established in [25, 26]:

$$\sqrt{\{Z_{\{0e\}} \cdot Z_{\{0o\}}\}} = Z_{\{0\}}, \tag{2}$$

$$\frac{Z_{0e}}{Z_{0o}} = \frac{(1+k)}{(1-k)}. \tag{3}$$

Equation (1) assumes lossless, quasi-TEM propagation, which is a valid approximation for microstrip lines at low microwave frequencies. The coupling level is directly linked to the difference between Z_{0e} and Z_{0o}, where larger separation between these impedances yields stronger coupling. For this work, a 10 dB coupling level was targeted at 2.4 GHz, corresponding to the ISM band. To satisfy both the coupling requirement and the matching condition in a 50-Ω system, the selected values were $Z_{0e} = 69.37\ \Omega$ and $Z_{0o} = 36.04\ \Omega$. These impedances form the theoretical foundation of the design and serve as the input for physical dimension extraction of the coupled microstrip lines. The choice of substrate material plays a principal role in determining both electrical performance and fabrication cost. Here, a widely available FR-4 laminate was employed, characterized by a relative dielectric constant (ε_r) of 4.4 and a thickness of 60 mils (1.524 mm). Although FR-4 exhibits relatively higher dielectric loss and greater material variability than specialized microwave laminates, its low cost, broad availability, and compatibility with standard PCB fabrication processes make it an appealing choice for many practical RF applications. Accurate knowledge of substrate parameters is critical, as they directly affect the guided wavelength, characteristic impedances, and coupling behavior of the coupled lines. Consequently, substrate properties serve as essential inputs for EM simulation and impedance-to-dimension conversion tools, ensuring that the designed structure achieves the intended specifications when fabricated.

B. Microstrip geometry calculation using ADS LineCalc

The transformation from the target even- and odd-mode impedances to the physical dimensions of the coupled microstrip lines requires precise EM modeling that accounts for substrate permittivity, thickness, and conductor geometry. For the present design, the required impedances were $Z_{0e} = 69.37\ \Omega$ and $Z_{0o} = 36.04\ \Omega$, as derived in section A. These values were selected because they simultaneously achieve the target 10 dB coupling coefficient and satisfy the impedance balance condition for a 50-Ω system, ensuring both proper coupling and port matching.

Using these impedance targets and the specified FR-4 substrate parameters ($\varepsilon_r = 4.4$, thickness = 60 mils), Keysight ADS LineCalc was employed to compute the initial physical dimensions of the coupled microstrip lines. The tool applies quasi-static closed-form equations tailored for coupled microstrip structures, enabling rapid and accurate estimation of conductor width (W) and spacing (S). The calculated dimensions were $W = 1.82$ mm and $S = 1.20$ mm.

To ensure robustness of the initial design, these values were cross-validated against classical analytical expressions from the microstrip design literature [1]. This verification confirmed strong consistency between LineCalc outputs and established theoretical models, providing confidence in proceeding to schematic-level simulations and full-wave EM optimization.

C. Initial schematic modeling in ADS

Using the calculated physical dimensions, a circuit-level schematic model was developed in Keysight ADS. The coupled-line sections were represented by Microstrip Coupled Lines (MCLIN) elements, which accurately emulate the transmission line behavior based on the specified conductor width (W), spacing (S), and electrical length (L).

Figure 1 shows the circuit schematic of the proposed design. This schematic abstraction enabled rapid evaluation of key performance parameters such as coupling magnitude, port-to-port isolation, reflection coefficients (S_{11}), and phase difference between the coupled output ports. Iterative simulations were performed to fine-tune L of the coupled sections, aiming to achieve an electrical length close to a quarter wavelength at the center frequency of 2.4 GHz. This tuning was critical to optimize the coupling level and ensure proper phase relationships required for the directional coupler to meet its design objectives.

D. Full-wave EM simulations

Full-wave EM simulations were conducted in Keysight ADS Momentum to capture physical effects that cannot be resolved through circuit-level analysis. In ADS Momentum, the microstrip lines and substrate are modeled using a Method of Moments (MoM) solver. The solver employs an open-region Green's function

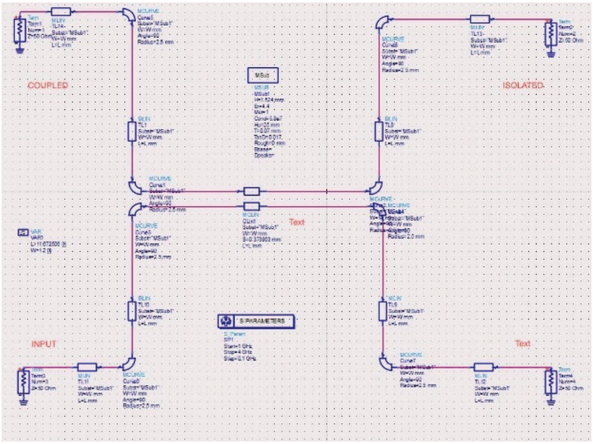

Fig. 1. Circuit schematic of the proposed design.

that inherently represents free space, eliminating the need for additional radiation boundary conditions. This approach minimizes unwanted reflections and enables accurate characterization of microstrip behavior, including fringing-field effects. The simulation frequency range was set to 2–3 GHz to encompass the operating band as well as adjacent frequencies relevant to the optimization process. This range ensured stable coupling behavior and supported reliable interpolation during adaptive meshing. Harmonic balance analysis was not required for this design. The complete physical layout, including all bends, tapers, and transmission-line transitions, was exported directly from the schematic to ADS Momentum so that the exact geometry of the coupler was analyzed. Adaptive mesh refinement was applied around edges, bends, and discontinuities where rapid current variations occur, improving accuracy without altering the layout. The simulation setup also considers losses in both the conductor and dielectric materials, based on FR-4 substrate properties such as dielectric constant, loss tangent, and conductor thickness. The fabrication errors are also considered to check how the directional coupler performs in real conditions. This helps to confirm that the simulation results are in good agreement with measurement results.

E. Optimization and final tuning

To address discrepancies between the initial schematic model and the full-wave EM simulations, mainly arising from parasitic capacitances, inductances, and higher-order effects, an iterative optimization procedure was applied. The coupled-line length was set to approximately one quarter of the guided wavelength at 2.4 GHz on FR-4 and then trimmed slightly in EM simulations (approximately 17.6 mm) to precisely meet the design frequency. The primary optimization focused on W and S since these directly determine the even- and odd-mode impedances and thus the coupling factor. Fine adjustments were made to W and S around the initial LineCalc estimates of 1.82 mm and 1.20 mm, resulting in $W = 1.78$ mm and $S = 1.25$ mm. In addition, supporting geometrical features were optimized, including the 50-Ω feed-line width, linear taper transitions between feeds and coupled lines, and SMA launch pad dimensions. With these refinements, the optimized design achieved 10 dB coupling at 2.4 GHz, reflection coefficient less than -20 dB, isolation less than -18 dB, and insertion loss approximately -0.65 dB. This process ensured that the final coupler maintains both compact size and robust performance when fabricated on a standard FR-4.

In this work, the fractional bandwidth (FBW) is defined as the frequency range over which the coupler maintains its target performance. Specifically, FBW is taken as the span of frequencies where the coupling remains within -10 ± 0.5 dB, the reflection coefficient is less than -15 dB, and the isolation exceeds -15 dB.

III. SIMULATION AND MEASUREMENT RESULTS

This section provides a comprehensive comparison between the simulated and measured performance of the proposed microstrip directional coupler. The design was rigorously evaluated through both schematic-level circuit simulations and full-wave EM modeling, capturing idealized and realistic EM behaviors respectively. The layout of the proposed design is shown in Fig. 2, and the fabricated prototype is presented in Fig. 3. The prototype was fabricated by PCB milling, equipped with SMA connectors, and characterized by using a calibrated vector network analyzer over the 2–3 GHz range to validate the design and simulation methodology. Measurements employed a two-port SOLT calibration with the reference plane set at the SMA pin interface. All unused ports were terminated with broadband 50 Ω loads.

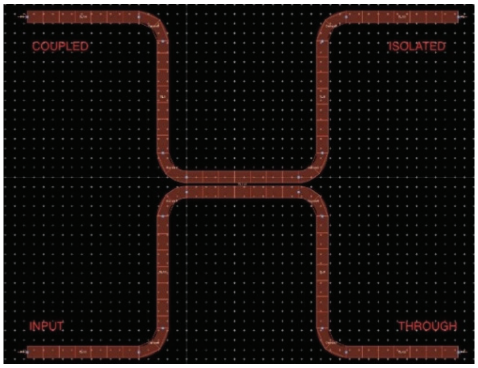

Fig. 2. Layout of the proposed design.

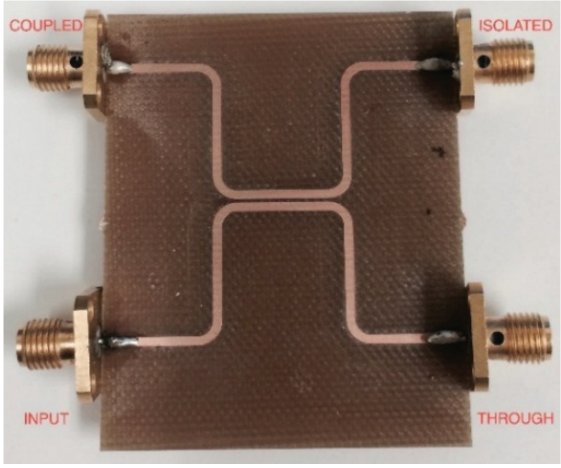

Fig. 3. Fabricated prototype of the proposed directional coupler.

The comparison focuses on critical S-parameters, including reflection coefficient (S_{11}), insertion loss (S_{21}), coupling (S_{31}), and isolation (S_{41}) analyzed at the center frequency of 2.4 GHz as well as across the operational bandwidth. The detailed evaluation highlights the close agreement between simulations and measurements, demonstrating the effectiveness of the design process and the suitability of the proposed coupler for practical RF applications.

A. Coupling response (S_{31})

The coupling factor at the design frequency of 2.4 GHz is a key performance parameter for the proposed 10 dB directional coupler. As illustrated in the circuit-level schematic results presented in Fig. 4, a coupling value of -10 dB is precisely achieved, matching the design target. Full-wave EM simulations, shown in Fig. 5, revealed a slight deviation, yielding -10.2 dB at 2.4 GHz. This shift is attributed to realistic EM effects, such as parasitic capacitance and fringe-field interactions. Measurement results from the fabricated prototype, presented in Fig. 6, indicated a coupling of -10.3 dB at the center frequency, with only a 0.1 dB difference from the EM simulation, demonstrating close agreement between simulation and measurement and confirming the robustness of the design approach.

B. Isolation performance (S_{41})

Isolation at the 2.4 GHz design frequency demonstrated robust performance across all design stages. As shown in the circuit-schematic simulation results (Fig. 4), the predicted isolation exceeded -15 dB, indicating effective suppression of unwanted coupling between the isolated ports. Full-wave EM simulations in Fig. 5 revealed a slight reduction, reflecting the more realistic modeling of parasitic coupling and substrate effects. Measurements of the fabricated prototype in Fig. 6 confirmed an isolation of -18 dB at 2.4 GHz. The reduction relative to the simulations is primarily attributed to fabrication tolerances, connector mismatches, and the inherent material-property variations of FR-4. While some FR-4 designs in the literature report higher isolation, they often achieve this at the expense of larger footprints or multi-layer complexity. Directivity was not measured; therefore, isolation is presented as the primary indicator of high-port separation. Because the reflection coefficient exceeds -20 dB at the center frequency, the measured isolation serves as an indication of expected directivity under these conditions. Overall, the achieved isolation is sufficient for typical WLAN and ISM-band applications.

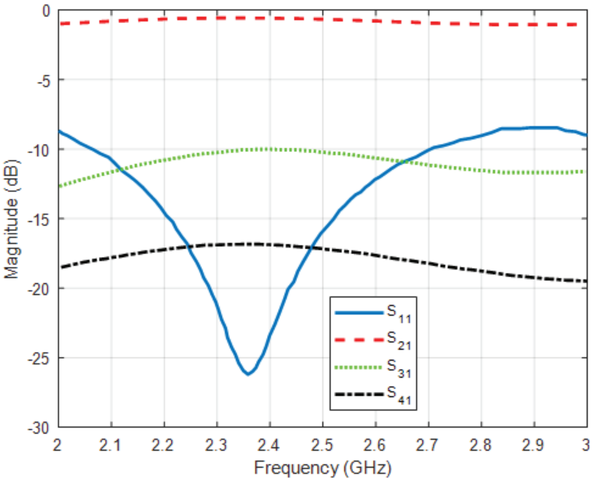

Fig. 4. Circuit simulation results of the proposed design.

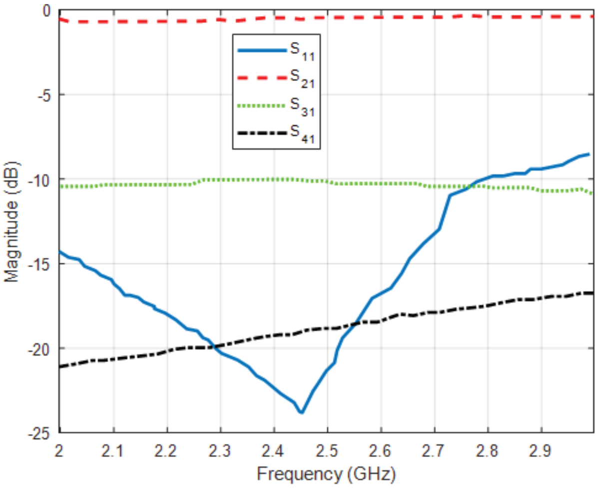

Fig. 5. EM simulation results of the proposed design.

Table 1: Comparison of -10 dB directional couplers fabricated on FR-4 substrates

Ref.	f0 (GHz)	S_{11} (dB)	S_{21} (dB)	S_{31} (dB)	S_{41} (dB)	FBW (%)	Δ (dB)	Size (cm)
[3]	2.45	−15	−0.6	−10	−18	11	N/A	∼35×25
[4]	2.40	−18	−0.8	−10	−20	∼15	N/A	∼30×20
[6]	2.40	−16	−0.7	−10	−19	13	∼0.7	∼40×25
[9]	2.45	−17	−0.7	−10	−21	10	∼0.4	∼28×22
[10]	2.40	−18	−0.9	−10	−20	12	∼0.6	∼25×18
[12]	2.40	−15	−0.9	−10	−22	∼14	∼0.8	∼38×20
[13]	2.40	16	−1.0	−10	−19	∼12	∼1.0	∼20×15
This Work	**2.40**	**>–20**	**–0.65**	**–10**	**–18**	**13**	**0.4**	**∼17×15**

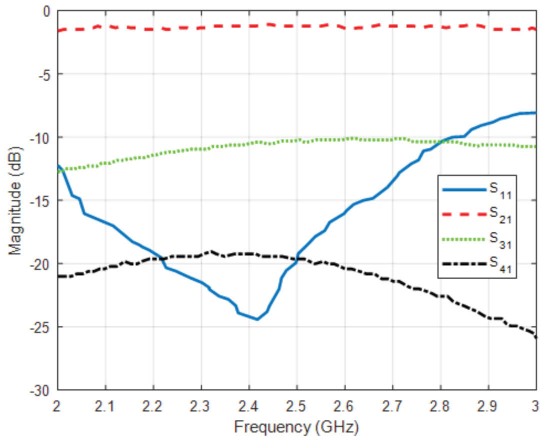

Fig. 6. Measured results of the proposed design.

C. Insertion loss (S_{21}) and reflection coefficient (S_{11})

Through-port insertion loss was consistently predicted to be approximately −0.57 dB in both the schematic simulations shown in Fig. 4 and the full-wave EM simulations shown in Fig. 5, indicating effective minimization of conductor and dielectric losses despite the relatively lossy FR-4 substrate. In Fig. 6, measurements of the fabricated prototype show a slightly higher insertion loss of −0.65 dB at 2.4 GHz, an increase of only 0.08 dB compared with the simulations. This minor increase is attributed to additional loss mechanisms, including connector mismatches, soldering imperfections, and small fabrication-induced variations. The reflection coefficient demonstrates strong impedance matching throughout the design process. Measurements confirm this performance, showing reflection coefficient less than −20 dB at the center frequency, indicating excellent input port matching and minimal signal reflection critical for efficient power transfer and low system noise. Based on the FBW definition, the measured FBW of the fabricated prototype is 2.33–2.64 GHz, which corresponds to approximately 13%.

Table 1 compares reported −10 dB directional couplers operating at 2.4 and 2.45 GHz on FR-4 substrates, compiled from the systematic literature survey presented in section I. The proposed design is placed alongside established works to highlight relative strengths and limitations. Earlier contributions [3, 4, 6] demonstrated isolation levels of 18–20 dB with insertion losses of approximately 0.6–0.8 dB, whereas [9, 10] achieved improved isolation of 20–21 dB but required more elaborate geometries. Other approaches, including shunt-inductor loading [12] and lumped-element compensation [13], provided enhanced bandwidth and directivity, albeit with increased design complexity and greater sensitivity to fabrication tolerances. In comparison, the proposed coupler provides a balanced performance, achieving 18 dB isolation and a low insertion loss of −0.65 dB within a straightforward single-layer layout. To the best of the authors' knowledge, among FR-4 couplers operating at around 2.4 GHz, the design exhibits the smallest reported simulation-to-measurement deviation ($\Delta =$ 0.4 dB), demonstrating strong fabrication tolerance. In addition, its compact core footprint of approximately 17 × 15 cm is smaller than many comparable designs. These results indicate that the proposed coupler not only delivers competitive performance but also satisfies practical requirements for cost-effectiveness and ease of fabrication, making it a strong candidate for WLAN and ISM-band.

IV. CONCLUSION

This study shows that low-cost FR-4 substrates can deliver performance close to that of premium laminates when accurate electromagnetic modeling is combined with fabrication-aware optimization. A compact −10 dB microstrip directional coupler at 2.4 GHz was designed, simulated, fabricated, and measured using a systematic workflow that included even–odd mode synthesis, circuit-level tuning, and full-wave EM analysis. The measured coupling differed by only 0.4 dB from simulation, confirming high dimensional accuracy and robustness against fabrication and substrate effects. The prototype achieved −18 dB isolation, reflection coefficient less than −20 dB, and insertion loss of −0.65 dB at the center frequency, with quadrature phase balance and a fractional bandwidth of 2.33–2.64 GHz (∼13%).

With its compact size, the design compares well with similar FR-4 couplers, offering strong performance in a simple single-layer layout without multilayer construction, expensive substrates, or lumped components.

The proposed methodology can also be applied to other passive microwave circuits where compactness and low cost are important. Future work may focus on improving bandwidth and isolation or adapting the design to other frequency bands, while maintaining the manufacturing simplicity that enables practical use in WLAN and ISM-band front ends, antenna feeding networks, radar systems, and sensors.

REFERENCES

[1] D. M. Pozar, *Microwave Engineering*, 4th ed. Hoboken, NJ: Wiley, 2012.

[2] R. E. Collin, *Foundations for Microwave Engineering*, 2nd ed. New York, NY: Wiley–IEEE Press, 2001.

[3] V. Solomko, B. Tanc, D. Kehrer, N. Ilkov, W. Bakalski, and W. Simbürger, "Tunable directional coupler for RF front-end applications," *Electron. Lett.*, vol. 51, no. 24, pp. 2012–2014, Nov. 2015.

[4] S. T. Imeci and K. Temur, "Center-slotted wideband hybrid 10-dB coupler," *J. Eng. Res.*, vol. 11, no. 1A, pp. 285–296, 2023.

[5] H. Zhu and A. M. Abbosh, "Directional coupler with two octaves band and high directivity using stepped-impedance coupled structure," in *2015 Asia-Pacific Microwave Conference* (*APMC*), Nanjing, China, pp. 1–3, 2015.

[6] S. Gruszczyński, K. Wincza, and K. Sachse, "Design of compensated coupled-stripline 3-dB directional couplers, phase shifters, and Magic-T's—Part II: Broadband coupled-line circuits," *IEEE Trans. Microw. Theory Techn.*, vol. 54, no. 9, pp. 3501–3507, Sep. 2006.

[7] I. Piekarz, J. Sorocki, K. Wincza, S. Gruszczyński, J. Müller, and T. Welker, "Miniaturized quasi-lumped coupled-line single-section directional coupler designed in multilayer LTCC technology," *Microw. Opt. Technol. Lett.*, vol. 55, no. 6, pp. 1401–1405, 2013.

[8] L. Wang, G. Wang, and J. Sidén, "Design of high-directivity wideband microstrip directional coupler with fragment-type structure," *IEEE Trans. Microw. Theory Techn.*, vol. 63, no. 12, pp. 3962–3970, Dec. 2015.

[9] Z.-B. Wang, X. Wei, H.-P. Fang, H.-M. Zhang, and Y.-R. Zhang, "A compact and broadband directional coupler for high-power radio-frequency applications," *IEEE Microw. Wireless Compon. Lett.*, vol. 30, no. 2, pp. 164–166, Feb. 2020.

[10] Y. Zhu, J. Zhang, H. Zhu, J. Cheng, and J. Li, "Compact microstrip line directional coupler with high directivity," *J. Electromagn. Waves Appl.*, vol. 26, no. 11–12, pp. 1619–1623, 2012.

[11] F. M. Z. Mahmood, "Design and implementation of microstrip directional coupler for satellite communication application," in *Proc. 4th Int. Conf. Commun. Eng. Comput. Sci.* (*CIC-COCOS'22*), Erbil, Iraq, pp. 144–150, Mar. 2022.

[12] S. Lee and Y. Lee, "A design method for microstrip directional couplers loaded with shunt inductors for directivity enhancement," *IEEE Trans. Microw. Theory Techn.*, vol. 58, no. 4, pp. 994–1002, Apr. 2010.

[13] T.-Y. Song, J.-H. Kim, S.-H. Kim, J.-S. Park, and J.-B. Lim, "Design of a novel lumped-element backward directional coupler based on parallel coupled-line theory," in *IEEE MTT-S Int. Microw. Symp. Dig.*, vol. 1, pp. 213–216, 2002.

[14] L. Wang, G. Wang, and J. Sidén, "High-performance tight coupling microstrip directional coupler with fragment-type compensated structure," *IET Microw. Antennas Propag.*, vol. 11, no. 7, pp. 1057–1063, 2017.

[15] R. Torres-Quispe and E. J. Zenteno-Bolaños, "Broadband microstrip directional coupler using capacitive compensation and matching networks," in *Proc. 2022 IEEE XXIX Int. Conf. Electronics* (*INTERCON*), Lima, Peru, pp. 1–3, Aug. 2022.

[16] N.-T. Doan and S.-W. Yoon, "Vertically symmetric broadband lumped element CMOS directional coupler," *Electron. Lett.*, vol. 54, no. 24, pp. 1372–1373, Nov. 2018.

[17] A. Kumar, S. Aniruddhan, and R. K. Ganti, "An asymmetric 2.4-GHz directional coupler using electrical balance," *IEEE Microw. Wireless Compon. Lett.*, vol. 26, no. 12, pp. 990–992, Dec. 2016.

[18] Z. Li, T. Han, L. Tian, X. Yu, and P. Chen, "Design of a compact wideband easy-to-integrate stripline directional coupler," in *Proc. 2022 Int. Conf. Microwave and Millimeter Wave Technology* (*ICMMT*), Nanjing, China, pp. 1–3, Aug. 2022.

[19] F. L. Peñaranda-Foix, J. M. Catalá-Civera, J. D. Gutiérrez-Cano, and B. García-Baños, "Directional coupler calibration for accurate online incident power measurements," *IEEE Microw. Wireless Compon. Lett.*, vol. 31, no. 6, pp. 624–627, June 2021.

[20] A. Gołaszewski, M. S. Żukociński, and A. Abramowicz, "High directivity microstrip couplers for impedance transforming," in *Proc. SPIE, vol. 11176, Photonics Applications in Astronomy, Communications, Industry, and High-Energy Physics Experiments 2019*, art. 111765X, Nov. 2019.

[21] C. Caloz, A. Sanada, and T. Itoh, "A novel composite right/left-handed coupled-line directional coupler with arbitrary coupling level and broad bandwidth," *IEEE Trans. Microw. Theory Techn.*, vol. 52, no. 3, pp. 980–992, Mar. 2004.

[22] L. Su, T. Itoh, and J. Rivera, “Design of an overlay directional coupler by a full-wave analysis,” *IEEE Trans. Microw. Theory Techn.*, vol. 31, no. 12, pp. 1017–1022, Dec. 1983.

[23] F. H. Ahmed, R. Saad, and S. K. Khamas, “A novel compact broadband quasi-twisted branch line coupler based on a double-layered microstrip line,” *Micromachines*, vol. 15, no. 1, art. 142, Jan. 2024.

[24] S. I. Yahya, F. Zubir, L. Nouri, A. Rezaei, and N. Md Jizat, “A novel ultra-compact microstrip coupler with low imbalance magnitudes and phases for wireless networks,” *IEEE Access*, vol. 12, pp. 99949–99956, 2024.

[25] A. Z. Elsherbeni, V. Rodriguez-Pereyra, and C. E. Smith, “The effect of an air gap on the coupling between two planar microstrip lines,” *Journal of The Franklin Institute*, vol. 333(B), no. 2, pp. 201–223, 1996.

[26] A. Z. Elsherbeni, C. E. Smith, H. Golestanian, and S. He, “Quasi-static characteristics of a two-conductor multilayer microstrip transmission line with dielectric overlay and a notch between the strips,” *J. Electromagnetic Waves and Applications* (*JEWA*), vol. 7, no. 6, pp. 769–789, 1993.

Mehmet O. Kok received M.Sc. and Ph.D. degrees in Electrical Engineering from Syracuse University, Syracuse, NY, USA, in 2012 and 2020, respectively. From 2015 to 2016, he was with Anaren Microwave, Inc., Syracuse, NY, as an RF Engineer. He served as an Electrical Engineer with PPC-Belden, Inc., Syracuse, NY, from 2017 to 2018, and as an RF Engineer with TTM Technologies, Syracuse, NY, from 2018 to 2020. He is currently working at the Department of Electrical and Electronics Engineering at Nevsehir Haci Bektas Veli University, Nevsehir, Turkey. His research interests include electromagnetics, wireless communications, and RF/microwave design.

Fatih Kaburcuk received M.Sc. and Ph.D. degrees in electrical engineering from Syracuse University, Syracuse, NY, USA, in 2011 and 2014, respectively. During his graduate studies, he was a Research Assistant with Syracuse University and PPC-Belden Inc., Liverpool, NY. In 2014, he was a Visiting Research Scholar with the Department of Electrical Engineering, Colorado School of Mines, Golden, CO. He joined Erzurum Technical University in 2015 and Sivas Cumhuriyet University in 2019. He was promoted to Associate Professor in 2020 and to Professor in 2025. In August 2024, he joined the Department of Electrical and Electronics Engineering, Sivas University of Science and Technology, Sivas, Turkiye, where he currently serves as Head of Department. Kaburcuk is an Associate Editor of *Applied Computational Electromagnetics Society (ACES) Journal*. His research interests include numerical methods in electromagnetics, biological effects of electromagnetic radiation, and finite-difference time-domain analysis of antennas and RF devices.

Atef Z. Elsherbeni received two honors B.Sc. degrees in Electronics and Communications, in Applied Physics, and M.Eng. degree in Electrical Engineering, all from Cairo University, Egypt, in 1976, 1979, and 1982, respectively, and a Ph.D. degree in Electrical Engineering from Manitoba University, Winnipeg, Manitoba, Canada, in 1987. He started his engineering career as a part time Software and System Design Engineer from March 1980 to December 1982 at the Automated Data System Center, Cairo, Egypt. Elsherbeni joined the faculty at the University of Mississippi in 1987 as an Assistant Professor of Electrical Engineering. He advanced to the ranks of Associate Professor and Professor in 1991 and 1997, respectively, and became Associate Dean for Research and Graduate Programs from 2009 to 2013. He joined the EECS Department at Colorado School of Mines in August 2013 as Dobelman Distinguished Professor. He was appointed Interim Department Head for EECS from 2015 to 2016 and became EE Department Head from 2016 to 2018. He spent a sabbatical term in 1996 at the EE Department, University of California at Los Angeles (UCLA) and was a visiting Professor at Magdeburg University in Germany and Tampere University of Technology in Finland during the summers of 2005 and 2007, respectively. In 2009, he was selected as Finland Distinguished Professor by the Academy of Finland and TEKES. Elsherbeni is Editor-in-Chief for *Applied Computational Electromagnetics Society (ACES) Journal*, a past Associate Editor for *Radio Science*, a past Chair of the Engineering and Physics Division of Mississippi Academy of Science, a past Chair of Educational Activity Committee for IEEE Region 3 Section, and general Chair for the 2014 APS-URSI Symposium, president of ACES from 2013 to 2015, and IEEE Antennas and Propagation Society (APS) Distinguished Lecturer for 2020–2023. Elsherbeni is a Fellow member of IEEE and ACES. He is a recipient of the 2023 IEEE APS Harington-Mittra Award for his contribution to computational electromagnetics with hardware acceleration and recipient of the 2025 Computational Electromagnetics Award from ACES.

Calculation of Bending Effects on the Lumped Inductance for Cables Using the Line Current Model

Xiao Chen[1], Haicheng Yin[2], Gang Zhang[1], Francesco de Paulis[3], and Xin He[4]

[1]School of Electrical Engineering and Automation
Harbin Institute of Technology, Harbin, HL 150001, China
chenxiaoshawn@foxmail.com, zhang_hit@hit.edu.cn

[2]No. 23 Research Institute of CETC Shanghai, SH 201900, China
gloriachild@126.com

[3]UAq Electromagnetic Compatibility Lab
University of L'Aquila, L'Aquila, Abruzzi 67100, Italy
francesco.depaulis@univaq.it

[4]Department of Mechanical Engineering and Automation
Harbin Institute of Technology, Shenzhen, GZ 518000, China
21B953013@stu.hit.edu.cn

Abstract – This paper presents a semi-analytical method to calculate the bending effects on cable inductance at low frequencies using the line current model (LCM). To deal with the divergent items of the self-inductance obtained by the LCM, some cautious treatments are adopted to counteract the divergent terms between the straightened LCM and bent LCM, leading to a semi-analytical formula for the inductance deviation of the parallel-pair cable. The LCM is then applied to the coaxial cable in collaboration with the decomposition of the conductors, to take into account the mutual inductance among the portions of each conductor. The results of the proposed semi-analytical method are compared with those obtained by the finite element method (FEM), which validates the accuracy of the method. Furthermore, the dependence of the inductance deviation on cable parameters is illuminated for reference of realistic inductance determination.

Index Terms – Cable inductance, line current model, partial inductance, semi-analytical method.

I. INTRODUCTION

The measurement method for coaxial cable inductance at low frequencies has been defined in a standard [1], where a cable sample longer than 10 m is required to be straightened for the accurate inductance measurement result. However, there is generally no adequate space to place a straightened cable with a length over 10 m in a laboratory, impairing the practical applicability of the standard. Therefore, if the deviations of cable inductance between the straight layout and bending layouts are determined, the inductance in a straight layout may be obtained through modification of that measured in a bending case where modest space is expected.

Despite closed-form formulas for the inductance in some ideal cases [2–4], the calculation of inductance for conductors characterized by complicated cross-sections and arbitrary shapes relies on numerical methods [5, 6]. Moreover, specific methods with the simplification of conductor shapes, such as the surface current model (SCM) and line current model (LCM), can be used to obtain analytical or analytical-numerical results for some less complicated cases like coils. SCM is used to handle the circular cross-section for an arbitrary-shaped coil, to reduce the complexity of the subsequent finite element method (FEM) for the calculation of the inductance [7]. The mutual inductance of circular and elliptic coils is analytically deduced in the LCM, resulting in expressions involving Bessel and Struve functions [8]. There has been yet no research that exploits the LCM for the calculation of the selfinductance, because the corresponding integral does not converge.

In this paper, the LCM is adopted to deduce the cable inductance, where both the self and mutual inductances of the conductors are necessary. The divergent self-inductance integral is specially treated such that the deviation of the cable inductance between the straightened and bent layouts can be calculated. The LCM is directly applied to the parallel-pair cable, generating an

Submitted On: April 21, 2025
Accepted On: December 12, 2025

1054-4887 © ACES

https://doi.org/10.13052/2025.ACES.J.401208

accurate and efficient semi-analytical formula for the inductance deviation, which is then utilized to acquire the inductance deviation of the coaxial cable precisely by decomposing into several parallel-pairs.

II. BASIC FORMULATION OF CABLE INDUCTANCE

When the lumped inductance of a cable is measured at low frequencies below 10 kHz, the cable is assumed to be configured as Fig. 1, where one end of the cable is connected to an LCR meter and the other end is shorted. The lumped impedance of the cable can be depicted as shown in Fig. 2, where R_1 and R_2 are the resistances of the two conductors, L_1 and L_2 are the partial self-inductances of the conductors, and M_{12} is the mutual inductance between the conductors. The impedance of the shorting wire and the capacitance between the conductors of the cable are neglected.

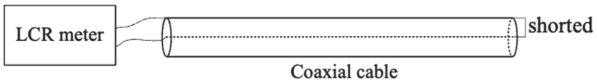

Fig. 1. Configuration for inductance measurement of the cable.

The (lumped) inductance L can be expressed as:

$$L = L_1 + L_2 - 2M_{12}. \tag{1}$$

If each conductor has a uniform cross-section and there is no ambient permeability magnetic material, those partial inductances at low frequencies can be calculated by the quasi-static formula as the following integral [9]:

$$L_{mn} = \frac{\mu_0}{4\pi S_m S_n} \int_{l_m} \int_{l_n} \int_{A_m} \int_{A_n} \frac{\vec{t}_m \cdot \vec{t}_n}{r_{mn}} \mathrm{d}A_n \mathrm{d}A_m \mathrm{d}l_n \mathrm{d}l_m, \tag{2}$$

where both m and n belong to $\{1,2\}$; L_{mn} is the partial inductance, and it is noted that $L_{11} = L_1, L_{22} = L_2$, and $L_{12} = L_{21} = M_{12}$; μ_0 is the permeability of vacuum; S_m and S_n are the areas of the conductor cross-sections; l_m and l_n are the one-dimensional integration regions along the axes. A_m and A_n are the two-dimensional integration regions in the cross-sections; $\vec{t}_m$ and $\vec{t}_n$ are the unit tangent vectors of l_m and l_n, respectively; r_{mn} is the distance between the integration cells in the two regions.

The six-fold integral in (2) is sophisticated but extremely hard for analytical solution. Hence, it is approximated that the integral kernel keeps constant in the integration cross-sections, which in fact ignores the cross-section shapes and converts the two conductors into LCMs. Then, the simplified integral reads:

$$L_{mn} \approx \frac{\mu_0}{4\pi} \int_{l_m} \int_{l_n} \frac{\vec{t}_m \cdot \vec{t}_n}{r_{mn}} \mathrm{d}l_n \mathrm{d}l_m. \tag{3}$$

The following section is to solve (3) for the parallel-pair and coaxial cables at the straightened layout and bent layouts, respectively. Consequently, the deviations of the inductance between different layouts are obtained.

III. DEDUCTION OF INDUCTANCE DEVIATION

A. Parallel-pair cable

It is assumed that, for the parallel-pair cable, the conductors have circular cross-sections and both the conductors and the insulation are composed of nonferromagnetic material.

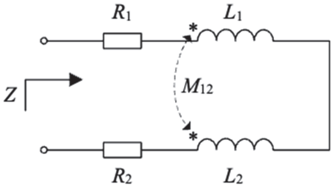

Fig. 2. Schematic diagram of the equivalent circuit for the cable under test.

In regard to a straightened parallel-pair cable with length l and conductor distance d, the LCM in Fig. 3 can be used to calculate partial inductances:

$$L_{11\mathrm{s}} = L_{22\mathrm{s}} = \frac{\mu_0}{4\pi} \int_0^l \int_0^l \frac{1}{|x_2 - x_1|} \mathrm{d}x_2 \mathrm{d}x_1, \tag{4}$$

$$L_{12\mathrm{s}} = L_{21\mathrm{s}} = \frac{\mu_0}{4\pi} \int_0^l \int_0^l \frac{1}{\sqrt{(x_2 - x_1)^2 + d^2}} \mathrm{d}x_2 \mathrm{d}x_1, \tag{5}$$

where $L_{mn\mathrm{s}}$ is the partial inductance for the straightened parallel-pair cable.

The inner integral in (4) includes a divergent improper integral that even does not have a finite Cauchy principal value due to the absolute value operator. However, the integral interval can be separated to constitute possible proper integrals:

$$\begin{aligned} &\int_0^l \frac{\mathrm{d}x_2}{|x_2 - x_1|} \\ &= \int_0^{x_1 - \delta} \frac{\mathrm{d}x_2}{x_1 - x_2} + \int_{x_1 - \delta}^{x_1 + \delta} \frac{\mathrm{d}x_2}{|x_2 - x_1|} + \int_{x_1 + \delta}^{l} \frac{\mathrm{d}x_2}{x_2 - x_1} \\ &= \ln\left(\frac{x_1}{\delta}\right) + \int_{x_1 - \delta}^{x_1 + \delta} \frac{\mathrm{d}x_2}{|x_2 - x_1|} + \ln\left(\frac{l - x_1}{\delta}\right), \end{aligned} \tag{6}$$

where $\delta > 0$ is the half length of the divergent interval and independent with x_1 or x_2.

The divergent second item in (6) is caused by the LCM and would converge if the integration were implemented in a two-dimensional or three-dimensional

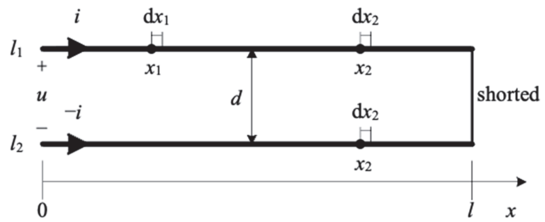

Fig. 3. LCM for the straightened parallel-pair cable.

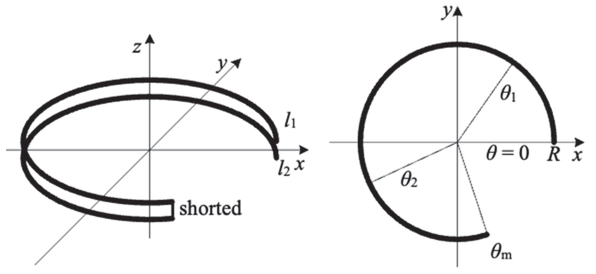

(a) (b)

Fig. 4. LCM for the bent parallel-pair cable: (a) illustrative diagram and (b) top view.

space. By denoting this item as I_0 and implementing the outer integration, $L_{11\mathrm{s}}$ can be expressed as:

$$L_{11\mathrm{s}} = \frac{\mu_0 l}{4\pi}(I_0 + 2\ln l - 2\ln\delta - 2). \tag{7}$$

The solution to (5) is trivial:

$$L_{12\mathrm{s}} = \frac{\mu_0 l}{2\pi}\left[l\ln(l+\sqrt{l^2+d^2}) + d - \sqrt{l^2+d^2} - l\ln d\right]. \tag{8}$$

Then, according to (1), the inductance of a straightened parallel-pair cable is:

$$\begin{aligned} L_\mathrm{s} &= 2L_{11\mathrm{s}} - 2L_{12\mathrm{s}} \\ &= \frac{\mu_0 l}{2\pi}\left[I_0 + 2\ln(ld) + \frac{2\sqrt{l^2+d^2}}{l}\right. \\ &\qquad \left. -2\ln(l+\sqrt{l^2+d^2}) - 2\ln\delta - \frac{2d}{l} - 2\right]. \end{aligned} \tag{9}$$

To investigate the bending effect on the inductance of a parallel-pair cable, an arc-shaped parallel-pair cable in the LCM is constructed as illustrated in Fig. 4. The cable in the same length l and conductor distance d is bent along the track of an arc of radius R and angle $\theta_\mathrm{m} \in (0, 2\pi)$, thus:

$$R = \frac{l}{\theta_\mathrm{m}}. \tag{10}$$

The self and mutual inductances can be calculated by the following integrals:

$$L_{11\mathrm{b}} = L_{22\mathrm{b}} = \frac{\mu_0 R_b}{8\pi}\int_0^{\theta_\mathrm{m}}\int_0^{\theta_\mathrm{m}} \frac{\cos(\theta_2-\theta_1)}{\left|\sin\frac{\theta_2-\theta_1}{2}\right|}\mathrm{d}\theta_2\mathrm{d}\theta_1, \tag{11}$$

$$\begin{aligned} &L_{12\mathrm{b}} = L_{21\mathrm{b}} \\ &\quad = \frac{\mu_0 R^2}{4\pi}\int_0^{\theta_\mathrm{m}}\int_0^{\theta_\mathrm{m}} \frac{\cos(\theta_2-\theta_1)\,\mathrm{d}\theta_2\mathrm{d}\theta_1}{\sqrt{2R^2 - 2R^2\cos(\theta_2-\theta_1) + d^2}}, \end{aligned} \tag{12}$$

where $L_{mn\mathrm{b}}$ is the partial inductance for the bent parallel-pair cable.

The inner integral in (11) can be treated similarly to the straightened case:

$$\int_0^{\theta_\mathrm{m}} \frac{\cos(\theta_2-\theta_1)}{\left|\sin\frac{\theta_2-\theta_1}{2}\right|}\mathrm{d}\theta_2 = K_1 + K_2 + K_3 \tag{13}$$

where:

$$\begin{aligned} K_1 &= \int_0^{\theta_1-\frac{\delta}{R}} \frac{\cos(\theta_2-\theta_1)}{\sin\frac{\theta_1-\theta_2}{2}}\mathrm{d}\theta_2 \\ &= 4\cos\frac{\theta_1}{2} + 2\ln\left(\tan\frac{\theta_1}{4}\right) \\ &\quad -4\cos\frac{\delta}{2R} - 2\ln\left(\tan\frac{\delta}{4R}\right), \end{aligned} \tag{14}$$

$$K_2 = \int_{\theta_1-\frac{\delta}{R}}^{\theta_1+\frac{\delta}{R}} \frac{\cos(\theta_2-\theta_1)}{\left|\sin\frac{\theta_2-\theta_1}{2}\right|}\mathrm{d}\theta_2, \tag{15}$$

and:

$$\begin{aligned} K_3 &= \int_{\theta_1+\frac{\delta}{R}}^{\theta_\mathrm{m}} \frac{\cos(\theta_2-\theta_1)}{\sin\frac{\theta_2-\theta_1}{2}}\mathrm{d}\theta_2 \\ &= 4\cos\frac{\theta_\mathrm{m}-\theta_1}{2} + 2\ln\left(\tan\frac{\theta_\mathrm{m}-\theta_1}{4}\right) \\ &\quad -4\cos\frac{\delta}{2R} - 2\ln\left(\tan\frac{\delta}{4R}\right). \end{aligned} \tag{16}$$

If δ is small enough, $\cos(\theta_2-\theta_1) \approx 1$ and $\sin\frac{\theta_1-\theta_2}{2} \approx \frac{\theta_1-\theta_2}{2}$ for $\theta_2 \in [\theta_1 - \delta/R, \theta_1 + \delta/R]$, converting (15) into:

$$K_2 = \int_{\theta_1-\frac{\delta}{R}}^{\theta_1+\frac{\delta}{R}} \frac{\cos(\theta_2-\theta_1)}{\left|\sin\frac{\theta_2-\theta_1}{2}\right|}\mathrm{d}\theta_2$$

$$\approx \int_{\theta_1-\frac{\delta}{R}}^{\theta_1+\frac{\delta}{R}} \frac{2\mathrm{d}\theta_2}{\left|\sin\frac{\theta_2-\theta_1}{2}\right|}$$

$$= \int_{x_1-\delta}^{x_1+\delta} \frac{2\mathrm{d}x_2}{\left|\sin\frac{\theta_2-\theta_1}{2}\right|} = 2I_0, \tag{17}$$

where the changes of variables $x_1 = R\theta_1$ and $x_2 = R\theta_2$ are applied.

After performing the outer integration and substituting (10), the self-inductance for the bent parallel-pair cable in (11) gives:

$$L_{11\mathrm{b}} = \frac{\mu_0 l}{4\pi}\left[\frac{8}{\theta_\mathrm{m}}\sin\frac{\theta_\mathrm{m}}{2} + \frac{2}{\theta_\mathrm{m}}\int_0^{\theta_\mathrm{m}} \ln\left(\tan\frac{\theta_1}{4}\right)\mathrm{d}\theta_1 \right.$$
$$\left. -2\ln\left(\tan\frac{\delta}{4}\right) + I_0 - 4\right], \tag{18}$$

where the second item in the square brackets includes a convergent improper integral that does not have a closed-form expression but can be easily obtained by numerical integration.

Through the changes of variables detailed in Appendix 1, the mutual inductance in (12) can be altered to the following integral:

$$L_{12\mathrm{b}} = \frac{\mu_0 l^2}{2\pi\theta_\mathrm{m}}\int_0^{\theta_\mathrm{m}} \frac{(\theta_\mathrm{m}-x)\cos x\mathrm{d}x}{\sqrt{2l^2-2l^2\cos x + d^2\theta_\mathrm{m}^2}}, \tag{19}$$

where the consequent integral is relative to the elliptic integral and has no closed-form expression but is also available through one-dimensional numerical integration.

According to (1), the inductance of a bent parallel-pair cable is given by:

$$L_\mathrm{b} = 2L_{11\mathrm{b}} - 2L_{12\mathrm{b}}$$
$$= \frac{\mu_0 l}{2\pi}\left[\frac{8}{\theta_\mathrm{m}}\sin\frac{\theta_\mathrm{m}}{2} + \frac{2}{\theta_\mathrm{m}}\int_0^{\theta_\mathrm{m}} \ln\left(\tan\frac{\theta_1}{4}\right)\mathrm{d}\theta_1 \right.$$
$$- 2\ln\left(\tan\frac{\delta}{4}\right) + I_0 - 4$$
$$\left. - \frac{2l}{\theta_\mathrm{m}}\int_0^{\theta_\mathrm{m}} \frac{(\theta_\mathrm{m}-x)\cos x\mathrm{d}x}{\sqrt{2l^2-2l^2\cos x + d^2\theta_\mathrm{m}^2}}\right]. \tag{20}$$

The inductance deviation between the bent parallel-pair cable and the straightened one is:

$$L_\Delta(\theta_\mathrm{m}, l, d)$$
$$= L_\mathrm{b} - L_\mathrm{s}$$
$$= \frac{\mu_0 l}{2\pi}\left[\frac{8}{\theta_\mathrm{m}}\sin\frac{\theta_\mathrm{m}}{2} + \frac{2}{\theta_\mathrm{m}}\int_0^{\theta_\mathrm{m}} \ln\left(\tan\frac{\theta_1}{4}\right)\mathrm{d}\theta_1 \right.$$
$$+ 2\ln(l+\sqrt{l^2+d^2}) + \frac{2d}{l} + 4\ln 2$$
$$- \frac{2l}{\theta_\mathrm{m}}\int_0^{\theta_\mathrm{m}} \frac{(\theta_\mathrm{m}-x)\cos x\mathrm{d}x}{\sqrt{2l^2-2l^2\cos x + d^2\theta_\mathrm{m}^2}}$$
$$\left. - \frac{2\sqrt{l^2+d^2}}{l} - 2\ln d - 2\ln\theta_\mathrm{m} - 2\right], \tag{21}$$

and by denoting the divergent item of the selfinductance inner integral as I_0 and introducing the divergent interval divergent interval, the lumped inductance of the straightened and bent parallel-pair cable can be calculated. Subtraction between the two inductance expressions counteracts the divergent items, of which the absence allows for semi-analytical calculation of L_Δ with one-dimensional numerical integration.

B. Coaxial cable

If directly depicting a coaxial cable with two-line currents, no effective LCM generates because the axes of the inner and outer conductors of the coaxial cable superpose and the two opposite line currents counteract exactly. In fact, each conductor of the coaxial cable cannot be represented by a single line current for inductance calculation due to the current distributions.

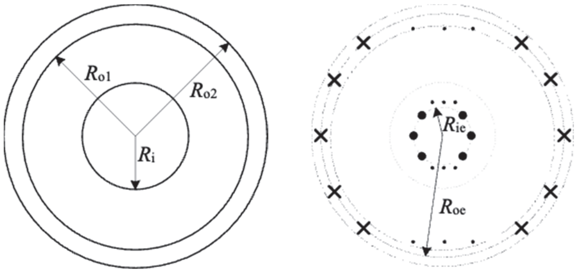

(a) (b)

Fig. 5. LCM for the coaxial cable: (a) cross-section of the coaxial cable and (b) decomposed line currents for the inner and outer conductors.

Therefore, the inner and outer conductors of the coaxial cable are decomposed into several line currents to determine the inductance deviation between the straightened case and bent cases, as shown in Fig. 5. The coaxial cable, with inner conductor of radius R_i, outer conductor of inside radius R_o1, and outside radius R_o2, is equivalent to n_i line currents lying uniformly along the circle of radius R_ie and n_o line currents lying uniformly along the circle of radius R_oe. The following formulas are adopted to determine the equivalent radii:

$$R_{\mathrm{ie}} = \frac{R_{\mathrm{i}}}{2}, \tag{22}$$

$$R_{\mathrm{oe}} = \frac{R_{\mathrm{o1}} + R_{\mathrm{o2}}}{2}. \tag{23}$$

During the calculation of the self-inductances for the inner and outer conductors, the mutual inductances among the decomposed line currents should be taken into account, and hence the self-inductances are:

$$L'_{11} = \frac{1}{n_{\mathrm{i}}} L_{11} + \frac{1}{n_{\mathrm{i}}} \sum_{k=1}^{n_{\mathrm{i}}-1} M_{\mathrm{i},k}, \tag{24}$$

$$L'_{22} = \frac{1}{n_{\mathrm{o}}} L_{22} + \frac{1}{n_{\mathrm{o}}} \sum_{k=1}^{n_{\mathrm{o}}-1} M_{\mathrm{o},k}, \tag{25}$$

where L'_{11} and L'_{22} are the self-inductances of the inner and outer conductors of the coaxial cable, L_{11} as well as $L_{22} (L_{11} = L_{22})$ is the self-inductance of a line current, and $M_{\mathrm{i},k}$ and $M_{\mathrm{o},k}$ are the mutual inductances between the two-line currents decomposed by the inner and outer conductor with the intervals of k/n_i and k/n_o circumference, respectively.

By regarding the inner and outer conductors as two complete line currents, their mutual inductance M_{12} can be calculated with the equivalent distance of R_{oe}.

To summarize, the inductance of the coaxial cable is:

$$\begin{aligned} L &= L'_{11} + L'_{22} - 2M_{12} \\ &= \frac{1}{n_{\mathrm{i}}} L_{11} + \frac{1}{n_{\mathrm{i}}} \sum_{k=1}^{n_{\mathrm{i}}-1} M_{\mathrm{i},k} + \frac{1}{n_{\mathrm{o}}} L_{22} \\ &\quad + \frac{1}{n_{\mathrm{o}}} \sum_{k=1}^{n_{\mathrm{o}}-1} M_{\mathrm{o},k} - 2M_{12} \\ &= (L_{11} + L_{22} - 2M_{12}) - \frac{1}{2n_{\mathrm{i}}} \sum_{k=1}^{n_{\mathrm{i}}-1} \left(2L_{11} - 2M_{\mathrm{i},k}\right) \\ &\quad - \frac{1}{2n_{\mathrm{o}}} \sum_{k=1}^{n_{\mathrm{o}}-1} \left(2L_{22} - 2M_{\mathrm{o},k}\right), \end{aligned} \tag{26}$$

where every item in parentheses is the expression of the inductance for a parallel-pair cable in LCM.

It is worth noting that (26) applies to both straightened and bent coaxial cable layouts. In the straightened case, (9) is leveraged to compute the inductances. Moreover, in bent cases, (20) is utilized to estimate the inductances, in which the mutual inductances of the decomposed line currents are approximated by (19) despite the deviation of the relative positions.

The difference between the inductance of the bent coaxial cable and that of the straightened case yields the inductance deviation for the coaxial cable:

$$\begin{aligned} L_{\Delta\,\mathrm{coa}} &= L_{\Delta}|_{d=R_{\mathrm{oe}}} - \frac{1}{2n_{\mathrm{i}}} \sum_{k=1}^{n_{\mathrm{i}}-1} L_{\Delta}|_{d=r_{\mathrm{i},k}} \\ &\quad - \frac{1}{2n_{\mathrm{o}}} \sum_{k=1}^{n_{\mathrm{o}}-1} L_{\Delta}|_{d=r_{\mathrm{o},k}}, \end{aligned} \tag{27}$$

where L_{Δ} is the inductance deviation for the parallelpair cable obtained by (21):

$$r_{\mathrm{i},k} = 2R_{\mathrm{ie}} \sin\left(\frac{k\pi}{n_{\mathrm{i}}}\right), \tag{28}$$

$$r_{\mathrm{o},k} = 2R_{\mathrm{oe}} \sin\left(\frac{k\pi}{n_{\mathrm{o}}}\right). \tag{29}$$

IV. NUMERICAL RESULTS AND DISCUSSION

The inductance deviation between the straightened layout and bent layouts for the parallel-pair cable and coaxial cable has been presented by a semi-analytical formula including non-closed-form expressions. In this section, the inductance deviation formula is solved for specific testing cases with numerical integration and compared with the results of the FEM. Then, the dependence of the inductance deviation on the parameters of the cable is investigated and the effect of the inductance deviation on realistic measurement of the lumped inductance is discussed. Besides, the frequency limitation of the semi-analytical formula and the measured inductance of a cable are also demonstrated to offer reference to realistic inductance measurement.

A. Comparison with FEM results

The inductance deviation between the straightened layout and the bent layouts in the angle from 0 to $11\pi/6$ of a parallel-pair consisting of two identical cylindrical conductors, with the parameters shown in Table 1, is calculated using (21), in which the non-closed-form integrals are handled by numerical integration. The corresponding three-dimensional FEM models are constituted in COMSOL Multiphysics software and solved by its Magnetic Fields, Current Only interface for the straightened layout and the bent layouts for the angle range $\pi/2 : \pi/6 : 11\pi/6$, of which the geometry and conductor terminal meshes are shown in Figs. 6 (a), 6 (c), and 7 (a), respectively. The inductance deviation results of the semi-analytical method and FEM are illustrated in Fig. 8.

The inductance deviation of a coaxial cable with the parameters in Table 2 is also calculated by (27) and (21) and COMSOL Multiphysics FEM software, in which the outer conductor is represented by a solid

Table 1: Parameters of the parallel-pair cable

Cable Length	**Conductor Axis Distance**	**Conductor Radius**
1 m	20 mm	5 mm

Table 2: Parameters of the coaxial cable

Cable Length	**Inner Conductor Radius**	**Outer Conductor Inner Radius**
1 m	5 mm	10 mm
Outer Conductor Outer Radius	Inner Conductor LCMs (n_i)	Outer Conductor LCMs (n_o)
12 mm	5	5

tube. The geometry and conductor terminal meshes are demonstrated in Figs. 6 (b), 6 (d), and 7 (a), respectively. The results of the semi-analytical formula and FEM method are shown in Fig. 9.

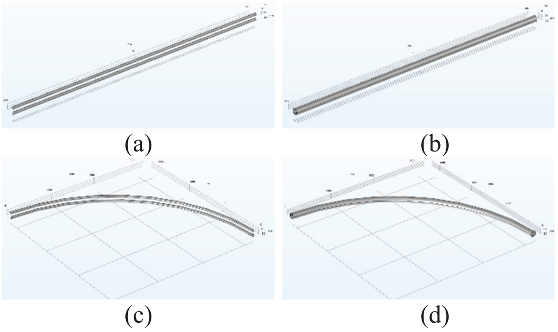
(a) (b)

(c) (d)

Fig. 6. Geometry for the cable FEM models in COMSOL Multiphysics: (a) parallel-pair cable in the straightened layout, (b) coaxial cable in the straightened layout, (c) parallel-pair cable in the bent layout with $\theta_\mathrm{m} = \pi/2$, and (d) coaxial cable in the bent layout with $\theta_\mathrm{m} = \pi/2$.

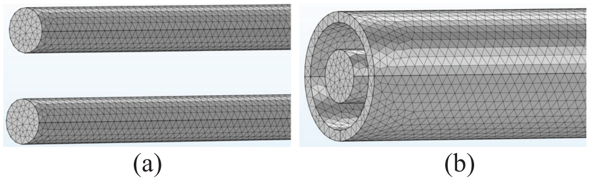
(a) (b)

Fig. 7. Meshing of the conductor terminals in COMSOL: (a) parallel-pair cable totally including 910324 mesh units for the straightened layout and (b) coaxial cable totally including 1178841 mesh units for the straightened layout.

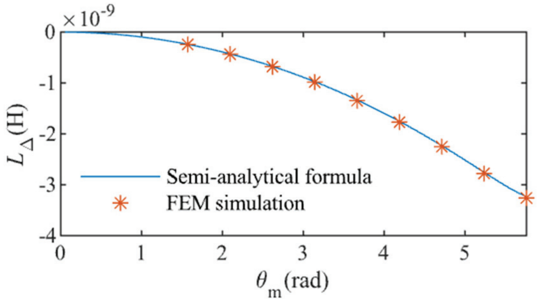

Fig. 8. Comparison between the results of the proposed semi-analytical formula and the FEM for the parallel-pair cable.

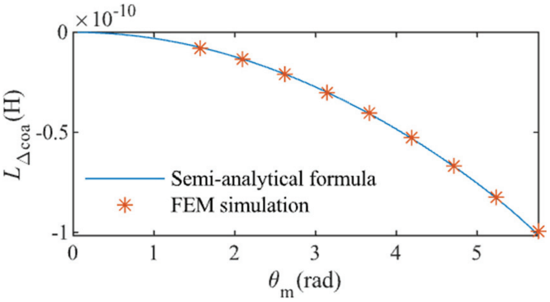

Fig. 9. Comparison between the results of the proposed semi-analytical formula and the FEM for the coaxial cable.

It can be seen that the inductance deviation obtained by the proposed semi-analytical formula for both the parallel-pair cable and coaxial cable manifests remarkable consistency with the FEM results, proving the accuracy of the proposed formula. Moreover, the average consuming time for a single calculation by the proposed formula and the FEM method is demonstrated in Table 3, where the two methods are executed by MATLAB R2021b and COMSOL Multiphysics 6.0 on a computer with two Intel Xeon Golden 5520R 2.2 GHz CPUs and 120 GB RAM. It can be seen that the proposed semi-analytical formula shows prominent efficiency in comparison with the FEM method.

Table 3: Average consuming time for a single calculation

Cable Type	**Parallel-Pair Cable**	**Coaxial Cable**
Proposed formula	1.344 ms	11.24 ms
FEM method	186.2 s	168.5 s

B. Dependence of the inductance deviation

The inductance deviations obtained in (21) and (27) demonstrate explicit dependence on the parameters of the parallel-pair and coaxial cables. The inductance deviation for a parallel-pair cable with different θ_m, l, and d is illustrated in Fig. 10. The absolute value of the inductance deviation shows a positive correlation with θ_m; larger θ_m means more severe bending and consequently larger inductance deviation. The absolute value of the inductance deviation manifests a negative correlation with l, because a longer cable leads to larger distance and weaker magnetic field coupling between cable segments, which exceeds the effect of the additional length. Moreover, the absolute value of the inductance deviation is positively correlated with d, since larger d contributes to less counteracting effect of the two opposite-current conductors and therefore less coupling between segments.

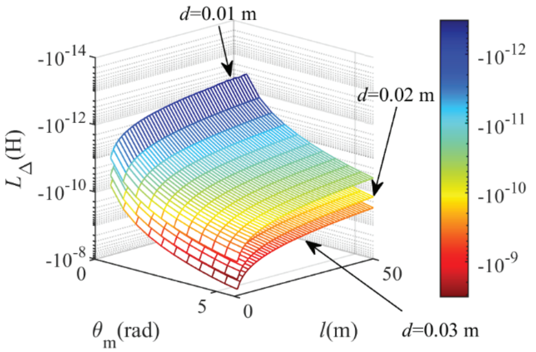

Fig. 10. Dependence of the inductance deviation on the bending angle, length, and conductor distance for the parallel-pair cable.

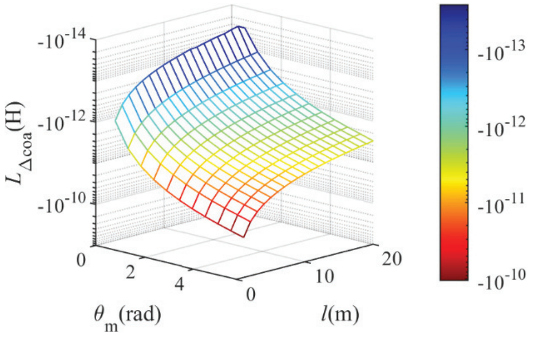

Fig. 11. Dependence of the inductance deviation on the bending angle and length for the coaxial cable, with $R_{\mathrm{oe}} = 0.011$ m and $R_{\mathrm{i}} = 0.005$ m.

The inductance deviation for a coaxial cable with different θ_{m} and l is illustrated in Fig. 11. Like a parallel-pair cable, the absolute value of the inductance deviation for a coaxial cable increases with θ_{m} and decreases with l. Furthermore, as shown in Fig. 12, the absolute value of the inductance deviation demonstrates negative and positive correlations with R_{i} and R_{oe}, respectively, in accordance with the relationship revealed by (27).

The number of decomposed line currents for the coaxial cable influences the accuracy and efficiency of the LCM. Figure 13 depicts the $L_{\Delta\mathrm{coa}-} - \theta_{\mathrm{m}}$ relationship with different n_{i} and n_{o} that are here taken as the same value for convenience. It can be seen that both the convergence and efficiency of the decomposition method are satisfying when n_{i} and n_{o} are equal to 5, while a greater decomposing number does not lead to apparently higher accuracy.

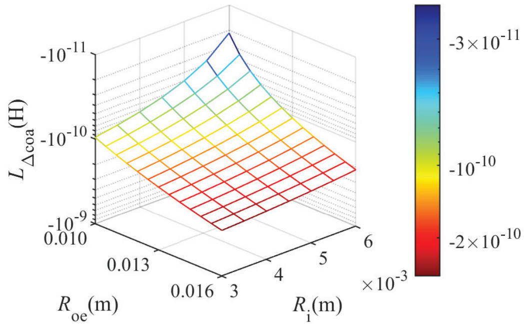

Fig. 12. Dependence of the inductance deviation on the radii of the efficient inner and outer conductors for the coaxial cable, with $\theta_{\mathrm{m}} = 11\pi/6$ and $l = 1$ m.

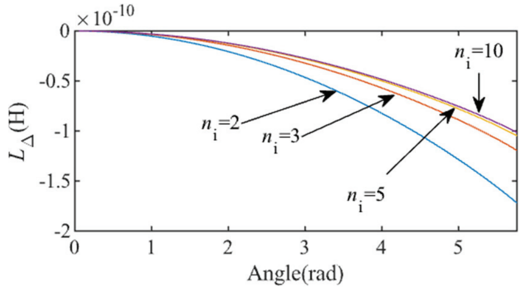

Fig. 13. Dependence of the inductance deviation on the number of decomposed line currents for the coaxial cable, with $R_{\mathrm{i}} = 0.005$ m, $R_{\mathrm{oe}} = 0.011$ m, and $l = 1$ m.

C. Valid frequency range of the semi-analytical method

The semi-analytical method is proposed to deal with the effects of bending on cable inductance at low frequencies. In the deduction of the method, the lumped inductance of the cable is calculated to indicate the inductive part of the input impedance. Therefore, the proposed method is valid if the lumped model can represent the cable impedance, i.e., the cable is electrically short. The valid frequency of the method satisfies:

$$f \leq \frac{v}{20l}, \tag{30}$$

where v is the propagation speed of electromagnetic wave along the cable, which is related to the structure and material of the cable. At higher frequencies, the input impedance of the cable cannot be represented by the lumped inductance such that the circuit model in Fig. 2 becomes invalid. Moreover, the quasi-static formulas for the partial inductance (2) and (3) are inaccurate at higher frequencies since the time delay shall be taken into account and the quasi-static approximation does not hold.

D. Inductance deviation in measurement

It is noted that the magnitude of the inductance deviation for a coaxial cable is quite small. For instance, in regard to a coaxial cable with $l = 1$ m, $R_{\mathrm{i}} = 0.005$ m, $R_{\mathrm{oe}} = 0.011$ m, and $\theta_{\mathrm{m}} = 11\pi/6, L_{\Delta\,\mathrm{coa}}$ is equal to -1.016×10^{-10} H, of which the absolute value is smaller than the precision of most inductance measurement instrument.

According to Fig. 11, the absolute value of the inductance deviation for a longer cable is smaller than a shorter one. Regarding a coaxial with the same cross-section and bending angle as above but $l = 10$ m, the inductance deviation reduces to -6.874×10^{-12} H, of which the absolute value is smaller than $1/10$ of the result with $l = 1$ m. Moreover, the lumped inductance of a longer cable is larger than a shorter one, such that the inductance deviation between the straightened layout and bent layouts makes much less difference to the measurement results of the inductance. In brief, if a 10m coaxial cable is bent to a non-closed-arc for realistic lumped inductance measurement, the effect of bending on coaxial cable inductance is negligible.

The lumped inductance of three coaxial cable samples, with $l = 1.0, 3.0$, and 10.0 m, respectively, and the same cross-section that $R_{\mathrm{i}} = 1.43$ mm and $R_{\mathrm{oe}} = 5.35$ mm, is measured using a HIOKI 3530-50 LCM meter at 50 Hz with different bending angles. The measurement results shown in Table 4 manifest no obvious relationship with the bending angles due to the stochastic noise of the LCM meter and the surrounding electromagnetic interference applied to the cable, where the effect of bending is drowned and immeasurable.

Table 4: Measured inductance at different bending angles for the coaxial cable with different length

Bending Angle	**1 m**	**3.3 m**	**10 m**
0	0.232 μH	0.844 μH	2.95 μH
$\pi/2$	0.326 μH	0.660 μH	3.31 μH
π	0.287 μH	1.12 μH	2.93 μH
$3\pi/2$	0.184 μH	0.565 μH	3.41 μH

V. CONCLUSION

A semi-analytical formula using the LCM is proposed in this paper for the bending effects on the inductance of the parallel-pair cable and then applied to the coaxial cable combined with the decomposition scheme of the conductors. The results demonstrate satisfying consistency with the inductance deviation extracted by the FEM method for both parallel-pair and coaxial cables.

The numerical results also show that the inductance of a parallel-pair or coaxial cable slightly decreases after bending and the deviation extends if the bending angle increases. The magnitude of the inductance deviation for a longer coaxial cable is small enough for instrument, indicating that the effect of non-closed-arc bending can be ignored in realistic measurement of the lumped coaxial cable inductance at low frequencies.

ACKNOWLEDGMENT

This work has been funded by the National Natural Science Foundation of China under grant No. 52377003.

APPENDIX 1

$L_{12\mathrm{b}}$ can be simplified by applying the change of variables $\theta_2 - \theta_1 = x$ and $\theta_2 + \theta_1 = y$:

$$
\begin{aligned}
L_{12\mathrm{b}} &= \frac{\mu_0 R^2}{4\pi} \int_0^{\theta_{\mathrm{m}}} \int_0^{\theta_{\mathrm{m}}} \frac{\cos(\theta_2 - \theta_1)\mathrm{d}\theta_2 \mathrm{d}\theta_1}{\sqrt{2R^2 - 2R^2\cos(\theta_2 - \theta_1) + d^2}} \\
&= \frac{\mu_0 R^2}{8\pi} \left[\int_{-\theta_{\mathrm{m}}}^{0} \frac{\cos x}{\sqrt{2R^2 - 2R^2 \cos x + d^2}} \int_{-x}^{x+2\theta_{\mathrm{m}}} \mathrm{d}y\mathrm{d}x \right. \\
&\quad \left. + \int_0^{\theta_{\mathrm{m}}} \frac{\cos x}{\sqrt{2R^2 - 2R^2 \cos x + d^2}} \int_{-x}^{x+2\theta_{\mathrm{m}}} \mathrm{d}y\mathrm{d}x \right] \\
&= \frac{\mu_0 R^2}{4\pi} \left[\int_{-\theta_{\mathrm{m}}}^{0} \frac{(x + \theta_{\mathrm{m}}) \cos x \mathrm{d}x}{\sqrt{2R^2 - 2R^2 \cos x + d^2}} \right. \\
&\quad \left. + \int_0^{\theta_{\mathrm{m}}} \frac{(\theta_{\mathrm{m}} - x) \cos x \mathrm{d}x}{\sqrt{2R^2 - 2R^2 \cos x + d^2}} \right] \\
&= \frac{\mu_0 R^2}{2\pi} \int_0^{\theta_{\mathrm{m}}} \frac{(\theta_{\mathrm{m}} - x) \cos x \mathrm{d}x}{\sqrt{2R^2 - 2R^2 \cos x + d^2}} \\
&= \frac{\mu_0 l^2}{2\pi\theta_{\mathrm{m}}} \int_0^{\theta_{\mathrm{m}}} \frac{(\theta_{\mathrm{m}} - x) \cos x \mathrm{d}x}{\sqrt{2l^2 - 2l^2 \cos x + d^2 \theta_{\mathrm{m}}^2}}
\end{aligned}
$$

REFERENCES

[1] "Coaxial communication cables – Part 1-114: Electrical test methods – Test for inductance," IEC 61196-1-114:2015 [Online], Sep. 2015. Available: https://webstore.iec.ch/en/publication/23418.

[2] A. E. Ruehli, "Inductance calculations in a complex integrated circuit environment," *IBM Journal of Research and Development*, vol. 16, no. 5, pp. 470–481, Sep. 1972.

[3] Z. Zhu, X. Xia, R. Streiter, G. Ruan, T. Otto, H. Wolf, and T. Gessner, "Closed-form formulae for frequency-dependent 3-D interconnect inductance," *Microelectronic Engineering*, vol. 56, no. 3, pp. 359–370, Aug. 2001.

[4] G. Zhong and C.-K. Koh, “Exact closed-form formula for partial mutual inductances of on-chip interconnects,” in *Proceedings IEEE International Conference on Computer Design: VLSI in Computers and Processors*, pp. 428–433, Sep. 2002.

[5] Z. Y. Li, D. Y. Hu, Z. H. Yao, Y. W. Wang, Z. Y. Hong, K. Ryu, Y. H. Ma, and H. S. Yang, “Inductance evaluation of a 22.9kV/50MVA HTS cable with shield by electrical method,” in *2015 IEEE International Conference on Applied Superconductivity and Electromagnetic Devices (ASEMD)*, pp. 568–570, Nov. 2015.

[6] A. C. Silva and A. De Conti, “Calculation of the external parameters of overhead insulated cables considering proximity effects,” in *2017 International Symposium on Lightning Protection (XIV SIPDA)*, pp. 127–131, Oct. 2017.

[7] H. Li, R. Banucu, and W. M. Rucker, “Accurate and efficient calculation of the inductance of an arbitrary-shaped coil using surface current model,” *IEEE Transactions on Magnetics*, vol. 51, no. 3, pp. 1–4, Mar. 2015.

[8] J. T. Conway, “Exact solutions for the mutual inductance of circular coils and elliptic coils,” *IEEE Transactions on Magnetics*, vol. 48, no. 1, pp. 81–94, Jan. 2012.

[9] A. Ruehli, G. Antonini, and L. Jiang, *Circuit Oriented Electromagnetic Modeling Using the PEEC Techniques*. Hoboken, NJ: John Wiley & Sons, 2017.

Xiao Chen was born in Yichang, China, in 1998. He received the B.Sc. and M.Sc. degrees in electrical engineering in 2020 and 2023, respectively, from the School of Electrical Engineering and Automation, Harbin Institute of Technology, Harbin, where he is currently pursuing a Ph.D. degree in electrical engineering. His research interests include transmission line theory, computational electromagnetics, and multiphysics field coupling simulations.

Haicheng Yin was born in Shanghai, China, in 1984. He graduated from Tongji University and holds a B.Sc. in EIE. He has been working for No. 23 Research Institute of CETC since 2008 and was appointed as an assistant chief engineer in 2020. His professional expertise lies in the international standardization work in the field of optical and electrical communication cable, connectors, and assemblies. He is an active member in the IEC community and has been project leader for 14 IEC standards. He was appointed as convenor for IEC/TC46/WG9 and IEC/SC46A/WG3, and as liaison for IEC/SC86A and IEC/ISO JTC3. For his outstanding work, he received an IEC 1906 award in 2022.

Gang Zhang was born in Tai’an, China, in 1984. He received the B.S. degree in electrical engineering from China University of Petroleum, Dongying, in 2007, and the M.S. and Ph.D. degrees in electrical engineering from Harbin Institute of Technology (HIT), Harbin, in 2009 and 2014, respectively. He is currently a Professor of Electrical Engineering with HIT. His research interests include electrical contact theory, uncertainty analysis of electromagnetic compatibility, and validation of CEM.

Francesco de Paulis was born in L’Aquila, Italy, in 1981. He received the Specialistic Laurea (summa cum laude) degree in electronic engineering from the University of L’Aquila (UAq), L’Aquila, in 2006, the M.S. degree in electrical engineering from Missouri University of Science and Technology, Rolla, MO, USA, in 2008, and the Ph.D. degree in electrical and information engineering from UAq in 2012. He is currently a Senior Research Professor with the UAq EMC Laboratory. His main research interests include the design of high-speed signals on PCBs, packages, and chips, RF interference in mixed-signal systems, and EMI problem investigation on PCBs.

Xin He was born in Wenshan, China, in 1996. He received the B.S. and M.Sc. degrees in electrical engineering from Harbin Institute of Technology (HIT), Harbin, in 2019 and 2021, respectively. He is currently pursuing a Ph.D. degree in electrical engineering with HIT, Shenzhen. His research interests include cable fault detection location and electromagnetic compatibility analysis.

Analysis of Velocity-Acceleration Double Closed-Loop Control for Double-Sided Switched Reluctance Linear Machine System

Hao Chen[1,2], Sergei Brovanov[3], Javokhir Toshov[4], Jingfu Liu[2],
Xing Wang[1,2], Antonino Musolino[5], Nurkhat Zhakiyev[6],
Murat Shamiyev[4], and Abror Obidovich Pulatov[4]

[1]Shenzhen Research Institute
China University of Mining and Technology, Shenzhen 515100, China
hchen@cumt.edu.cn, 3512@cumt.edu.cn

[2]School of Electrical Engineering
China University of Mining and Technology, Xuzhou 221116, China

[3]Novosibirsk State Technical University
Novosibirsk 630073, Russia
brovanov@corp.nstu.ru

[4]Tashkent State Technical University
University Street No2, 100095 Tashkent, Uzbekistan
javokhir.toshov@yandex.ru, Hello_murat@mail.ru, abrorobidovich@mail.ru

[5]Department of Energy, System, Territory and Construction Engineering (DESTEC)
University of Pisa, 56122 Pisa, Italy
antonino.musolino@unipi.it

[6]Department of Science and Innovation
Astana IT University, Astana, Kazakhstan
nurkhat.zhakiyev@astanait.edu.kz

Abstract – A model of a velocity-acceleration double closed-loop control for a double-sided switched reluctance linear machine (DSRLM) system is presented in this paper. The velocity single closed-loop control with PI or Fuzzy regulators is contrasted with the velocity-acceleration double closed-loop controller. The response time and response characteristics under six distinct control algorithms are compared, and the most appropriate speed regulation controller is chosen.

Index Terms – Double closed-loop, linear machine, switched reluctance, velocity regulation control.

I. INTRODUCTION

Switched reluctance machines (SRMs) show good speed regulation performance, so they have been successfully used in electric vehicles (EVs), aerospace, and some high-velocity drives [1–4]. Switched reluctance linear machines (SRLMs) evolved from rotary SRMs by cutting the stator and the rotor in the radial direction and stretching them into straight lines as the stator and the mover of linear machine, respectively [5]. They have inherited some merits from rotary SRMs, such as simple structure, high reliability, good fault tolerance, and flexible control methods [6–9]. Good velocity regulation control makes SRLMs possible to apply on some occasions, for instance, rail transit, lifting systems, and direct-drive systems [8–11]. However, compared with rotary motors, SRLMs pose more challenges in the operation and control of linear motors. In SRLMs, the axial end effect is an inherent phenomenon caused by the finite length of the stator and mover, which distinguishes linear machines from their rotary counterparts. Due to the interruption of the magnetic circuit at the motor ends, the magnetic flux distribution becomes asymmetric, resulting in nonuniform phase inductance and flux linkage along the motion direction. This effect is particularly pronounced near the entry and exit regions of the mover, where magnetic flux leakage increases and the effective air-gap permeance decreases. Consequently, the electromagnetic characteristics of different phases become

Submitted On: December 02, 2024
Accepted On: January 01, 2025

https://doi.org/10.13052/2025.ACES.J.401209

unbalanced, leading to variations in force production capability and phase coupling characteristics. In addition, the axial end effect exacerbates electromagnetic force ripple during phase commutation, thereby degrading force smoothness and control performance. Since the end effect is highly position-dependent and exhibits strong nonlinearity, it poses significant challenges to accurate modeling and control of SRLMs, especially under varying operating conditions or fault scenarios. For this reason, SRLMs require a more advanced method to regulate the speed.

A proportion integration differentiation (PID) controller has been widely used in industrial production to adjust the deviation of the system [12–14]. According to different production processes, different control rules must be selected properly, otherwise the PID controller could not achieve the desired control effect. The traditional control theory has powerful control ability in mathematically clear systems, but it is powerless for systems that are complex or difficult to describe accurately. According to this, Fuzzy mathematics has been used to deal with these complex control problems, and a Fuzzy controller arises [15–17]. A variety of speed control methods for other types of machines have been investigated [18–20]. In [18], a new method to design a data-based PI regulator for induction machines in closed-loop speed control has been presented. Khooban et al. [19] proposed an optimal multi-objective Fuzzy fractional-order PID controller for the speed control of direct current motors in EV systems, and the good performance of the proposed regulator is verified by experiments and simulations. Ashouri-Zadeh et al. [20] proposed a Fuzzy-based speed controller for the doubly fed induction generator-based wind turbines, which takes the rotor speed and wind speed as inputs. It designs a speed regulator to control the torque of the generator and extract the maximum power from the wind by adjusting the rotor speed. In the PID controller, the differential link can reduce the oscillation and increase the stability of the closed-loop system, but it is not suitable for adjusting signals with high frequency and big noise. SRMs have the shortcoming of large noise so that the differential link is generally not used in their single-loop speed control system, and the PI regulator is always selected. In [5], an acceleration closed-loop control with the Fuzzy regulator is designed and successfully used in a single-sided SRLM.

This paper investigates the velocity regulation control of a double-sided switched reluctance linear machine (DSRLM), shown in Fig. 1 and Table 1. A double closed-loop control algorithm is proposed, in which the acceleration loop is the inner loop, and the velocity loop is the outer loop. The PI regulator and the Fuzzy regulator are used in inner and outer loops alternately. Their regulation performances are compared with single-loop control algorithms.

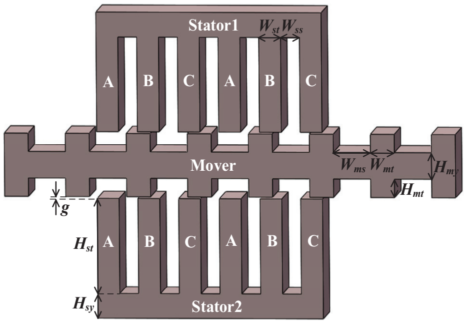

Fig. 1. Structure of DSRLM.

Table 1: Key dimensions of DSRLM

Name	Parameter	Dimension (mm)
Stator tooth width	W_{st}	21.5
Stator slot width	W_{ss}	18.5
Stator tooth length	H_{st}	95.0
Stator yoke thickness	H_{sy}	23.5
Mover tooth width	W_{mt}	23.5
Mover slot width	W_{ms}	36.5
Mover tooth length	H_{mt}	17.5
Mover yoke thickness	H_{my}	25.0
Air gap thickness	g	0.5
Laminated thickness	L	86.0

II. CONTROLLER DESIGN

A. Design of Fuzzy regulator

The design process of a Fuzzy regulator can be divided into five steps.

(1) The first step is to determine the inputs and outputs of the regulator. In this paper, the two-dimensional Fuzzy regulator with double inputs and a single output (U) is selected to adjust the velocity or acceleration. Two inputs are the error (E) and the error variation (EC) of the variable.

(2) The second step is to determine the universe and the scale factor of every variable. In this paper, the basic universe of velocity is $[-1, 1]$ m/s, the basic universe of acceleration is $[-2, 2.5]$ m/s^2, and the basic universe of current reference values is [0, 6] A which always adds to a bias. The Fuzzy universe of the E, EC, and U is $[-6, 6]$.

(3) The third step is to determine the number of Fuzzy linguistic variables and their membership functions. In the design process of the Fuzzy regulator, what is the most important is to determine the number of Fuzzy linguistic variables and their membership

functions. When the number of Fuzzy linguistic variables is large, the language rules would be more specific. Then its control effect will be more flexible and more accurate. However, sometimes the number is too large to implement and draw up its rules. Finally, under comprehensive consideration, there are 7 Fuzzy linguistic variables in total, which are sorted in terms of negative big (NB), negative medium (NM), negative small (NS), zero (ZE), positive small (PS), positive medium (PM), and positive big (PB). The frequently used membership functions are the triangular, trapezoidal, Gaussian, bell, and sigmoidal. The triangular membership function is selected in this paper owing to its concise notation and great interference immunity, which is shown in Fig. 2.

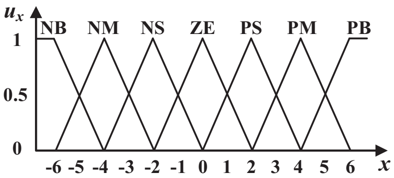

Fig. 2. Triangular membership function.

Table 2: Language rules of the Fuzzy regulator

EC	E						
	NB	**NM**	**NS**	**ZE**	**PS**	**PM**	**PB**
NB	NB	NB	NB	NB	NM	NS	ZE
NM	NB	NB	NB	NM	NS	ZE	PS
NS	NB	NB	NM	NS	ZE	PS	PM
ZE	NB	NM	NS	ZE	PS	PM	PB
PS	NB	NS	ZE	PS	PM	PB	PB
PM	NB	ZE	PS	PM	PB	PB	PB
PB	ZE	PS	PM	PB	PB	PB	PB

(4) The fourth step is to summarize the expert experience and express a series of language rules. The language rules of the Fuzzy regulator used in this paper are shown in Table 2. This step is the Fuzzy inference system (FIS). Some of the language rules of the Fuzzy regulator shown in Table 2 are introduced in this part briefly. For example, if E is NB, and EC is NB. It means that the value of the controlled object (velocity or acceleration) is much bigger than its reference value, and it has a trend to continue to expand this difference. Therefore, the output of the Fuzzy regulator should stop this trend and greatly reduce this difference. Related to the current acceleration reference values, they both should be reduced greatly. So, the output of the Fuzzy regulator is NB.

(5) The final step is defuzzification, which converts the Fuzzy values to the non-Fuzzy values according to a strategy. The centroid strategy is selected owing to its rationality. In the experiments, a two-dimensional decision table is established after the offline calculation according to the centroid strategy. Its curved surface is shown in Fig. 3. The fuzzification and defuzzification are expressed as

$$\begin{cases} E = int(e \cdot ke) \\ EC = int(e \cdot kec) \\ u = U \cdot ku + c \end{cases}, \tag{1}$$

where e is the error between the controlled parameter and its reference value, ec is the error variation, u is the final output of the regulator, k_e is the coefficient scale of e, k_{ec} is the coefficient scale of ec, k_u is the coefficient scale of u, c is a bias, and int() is a numerical function to get a numeric value down to the nearest integer.

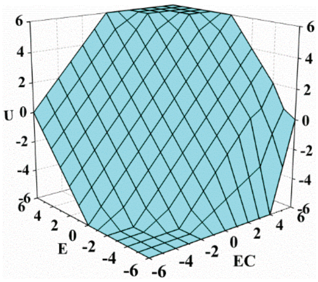

Fig. 3. Offline calculation results of defuzzification.

B. Design of the PI regulator

The PI regulator is a widely used linear regulator. It implements the control of the object by the combination of the proportion and integral values of the deviation. The deviation is the difference between the given value and the actual value. The proportional link mainly affects the response speed and overshot value of the system. Generally, with the increase of the coefficient scale of the proportion link, the overshoot of the closed-loop system is increased, and the response speed of the system is accelerated. The integral link can help eliminate the steady state error of the system. The greater the coefficient scale of the integral link, the weaker the integral function, the smaller the overshoot of the closed-loop system and the lower the response speed of the system becomes. The equation of the principle of PI regulator can be expressed as

$$u = e \cdot kp + ki \cdot \int edt, \tag{2}$$

where kp is the coefficient scale of the proportion link, ki is the coefficient scale of the integral link, and t is the time.

C. Single closed-loop control

The velocity single closed-loop control with PI regulator and Fuzzy regulator are investigated, respectively, whose control diagram is presented in Fig. 4. The velocity difference e is input in the PI/Fuzzy regulator which outputs the corresponding current reference value I_{ref}. The phase currents $i_{\mathrm{a1}}, i_{\mathrm{a2}}, i_{\mathrm{b1}}, i_{\mathrm{b2}}, i_{\mathrm{c1}}$, and i_{c2} are compared with the reference current of every phase, respectively in the hysteresis comparator. An AND logic operation is conducted between its output and the output of the position judgment to control the switches on the power converter. The mover of the DSRLM runs and feeds back the real-time velocity v to the regulator, and position x to the position judgment link with the position sensor.

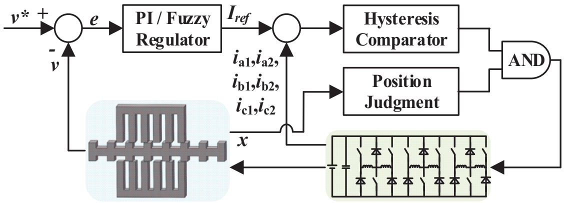

Fig. 4. Diagram of velocity single closed-loop control.

D. Double closed-loop control

In the velocity-acceleration double closed-loop control, the PI regulator and the Fuzzy regulator are used in inner and outer loops alternately, whose diagram is presented in Fig. 5.

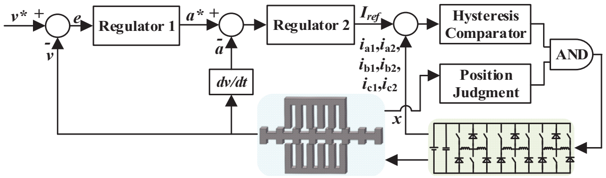

Fig. 5. Diagram of velocity-acceleration double closed-loop control.

The velocity loop is the outer loop which outputs the acceleration reference values according to the velocity difference. The acceleration loop is the inner loop that outputs the current reference values according to the acceleration difference. The following process is the same as the velocity single closed-loop diagram. An AND logic operation is conducted between the hysteresis comparator's output and the output of the position judgment to control the switches on the power converter. The deviation between real-time velocity and the given velocity is input to regulator 1, and position x to the position judgment link with the position sensor. The acceleration of the mover is achieved after the differential calculation of velocity, and it is fed back to regulator 2 in the inner loop.

III. SIMULATION RESULTS AND ANALYSIS

As shown in Fig. 5, the PI regulator and the Fuzzy regulator are used as regulator 1 and regulator 2 alternately. There are four double closed-loop controllers in total. The simulation results of four double closed-loop controllers and two single-loop controllers are conducted. Under no load and 24 V power supply, the model of the DSRLM is established by the Fourier modeling method proposed in [21]. Two simulation results of 0.4 m/s are shown in Fig. 6.

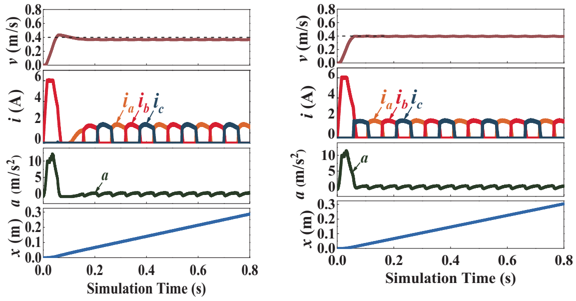

(a) (b)

Fig. 6. Simulation results under 0.4 m/s given velocity: (a) PI controller and (b) Fuzzy controller.

The simulation results of 0.6 m/s are shown in Fig. 7. In these figures, v is the mover velocity. Owing to the symmetry of double-sided currents, the currents of only one side are given, where i_a, i_b, and i_c are the current values of phases A1, B1, and C1, respectively, arf is the acceleration reference output by the regulator 1, a is the simulated mover acceleration, and x is the mover position.

In the simulation results of Fuzzy-Fuzzy double closed-loop velocity regulation, there is no overshoot in the process of velocity regulation, and the arising time and steady-state error of the controller are about 0.232 s and 0.013 m/s. In the simulation results of PI-Fuzzy double closed-loop velocity regulation, there is no overshoot, and its arising time and steady-state error of the controller are about 0.300 s and 0.024 m/s. Also, there is no overshoot in the process of velocity regulation with the PI-PI controller. Its arising time and steady-state error of the controller are about 0.411 s and −0.006 m/s. The simulation results of Fuzzy-PI double closed-loop velocity regulation show that there is no overshoot in the process of velocity regulation with the Fuzzy-PI controller, and its arising time and steady-state error of the controller are about 0.268 s and 0.05 m/s. The

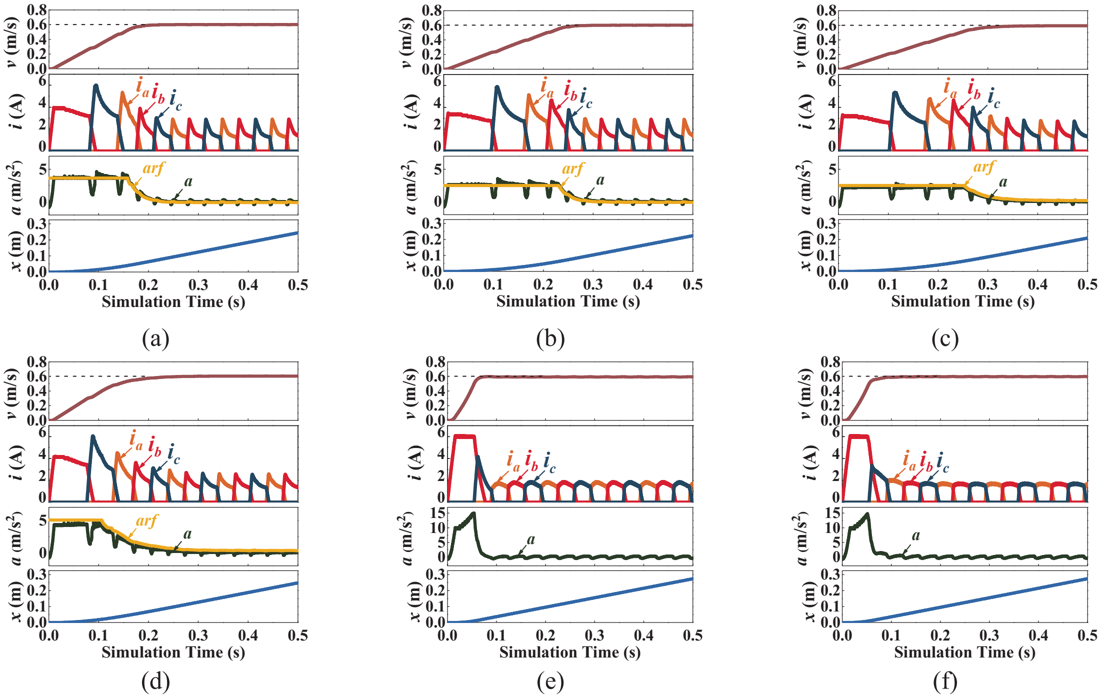

Fig. 7. Simulation results under given velocity 0.6 m/s: (a) Fuzzy-Fuzzy controller, (b) PI-Fuzzy controller, (c) PI-PI controller, (d) Fuzzy-PI controller, (e) PI controller, (f) Fuzzy controller.

simulation results of PI single closed-loop velocity regulation and Fuzzy single closed-loop velocity regulation are shown in Figs. 7 (e) and 7 (f), respectively. With the PI regulator, when the given velocity is 0.4 m/s, the arising time and static state error of the controller are about 0.063 s and 0.035 m/s, and there is an overshoot which is about 0.035 m/s. When the given velocity is 0.6 m/s, the arising time and steady-state error of the controller are about 0.080 s and −0.009 m/s, and there is no overshoot. With a Fuzzy regulator, it can be seen that there is no overshoot in the velocity regulation results. When the given velocity is 0.4 m/s, the arising time and static state error of the controller are about 0.056 s and −0.006 m/s. When the given velocity is 0.6 m/s, the arising time and static state error of the controller are about 0.115 s and −0.005 m/s.

The control performances of the six controllers are compared in Table 3. The overshoot, arising time, and steady-state error are quantized at two different given velocities. It can be seen that two single closed-loop controllers have a shorter arising time than four double closed-loop controllers, but the PI controller shows an overshoot when the given velocity is 0.4 m/s. In many applications, a small overshoot may cause huge damage to the whole system. Therefore, although four double closed-loop controllers have relatively longer arising time than PI controllers, they are still thought better for no overshoot. Among the four double closed-loop controllers, it is apparent that the arising times of the PI-Fuzzy controller and PI-PI controller are larger than those of the Fuzzy-Fuzzy controller and Fuzzy-PI controller. The Fuzzy-PI controller is better than the Fuzzy-Fuzzy controller in steady state error but is worse in arising time. Thus, further comparisons of the Fuzzy controller, Fuzzy-Fuzzy controller, and Fuzzy-PI controller should be conducted by variable-given velocity tests. These conclusions obtained by simulations should be verified by experiments.

IV. EXPERIMENTAL VERIFICATIONS

A. Hardware platform and coefficients of controllers

The whole velocity regulation system is shown in Fig. 8, which includes a DSRLM prototype, an RT-LAB digital controller, an isolator, a drive circuit, a sampling circuit, a linear encoder, and a power converter. In experiments with different controllers, coefficients are different. There are two main control objects in this paper, which are the mover velocity and its acceleration. The basic universe of velocity is [−1, 1] m/s, the basic universe of acceleration is [−2, 2.5] m/s^2, and the basic universe of current reference values is [0, 6] A which always adds to a bias, thus some coefficients in the Fuzzy regulator and PI regulator can be determined. For example, when the Fuzzy regulator is used in the outer loop, its output u is the acceleration reference value. And the Fuzzy universe of the E, EC, and U

Table 3: Velocity regulation performance comparisons of the six controllers in simulations

Controller	Given Velocity (m/s)	Arising Time (s)	Steady-State (m/s) (m/s)	Overshoot (%)
Fuzzy-Fuzzy	0.4	0.159	0.005	0
	0.6	0.232	0.005	0
PI-Fuzzy	0.4	0.188	0.002	0
	0.6	0.300	0.002	0
PI-PI	0.4	0.318	−0.006	0
	0.6	0.411	−0.006	0
Fuzzy-PI	0.4	0.219	0.002	0
	0.6	0.268	0.001	0
PI	0.4	0.063	0.035	8.875
	0.6	0.080	−0.009	0
Fuzzy	0.4	0.060	−0.006	0
	0.6	0.115	−0.005	0

is [−6, 6], so the value of k_u in Fig. 9 (a) is 2.25/6, and the bias is 0.25. The purpose is to change the universe of the output of the Fuzzy to the universe of the acceleration. Similarly, when the Fuzzy regulator is used in the inner loop, its output u is the current reference value, so the value of k_u in Fig. 9 (a) is 3/6, and the bias is 3. When the PI regulator is used in the outer loop, its output u is the acceleration reference value, so it sets −2 as the lower limit and 2.5 as the upper limit in the saturation in Fig. 9 (b). When the PI regulator is used in the inner loop, its output u is the current reference value, so it sets 0 as the lower limit and 6 as the upper limit in the saturation in Fig. 9 (b). Then detailed coefficients in different controllers used in experiments are summarized in Table 4. Besides, the flux-linkage of the DSRLM is calculated by the Fourier series modeling method, which is the same as section III.

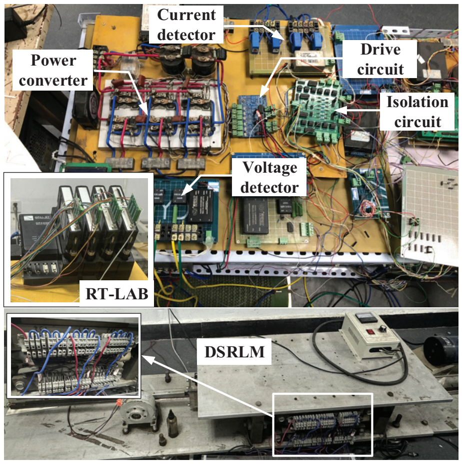

Fig. 8. Prototype and hardware platform.

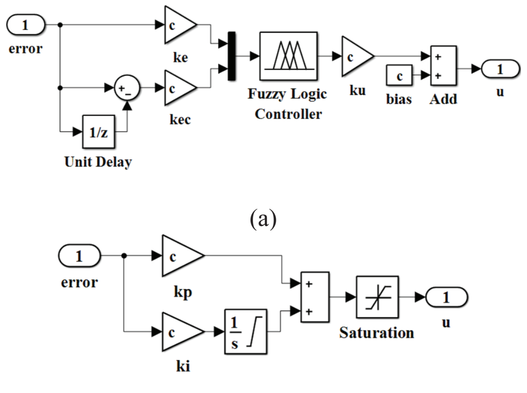

(a)

(b)

Fig. 9. Regulator modules in Simulink: (a) Fuzzy regulator and (b) PI regulator.

B. Experiments

The velocity regulation experiments with different controllers are conducted using the shown hardware platform. In these results, a_{rf} is the acceleration reference value output by regulator 1. The results of the Fuzzy-Fuzzy double closed-loop controller are presented in Fig. 10 (a). It can be observed that there is no overshoot in the velocity regulation process with this controller. When the given velocity is 0.6 m/s, the arising time and steady-state error of the controller are approximately 0.160 s and 0.038 m/s. The results of velocity regulation experiments with the PI-Fuzzy double closed-loop controller are shown in Fig. 10 (b). There is no overshoot in the velocity regulation process. When the given velocity is 0.6 m/s, the arising time and steady-state error of the controller are about 0.266 s and −0.010 m/s. Figure 10 (c) presents the results of velocity regulation experiments with the PI-PI double closed-loop controller at a given velocity of 0.6 m/s. There is no overshoot in the velocity regulation process in the figure, and the arising time and steady-state error of the controller are approximately 0.262 s and 0.021 m/s. The results of velocity regulation experiments with the Fuzzy-PI double closed-loop controller are shown in Fig. 10 (d). It can be seen that there is no overshoot in the velocity regulation process when the given velocity is 0.6 m/s. Its arising time and steady-state error of the controller are about 0.250 s and 0.009 m/s. Velocity regulation experiments with the PI single closed-loop controller are also conducted. Their results are shown in Figs. 11 (a) and 11 (b). When the given velocity is 0.4 m/s, the arising time and steady-state error of the controller are about 0.060 s and −0.049 m/s, with approximately 14.325% overshoot. When the given velocity is 0.6 m/s, the arising time and steady-state error of the controller are about 0.096 s and −0.016 m/s, and there is no overshoot. The velocity regulation experiments with the

Table 4: Detailed coefficients in different controllers

Controller	**PI-PI Controller**	**PI-Fuzzy Controller**	**Fuzzy-PI Controller**	**Fuzzy-Fuzzy Controller**
Regulator 1 in the outer loop	$k_p = 16$	$k_p = 16$	$k_e = 20$	$k_e = 20$
	$k_i = 0.05$	$k_i = 0.05$	$k_{ec} = 2.6$	$k_{ec} = 2.6$
	Lower limit $= -2$	Lower limit $= -2$	$k_u = 2.25/6$	$k_u = 2.25/6$
	Upper limit $= 2.5$	Upper limit $= 2.5$	bias $= 0.25$	bias $= 0.25$
Regulator 2 in the inner loop	$k_p = 6.5$	$k_e = 35$	$k_p = 6.5$	$k_e = 35$
	$k_i = 0.03$	$k_{ec} = 2.8$	$k_i = 0.03$	$k_{ec} = 2.8$
	Lower limit $= 0$	$k_u = 3/6$	Lower limit $= 0$	$k_u = 3/6$
	Upper limit $= 6$	bias $= 3$	Upper limit $= 6$	bias $= 3$

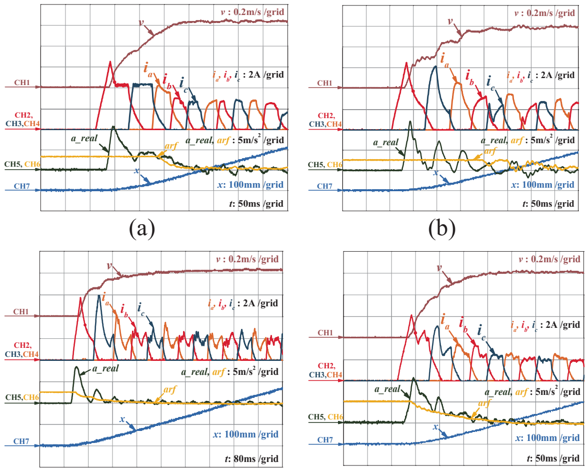

(a) (b) (c) (d)

Fig. 10. Experiment results of different controllers under 0.6 m/s: (a) Fuzzy-Fuzzy controller, (b) PI-Fuzzy controller, (c) PI-PI controller, (d) Fuzzy-PI controller.

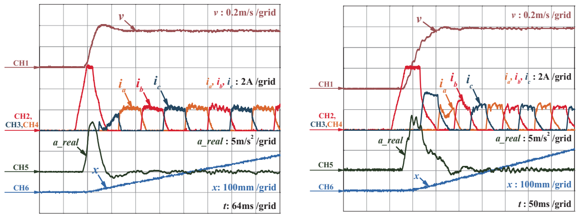

(a) (b)

Fig. 11. Experiment results of PI controller: (a) under 0.4 m/s and (b) under 0.6 m/s.

Fuzzy single closed-loop controller are shown in Fig. 12. There is no overshoot in the velocity regulation process when the given velocity is 0.6 m/s. Its arising time and steady-state error of the controller are about 0.150 s and 0.010 m/s.

On the other hand, from the invariable given velocity tests, it can be found that the single closed-loop Fuzzy controller, the double closed-loop Fuzzy-Fuzzy controller, and the double closed-loop Fuzzy-PI controller have better performances among the six controllers. To further investigate their stability and anti-disturbance ability, the given velocity is changed from 0.4 m/s to 0.6 m/s suddenly, and the velocity regulation processes of the three controllers are shown in Fig. 13.

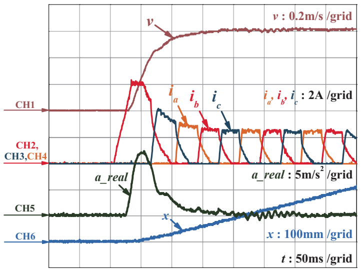

Fig. 12. Experiment results of Fuzzy controller under 0.6 m/s.

Figure 13 (a) is the given velocity step test results of the Fuzzy controller. It is shown that the real-time velocity follows the given velocity well, and it responds quickly. The parameters in a single closed-loop controller are less than those in a double closed-loop controller, so the parameter adjustment of the Fuzzy controller is easy. Figure 13 (b) is the variable given the velocity test results of the Fuzzy-Fuzzy controller, which shows that it responds slowly, and the velocity waveform is not stable. It indicates that the Fuzzy-Fuzzy cannot work well in variable-given velocity tests. Figure 13 (c) is the variable given the velocity test results of the Fuzzy-PI controller. It can be seen that the real-time velocity follows the given velocity well with a quick response.

C. Analysis

The control performances of the six controllers shown in the experiments are compared in Table 4. In the arising time column, the values of the PI controller at 0.4 m/s and 0.6 m/s are 0.060 s and 0.096 s, and those of the Fuzzy controller at 0.4 m/s and 0.6 m/s are 0.096 s and 0.150 s. They are shorter than those of four double closed-loop controllers under the same given velocity. That means that single closed-loop controllers are more flexible, and they have quicker

Table 5: Velocity regulation performance comparisons of the six controllers in experiments

Controller	**Given Velocity (m/s)**	**Arising Time (s)**	**Steady-State Error (m/s)**	**Overshoot (%)**	**α (%)**	
					Invariable	**Variable**
Fuzzy-Fuzzy	0.4	0.151	0.012	0	7.77	9.9
	0.6	0.160	0.038	0	7.52	
PI-Fuzzy	0.4	0.213	0.028	0	7.48	–
	0.6	0.266	−0.010	0	8.11	
PI-PI	0.4	0.260	0.022	0	3.79	–
	0.6	0.262	0.021	0	3.86	
Fuzzy-PI	0.4	0.192	0.001	0	3.99	4.03
	0.6	0.250	0.009	0	3.94	
PI	0.4	0.060	−0.049	14.325	4.56	–
	0.6	0.096	−0.016	0	4.11	
Fuzzy	0.4	0.096	0.005	0	3.95	4.08
	0.6	0.150	0.010	0	3.93	

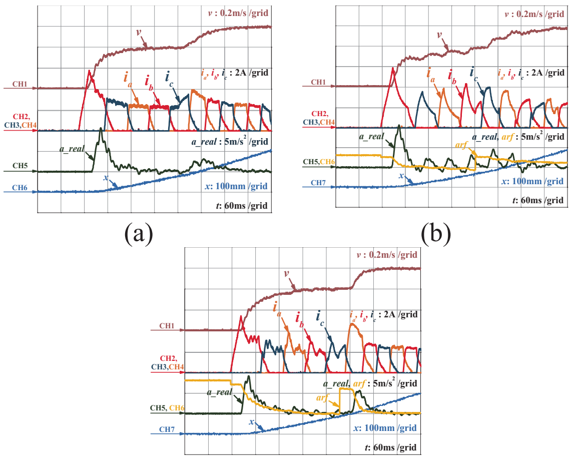

(a) (b)

(c)

Fig. 13. Variable given velocity test results: (a) Fuzzy controller, (b) Fuzzy-Fuzzy controller, (c) Fuzzy-PI controller.

response speeds. However, in the PI controller, experiment results appear unexpected steady-state errors and a 14.325% overshoot at a given velocity of 0.4 m/s. Among four double closed-loop controllers, the Fuzzy-Fuzzy controller has the shortest arising times. In the steady state error column, the values of the Fuzzy-PI controller can be maintained within 0.01 m/s. It is better than other controllers, including single closed-loop controllers and double closed-loop controllers. The static state errors in these experiments may be caused by the impacts of the coefficients of these controllers. DSRLM system is a nonlinear system. Its motion stroke is only 380 mm, which is a limited distance so the real-time regulation of these coefficients is difficult to realize. In general, the coefficients of these controllers are chosen to apply to a majority of situations in the SRLM velocity regulation system. Under these situations, these controllers can perform well without changing these coefficients. Nevertheless, achieving the optimal outcomes consistently is challenging, and static state errors might emerge in certain circumstances due to the coefficients. However, it can be observed from Tables 3 and 5 that significant static state errors rarely occur, indicating that the majority of the results are acceptable.

Comparing Tables 3 and 5, both the simulated results and the tested results of the PI controller appear big steady-state errors at a given velocity of 0.4 m/s. All steady-state errors of tested results are greater than those of simulated results. In addition, the arising times of tested results are different from those of simulated results. These differences between tested results and simulated results may be caused by the calculated frequency of the real-time simulator, the accuracy of flux linkage curves used in Fourier series nonlinear modeling, or the effect of mutual coupling characteristics between phase to phase.

The smaller the smoothness coefficient α, the better the stability of the system. In Table 5, “Invariable” shows the smoothness coefficients α of invariable given velocity tests, and “Variable” shows the smoothness coefficients α of the variable given velocity tests. The α values of the Fuzzy-Fuzzy controller and PI-Fuzzy controller are bigger than those of the other four controllers in invariable given velocity tests. The α values of the Fuzzy-PI controller keep the same level as the Fuzzy controller. The smoothness of real-time velocity with Fuzzy-PI controller and Fuzzy controller is great, both in invariable given velocity tests or variable given tests. The smoothness of real-time velocity with a Fuzzy-PI controller is better than that with a Fuzzy controller in variable-given velocity tests. In its process of parameter adjustment, we found that the Fuzzy-PI controller is flexible and easy to adjust. Above all, in the further velocity regulation of DSRLM, the Fuzzy-PI controller can be chosen.

V. CONCLUSION

In a velocity regulation system of a DSRLM, the velocity single closed-loop control employing either the PI regulator or the Fuzzy regulator is contrasted with the velocity-acceleration double closed-loop control in this paper. The velocity regulation control is executed using an RT-LAB digital controller. The velocity regulation experiments are carried out, and corresponding simulations are established in MATLAB. Moreover, the modules in MATLAB/Simulink are presented. Another contribution of this paper lies in comparing and analyzing the performances of different velocity regulation controllers on SRLMs through simulations and experiments. The establishment processes of different controllers are introduced in detail, and their specifications are provided. Through a succession of velocity regulation tests, the conclusion can be drawn that the Fuzzy-PI controller possesses the optimal velocity regulation performance in the DSRLM. These simulated and experimental experiences can serve as a reference for velocity regulation research on other SRLMs. Although the proposed velocity–acceleration double closed-loop control strategy demonstrates satisfactory performance for DSRLM velocity regulation, several aspects warrant further investigation. First, the current controller design relies on empirically tuned PI and Fuzzy parameters, and future work will focus on developing adaptive or self-tuning mechanisms to enhance robustness under varying operating conditions. Second, the strong nonlinearities and axial end effects inherent to SRLMs are not explicitly compensated in the control law; incorporating end-effect-aware models or data-driven compensation strategies is a promising direction. In addition, performance evaluation in this study is limited to low-speed and constant-load conditions. Future experimental validation under wider speed ranges, load disturbances, and parameter uncertainties will be conducted. Finally, comparisons with more advanced control approaches, such as model predictive control or learning-based methods, will be explored to further improve dynamic performance and broaden the applicability of the proposed framework.

ACKNOWLEDGMENTS

This work is supported by the Shenzhen Collaborative Innovation Special Plan International Cooperation Research Project under Grant GJHZ2024021811 4300002.

REFERENCES

[1] J. B. Bartolo, M. Degano, J. Espina, and C. Gerada, “Design and initial testing of a high-speed 45-kW switched reluctance drive for aerospace application,” *IEEE Transactions on Industrial Electronics*, vol. 64, no. 2, pp. 988–997, Feb. 2017.

[2] X. Cao, H. Yang, L. Zhang, and Z. Q. Deng, “Compensation strategy of levitation forces for single-winding bearingless switched reluctance motor with one winding total short circuited,” *IEEE Transactions on Industrial Electronics*, vol. 63, no. 9, pp. 5534–5546, Sep. 2016.

[3] H. Chen, H. Yang, Y. X. Chen, and H. H. C. Iu, “Reliability assessment of the switched reluctance motor drive under single switch chopping strategy,” *IEEE Transactions on Power Electronics*, vol. 31, no. 3, pp. 2395–2408, Mar. 2016.

[4] A. Chiba, K. Kiyota, N. Hoshi, M. Takemoto, and S. Ogasawara, “Development of a rare-earth-free SR motor with high torque density for hybrid vehicles,” *IEEE Transactions on Energy Conversion*, vol. 30, no. 1, pp. 175–182, Mar. 2015.

[5] H. Chen, Q. L. Wang, and H. H. C. Iu, “Acceleration closed-loop control on a switched reluctance linear launcher,” *IEEE Transactions on Plasma Science*, vol. 41, no. 5, pp. 1131–1137, May 2013.

[6] D. H. Wang, X. F. Du, D. X. Zhang, and X. H. Wang, “Design, optimization, and prototyping of segmental-type linear switched-reluctance motor with a toroidally wound mover for vertical propulsion application,” *IEEE Transactions on Industrial Electronics*, vol. 65, no. 2, pp. 1865–1874, Feb. 2018.

[7] J. F. Pan, N. C. Cheung, and Y. Zou, “Design and analysis of a novel transverse-flux tubular linear machine with gear-shaped teeth structure,” *IEEE Transactions on Magnetics*, vol. 48, no. 11, pp. 3339–3343, Nov. 2012.

[8] Z. Zhang, N. C. Cheung, K. W. E. Cheng, X. D. Xue, and J. K. Lin, “Direct instantaneous force control with improved efficiency for four-quadrant operation of linear switched reluctance actuator in active suspension system,” *IEEE Transactions on Vehicular Technology*, vol. 61, no. 4, pp. 1567–1576, May 2012.

[9] J. F. Pan, Y. Zou, G. Z. Cao, N. C. Cheung, and B. Zhang, “High-precision dual-loop position control of an asymmetric bilateral linear hybrid switched reluctance motor,” *IEEE Transactions on Magnetics*, vol. 51, no. 11, Nov. 2015.

[10] J. H. Du, D. L. Liang, L. Y. Xu, and Q. F. Li, “Modeling of a linear switched reluctance machine and drive for wave energy conversion using matrix and tensor approach,” *IEEE Transactions on Magnetics*, vol. 46, no. 6, pp. 1334–1337, Jun. 2010.

[11] D. H. Wang, C. L. Shao, X. H. Wang, and C. H. Zhang, “Performance characteristics and

preliminary analysis of low cost tubular linear switch reluctance generator for direct drive WEC," *IEEE Transactions on Applied Superconductivity*, vol. 26, no. 7, Oct. 2016.

[12] N. Alibeji and N. Sharma, "A PID-type robust input delay compensation method for uncertain Euler-Lagrange systems," *IEEE Transactions on Control Systems Technology*, vol. 25, no. 6, pp. 2235–2242, Nov. 2017.

[13] Y. D. Song, X. C. Huang, and C. Y. Wen, "Robust adaptive fault-tolerant PID control of MIMO nonlinear systems with unknown control direction," *IEEE Transactions on Industrial Electronics*, vol. 64, no. 6, pp. 4876–4884, Jun. 2017.

[14] T. Mahto and V. Mukherjee, "Fractional order fuzzy PID controller for wind energy-based hybrid power system using quasi-oppositional harmony search algorithm," *IET Generation Transmission & Distribution*, vol. 11, no. 13, pp. 3299–3309, Sep. 2017.

[15] X. Chen, J. Hu, M. Wu, and W. H. Cao, "T-S fuzzy logic based modeling and robust control for burning-through point in sintering process," *IEEE Transactions on Industrial Electronics*, vol. 64, no. 12, pp. 9378–9388, Dec. 2017.

[16] D. Sun, Q. F. Liao, and H. L. Ren, "Type-2 fuzzy modeling and control for bilateral teleoperation system with dynamic uncertainties and time-varying delays," *IEEE Transactions on Industrial Electronics*, vol. 65, no. 1, pp. 447–459, Jan. 2018.

[17] S. Demirbas, "Self-tuning fuzzy-PI-based current control algorithm for doubly fed induction generator," *IET Renewable Power Generation*, vol. 11, no. 13, pp. 1714–1722, Nov. 2017.

[18] M. A. Fnaiech, "A measurement-based approach for speed control of induction machines," *IEEE Journal of Emerging and Selected Topics in Power Electronics*, vol. 2, no. 2, pp. 308–318, Jun. 2014.

[19] M. H. Khooban, M. Sadeghi, T. Niknam, and F. Blaabjerg, "Analysis, control and design of speed control of electric vehicles delayed model: Multi-objective fuzzy fractional-order controller," *IET Science Measurement & Technology*, vol. 11, no. 3, pp. 249–261, May 2017.

[20] A. Ashouri-Zadeh, M. Toulabi, S. Bahrami, and A. M. Ranjbar, "Modification of DFIG's active power control loop for speed control enhancement and inertial frequency response," *IEEE Transactions on Sustainable Energy*, vol. 8, no. 4, pp. 1772–1782, Oct. 2017.

[21] I. Mahmoud and H. Rehaoulia, "Nonlinear modelling improvement approach for linear actuator," in *Proc. International Conference on Control, Automation and Diagnosis (ICCAD)*, Hammamet, Tunisia, pp. 482–486, Jan. 2017.

Hao Chen (Senior Member, IEEE) received his B.S. and Ph.D. degrees in electrical engineering from the Department of Automatic Control, Nanjing University of Aeronautics and Astronautics, Nanjing, China, in 1991 and 1996, respectively. In 1998, he became an Associate Professor at the School of Information and Electrical Engineering, China University of Mining and Technology, Xuzhou, where he has been a Professor since 2001. From 2002–2003, he was a Visiting Professor at Kyungsung University, Busan, Korea. Since 2008, he has also been an Adjunct Professor at the University of Western Australia, Perth, Australia. He is the author of one book and has authored more than 300 papers. He is a holder of 15 US patents, 23 Australian patents, one Danish patent, seven Canadian patents, three South African patents, 10 Russian patents, 86 Chinese invention patents, and six Chinese Utility Model patents.

Sergei Brovanov received the engineer degree from the Industrial Electronics Department, Novosibirsk Electrotechnical Institute in 1987. In 1999, he became an Associate Professor in the Industrial Electronics Department, Novosibirsk State Technical University, where he has been a Professor since 2013. In 2004, he was a Visiting Professor at Ulsan University, South Korea. He is the author of one book and has authored more than 150 papers. He has 17 Russian patents. His current research interests include semiconductor converters, vector PWM of multilevel NPC converters, and semiconductor converters for electrical energy storage systems. In 1996–1997, he was awarded a scholarship from the Swiss Academy of Engineering Sciences. In 2023, he was awarded the State Prize of the Novosibirsk Region for the development of intelligent power electronic systems and devices. Brovanov currently is a professor in the electronics and electrical engineering Department at Novosibirsk State Technical University.

Javokhir Toshov received the B.S. degree from Navoi State Mining Institute, Navoi, Uzbekistan, in 1999, M.S. degree from Tashkent State Technical University, Tashkent, in 2002, Dr.Sci. in 2017, and Professor of the Tashkent State Technical University since 2020. He has about 250 published and reviewed works. His current research interests include drilling control for drilling operations, as well as electrical installations and motors for mining equipment. For many years he worked as the dean of the energy faculty, and today he works as the head of the department at Tashkent State Technical University.

Jinfu Liu received the B.S. degree in Mechanical and Electrical Engineering, from Northeast Forestry University, Harbin, Heilongjiang, China, in 2017, M.S. degree from the School of Electrical Engineering, China University of Mining and Technology, Xuzhou, Jiangsu, in 2021, and is currently pursuing a Ph.D. degree in electrical engineering at the China University of Mining and Technology, Xuzhou. His research interests include switched reluctance linear motor control, ocean wave power generation, and electric vehicles.

Xing Wang received the B.S. degree from China University of Mining and Technology, Xuzhou Jiangsu, China, in 1996, and M.S. degree from China University of Mining and Technology, Xuzhou Jiangsu, in 1999. In 2007, she became an Associate Professor with China University of Mining and Technology, Xuzhou, China. She is a holder of four US Patents, nine Australian Patents, two Canadian Patents, four Russian Patents, 12 Chinese Invention Patents, three Chinese Utility Model Patents, and has authored 15 papers.

Antonino Musolino received his Ph.D. degree in electrical engineering from the University of Pisa, Pisa, Italy, in 1994. He is currently a Full Professor of electrical machines at the University of Pisa. He has co-authored more than 130 papers published in international journals/conferences. He holds three international patents in the field of magnetorheological devices. His current research activities are focused on linear electromagnetic devices, motor drives for electric traction, and the development of analytical and numerical methods in electromagnetics. Musolino was involved in the organization of several international conferences, where he has served as the session chairman and an organizer, and as a member of the editorial board.

Nurkhat Zhakiyev is a computer modeler of energy systems and physical processes. Developed modeling tools and data science for Energy and Environment economics. Climate Change Mitigation Analyst. He is now a Senior Research, Assoc. Prof., Head of the Department of Science and Innovation, Astana IT University.

Murat Shamiyev received the B.S. and M.S. degrees from Tashkent State Technical University, Tashkent, Uzbekistan, in 1999 and 2001, respectively. He served as a Professor's Assistant at the Department of Electromechanics and Electrotechnology, Faculty of Energy, Tashkent State Technical University from 2001 to 2005. Following that, he held the position of Head Specialist at Azia Triol Joint Venture (Russia and Uzbekistan) from 2005 to 2007. Subsequently, he served as a Technical Director at "Энерготежаш" LLC from 2007 to 2010. He then took on the role of Director at Techno Energo Group LLC. Currently, he holds the position of Head Engineer at Techno Energo Group LLC.

Abror Abidovich Pulatov is the head of the Department of Electrical Machinery and Electrical Technology of Tashkent State Technical University. His main monographs include "Thermal Operating Conditions of Induction Crucible Furnaces," "Instruction Manual for Electrical Equipment and Power Supply in Mining Enterprises," "Guide to Laboratory Work in Electrical Technology Fundamentals," and "Design and Operation of Electrical Technology Devices." His main research directions include the research on inductors of smelting devices, and monitoring, control and regulation of asynchronous motor devices. He is a Member of the Academic Committee of the International Joint Research Center for New Energy Electric Vehicle Technology and Equipment in Central and Eastern European Countries of the Ministry of Science and Technology of China, member of the Academic Committee of the International Cooperation Joint Laboratory for New Energy Generation and Electric Vehicles of Jiangsu Province's Universities, and member of the New Energy Generation and Electric Vehicles Foreign Expert Studio in Jiangsu Province.

Multi-Objective Optimization of Permanent Magnet Motor Based on the Stochastic Collocation Method

Haichuan Cao, Jian Xiao, Chengzhou Yang, and Jingwei Zhu

College of Marine Electrical Engineering
Dalian Maritime University, Dalian 116026, China
haichuan@dlmu.edu.cn, xj2220190706@dlmu.edu.cn, 292575223@qq.com, zjwdl@dlmu.edu.cn

Abstract – In this paper, a novel multi-objective optimization method based on the stochastic collocation method (SCM) is proposed, and the effectiveness of this method is verified by finite element method (FEM) simulations on a permanent magnet synchronous motor (PMSM) with a two-layer Halbach array structure for electric vehicles (EVs). First, the proposed optimization method is introduced; then, the multi-objective optimization problem of the PMSM is defined; third, the optimization parameters are divided into two different subspaces according to their influence on the optimization objective; finally, each subspace is optimized sequentially. The FEM results show that the optimized motor has higher torque, lower torque ripple, and higher sinusoidal back-EMF.

Index Terms – Design optimization, finite element method, multi-objective optimization, permanent magnet synchronous motor, stochastic collocation method, two-layer Halbach array.

I. INTRODUCTION

Electric vehicles (EVs) are powered by a battery pack and an electric motor. EVs do not produce tailpipe emissions, which helps protect the environment and improve air quality. They have become increasingly popular in recent years. Among drive motors, permanent magnet synchronous motors (PMSMs) are a promising choice because of their high energy density, high efficiency, compact size, and fast response. PMSMs are widely used for EV traction (e.g., BYD and NIO) [1, 2].

The key to improving the performance of EVs is to improve the performance of PMSMs. Research on new topologies and the optimization of design parameters are two main ways to improve the performance of the PMSMs. In recent years, many new topologies have been designed and applied to PMSMs. In [3], a consequent pole (CP) rotor topology is proposed in which the permanent magnet (PM) volume is reduced when compared with the conventional surface PMSM of EVs. Multilayer windings and non-ferromagnetic barriers are proposed to increase the torque density. In [4], a novel rotor structure with a magnetic stripe is proposed, based on the “dual stator with Halbach array” topology of the PMSM, which leads to a PMSM with greater power density. The results show that the novel rotor structure can increase the average torque. In [5], a novel interior PM rotor topology referred to here as Y-type is proposed. The new design can combine the goodness of both V- and spoke-type rotors for an FSCW stator. The goals of achieving maximum efficiency, minimum cost, and wide CPSR are accomplished in the proposed Y-type FSCW IPMSM. In [6], a novel low-cost consequent-pole permanent magnet (CPM) synchronous machine structure is proposed, considering the reluctance torque utilization. The results show that the ISCP-PMSM can obtain an almost equivalent torque and torque ripple, but with reduced PM (NdFeB) usage and cost when compared to the SPMSM.

For the optimization of design parameters, in [7], a novel automatic design method for PM motors using a Monte Carlo tree search is proposed. The optimal motor structures are determined through a tree search, in which the motors with different numbers of poles, current phase angles, PM configurations, and numbers of PMs are simultaneously considered. In [8], a robust optimization design method considering magnet material uncertainties is proposed for PM machines. The Kriging surrogate model and non-dominated sorting genetic algorithm II (NSGA-II) are adopted to solve the optimization model. In [9], a synergetic optimization approach considering both PM and armature airgap harmonics simultaneously is proposed to improve the power factor of the PM vernier machine. In [10], aiming at the uncertainty analysis method (MEAM) used in electromagnetic compatibility simulation, an uncertainty analysis method based on MEAM is proposed to test whether the uncertainty analysis method converges, and improve the efficiency and accuracy of the uncertainty analysis method. In [11], the design of experiments with the Taguchi method has been used, which is a

Submitted On: July 20, 2025
Accepted On: December 11, 2025

https://doi.org/10.13052/2025.ACES.J.401210

simple and effective optimization method and requires a small number of experiments and experience. To select the best combination in multi-objective optimization, the TOPSIS method has been utilized to prioritize the optimal solutions.

Generally, motor design and optimization follow Pareto's law, that is, the initial electromagnetic design of the motor accounts for 20% of the total time cost, and the motor parameter optimization and adjustment after the initial design account for 80%. This is because there are many design parameters of the motor, and the traditional optimization method is time-consuming; the parameters are highly nonlinear and strongly coupled. Combining individually optimized parameters does not necessarily yield a globally optimal system.

The stochastic collocation method (SCM) is a non-embedded uncertainty analysis method, which has the characteristics of high calculation accuracy and high calculation efficiency, so it is very suitable for the application of optimization design [12, 13]. Therefore, this paper selects it as an extended application of the uncertainty analysis method in optimization design and discusses its optimization performance in detail. The structure of this paper is as follows. Section II describes the principle of SCM. Section III investigates an example study for the optimization of a PMSM based on finite element method (FEM). Specific implementation and results are provided in section IV. Section V concludes the paper.

II. PRINCIPLE OF STOCHASTIC COLLOCATION METHOD

SCM performs uncertainty analysis without modifying the solver. It is, therefore, a non-intrusive method. The mathematical basis of this method is the Lagrange interpolation theorem.

In many practical problems, relationships between variables are not given by explicit functions and must be determined from experiments or observations. However, if a certain physical quantity in practice is observed and the corresponding observation value is obtained in several different places, interpolation technology can be used. The Lagrange interpolation method constructs a polynomial that exactly matches the observed values at the interpolation points. Such a polynomial is called a Lagrange interpolation polynomial. The specific form of one-dimensional Lagrange interpolation is:

$$y(x) = Lag(f(x)) = \sum_{j=0}^{m} f(x_j) l_j(x), \tag{1}$$

where $y(x)$ is the m-th polynomial of the independent variable x and is the function used to approximately describe $f(x)$; $x_j (j = 0, 1, \ldots, m)$ is the $m+1$-th interpolation point, while the function value is known at the interpolation point, and $l_j(x)$ is:

$$l_j(x) = \frac{(x-x_0)\cdots(x-x_{j-1})(x-x_{j+1})\cdots(x-x_m)}{(x_j-x_0)\cdots(x_j-x_{j-1})(x_j-x_{j+1})\cdots(x_j-x_m)}. \tag{2}$$

For the general polynomial approximation theory, the random variable polynomial form is used to approximate the unknown FEM results. According to the Lagrange interpolation theorem, the approximate random variable polynomial can be obtained by following strategies [14]:

1. Regard the random variable as the independent variable x in equation (1);
2. Select certain points according to the random variable, which correspond to the interpolation point x_j in equation (1);
3. When FEM simulation is carried out at these points, the simulation results can be regarded as the function value $f(x_j)$ at the interpolation point in equation (1);
4. By using the Lagrange interpolation formula as shown in equation (1), a random variable polynomial can be obtained, which can be regarded as the result of FEM uncertainty analysis. The mathematical expression of the above process is:

$$\begin{aligned}\widetilde{FEM}_{\mathrm{SCM}}(\xi^1) &= Lag(\widetilde{FEM}_{\mathrm{SCM}}(\xi^1)) \\ &= \sum_{j=0}^{M} FEM_{\mathrm{SCM}}(\xi_j^1) l_j^1(\xi_j^1),\end{aligned} \tag{3}$$

where ξ^1 is a random variable introduced by uncertain input, and ξ^1 represents a random variable involving only one dimension in equation (3). $\widetilde{FEM}_{\mathrm{SCM}}(\xi^1)$ is the result of uncertainty analysis in the form of polynomials of random variables, and it is the approximate function of the real result of $\widetilde{FEM}_{\mathrm{SCM}}(\xi^1)$. ξ^1 represents the interpolation point selected according to random variables, which is called the collocation point in SCM. $\widetilde{FEM}_{\mathrm{SCM}}(\xi^1)$ represents the simulation results after a deterministic FEM simulation at the collocation point ξ^1. Finally, $l_j^1(\xi_j^1)$ is the Lagrange polynomial at the matching point.

Equation (3) gives the basic principle of SCM in the simulation analysis of FEM uncertainty, but only when the random variable is one-dimensional. In the case of multidimensional random variables, it is necessary to use the multidimensional Lagrange interpolation theorem. The interpolation point in the multidimensional Lagrange interpolation theorem is in the form of a tensor product in the one-dimensional case:

$$\begin{aligned}\widetilde{FEM}(\xi) &= (U_{FEM}^{i_1} \otimes U_{FEM}^{i_2} \otimes \cdots \otimes U_{FEM}^{i_1}) \\ &= \sum_{j_1=0}^{m_1} \cdots \sum_{n_1=0}^{m_n} FEM_{\mathrm{SCM}}(\xi_{j_1}^{i_1}, \ldots, \xi_{j_n}^{i_n}), \\ &\quad \times (a_{j_1}^{i_1} \otimes \cdots \otimes a_{j_n}^{i_n}) \end{aligned} \tag{4}$$

where $a_j^i = Lag_j^i(\xi)$ represents the Lagrange interpolation formula at the point j in the i-th dimension, such as in equation (2), $U_{FEM}^i = \sum_{j=0}^{m_i} FEM_{\mathrm{SCM}}(\xi_j^i) \times a_j^i$ denotes the global Lagrange interpolation formula in i-th dimension, such as equation (3), and m_i represents the number of matching points in dimension i.

Equation (4) is the calculation equation of SCM, in which the number of random variables is n and the total number of collocation points is $M = m_{i_1} \times \cdots \times m_{i_n}$. Based on equation (4), an FEM uncertainty analysis problem can be transformed into M deterministic FEM simulation problems, and the results of uncertainty analysis in the form of random variables are obtained.

In the optimization process, the parameters to be optimized also change within a certain range. If the range is treated as a random variable with a uniform distribution, the optimization process can be equivalent to an uncertainty analysis problem. The one-to-one correspondence between the value range $[A_{min}, A_{max}]$ and the random variable is:

$$A(\xi_i) = \frac{A_{\max} + A_{\min}}{2} + \frac{A_{\max} - A_{\min}}{2} \times \xi_i, \tag{5}$$

where ξ_i is the random variable obeying the uniform distribution in the range of $[-1, 1]$.

According to the generalized polynomial chaos theory, SCM uses the Legendre polynomials to deal with uncertainty analysis problems with random variables of uniform distribution. The first terms of Legendre polynomials in one dimension are [15]:

$$\begin{cases} \varphi_0(\xi_i) = 1 \\ \varphi_1(\xi_i) = \sqrt{3}\xi_i \\ \varphi_2(\xi_i) = \dfrac{\sqrt{5}}{2}(3\xi_i^2 - 1) \\ \varphi_3(\xi_i) = \dfrac{\sqrt{7}}{2}(5\xi_i^3 - 3\xi_i). \end{cases} \tag{6}$$

According to the theory above, the core idea of SCM is to use the random variable polynomials to replace the FEM simulation process, and then the agent model $\widetilde{FEM}_{SCM}(\xi)$ can be sampled to obtain the uncertainty analysis results. For the optimization problem, we can also build a similar agent model and then use the exhaustive method to obtain the optimization results. As SCM has excellent computational efficiency, the establishment of the agent model only requires several forward FEM simulations, and the number of simulations is the number of collocation points. Unlike the traditional intelligent optimization algorithm, which requires repeated iterations, the proposed algorithm does not need iterations, but only a single computation; the efficiency of the proposed optimization algorithm is obviously better. However, the number of collocation points grows exponentially with the dimensionality of stochastic variables; a manifestation of the curse of dimensionality. With numerous parameters to identify, the required forward simulations increase combinatorially, thereby undermining the computational efficiency intrinsic to SCM. This inherent limitation restricts the proposed optimization framework to applications involving only a limited set of parameters. Therefore, a sensitivity analysis will be introduced in the following section to address this limitation.

III. OPTIMIZATION EXAMPLE OF A DOUBLE-LAYER HALBACH PERMANENT MAGNET ARRAY MOTOR

Figure 1 shows a brief flow chart of the application of the SCM optimization method for the double-layer Halbach PM array motor.

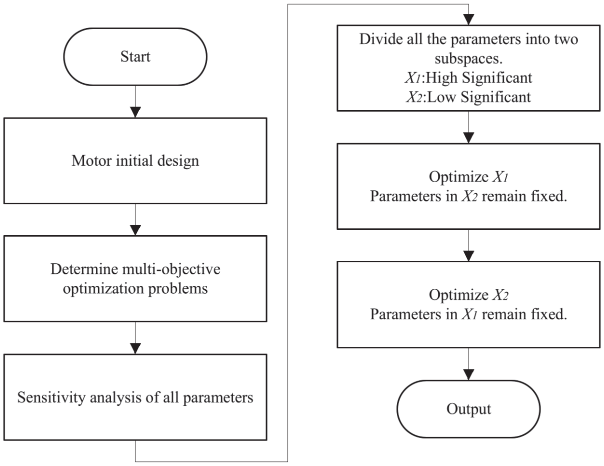

Fig. 1. Flowchart of the SCM multi-objective optimization method for the Halbach motor.

Step 1: According to the practical application and design requirements of the motor, determine the initial design parameters, including structural parameters and electromagnetic parameters.

In this example, the double-layer Halbach PM array slotless motor is designed for the application of EVs. Figure 2 shows the structure of the 4-pole PM rotor with the double-layer Halbach PM array structure and the magnetization direction of the PM.

As shown in Fig. 2, the array consists of T_1 (green) and T_2 (purple) PMs arranged at regular intervals. The two types of PMs are magnetized in parallel, but the magnetizing direction is different. The magnetization direction of T_1 PM is parallel to the radial centerline, while that of the T_2 PM is perpendicular to the radial centerline. The PMs of two shapes are arranged at intervals according to the magnetizing direction in the figure to form a Halbach array. Because the magnetic fields of the PMs can be superimposed, the double-layer Halbach array is equivalent to the superposition of its upper and lower layers.

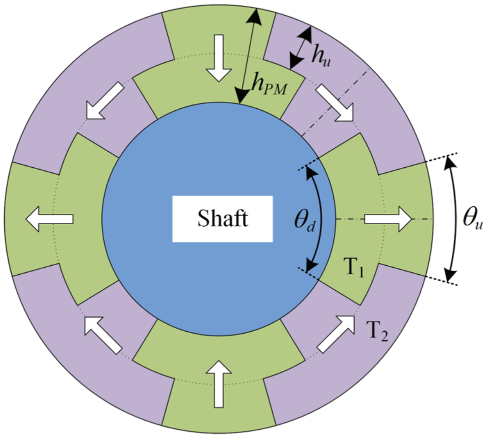

Fig. 2. Rotor structure with double-layer Halbach array.

In this paper, the Halbach array near the stator is called the upper layer (subscript "u"), and the layer near the rotor shaft is called the lower layer (subscript "d"). As shown in Fig. 2, the ratio of upper and lower layer angles, θ_u and θ_d, to rotor pole angle π/p is defined as the upper pole arc coefficient $\alpha_u = p\theta_u/\pi$ and lower-layer pole arc coefficient $\alpha_d = p\theta_d/\pi$, respectively. Thus, the structure size of the double-layer Halbach PM array has two defined parameters: α_u and α_d. At the same time, for the convenience of optimization, the parameter $\beta_{PM} = h_u/h_{PM}$ is defined as the ratio of the thickness of the upper PM to the total PM thickness, and PM_{TRS} is defined as the tangential radius size that can be reduced by the PM. A higher value of this parameter indicates less PM material is used.

As shown in Fig. 2, the two-layer magnet structure can effectively adjust the flux distribution and reduce harmonic distortion. In our previous work [16], it was shown that if α_u and α_d are exchanged, *THDB* remains nearly unchanged, but the fundamental flux density B_{rm1} decreases by about 8%, which leads to a reduction of T_{avg}. Therefore, the optimization should be performed within the range of $\alpha_u < \alpha_d$. The electrical parameters and initial design parameters of the motor are presented in Table 1.

Table 1: Specifications and initial design parameters of the motor

Parameter	Description	Unit	Value
P_N	Rated power	kW	4.9
n	Rated speed	r/min	7500
I_N	Rated current	A	15
D_{SO}	Stator outer diameter	mm	46
l	Axial length	mm	80
N_{ph}	Number of phases		3
p	Number of pole pairs		4
α_u	Upper pole arc coefficient		0.4
α_d	Lower pole arc coefficient		0.6
g	Air gap	mm	1.0
h_{PM}	Total PM thickness	mm	11
h_u	Thickness of upper PM	mm	6.6
β_{PM}	Ratio of upper and total PM		0.6
PM_{TRS}	PM of tangential reducible size	mm	1.0

Table 2: Parameters to be optimized and their value range

Parameter	Initial Value	Range
α_u	0.4	0.3~0.7
α_d	0.6	0.2~0.8
g(mm)	1.0	0.5~1.5
h_{PM}(mm)	11	11~14
β_{PM}	0.6	0.3~0.7
PM_{TRS}(mm)	1.0	0~2

Step 2: Determine the SCM multi-objective optimization problem, including the determination of the parameters to be optimized, the multi-objective optimization model, and selection criteria. Selecting six of the more significant parameters according to experience as the parameters to be optimized. The selected parameters and the range to be optimized are shown in Table 2.

The optimization objectives for the motor therefore include average torque, torque ripple, and the sinusoidal quality of the back-EMF waveform. In this application, the optimization problem can be defined by:

$$\min : \begin{cases} f_1(x_s) = -T_{avg} \\ f_2(x_s) = THD\% \\ f_3(x_s) = T_{ripple} \end{cases}, \tag{7}$$

where x_s are optimization parameters, and T_{avg}, $THD\%$, and T_{ripple} are three optimization objectives, which represent average torque, distortion rate of back-EMF waveform, and torque ripple, respectively. In the field of electric machine optimization, the weighted-sum single-objective approach is prevalent in engineering-oriented applications. In order to facilitate the selection of the optimal solution in an example, the selection criteria can be defined as:

$$\min: F = w_1 \frac{T_{avg\_initial}}{T_{avg}} + w_2 \frac{THD\%}{THD\%_{initial}} + w_3 \frac{T_{ripple}}{T_{ripple\_initial}}, \tag{8}$$

where $T_{avg\_initial}$, $THD\%_{initial}$, and $T_{ripple\_initial}$ are the average torque, distortion rate of the back-EMF waveform and torque ripple of the initial design, and w_1, w_2 and w_3 are weight factors. In this example, w_1, w_2 and w_3 are set to 0.6, 0.2, and 0.2, respectively. A single objective function can provide a fast optimization convergence process.

Step 3: Sensitivity analysis of all parameters to be optimized.

Sensitivity analysis is suitable for high-dimensional optimization problems. FEM provides high accuracy but is time-consuming. The increase of each parameter to be optimized will lead to an increase in the exponential level of FEM sampling time cost, and sensitivity analysis helps significantly reduce the computation time.

Step 4: Divide all the parameters into different subspaces.

Referring to the results of the sensitivity analysis in Step 3, input parameters are divided into two subspaces based on their influence on the output: highly significant and less significant.

Step 5: Optimize subspace X_1.

In this step, it is determined that the parameters in subspace X_2 remain unchanged; the parameters in subspace X_1 are optimized, and the optimized parameters are passed to the next subspace.

Step 6: Optimize subspace X_2.

Like the previous step, when optimizing subspace X_2, ensure that the optimization results of subspace X_1 from the previous step remain unchanged, and optimize the parameters in subspace X_2.

Step 7: Output the optimization results

The above seven steps constitute a complete optimization process. After optimization, the results can be substituted into FEM for verification, and the performance parameters before and after optimization are compared.

IV. IMPLEMENTATION AND RESULTS

First, local sensitivity analysis is carried out, and all parameters are divided into two different subspaces to reduce the computational burden. Second, the proposed multi-objective optimization based on SCM is studied. Then, the accuracy of SCM is verified using FEM results. Finally, the optimal solution is compared with the initial design results, and the results are analyzed and discussed.

A. Sensitivity analysis

In order to reduce the computational burden, the parameters to be optimized are divided into different subspaces, and the sensitivity of the parameters is analyzed. Since the model is based on FEM, there is no clear mathematical expression between input and output, so the incremental change method is used to determine sensitivity. Because different output parameters have different units, the normalized sensitivity expression is [17]:

$$S_i = \left| \frac{[f(\boldsymbol{x}_0 \pm \Delta \boldsymbol{x}_i) - f(\boldsymbol{x}_0)]/f(\boldsymbol{x}_0)}{\pm \Delta \boldsymbol{x}_i / \boldsymbol{x}_i} \right|, \tag{9}$$

where S_i is the sensitivity studied and $f(x)$ is the objective function. In this paper, increment $\Delta \boldsymbol{x}_i$ is determined to be ±10% and ±20% of the initial value, respectively.

There are six parameters to be determined with sensitivity. Each parameter requires four FEM simulations (−20%, −10%, 10%, 20%). Together with the simulation of the initial parameters, a total of $25 \times (6 \times 4 + 1)$ FEM samples are required.

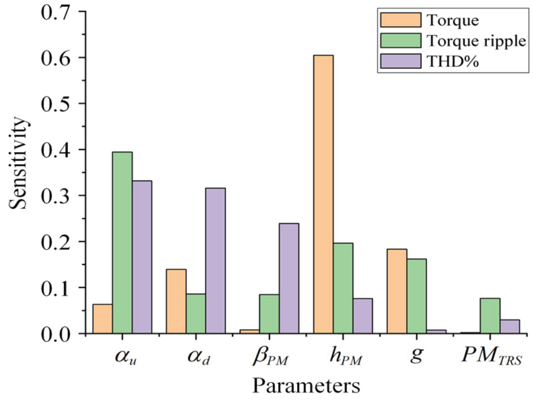

Fig. 3. Local sensitivity indices of torque, distortion rate of back-EMF waveform, and torque ripple.

The results of the sensitivity analysis are shown in Fig. 3. According to the results, the parameters to be optimized are divided into two subspaces. The parameters in subspace X_1 have a significant influence on the optimization objectives, including three parameters α_u,

α_d, and h_{PM}. The parameters in subspace X_2 have a less significant influence on the optimization objectives, including the remaining three parameters of g, β_{PM}, and PM_{TRS}.

B. Sequential subspace optimization

According to the SCM optimization method in the second section, the sequential optimization of X_1 and X_2 subspaces is carried out, respectively. The collocation points for the X_1 and X_2 subspaces are selected in the form of a tensor product in equation (4) using the zeros of fifth-order Legendre polynomials in equation (5). These points are presented in equations (10) and (11), respectively.

$$X_1 = \{\alpha_u, \alpha_d, h_{PM}\} = \{0.32, 0.39, 0.50, 0.61, 0.68\} \otimes \{0.23, 0.34, 0.50, 0.66, 0.77\} \otimes \{11.14, 11.69, 12.50, 13.31, 13.86\}. \tag{10}$$

$$X_2 = \{\beta_{PM}, g, PM_{TRS}\} = \{0.32, 0.39, 0.50, 0.61, 0.68\} \otimes \{0.55, 0.73, 1.00, 1.27, 1.45\} \otimes \{0.09, 0.46, 1.00, 1.54, 1.90\}. \tag{11}$$

The results of parameter identification calculated using SCM are $X_1 = \{\alpha_u, \alpha_d, h_{PM}\} = \{0.37, 0.79, 12.49\}$ and $X_2 = \{\beta_{PM}, g, PM_{TRS}\} = \{0.31, 0.51, 0.39\}$.

It is worth noting that, due to the introduction of sensitivity analysis, the sequential subspace optimization method is adopted and the optimization efficiency is greatly improved. For this case, the fifth-order zeros of Legendre polynomials are selected according to equation (6) and are in the form of a tensor product as shown in equation (4). In the context of finite element simulation for electrical machines, a single simulation sample requires approximately 5 minutes. If a single-level method were used to optimize all six parameters, $5^6 = 15{,}625$ FEM samples would be required. In contrast, the proposed sequential subspace method needs only $2 \times 5^3 = 250$ FEM samples, reducing the number of required simulations by 98.4% and greatly improving efficiency. Meanwhile, computational time was substantially reduced from $5 \times 15625/60 = 1302$ hours to $5 \times 250/60 = 20.8$ hours. In addition, verification through FEM showed that the optimized parameter grouping does not affect the final trend.

Figures 4 and 5 illustrate the relationships of the objective function in equation (8) with the parameters of subspaces X_1 and X_2, based on the SCM formulation in equation (4). The red star in Figs. 4 and 5 represents the optimization result given by SCM, which clearly verifies the effect of SCM in the area where the optimal value (i.e., the minimum value) is located.

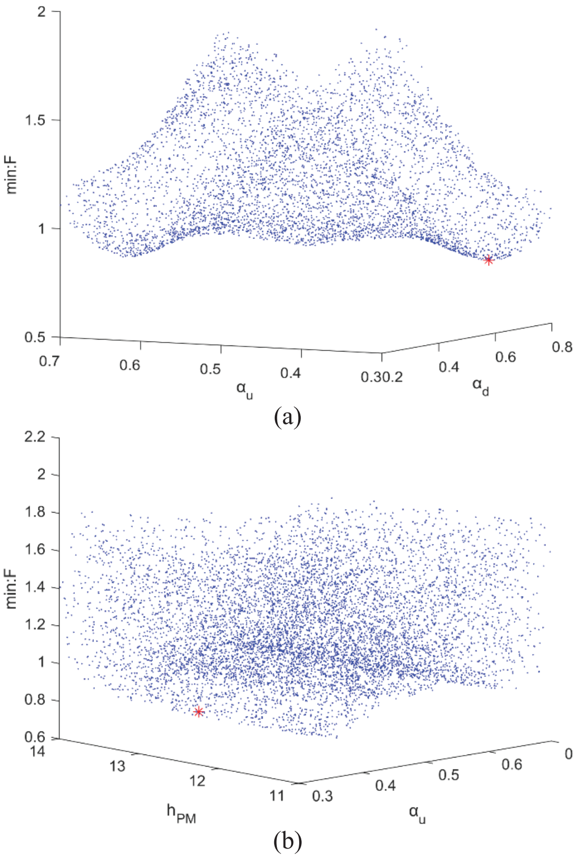

(a)

(b)

Fig. 4. Relationship between objective function and optimization variables in subspace X_1: (a) relationship between F and α_u, α_d and (b) relationship between F and h_{PM}, α_u.

C. Verification of SCM accuracy

Since optimization relies on SCM, it is necessary to verify its accuracy. SCM using equation (4) and FEM are used to sample the torque, sinusoidal distortion rate of the back-EMF waveform, and torque ripple, respectively. When optimizing X_1, X_2 takes the initial design value. Table 3 shows the parameters obtained after the two SCM optimizations, along with the corresponding FEM results.

The initially optimized structural parameters are: $\{\alpha_u, \alpha_d, h_{PM}, \beta_{PM}, g, PM_{TRS}\} = \{0.37, 0.79, 12.49, 1.0, 0.6, 1.0\}$. The final optimized structural parameters are: $\{\alpha_u, \alpha_d, h_{PM}, \beta_{PM}, g, PM_{TRS}\} = \{0.37, 0.79, 12.49, 0.56, 0.31, 0.39\}$; the average torque of the motor is 5.07 N·m, the sine wave distortion rate of back-EMF is 0.58%, and the torque ripple is 0.97%. These results yield the min $F = 0.78746$.

D. Comparison with genetic algorithm

To verify the superiority of the proposed algorithm, it is compared with the classical Genetic Algorithm

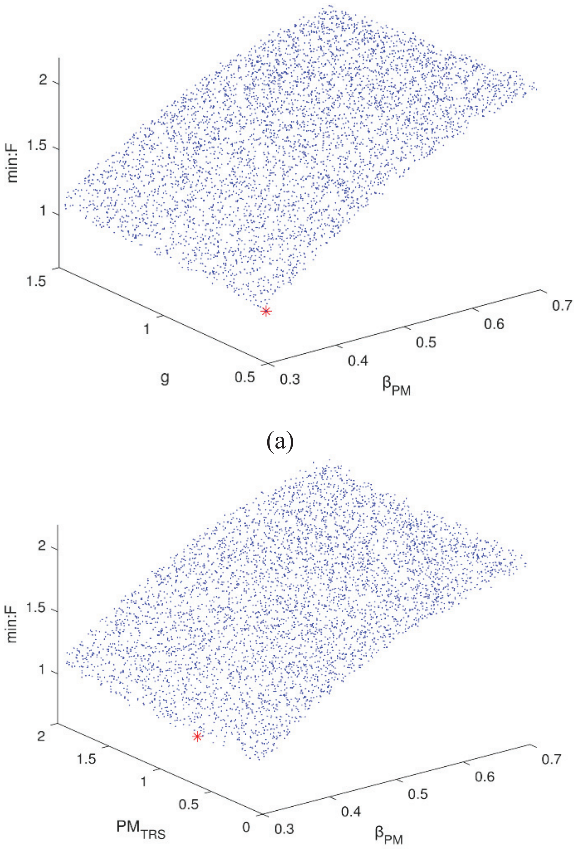

(a)

(b)

Fig. 5. Relationship between objective function and optimization variables in subspace X_2: (a) relationship between F and g, β_{PM} and (b) relationship between F and PM_{TRS}, β_{PM}.

Table 3: Optimization results of SCM and FEM

Parameter	**Initial Value**	$\boldsymbol{X_1}$ **Optimized**	$\boldsymbol{X_2}$ **Optimized**
α_u	0.4	0.37	0.37
α_d	0.6	0.79	0.79
h_{PM} (mm)	11	12.49	12.49
g (mm)	1	1	0.56
β_{PM}	0.6	0.6	0.31
PM_{TRS} (mm)	1	1	0.39
	FEM		
T_{avg} (N·m)	4.47	4.78	5.07
$THD(\%)$	1.11	1.22	0.58
$T_{ripple}(\%)$	1.26	1.11	0.97
	min $\boldsymbol{F}$		
	1	0.95709	0.78746

Table 4: Optimization results of GA (80-12)

Iteration times	**Simulation times**	**min** F
1	160	1
2	240	0.99353
3	320	0.99203
4	400	0.96367
5	480	0.93284
6	560	0.92226
7	640	0.90597
8	720	0.83544
9	800	0.78753
10	880	0.77665
11	960	0.77665
12	1040	0.77665

(GA). GA is a heuristic search algorithm that simulates the process of biological evolution and finds the optimal or near-optimal solution by iteratively evolving candidate solutions. In [18], the structural parameters of the motor to be optimized are first stratified based on sensitivity, and then NSGA-II is used to optimize multiple objective parameters. In [19], classical GA is used to optimize two typical electromagnetic compatibility problems, one configured with a population size of 60 for 20 iterations and the other with a population size of 60 for 10 iterations.

In this paper, three objective functions have been combined into one F function; therefore, classical GA is chosen. First, the pre-experiment is configured with a population size of 80 and conducted through 12 iterations. The results are shown in Table 4.

In addition to the GA configuration with a population size of 80 and 12 iterations (used for preliminary comparison in this study), we also tested a more common configuration with a population size of 30 and 20 iterations, as suggested in the literature. The results are shown in Table 5.

The crossover probability and mutation probability of the two sets of genetic algorithms are set to be the same, namely $p_c = 0.85$ and $p_m = 0.02$. The finally converged simulation results are: the average torque of the motor is 5.07 N·m, the sine wave distortion rate of back-EMF is 0.52%, and the torque ripple is 0.97%. These results make min $F = 0.77665$.

Finally, for reference, the optimized result for the composite objective function F using SCM methodology was 0.78746. For comparison, as can be seen from Table 4, the GA with a population size of 80 and 12 iterations reached a value of 0.78753 for the objective function F by the 9th generation. From Table 5, it is observed that the GA with a population size of 30 and 20 iterations achieved a slightly higher value of 0.78768 for F by the 18th generation. Under the same parameters, compared to the latter, the former can converge more quickly due to having more samples. Thus, the GA requires 630∼1040 FEM runs, which is much larger than the SCM's 250 runs.

Both GA cases confirm that SCM achieves comparable accuracy with far fewer FEM evaluations, while the GA needs many more iterations to converge.

Table 5: Optimization results of GA (30-20)

Iteration times	**Simulation times**	**min *F***
1	60	1
2	90	0.99703
3	120	0.99190
4	150	0.96867
5	180	0.96303
6	210	0.95720
7	240	0.95139
8	270	0.93949
9	300	0.93201
10	330	0.92726
11	360	0.91097
12	390	0.90336
13	420	0.86479
14	450	0.86267
15	480	0.84044
16	510	0.83531
17	540	0.81726
18	570	0.78768
19	600	0.77665
20	630	0.77665

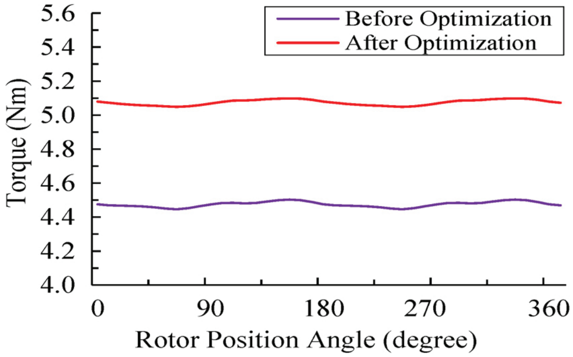

Fig. 6. Comparison of torque before and after optimization.

E. Results comparison

After validating the SCM model, the optimal solution in Figs. 4 and 5 is credible. Figures 6 and 7 show comparisons of torque and back-EMF waveforms between the optimal solution and the initial design, respectively, and a detailed numerical comparison is shown in Table 3. In the initial design, the average torque of the motor is 4.47 N·m, the sine wave distortion rate of back-EMF is 1.11%, and the torque ripple is 1.26%. After optimization by the SCM method, the average torque reaches 5.07 N·m, the sine wave distortion rate of back-EMF is 0.58%, and the torque ripple is 0.97%. It can be seen that the motor optimized by SCM not only achieves higher torque and lower torque ripple but also improves the sinusoidal quality of back-EMF.

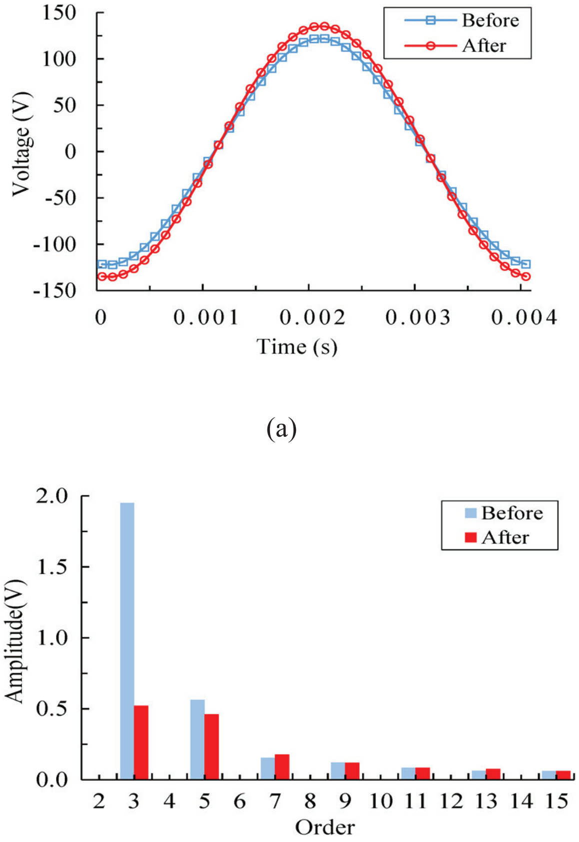

(b)

Fig. 7. Comparison of back-EMF and harmonic waveform before and after optimization: (a) back-EMF and (b) harmonic wave.

V. CONCLUSION

This paper proposes a multi-objective optimization algorithm based on SCM to achieve an efficient structural design of PM motors. A double-layer Halbach PM motor is used as an example, with torque, back-EMF, THD, and torque ripple as optimization objectives. The design parameters are divided into two subspaces through sensitivity analysis and optimized separately under the SCM framework to improve efficiency and reduce computation. Compared with GA, FEM-based results show that SCM provides clear advantages in optimization efficiency.

ACKNOWLEDGMENT

This research was funded by the National Natural Science Foundation of China under grant number 52377037.

REFERENCES

[1] T. A. Huynh and M. F. Hsieh, "Performance analysis of permanent magnet motors for electric vehicles (EV) traction considering driving cycles," *Energies*, vol. 11, no. 6, p. 1385, May 2018.

[2] C. Gong, Y. Hu, J. Gao, Z. Wu, J. Liu, H. Wen, and Z. Wang, "Winding-based DC-bus capacitor discharge technique selection principles based on parametric analysis for EV-PMSM drives in post-crash conditions," *IEEE Transactions on Power Electronics*, vol. 36, no. 3, pp. 3551–3562, Mar. 2021.

[3] H. Dhulipati, S. Mukundan, Z. Li, E. Ghosh, J. Tjong, and N. C. Kar, "Torque performance enhancement in consequent pole PMSM based on magnet pole shape optimization for direct-drive EV," *IEEE Transactions on Magnetics*, vol. 57, no. 2, pp. 1–7, Feb. 2021.

[4] W. Wei, J. Zhang, J. Yao, S. Tang, and S. Zhang, "Performance analysis and optimization of power density enhanced PMSM with magnetic stripe on rotor," *Energies*, vol. 13, no. 17, p. 4457, Sep. 2020.

[5] R. Dutta, A. Pouramin, and M. F. Rahman, "A novel rotor topology for High-Performance fractional slot concentrated winding interior permanent magnet machine," *IEEE Transactions on Energy Conversion*, vol. 36, no. 2, pp. 658–670, June 2021.

[6] W. Chai, Z. Cai, B. I. Kwon, and J. W. Kwon, "Design of a novel low-cost consequent-pole permanent magnet synchronous machine," *IEEE Access*, vol. 8, pp. 194251–194259, 2020.

[7] H. Sato and H. Igarashi, "Automatic design of PM motor using Monte Carlo tree search in conjunction with topology optimization," *IEEE Transactions on Magnetics*, vol. 58, no. 9, pp. 1–4, Sep. 2022.

[8] J. Wu, X. Zhu, D. Fan, Z. Xiang, L. Xu, and L. Quan, "Robust optimization design for permanent magnet machine considering magnet material uncertainties," *IEEE Transactions on Magnetics*, vol. 58, no. 2, pp. 1–7, Feb. 2022.

[9] L. Xu, W. Wu, and W. Zhao, "Airgap magnetic field harmonic synergetic optimization approach for power factor improvement of PM vernier machines," *IEEE Transactions on Industrial Electronics*, vol. 69, no. 12, pp. 12281–12291, Dec. 2022.

[10] J. Bai, L. Wang, D. Wang, A. P. Duffy, and G. Zhang, "Validity evaluation of the uncertain EMC simulation results," *IEEE Transactions on Electromagnetic Compatibility*, vol. 59, no. 3, pp. 797–804, June 2017.

[11] M. Naseh, S. Hasanzadeh, S. M. Dehghan, H. Rezaei, and A. S. Al-Sumaiti, "Optimized design of rotor barriers in PM-assisted synchronous reluctance machines with Taguchi method," *IEEE Access*, vol. 10, pp. 38165–38173, 2022.

[12] J. Bai, G. Zhang, A. P. Duffy, and L. Wang, "Dimension-reduced sparse grid strategy for a stochastic collocation method in EMC software," *IEEE Transactions on Electromagnetic Compatibility*, vol. 60, no. 1, pp. 218–224, Feb. 2018.

[13] J. Bai, K. Gou, J. Sun, and N. Wang, "Application of the multi-element grid in EMC uncertainty simulation," *Appl. Comput. Electromagn. Soc. J.*, vol. 37, no. 4, pp. 428–434, Apr. 2022.

[14] Y. M. You, "Optimal design of PMSM based on automated finite element analysis and metamodeling," *Energies*, vol. 12, no. 24, p. 4673, Dec. 2019.

[15] D. Xiu and G. Karniadakis, "The Wiener-Askey polynomial chaos for stochastic differential equations," *SIAM Journal on Scientific Computing*, vol. 24, no. 2, pp. 619–644, Oct. 2002.

[16] B. Kou, H. Cao, W. Li, and X. Zhang, "Analytical analysis of a novel double layer Halbach permanent magnet array," *Transactions of China Electrotechnical Society*, vol. 30, no. 10, pp. -76, 2015.

[17] J. Morio, "Global and local sensitivity analysis methods for a physical system," *European Journal of Physics*, vol. 32, no. 6, pp. 1577–1583, Nov. 2011.

[18] W. Yan, H. Chen, H. Liu, X. Ma, Z. Lv, X. Wang, R. Palka, L. Chen, and K. Wang "Design and multi-objective optimization of switched reluctance machine with iron loss," *IET Electr. Power Appl.*, vol. 13, no. 4, pp. 435–444, Apr. 2019.

[19] X. Niu, S. Liu, and R. Qiu, "Efficient electromagnetic compatibility optimization design based on the stochastic collocation method," *Appl. Comput. Electromagn. Soc. J.*, vol. 39, no. 6, pp. 533–541, June 2024.

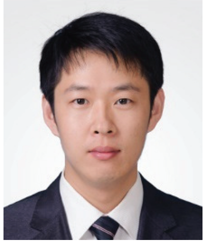

Haichuan Cao was born in China and is a Ph.D. lecturer. His current research interests are permanent magnet motors, marine rim propulsion motors and related fields. His main research areas are motor structure design and optimization, motor magnetic field analysis and optimization calculation, and drive and control technology.

Jian Xiao received the bachelor's degree in engineering. In 2023, he graduated from Dalian Maritime University, majoring in marine electronics and electrical engineering. He is currently a graduate student in electrical engineering at Dalian Maritime University, and his main research direction is the design and optimization analysis of six-phase permanent magnet linear motors.

Chengzhou Yang was born in 1996. He completed a master's degree in Electrical Engineering at Dalian Maritime University from 2020 to 2023, with research specializing in the design and optimization of switched reluctance motors. Since 2023, he has been employed at State Grid Shandong Electric Power Company Laiwu Power Supply Company.

Jingwei Zhu (Member, IEEE) received the B.S. degree in automation instrumentation engineering from Jinzhou Institute of Technology, Jinzhou, China, in 1985, the M.S. degree in electronic engineering from the Shenyang University of Technology, Shenyang, in 1990, and the Ph.D. degree in electrical engineering from Adelaide University, Adelaide, SA, Australia, in 2008. He was a Lecturer and an Associate Professor with the Jinzhou Institute of Technology, from 1985 to 1999. In 2000, he joined the Marine Electrical Engineering College, Dalian Maritime University, Dalian, where he is currently a Professor. His research interests include design and control for electrical machine systems, power electronic devices, and sustainable energy generation.